

Martin Hohenadler

---

---

**Numerical investigation of strongly correlated  
electron-phonon models**

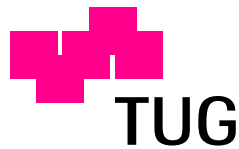
---

---

**DISSERTATION**

zur Erlangung des akademischen Grades  
Doktor der Technischen Wissenschaften  
an der

Technischen Universität Graz



Begutachter:

Univ.-Prof. Dipl.-Ing. Dr. rer. nat. Wolfgang von der Linden  
Institut für Theoretische Physik – Computational Physics  
TU Graz

und

Prof. Dr. rer. nat. habil. Holger Fehske  
Institut für Physik  
Ernst-Moritz-Arndt-Universität Greifswald

Graz, September 2004

This document is available online at [www.hohenadler.com](http://www.hohenadler.com).

*for Kathrin*



**You can't wait for inspiration. You have to go after it with a club.**

(Jack London)

## Richard Feynman and the polaron problem

One day, towards the end of August 1954, Feynman was feeling low, with nothing to do, and felt like goofing off. At that time, there was a pretty librarian working at the Caltech library, so he went to the library to look at her. There, as a cover, he just picked up a journal in order to have something to do to appear busy, and it was an issue of *Advances in Physics*: there was an article in it by Herbert Fröhlich on slow electrons moving in a polarizable crystal like sodium chloride. Fröhlich described the problem, and said that if this problem were solved it would go a long way toward understanding superconductivity, a remark which Feynman did not understand in the slightest; it was, in fact, not correct.

[...]

On 8 September 1954, Richard Feynman wrote to Herbert Fröhlich: “*We have very pretty librarians. Last week I went to enjoy the scenery and picked up Advances in Physics as a cover. I read your article. I became more interested in it than in the librarians and resolved to accept your challenge to find a method uniformly valid over the entire range of [the coupling constant]. Enclosed is my solution. ... What do we have to do to understand superconductivity?*”

From *The beat of a different drum* by J. Mehra [1].



# Abstract

Strongly correlated electron-phonon models with dispersionless phonons and a coupling term of the Holstein type are studied using quantum Monte Carlo (QMC), cluster perturbation theory (CPT), exact diagonalization (ED) and variational approaches. The emphasis lies on the adiabatic regime, which represents a serious challenge and cannot be accurately described analytically at intermediate or strong electron-phonon coupling. The calculations focus on spectral properties, which contain a wealth of information about the excitations of the systems.

The small-polaron cross over in the Holstein model with one electron is investigated in one to three dimensions at zero and finite temperature. Using CPT together with the Lanczos method, the one-electron spectral function is obtained at continuous wavevectors. A novel QMC method is developed based on the canonical Lang-Firsov transformation. It is free of any autocorrelations and employs an exact sampling of the phonon degrees of freedom. Consequently, it can be used to study any phonon frequency and electron-phonon coupling strength. It is found that the physics of the Holstein polaron can be described by a simple variational approach, based on an extended Lang-Firsov transformation, which is shown to yield surprisingly good results in parameter regimes where the standard strong-coupling approach fails completely.

Furthermore, the one-electron spectrum of the Holstein-Hubbard model with two electrons is studied by means of CPT. It reveals the competition between polaron and bipolaron states as the electron-phonon coupling and the Coulomb interaction are varied. The dispersion of the bipolaron band is found to display significant deviations from a simple tight-binding band, which may be attributed to next-nearest-neighbor hopping processes. The one-electron QMC algorithm is extended to study the Holstein-Hubbard bipolaron in the adiabatic regime. Investigating the evolution of bipolaron states with increasing temperature, a thermal dissociation of the intersite bipolaron is found at high temperatures, as predicted for the paramagnetic state of some manganites. A variational approach is presented which reproduces qualitatively the effect of retardation on bipolaron formation.

Finally, the spinless Holstein model with many electrons is studied in one and two dimensions using CPT in combination with the exact atomic-limit Green function, QMC and the kernel polynomial method. The combination of an improved determinant QMC method and ED calculations on shared-memory systems produces accurate results in the adiabatic regime over the whole range of electron-phonon coupling. Most importantly, starting from the low-density limit, we observe a cross over from a polaronic state to a metallic state with increasing band filling in the intermediate coupling regime. Similar effects are expected to play an important role in materials with strong electron-phonon interaction and high carrier density such as, e.g., the manganites.





# Kurzfassung

Die Wechselwirkung zwischen Elektronen und Gitterschwingungen (Phononen) spielt eine wesentliche Rolle in stark korrelierten Materialien wie, z.B. Manganaten. Da für den Bereich kleiner Phononenfrequenzen und mittlerer oder starker Elektron-Phonon Kopplung keine verlässlichen analytischen Zugänge existieren, erfordert eine theoretische Beschreibung dieser Systeme die Verwendung numerischer Verfahren. Die Komplexität der zugehörigen Modelle schränkt Rechnungen mit herkömmlichen Methoden oft stark ein, was die Entwicklung neuer Zugänge motiviert. Im Mittelpunkt dieser Arbeit stehen eine neue Quanten Monte Carlo Methode, sowie die Anwendung der kürzlich entwickelten Cluster Perturbation Theory auf Elektron-Phonon Systeme. Zusätzlich kommen einfache Variationsansätze und exakte Diagonalisierung zum Einsatz. Gemeinsam erlaubt dies die Berechnung von statischen und dynamischen Größen, sowohl bei endlichen Temperaturen als auch im Grundzustand. Zur Vereinfachung beschränkt sich die vorliegende Arbeit auf Modelle mit Holstein Phononen. Die obengenannten Methoden werden verwendet, um den Übergang von freien Elektronen zu Polaronen und Bipolaronen mit zunehmender Stärke der Wechselwirkung, sowie den Einfluss von endlichen Temperaturen, der Phononenfrequenz, der Coulombwechselwirkung und der Ladungsträgerdichte zu untersuchen. Insbesondere richtet sich das Augenmerk auf die Berechnung von Photoemissionsspektren.



# Contents

<b>1</b>	<b>Introduction</b>	<b>1</b>
1.1	Some physics of the manganites . . . . .	2
1.2	Angle-resolved photoemission spectroscopy . . . . .	6
1.3	Microscopic models . . . . .	6
1.3.1	Electron-phonon interaction in the manganites . . . . .	7
1.3.2	Holstein models . . . . .	9
<b>2</b>	<b>Numerical methods</b>	<b>15</b>
2.1	Quantum Monte Carlo . . . . .	16
2.1.1	Basic ideas and importance sampling . . . . .	16
2.1.2	Markov chains and updating schemes . . . . .	18
2.1.3	Sign problem . . . . .	18
2.1.4	Suzuki-Trotter decomposition . . . . .	19
2.1.5	Autocorrelations and the Jackknife method . . . . .	20
2.1.6	Maximum entropy method . . . . .	22
2.2	Cluster perturbation theory . . . . .	23
2.3	Lanczos method . . . . .	28
2.3.1	Basis states and Hilbert space truncation . . . . .	28
2.3.2	Ground state and static properties . . . . .	30
2.3.3	Dynamic properties . . . . .	31
2.4	Kernel polynomial method . . . . .	32
<b>3</b>	<b>Holstein polaron</b>	<b>35</b>
3.1	Holstein polaron . . . . .	35
3.2	One-particle spectral function . . . . .	37
3.2.1	Introduction . . . . .	37
3.2.2	Application of cluster perturbation theory . . . . .	38
3.2.3	Comparison with exact diagonalization . . . . .	39
3.2.4	Results in one dimension . . . . .	41
3.2.5	Results in two dimensions . . . . .	43
3.3	Transformed Hamiltonians . . . . .	44
3.4	Variational polaron approach . . . . .	47
3.4.1	Results . . . . .	50

3.5	Quantum Monte Carlo approach . . . . .	53
3.5.1	Introduction . . . . .	53
3.5.2	Monte Carlo for the transformed model . . . . .	55
3.5.3	Results . . . . .	70
3.5.4	Performance . . . . .	80
3.6	Conclusions . . . . .	80
<b>4</b>	<b>Holstein-Hubbard bipolaron</b>	<b>83</b>
4.1	Holstein-Hubbard bipolaron . . . . .	83
4.2	One-particle spectral function . . . . .	86
4.2.1	Method . . . . .	86
4.2.2	Results . . . . .	88
4.3	Transformed Hamiltonians . . . . .	98
4.4	Quantum Monte Carlo . . . . .	99
4.4.1	Partition function . . . . .	99
4.4.2	Observables . . . . .	101
4.4.3	Numerical details and performance . . . . .	101
4.4.4	Results . . . . .	103
4.5	Variational approach . . . . .	108
4.5.1	Results . . . . .	110
4.6	Conclusions . . . . .	114
<b>5</b>	<b>Photoemission spectra of many-polaron systems</b>	<b>115</b>
5.1	Spinless Holstein model . . . . .	116
5.2	Strong-coupling perturbation theory . . . . .	117
5.2.1	Many-body coherent potential approximation . . . . .	117
5.2.2	Strong coupling perturbation theory . . . . .	119
5.3	Quantum Monte Carlo method . . . . .	120
5.3.1	Partition function . . . . .	121
5.3.2	Observables . . . . .	123
5.3.3	Sign problem . . . . .	125
5.4	QMC and ED results . . . . .	127
5.4.1	Limiting cases . . . . .	129
5.4.2	Intermediate coupling . . . . .	133
5.4.3	Nonadiabatic regime . . . . .	137
5.4.4	Kinetic energy . . . . .	139
5.5	Conclusions . . . . .	140
	<b>Summary</b>	<b>141</b>
	<b>Acknowledgments</b>	<b>153</b>
	<b>Curriculum Vitae</b>	<b>155</b>

# List of Figures

1.1	Crystal field and Jahn-Teller splitting. . . . .	2
1.2	The ideal cubic perovskite structure of $\text{LaMnO}_3$ . . . . .	3
1.3	Phase diagrams of LSMO and LCMO. . . . .	4
1.4	Resistivity of LSMO and LCMO. . . . .	5
1.5	The $\text{MnO}_6$ octahedron. . . . .	7
1.6	Normal phonon modes. . . . .	8
2.1	Cluster tilings. . . . .	25
3.1	Comparison of ED and CPT spectra for the Holstein polaron. . . . .	39
3.2	Spectral function of the Holstein polaron (1D, $\bar{\omega} = 0.8$ , $\lambda = 0.25$ ). . . . .	40
3.3	Spectral function of the Holstein polaron (1D, $\bar{\omega} = 1.0$ , $\lambda = 0.5$ ). . . . .	41
3.4	Spectral function of the Holstein polaron (1D, $\bar{\omega} = 1.0$ , $\lambda = 1.0$ ). . . . .	42
3.5	Spectral function of the Holstein polaron (1D, $\bar{\omega} = 1.0$ , $\lambda = 2.0$ ). . . . .	43
3.6	Spectral function of the Holstein polaron (2D, $\bar{\omega} = 2.0$ , $\lambda = 0.945$ ). . . . .	44
3.7	Illustration of the Lang-Firsov transformation. . . . .	46
3.8	Total energy and QP weight from VPA. . . . .	51
3.9	Comparison of total energy from VPA and Global-Local method. . . . .	51
3.10	Distortion fields from VPA. . . . .	52
3.11	Kullback-Leibler number for Holstein polaron. . . . .	62
3.12	Sign problem for different cluster sizes (1D). . . . .	66
3.13	Sign problem for different boundary conditions (2D). . . . .	67
3.14	Sign problem for different $\beta$ and $\bar{\omega}$ (2D). . . . .	68
3.15	Sign problem for different cluster sizes (3D). . . . .	69
3.16	Kinetic energy for different $\bar{\omega}$ (1D). . . . .	71
3.17	Total energy for different $\bar{\omega}$ (1D). . . . .	72
3.18	Momentum distribution and $\langle p^2 \rangle$ (1D). . . . .	73
3.19	Kinetic energy for different $\bar{\omega}$ (2D). . . . .	74
3.20	Kinetic energy for different cluster sizes (2D). . . . .	75
3.21	Finite-size scaling of the kinetic energy (2D). . . . .	76
3.22	Kinetic energy for different $\beta$ (2D). . . . .	77
3.23	Temperature-scaling of the kinetic energy (2D). . . . .	78
3.24	Kinetic energy (1D – 3D). . . . .	79

4.1	Spectral function for $\bar{\omega} = 4$ , $\bar{U} = 0$ and various $\lambda$ . . . . .	90
4.2	Density plot of the spectral function for $\bar{\omega} = 4$ and $\bar{U} = 0$ . . . . .	91
4.3	Spectral function for $\bar{\omega} = 1$ , $\bar{U} = 0$ and various $\lambda$ . . . . .	93
4.4	Spectral function for $\bar{\omega} = 1$ , $\bar{U} = 4$ and various $\lambda$ . . . . .	95
4.5	Comparison of CPT and ED for $\bar{\omega} = 1$ , $\bar{U} = 4$ and $\lambda = 0.5$ . . . . .	96
4.6	Bipolaron band dispersion for different $\bar{U}$ and $\lambda$ . . . . .	98
4.7	Finite-size effects of the kinetic energy. . . . .	103
4.8	Kinetic energy for different phonon frequencies from QMC. . . . .	104
4.9	Finite-temperature effects of the kinetic energy. . . . .	104
4.10	$\langle n_{i\uparrow} n_{i+\delta\downarrow} \rangle$ from QMC. . . . .	105
4.11	Kinetic energy and $\langle n_{i\uparrow} n_{i+\delta\downarrow} \rangle$ from QMC. . . . .	106
4.12	Temperature dependence of $\langle n_{i\uparrow} n_{i+\delta\downarrow} \rangle$ from QMC. . . . .	107
4.13	Comparison of the ground-state energy. . . . .	110
4.14	Variational kinetic energy. . . . .	111
4.15	$\bar{E}_k$ , $\rho(0)$ and $\rho(1)$ from variational approach. . . . .	112
4.16	$U_{\text{eff}}$ and $\rho(\delta)$ from variational approach. . . . .	113
5.1	Charge density wave and Peierls state. . . . .	116
5.2	Spectral function of the spinless Holstein model by SCPT and CPA. . . . .	119
5.3	Sign problem for different temperatures and phonon frequencies. . . . .	126
5.4	Sign problem for different fillings and system sizes. . . . .	126
5.5	QMC spectral function for different $n$ and $\lambda = 0.1$ . . . . .	130
5.6	Energy band and wavevectors of free electrons. . . . .	131
5.7	QMC spectral function for different $n$ and $\lambda = 2.0$ . . . . .	132
5.8	QMC spectral function for different $n$ and $\lambda = 1.0$ . . . . .	133
5.9	Density of states for different band fillings. . . . .	135
5.10	ED and QMC spectral function for different $n$ and $\lambda = 1.0$ . . . . .	136
5.11	ED spectral function in the nonadiabatic regime. . . . .	138
5.12	Kinetic energy as a function of $\lambda$ . . . . .	139

# 1 Introduction

The coupling of charge carriers to the lattice degrees of freedom is known to play an important role in many *strongly correlated materials*, in which the strong mutual interaction between electrons and electrons, on the one hand, and between electrons and phonons, on the other hand, gives rise to new collective phenomena which cannot be described within the approximation of independent electrons. Upon the most prominent members of this family are the high-temperature superconductors, e.g., the cuprates. Despite the still hotly debated key mechanism for the high transition temperature in these systems, electron-lattice effects have been identified as a nonnegligible component for realistic models [2]. Apart from this very active field, electron-phonon interaction is also of great importance in more recently discovered transition metal oxides, namely the manganites [3] and the vanadates [4].

As a result of the above discoveries, interest in electron-phonon models has revived. Owing to the complexity of such systems, theoretical efforts usually rely on rather crude approximations. In fact, even for the simple and therefore widely studied Holstein molecular-crystal model, no exact solution—valid over the entire range of parameters—exists except for the case of a single electron with a relativistic band structure [5, 6] or in infinite dimensions [7, 8]. As a consequence, a lot of numerical work has been devoted to an understanding of the effects of strong electron-phonon interaction. While the model with one and two electrons is by today quite well understood, the many-electron case—realized in experiments—is still in the focus of intensive research. Despite the known shortcomings of, e.g., small-polaron theory [9], unjustified approximations are still widely used to explain experimental data [3]. This often leads to inconsistent and confusing descriptions and makes progress towards a more complete understanding of electron-phonon models highly desirable.

In this work, numerical methods are employed to study the Holstein model, with and without Coulomb interaction. To be more specific, we use quantum Monte Carlo (QMC), which has contributed a lot to the advances in condensed matter theory in the last decades [10], cluster perturbation theory [11, 12] and exact diagonalization. In combination, these techniques, which are reviewed in Chap. 2, will enable us to study the ground state as well as finite temperatures by calculating static and dynamic properties.

As the complexity of the physics increases significantly with the number of electrons, we shall first consider the one-electron case. To this end, we study in Chap. 3 the cross over from a weakly dressed quasiparticle for weak electron-phonon coupling, to a heavy small polaron in the strong-coupling regime. We then proceed to the case of two electrons in the

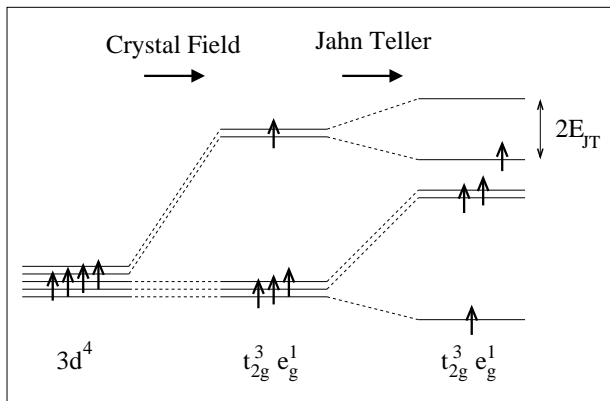


Figure 1.1: Energy levels of  $\text{Mn}^{3+}$  in the presence of crystal-field and JT splitting. Here  $E_{\text{JT}}$  is the JT splitting energy.

Holstein-Hubbard model (Chap. 4), which can form a bound state even in the presence of strong Coulomb repulsion due to the phonon-mediated, attractive interaction. Although theories of high-temperature superconductivity based on a condensation of bipolarons into a Bose-Einstein state have been shown to exhibit several shortcomings [13, 14], similar to other approaches, they are capable of explaining several experiments. Some authors also argue that bipolarons play a dominant role in the manganites, and may even account for the metal-insulator transition and colossal magnetoresistance (CMR) [15]. Finally, in Chap. 5, we study the spinless Holstein model with many electrons, which represents a system of interacting polarons. In addition to the purely numerical methods, we present simple variational approaches to the Holstein model with one and two electrons, as well as a strong-coupling perturbation theory, based on the exact atomic-limit Green function, for the spinless Holstein model at half filling.

In the remainder of this chapter, we first give a short review of the manganites (Sec. 1.1)—focusing on the ferromagnetic regime—and briefly discuss angle-resolved photoemission spectroscopy, which has proved to be extremely useful to obtain information about the electronic states of strongly correlated materials (Sec. 1.2). Finally, in Sec. 1.3, we derive the model Hamiltonians considered in this work, and motivate the study of Holstein models.

## 1.1 Some physics of the manganites

Interest in manganites of the form  $\text{R}_{1-x}\text{A}_x\text{MnO}_3$ , where R is a trivalent rare-earth ion such as La or Nd, and A is a divalent alkaline-earth ion such as Ca or Sr, has revived in the 1990's due to the discovery of CMR. Originally, these compounds have already been studied by Jonker and van Santen in the 1950's [16, 17], and an extensive review of the early work on perovskite manganites is by Coey *et al.* [18]. Similar to the high-temperature superconductors, the metallic state obtained by sufficiently large doping  $x$  is very different



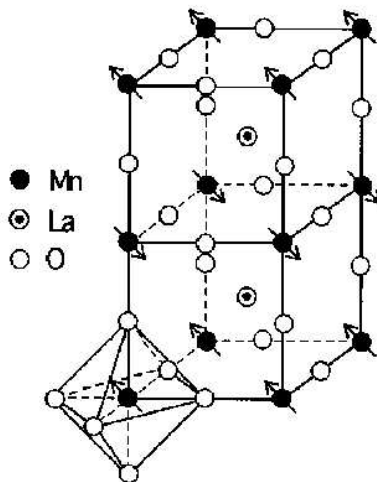


Figure 1.2: The ideal cubic perovskite structure of  $\text{LaMnO}_3$  [19].

from ordinary metals. In fact, the understanding of its properties was the starting point for a lot of research activity which has recently been reviewed by Edwards [3].

Two of the most studied materials are  $\text{La}_{1-x}\text{Sr}_x\text{MnO}_3$  (LSMO) and  $\text{La}_{1-x}\text{Ca}_x\text{MnO}_3$  (LCMO). The parent compound  $\text{LaMnO}_3$  ( $x = 0$ ) is an antiferromagnetic insulator, in which each Mn ion has four d electrons corresponding to a  $\text{Mn}^{3+}$  configuration. As illustrated in Fig. 1.1, the crystal field splits the 3d orbitals into a lower-lying  $t_{2g}$  triplet of  $xy$ ,  $yz$  and  $zx$  symmetry, and a higher-lying  $e_g$  doublet of  $x^2 - y^2$  and  $3z^2 - r^2$  symmetry. Due to Hund's rule, the d electrons align their spins to form a  $t_{2g}^3 e_g^1$  state with total spin  $S = 2$ . Upon doping,  $x$  electrons per Mn atom are removed, and a narrow  $e_g$  band—resulting from the overlap with the p levels of bridging  $\text{O}^{2-}$  ions—gives rise to metallic behavior with  $n = 1 - x$  carriers per atom. The insulating state for  $x = 0$  can be understood within the Mott-Hubbard picture, with the strong correlations due to Hund's rule suppressing double occupation of sites. For  $x > 0$ , the three  $t_{2g}$  electrons are usually regarded as forming a localized spin with  $S = 3/2$  [3]. The itinerant  $e_g$  electrons are completely spin-polarized, and align the local spins ferromagnetically via the so-called double exchange (DE) mechanism. The latter involves strong Hund's exchange interaction at two neighboring lattice sites, and has first been proposed by Zener [20].

The crystal structure of  $\text{LaMnO}_3$  is based on the perovskite structure shown in Fig. 1.2. In the manganites, the lattice is modified by two types of distortions of the oxygen octahedrons surrounding each Mn site (see Fig. 1.2). The first consists of a rotation and tilting due to the smaller size of the  $\text{La}^{3+}$  ions compared to the  $\text{O}^{2-}$  ions, and the second is a tetragonal distortion due to the Jahn-Teller (JT) effect. The latter splits the degeneracy of the  $e_g$  orbitals (see Fig. 1.1), and gives rise to strong electron-phonon interaction. The resulting distortions in  $\text{LaMnO}_3$  are large, with displacements of the oxygen ions from their ideal positions of about  $0.15 \text{ \AA}$ , compared to a typical Mn–Mn spacing of  $4 - 5 \text{ \AA}$  [19]. The JT effect will be discussed in more detail in Sec. 1.3.1, where we derive a model Hamil-

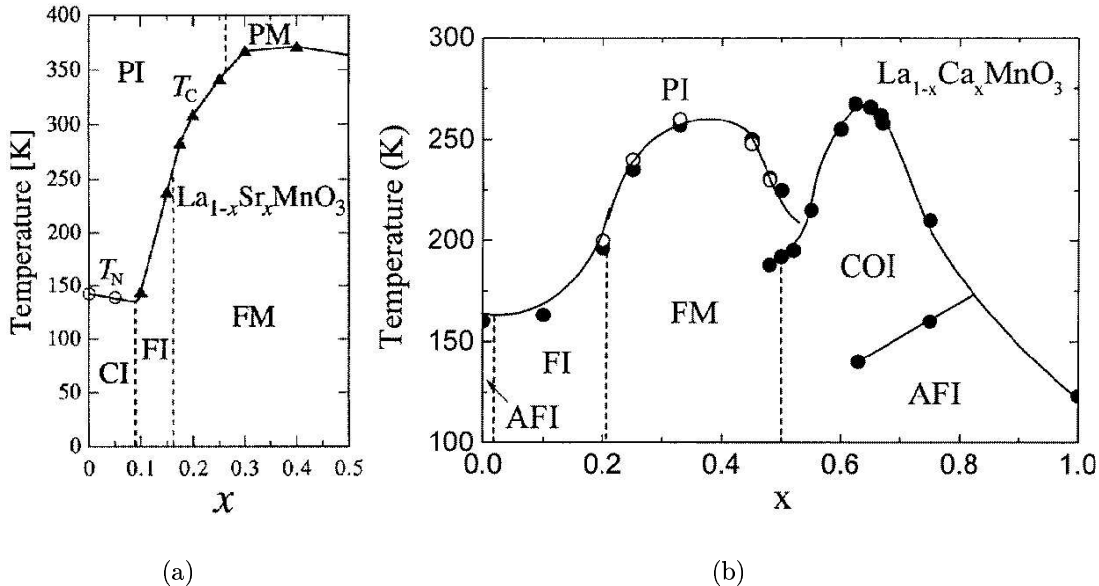


Figure 1.3: Phase diagrams for (a) LSMO [21] and (b) LCMO [22]. The various states are: paramagnetic insulating (PI), paramagnetic metal (PM), canted insulating (CI), ferromagnetic insulating (FI), ferromagnetic metal (FM), antiferromagnetic insulating (AFI) and charge-ordered insulating (COI).  $T_C$ ,  $T_N$  are Curie and Neél temperatures, respectively.

tonian for the manganites. As discussed by Edwards [3], the Mn–O–Mn bond angle is a very important parameter. Even small reductions from the ideal value of  $180^\circ$  as a result of lattice distortions lead to a narrowing of the  $e_g$  conduction band which dramatically affects the physical properties.

In Fig. 1.3, we show phase diagrams as a function of doping  $x$  and temperature  $T$ , both for LSMO and LCMO. At low temperatures, there is a transition from an antiferromagnetic insulator near  $x = 0$ , to a ferromagnetic insulator up to  $x \approx 0.2$ , to a ferromagnetic metal for  $x > 0.2$ . As we approach  $x = 0.5$ , charge and orbital order set in, but for  $x \simeq 0.2$ – $0.4$ , such effects are expected to be negligible. At first sight, the diagrams for LSMO and LCMO look very similar for  $x < 0.5$ . However, a closer look reveals important differences. While LSMO remains metallic upon heating from the ferromagnetic state, LCMO exhibits a metal-insulator transition with a relatively large resistivity in the paramagnetic phase above the Curie temperature  $T_C$ . The latter takes on a maximum near  $x \approx 1/3$  in both materials. The differences between LSMO and LCMO are better illustrated by the dc resistivity data depicted in Fig. 1.4. For LSMO [Fig. 1.4(a),  $x = 0.3$ ], we see that the resistivity  $R$  increases with temperature in the whole range of  $T$  shown. This is in strong contrast to LCMO [Fig. 1.4(b)], for which the behavior of  $R$  changes from  $\partial R/\partial T > 0$  for  $T < T_C$  to  $\partial R/\partial T < 0$  for  $T > T_C$ . Additionally,  $T_C$  is significantly lower in LCMO ( $\approx 260$  K) than in LSMO ( $\approx 370$  K), and the value of  $\rho$  above the Curie temperature is about one

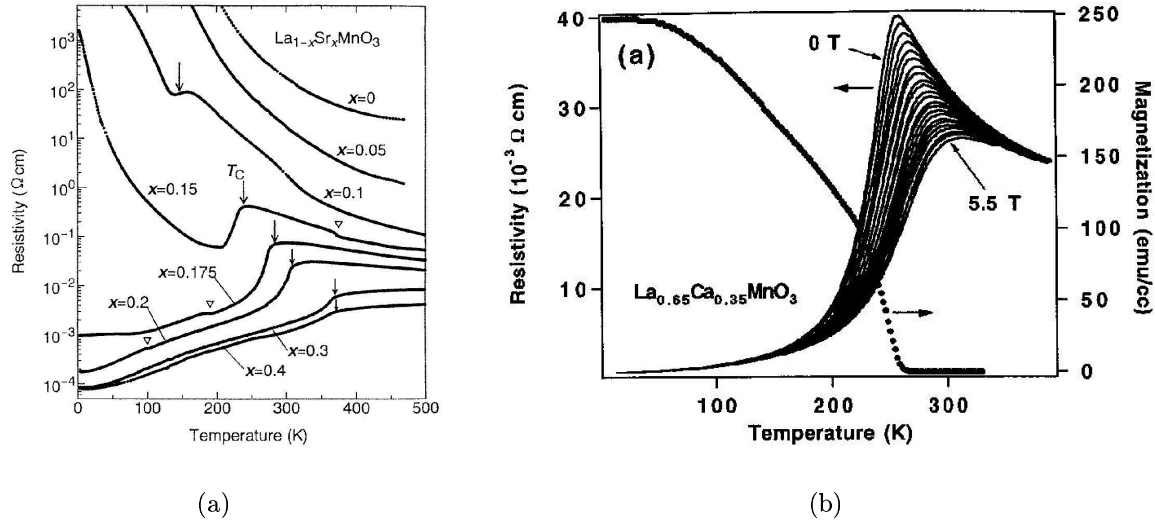


Figure 1.4: (a) Resistivity versus temperature for  $\text{La}_{1-x}\text{Sr}_x\text{MnO}_3$  crystals. Arrows indicate the Curie temperature  $T_C$  for the ferromagnetic phase transition [23]. (b) Resistivity (solid lines) of  $\text{La}_{0.65}\text{Ca}_{0.35}\text{MnO}_3$ , acquired in applied fields ranging from 0 to 5.5 T, and the bulk magnetization in an in-plane applied field of 50 G ( $\bullet$ ), both as a function of temperature [24].

order of magnitude larger in LCMO. Keeping in mind the minimal size difference between Ca and Sr ions, this is very surprising. A consistent analytical theory explaining many of the observed phenomena has been proposed by Green [25]. It is based on the assumption of a slightly stronger electron-phonon interaction in LCMO, caused by a reduced bandwidth due to smaller Mn–Mn bond angles [3].

For completeness, we would like to briefly discuss the CMR effect, which can be seen in Fig. 1.4(b). In the vicinity of  $T_C$ , the resistivity of LCMO can be reduced by about 50% by applying a magnetic field of about 5 T, while no such effect occurs for LSMO. This suggests that the underlying mechanism is closely related to the metal-insulator transition. Actually, it was the CMR effect and its potential application in magnetic sensors used, e.g., in storage devices, which drove much of the recent work on manganites. However, despite the fact that the CMR effect can be increased to relative changes in resistivity of up to  $10^5$  [26] by using thin films instead of bulk samples, the future use in, e.g., hard drives is unlikely. The reasons for this are on the one hand the large required fields as compared to giant magnetoresistance materials currently in use and, on the other hand, the high sensitivity of CMR to small changes in temperature.

## 1.2 Angle-resolved photoemission spectroscopy

In recent years, angle-resolved photoemission spectroscopy (ARPES) has emerged as one of the most important tools for studying strongly correlated systems. The increasing popularity of this method is a result of the continuous improvement of experimental techniques, which has significantly increased the accuracy (energy and momentum resolution) and reliability. One of the main advantages of ARPES, which also makes it very attractive to theoretical physicists, is the fact that results can often [27] be compared directly to the one-electron spectral function, a quantity of great importance in the description of many-particle systems. Here we shall only give a brief discussion of the physical ideas, without going into details about the experimental setup. For more information, see, e.g., [28].

The principle underlying ARPES is the photoelectric effect. Using, e.g., a helium-discharging lamp, light of a single frequency  $\omega_0$  is emitted onto a small, thin specimen of the material of interest. The incident photons cause emission of electrons, which are then analyzed in terms of intensity, momentum and kinetic energy. This provides one with information about the properties of the electron after it has left the specimen, which can be related, for example, to the energy of the particle before the emission process by exploiting the conservation of energy. This is expressed in the equation

$$\hbar\omega_0 = E_{\text{kin}} + \phi + |E_{\text{B}}|, \quad (1.1)$$

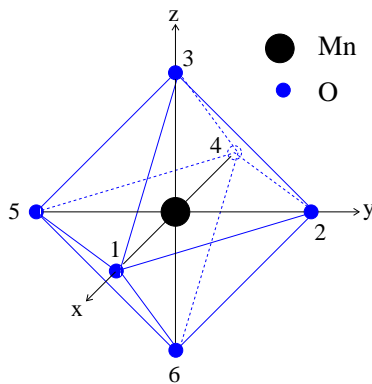
where  $\hbar\omega_0$  is the photon energy,  $E_{\text{kin}}$  and  $E_{\text{B}}$  denote the kinetic and binding energy of the electron, respectively, and  $\phi$  corresponds to the so-called work function. The latter is a property of the material, and equals the minimum energy required to emit a single electron.

Similarly, the conservation of momentum, together with the measured angles at which the electron leaves the sample, can be used to extract the momentum of the electron before the emission from the specimen. We would like to point out that, owing to the discontinuity of the surface of the sample, only the component of momentum parallel to the surface is conserved. Moreover, the momentum of the photon can be neglected in the analysis.

Using these ideas, ARPES yields the intensity of electrons as a function of energy and momentum. As a consequence of scattering processes, the peaks obtained with ARPES are always broadened. Nevertheless, the results provide detailed information about the nature and lifetime of quasiparticle states, which can be compared to theoretical calculations.

## 1.3 Microscopic models

As pointed out above, progress in condensed matter theory is often based on the use of simplified models, which can be treated either by analytical or numerical techniques. To illustrate the process of finding a microscopic model for a given material, we present here a derivation of the model Hamiltonian for the electron-phonon interaction in the manganites. Since an exact quantum-mechanical treatment of the lattice degrees of freedom is not yet possible, we will then restrict ourselves to models of the Holstein type.

Figure 1.5: The  $\text{MnO}_6$  octahedron.

### 1.3.1 Electron-phonon interaction in the manganites

In general, the orbital states of electrons are strongly coupled to the lattice. In the manganites, the double degeneracy of the  $e_g$  orbitals gives rise to a JT effect, which consists of the splitting of otherwise degenerate orbitals by lattice distortions, so as to reduce the symmetry. This lowers the energy of the orbitals involved, since the energy cost is proportional to the square of the displacement, while the gain in energy—given by twice the JT energy  $E_{\text{JT}}$  (see Fig. 1.1)—depends linearly on the size of the distortion [29]. Therefore, for small enough displacements, the JT splitting always wins and the orbitals will be energetically split. In the sequel, we shall derive the Hamiltonian for the JT effect in  $\text{LaMnO}_3$ , neglecting the dynamics of the lattice. The discussion follows closely the article by Allen and Perebeinos [30].

The key structural element here is the  $\text{MnO}_6$  octahedron, shown in Fig. 1.5. As discussed by Yosida [29], only vibration modes with distortions along the bonds between neighboring Mn ions, corresponding to the  $x$ -,  $y$ - and  $z$ -axes in Fig. 1.5, couple to the  $e_g$  orbitals. To derive the form of the electron-phonon interaction, it is useful to work in the following overcomplete basis of the  $e_g$  subspace [30]

$$\psi_x = 3x^2 - r^2, \quad \psi_y = 3y^2 - r^2, \quad \psi_z = 3z^2 - r^2, \quad (1.2)$$

where  $\psi_x + \psi_y + \psi_z = 0$ , and  $r^2 = x^2 + y^2 + z^2 = 1$ . We assume a harmonic restoring force  $-Ku_\alpha$  for a distortion  $u_\alpha$  of an oxygen ion along the  $\alpha$  direction, with  $\alpha = x, y, z$ . The distortion of the  $\text{O}_6$  octahedron surrounding the Mn ion at lattice site  $i$  along the  $\alpha$  axis can be described in terms of the variable  $Q_{i\alpha} = u_\alpha(i + \frac{1}{2}\hat{\alpha}) - u_\alpha(i - \frac{1}{2}\hat{\alpha})$ . Here  $\hat{\alpha}$  denotes a unit vector pointing along the  $\alpha$  direction on the Mn lattice. For an undistorted lattice, the positions of the oxygen ions around site  $i$  are thus given by  $i \pm \frac{1}{2}\hat{\alpha}$ .

The change of energy associated with a distortion  $Q_\alpha$  may be written as  $\partial\epsilon_\alpha/\partial Q_\alpha = -4g/\sqrt{3}$ , where  $\epsilon_\alpha$  denotes the energy of the orbital  $\alpha$  [Eq. (1.2)]. Neglecting any lattice

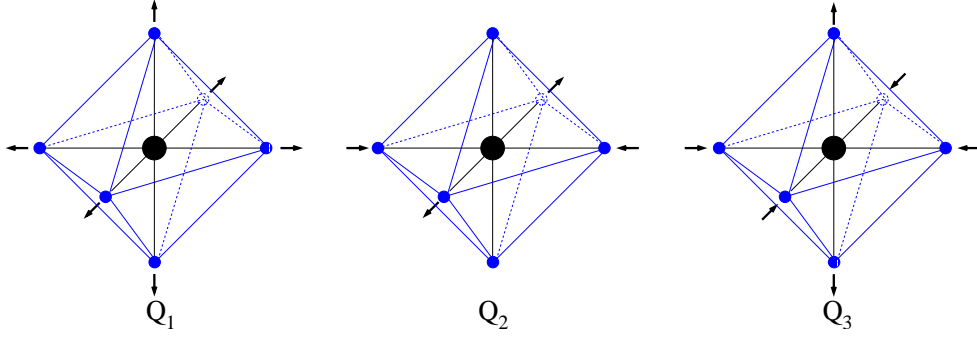


Figure 1.6: The relevant phonon modes in the cubic manganites. Arrows indicate the distortions of the  $\text{MnO}_6$  octahedron.

dynamics, the electron-phonon Hamiltonian takes the form [30]

$$H_{\text{e-ph}} = -\frac{4g}{\sqrt{3}} \sum_{i\alpha} c_{i\alpha}^\dagger c_{i\alpha} Q_{i\alpha} + \frac{K}{2} \sum_{i\alpha} [u_\alpha(i + \hat{\alpha}/2)]^2, \quad (1.3)$$

where  $c_{i\alpha}^\dagger$  is a creation operator for an electron at site  $i$  in orbital state  $\alpha$ , and spin indices have been omitted for simplicity. The second term in Eq. (1.3) corresponds to the elastic energy associated with distortions of the  $\text{O}_6$  octahedrons. A more useful representation of the electron-phonon interaction can be obtained by a transformation to the orbitals [30]

$$\psi_X = \frac{1}{\sqrt{6}} [(\sqrt{3} + 1)\psi_x + (\sqrt{3} - 1)\psi_y] \quad , \quad \psi_Y = \frac{1}{\sqrt{6}} [(\sqrt{3} - 1)\psi_x + (\sqrt{3} + 1)\psi_y] .$$

In terms of these states, the first term of the Hamiltonian (1.3) separates into JT and breathing parts, i.e.,  $H_{\text{el-ph}} = H_{\text{JT}} + H_{\text{br}}$ , with

$$\begin{aligned} H_{\text{JT}} &= -g \sum_i (c_{iX}^\dagger, c_{iY}^\dagger) \begin{pmatrix} Q_{i2} & Q_{i3} \\ Q_{i3} & -Q_{i2} \end{pmatrix} \begin{pmatrix} c_{iX} \\ c_{iY} \end{pmatrix}, \\ H_{\text{br}} &= -\sqrt{2}g \sum_i Q_{i1} [c_{iX}^\dagger c_{iX} + c_{iY}^\dagger c_{iY}]. \end{aligned} \quad (1.4)$$

Here,  $Q_{i1}$ ,  $Q_{i2}$  and  $Q_{i3}$  denote the vibrational eigenmodes [30]

$$\begin{aligned} Q_{i1} &= \sqrt{\frac{2}{3}}(Q_{ix} + Q_{iy} + Q_{iz}), \\ Q_{i2} &= Q_{ix} - Q_{iy}, \\ Q_{i3} &= \frac{1}{\sqrt{3}}(2Q_{iz} - Q_{ix} - Q_{iy}) \end{aligned} \quad (1.5)$$

The JT modes  $Q_2$  and  $Q_3$  (we omit site indices) are of  $e_g$  symmetry and have the same frequency [29], while the  $Q_1$  distortion corresponds to a simple breathing mode.

It is instructive to rewrite the complete electron-phonon Hamiltonian (1.4) in the form

$$\begin{aligned}
 H_{\text{el-ph}} = & -g \sum_{i\sigma} \left[ Q_{i3}(\hat{n}_{iX\sigma} - \hat{n}_{iY\sigma}) + Q_{i2}(c_{iX\sigma}^\dagger c_{iY\sigma} + c_{iY\sigma}^\dagger c_{iX\sigma}) \right] \\
 & - \sqrt{2}g \sum_{i\sigma} Q_{i1}(\hat{n}_{iX\sigma} + \hat{n}_{iY\sigma}) + \frac{1}{2} \sum_i [k_{\text{br}}Q_{i1}^2 + k_{\text{JT}}(Q_{i2}^2 + Q_{i3}^2)] .
 \end{aligned} \tag{1.6}$$

Here we have restored spin indices, and introduced spring constants  $k_{\text{br}}$ ,  $k_{\text{JT}}$  for the energy associated with the breathing and JT modes, respectively. The density operator  $\hat{n}_{iX\sigma}$ , measuring the number of electrons with spin  $\sigma$  in orbital  $X$  at lattice site  $i$ , is defined as  $\hat{n}_{iX\sigma} = c_{iX\sigma}^\dagger c_{iX\sigma}$ . From Eq. (1.6), one can see that the coupling to the mode  $Q_2$  allows a transfer of electrons between  $e_g$  orbitals  $X$  and  $Y$  on the same lattice site. As we shall see in the following section, the coupling to the breathing mode is exactly of the Holstein type. Approximations inherent to Hamiltonian (1.6) are the restriction to static distortions, and the neglect of the coupling between distortions of neighboring oxygen octahedrons, which give rise to long-range orbital order in the manganites. The JT distortion in the latter is predominantly of the  $Q_2$  type. While static displacements have been observed in undoped  $\text{LaMnO}_3$ , there is no experimental evidence for such frozen-in distortions in the metallic compounds with  $x > 0.2$ , and doped manganites therefore have a much more nearly cubic crystal structure. However, dynamical JT effects—in which itinerant  $e_g$  electrons cause a local lattice distortion at the site they occupy—are likely to occur, and the compound object consisting of an electron and the accompanying lattice distortion is often referred to as a *JT polaron*. Although the Holstein models discussed in the following section only include a coupling of electrons to a breathing mode distortion, they do contain the important dynamical lattice effects, in contrast to Eq. (1.6).

### 1.3.2 Holstein models

If lattice fluctuations are taken into account, even the simplified electron-phonon coupling described by Hamiltonian (1.6) usually requires further approximations before numerical methods such as QMC can be applied. While existing work on the manganites often treated the phonons classically, or even on a mean-field level, here we wish to address the case of quantum phonons. The importance of the lattice dynamics results from the fact that the manganites fall into the adiabatic regime of small phonon frequencies, as compared to the width of the conduction band. Therefore, substantial zero-point fluctuations of the  $\text{MnO}_6$  octahedrons around their equilibrium positions occur, which makes a static treatment highly questionable. Moreover, the above-mentioned dynamic JT effects can not be described using a model with classical phonons. Apart from the Holstein model, several other models for electron-phonon interaction have been proposed. Among them are the Fröhlich model [31] with a long-range electron-phonon interaction, and the Su-Schrieffer-Heeger (SSH) model [32], in which the phonons couple to the electronic hopping. However, in the context of the manganites, a local coupling as in the Holstein model seems to be most reasonable, since (a) long-range interactions are screened by the itinerant  $e_g$  electrons, and (b) the coupling to the charge density models well the JT effect.

In principle, it is possible to study a model with dynamical phonons and a coupling term as given in Eq. (1.6) using numerical methods. However, such calculations face severe restrictions of the accessible range of temperature, phonon frequency, electron-phonon coupling strength and system size. We would like to mention that a small cluster of four Mn sites—including all relevant degrees of freedom—has been studied by Weiße and Fehske [33] using exact diagonalization. Moreover, the dynamic JT polaron and bipolaron have been investigated by El Shawish *et al.* [34].

Many interesting phenomena such as, e.g., charge and orbital order, which have been observed in experimental studies of the manganites, can only be described when the cooperative nature of the lattice distortions is taken into account. Work along this line has been done by Benedetti and Zehyer [35] using dynamical mean-field theory (DMFT), and by Vergés *et al.* [36] using the Monte Carlo method. In both approaches, the phonon degrees of freedom are treated in the static approximation. Furthermore, to understand the magnetic phase diagram for  $x > 0.5$  (see Sec. 1.1), it is crucial to take into account the degeneracy of the  $e_g$  band. Corresponding models, either with local or cooperative JT modes, have been considered by Millis *et al.* [37], Zang *et al.* [38], Benedetti and Zehyer [35], Allen and Perebeinos [30], and Hotta *et al.* [39]. Except for the work in [38], which used a variational Lang-Firsov transformation to treat the lattice degrees of freedom, all these studies were restricted to classical phonons.

In the doping regime  $x \simeq 0.2-0.4$ , the only experimentally relevant phases are the ferromagnetic and paramagnetic phases, which can be described even within a one-band model [25]. Furthermore, the manganites fall into the regime  $J_H S \gg t$  [3], where  $J_H \approx 1$  eV denotes the Hund’s rule coupling between local and itinerant spins,  $t \approx 0.1-0.2$  eV [19] is the electron hopping integral, and  $S = 3/2$ . This leads to a splitting of the two  $e_g$  orbitals at each site, which is of the order of  $J_H(2S + 1)$ . If  $J_H S \gg k_B T, t$ , double occupancy of a site is strongly suppressed, and the use of a one-band model is reasonable. Moreover, the degeneracy of the  $e_g$  orbitals is also lifted by JT distortions for  $x \lesssim 0.4$ , and the distortions of  $Q_2$  and  $Q_3$  symmetry (see Sec. 1.3.1) may be modeled by one effective phonon mode of the Holstein type [40]. As long as we are not interested in states with orbital order, this does not represent a loss of generality.

#### Double exchange model

While Eq. (1.6) approximately describes the electron-phonon coupling in the manganites, several other relevant contributions are still missing. Among them is the DE interaction, which is commonly believed to give rise to the ferromagnetism observed at low temperatures in the manganites. The *DE model* is defined as

$$H_{\text{DE}} = -t \sum_{\langle ij \rangle \sigma} c_{i\sigma}^\dagger c_{j\sigma} - J_H \sum_i \boldsymbol{\sigma}_i \cdot \mathbf{S}_i. \quad (1.7)$$

Here the first term describes the hopping of electrons with amplitude  $t$  which gives rise to a free band of width

$$W = 4tD \quad (1.8)$$



in  $D$  dimensions. The symbol  $\langle ij \rangle$  in Eq. (1.7) stands for the hopping processes  $i \rightarrow j$  and  $j \rightarrow i$ , and we have therefore dropped the usual hermitian conjugated term  $c_{j\sigma}^\dagger c_{i\sigma}$ . The second term accounts for the (ferromagnetic) coupling between the itinerant  $e_g$  electrons—described by spin operators  $\boldsymbol{\sigma}_i$ —and the local  $t_{2g}$  spins of magnitude  $3/2$ , denoted as  $\mathbf{S}_i$ . The components of the spin operator  $\boldsymbol{\sigma}_i = (\sigma_i^x, \sigma_i^y, \sigma_i^z)$  of an  $e_g$  electron at site  $i$  are defined by

$$\sigma_i^+ = \sigma_i^x + i\sigma_i^y = c_{i\uparrow}^\dagger c_{i\downarrow}, \quad \sigma_i^- = \sigma_i^x - i\sigma_i^y = c_{i\downarrow}^\dagger c_{i\uparrow}, \quad \sigma_i^z = \frac{1}{2}(\hat{n}_{i\uparrow} - \hat{n}_{i\downarrow}). \quad (1.9)$$

Within the DE model, the mobile carriers can maximize their kinetic energy by aligning all local spins ferromagnetically. However, with increasing temperature, spin fluctuations start to develop, and there is a transition to a paramagnetic state at a Curie temperature  $T_C$  [3]. The disorder of the local spins leads to a narrowing of the  $e_g$  band. However, in the vicinity of  $T_C$ , an applied magnetic field will line up the local spins, thereby increasing the bandwidth. In principle, this explains the decrease of resistivity in a magnetic field near  $T_C$ , but the effect is much smaller than observed experimentally (see Sec. 1.1).

In addition to the DE term, there is an antiferromagnetic coupling of neighboring Mn spins, which is responsible for the antiferromagnetic ground state of the undoped parent compound  $\text{LaMnO}_3$ . The corresponding term in a model Hamiltonian takes the familiar Heisenberg form  $J_{\text{AF}} \sum_{\langle ij \rangle} \mathbf{S}_i \cdot \mathbf{S}_j$ . However, for doping  $x \simeq 0.2 - 0.4$ , the regime in which we are interested here, the antiferromagnetic coupling is much weaker than the ferromagnetic DE interaction, and may therefore be neglected.

In the case of the manganites,  $J_H$  in the DE term in Eq. (1.7) is positive. For  $J_H < 0$ , the antiferromagnetic coupling between local and itinerant spins gives rise to the Kondo effect, and the Hamiltonian (1.7) is usually referred to as the Kondo lattice model. Although this name is also used for the ferromagnetic case  $J_H > 0$  by some authors, it is misleading since there is no connection with the Kondo effect.

As discussed above, the manganites fall into the strong-coupling or DE limit  $J_H S \gg t$ . Therefore, low-spin states—with an  $e_g$  electron having its spin antiparallel to the local spin—are strongly suppressed. In a one-band model like Hamiltonian (1.7), this has the same effect as strong Coulomb repulsion between  $e_g$  electrons at the same site. For the manganites, this onsite repulsion, which has been left out of the discussion until now, is the largest energy ( $\approx 8$  eV for both the repulsion of electrons in the same and different  $e_g$  orbitals [41]). As pointed out by Held and Vollhardt [41], a two-band DE model with electron-electron interaction cannot account for, e.g., the CMR effect. Nevertheless, the Coulomb repulsion between electrons at the same lattice site plays an important role. For example, it gives rise to the Mott insulating state for  $x = 0$ , in which electrons cannot hop due to strong correlations. In principle, the above-mentioned Hund's rule coupling is a direct consequence of the intraatomic Coulomb interaction [42]. However, while the one-band DE model without Coulomb interaction and large  $J_H$  correctly describes the insulating behavior for  $x = 0$  [3], a two-band model without an onsite repulsion—as employed, e.g., by Millis *et al.* [43]—exhibits a spurious metallic state for  $x = 0$  ( $n = 1$ ) even for  $J_H = \infty$ .

### Holstein double-exchange model

Whereas the pure DE model can explain the origin of ferromagnetism in the doped manganites, as well as some properties of LSMO, Millis *et al.* [44] have pointed out the necessity to include electron-phonon coupling. Green [25] has proposed the following *Holstein double-exchange* (Holstein-DE) model

$$H_{\text{HDE}} = -t \sum_{\langle ij \rangle \sigma} c_{i\sigma}^\dagger c_{j\sigma} - J_{\text{H}} \sum_i \boldsymbol{\sigma}_i \cdot \mathbf{S}_i + \omega \sum_i b_i^\dagger b_i - g \sum_i \hat{n}_i (b_i^\dagger + b_i). \quad (1.10)$$

The third and fourth terms in Eq. (1.10) describe Einstein phonons with frequency  $\omega$ , created (annihilated) by operators  $b_i^\dagger$  ( $b_i$ ), which couple to the local electron density  $\hat{n}_i$  with coupling strength  $g$ . Here  $\hat{n}_i \equiv \sum_\sigma \hat{n}_{i\sigma}$  and  $\hat{n}_{i\sigma} \equiv c_{i\sigma}^\dagger c_{i\sigma}$ . The description of the phonon degrees of freedom in terms of an Einstein model with a constant dispersion  $\omega(\mathbf{k}) = \omega$  for all  $\mathbf{k}$  is justified for optical phonon modes [42]. In contrast to acoustic modes, the latter correspond to noncooperative, local distortions similar to the JT effects discussed above. The electron-phonon interaction in Eq. (1.10) is of the  $Q_1$  breathing mode type [see Eq. (1.6)], but in the context of the manganites it is regarded as an effective JT coupling of  $Q_2$  symmetry.

Green [25] developed a many-body coherent potential approximation for the model (1.10), which can explain the differences between LSMO and LCMO discussed in Sec. 1.1 by assuming a slightly stronger electron-phonon interaction in LCMO. Moreover, it can qualitatively account for the CMR, pressure and isotope effects, as well as for some spectral properties observed experimentally [3, 25, 45]. At the moment, Green's work [25] represents the only theory which provides a satisfactory description of the cross over from quantum to classical phonons, and from weak coupling to the small-polaron limit.

For the manganites, a common simplification consists in treating the local spins as classical vectors of magnitude  $S = 3/2$ . Although this is only exact in the limit  $S \rightarrow \infty$ , it is usually regarded as a reasonable approximation. Moreover, many authors also take the limit  $J_{\text{H}} \rightarrow \infty$ , in which double occupation of a given site is forbidden by the Pauli exclusion principle. This is justified by the fact that in the manganites we have  $J_{\text{H}} S \gg t$ , as mentioned before. In the limit  $S = J_{\text{H}} = \infty$ , the Holstein-DE model simplifies to

$$H_{\text{HDE}} = -t \sum_{\langle ij \rangle} c_i^\dagger c_j \cos(\theta_{ij}/2) + \omega \sum_i b_i^\dagger b_i - g \sum_i \hat{n}_i (b_i^\dagger + b_i), \quad (1.11)$$

where  $\theta_{ij}$  denotes the relative angle between the local spins  $\mathbf{S}_i$ ,  $\mathbf{S}_j$ . The cosine factor arises from the scalar product of two spin- $\frac{1}{2}$  eigenstates with different axes of quantization. Obviously, the assumption of classical spins and  $J_{\text{H}} = \infty$  has reduced the problem to the case of spinless fermions interacting with local phonons, and with a hopping amplitude that depends on the orientation of the local spins. Our motivation for studying the pure Holstein model in the context of the manganites comes from the fact that Eq. (1.11) reduces to the pure Holstein Hamiltonian in the completely saturated ferromagnetic state [ $\cos(\theta_{ij}/2) = 1$ ] or the paramagnetic state above  $T_{\text{C}}$ , in which the average over all spin

orientations gives  $\langle \cos(\theta_{ij}/2) \rangle = 2/3$ . Hence, in these cases, the coupling to the local spins only manifests itself in terms of a uniform modification of the bare hopping integral  $t$ . We shall see below that even the simple Holstein model—for parameters as realized in the manganites—represents a serious challenge for numerical methods. Therefore, in this work, we restrict our attention to pure electron-phonon models, not taking into account the dynamics of the localized  $t_{2g}$  spins.

### Holstein model

As discussed in the previous section, the Holstein-DE model is equivalent to the pure Holstein model if the local spins are either completely aligned or completely disordered. The Holstein Hamiltonian, which has first been studied by Holstein [46] to understand the effects of electron-phonon interaction in molecular crystals, takes the form

$$H_{\text{H}} = -t \sum_{\langle ij \rangle \sigma} c_{i\sigma}^\dagger c_{j\sigma} + \sum_i \left( \frac{\hat{p}_i^2}{2M} + \frac{k}{2} \hat{x}_i^2 \right) - \alpha' \sum_i \hat{n}_i \hat{x}_i. \quad (1.12)$$

Here  $k$  is the spring-constant, and  $M$  denotes the mass of the vibrating described by coordinates  $\hat{x}_i$  and momenta  $\hat{p}_i$ . The phonon degrees of freedom in the Holstein model are equivalent to independent harmonic oscillators at each lattice site, which couple to the local electron density with coupling strength  $\alpha'$ .

The second-quantized representation of the model can be obtained by setting  $J_{\text{H}} = 0$  in Eq. (1.10), leading to

$$H_{\text{H}} = -t \sum_{\langle ij \rangle \sigma} c_{i\sigma}^\dagger c_{j\sigma} + \omega \sum_i b_i^\dagger b_i - g \sum_i \hat{n}_i (b_i^\dagger + b_i). \quad (1.13)$$

The phonon operators in first and second quantization are related as follows ( $\hbar = 1$ ):

$$b_i = \sqrt{\frac{M\omega}{2}} \hat{x}_i + i \sqrt{\frac{1}{2M\omega}} \hat{p}_i, \quad b_i^\dagger = \sqrt{\frac{M\omega}{2}} \hat{x}_i - i \sqrt{\frac{1}{2M\omega}} \hat{p}_i$$

or, equivalently,

$$\hat{x}_i = \sqrt{\frac{1}{2M\omega}} (b_i^\dagger + b_i), \quad \hat{p}_i = i \sqrt{\frac{M\omega}{2}} (b_i^\dagger - b_i). \quad (1.14)$$

Moreover, we have

$$\alpha' = \sqrt{2M\omega} g. \quad (1.15)$$

For the QMC simulations presented in this work, it is more convenient to work with Eq. (1.12), and to express the phonon variables in terms of their natural units

$$\hat{x}_i \mapsto (M\omega)^{-1/2} \hat{x}_i, \quad \hat{p}_i \mapsto (M\omega)^{1/2} \hat{p}_i. \quad (1.16)$$

Setting  $M = 1$  and  $k = \omega^2$ , and defining  $\alpha = \alpha'/\sqrt{\omega} = \sqrt{2}g$ , the Holstein Hamiltonian becomes

$$H_{\text{H}} = -t \sum_{\langle ij \rangle \sigma} c_{i\sigma}^\dagger c_{j\sigma} + \frac{\omega}{2} \sum_i (\hat{p}_i^2 + \hat{x}_i^2) - \alpha \sum_i \hat{n}_i \hat{x}_i. \quad (1.17)$$

### 1.3. Microscopic models

---

For future purposes, we introduce the dimensionless electron-phonon coupling constant

$$\lambda = \frac{\alpha'^2}{\omega^2 W} = \frac{\alpha^2}{\omega W} = \frac{2g^2}{\omega W}, \quad (1.18)$$

where  $W$  has been defined in Eq. (1.8), and the *adiabatic ratio*

$$\bar{\omega} = \omega/t. \quad (1.19)$$

In the sequel, we shall also use the *polaron binding energy*

$$E_P = \lambda W/2, \quad (1.20)$$

which emerges as a natural parameter from the Lang-Firsov transformation [47]. Furthermore, we take the lattice constant to be unity.

#### Holstein-Hubbard model

The Holstein-Hubbard model is defined by the Hamiltonian

$$H_{\text{HH}} = -t \sum_{\langle ij \rangle \sigma} c_{i\sigma}^\dagger c_{j\sigma} + \frac{\omega}{2} \sum_i (\hat{p}_i^2 + \hat{x}_i^2) - \alpha \sum_i \hat{n}_i \hat{x}_i + U \sum_i \hat{n}_{i\uparrow} \hat{n}_{i\downarrow} \quad (1.21)$$

or, equivalently,

$$H_{\text{HH}} = -t \sum_{\langle ij \rangle \sigma} c_{i\sigma}^\dagger c_{j\sigma} + \omega \sum_i b_i^\dagger b_i - g \sum_i \hat{n}_i (b_i^\dagger + b_i) + U \sum_i \hat{n}_{i\uparrow} \hat{n}_{i\downarrow}. \quad (1.22)$$

It describes the competition between the attractive interaction between electrons mediated by the coupling to phonons, and an onsite Coulomb repulsion between two electrons of opposite spin.

## 2 Numerical methods

In condensed matter theory, strongly correlated materials such as the manganites are described using simplified models, which only contain the most important interactions. However, despite the approximations, exact solutions of the resulting models are usually not attainable. Therefore, one has to resort to analytical treatments involving uncontrolled approximations, or based on perturbation theory which is bound to fail in certain parameter regimes. Consequently, if calculations disagree with experiment, it is not clear whether the discrepancies are a result of the approximations made, or if the model is not sufficient to explain the actual physics. Moreover, a particular method can rarely be applied to other problems in the field.

Recently, the combination of analytical and numerical techniques has led to considerable advances in the understanding of many aspects of condensed matter physics. While analytical methods often give a rough overview of the properties of the system under consideration, numerical calculations can be used to test the validity of the assumptions made, and to investigate whether a given model contains all the physics that is seen in experiment. Hence, numerical techniques are no longer regarded as mere tools to check analytical results, but represent an alternative way to predict new physics. In other words, numerically exact approaches such as, e.g., QMC or exact diagonalization (ED), open up the possibility of carrying out unbiased studies of different models, both at zero and finite temperature. The price to be paid in many cases is the restriction to relatively small clusters, often in low dimensions  $D = 1, 2$ . This drawback can be overcome by combining analytical and numerical techniques as, e.g., in the case of cluster perturbation theory and DMFT.

This chapter provides an introduction to the computational methods used here, and is organized as follows. In Sec. 2.1, we present the principles of the QMC method, which has experienced a tremendous development over the last decades. A review focusing on the application to strongly correlated models has been given by von der Linden [10]. In contrast, cluster perturbation theory, which is reviewed in Sec. 2.2, has been proposed only a couple of years ago, and belongs to the so-called cluster methods [48]. The latter, which also include DMFT and its various extensions, are in the focus of much recent theoretical work, since they bridge the gap between numerical studies of small, one- and two-dimensional systems, and realistic calculations for three-dimensional, infinite solids. Section 2.3 introduces the Lanczos method for the diagonalization of very large sparse matrices. Finally, in Sec. 2.4, we briefly discuss the kernel polynomial method which allows one to perform accurate calculations of spectral functions.

## 2.1 Quantum Monte Carlo

The first application of a Monte Carlo (MC) method dates back to von Neumann and Ulam (1950), who used it to stochastically evaluate the inverse of a matrix [10]. Since a complete review of the development of the MC approach is far beyond the scope of this work, here we shall focus on those aspects which are necessary for an understanding of simulations of coupled electron-phonon systems on a lattice. For a comprehensive overview of the field, we refer the reader to the book by Landau and Binder [49], and to [10].

In the field of strongly correlated systems, the QMC method has been used extensively, as it allows simulations on relatively large lattices and gives quasiexact results<sup>1</sup> also at finite temperatures. This permits one to study fascinating phenomena such as high-temperature superconductivity or CMR.

Despite some principle advantages, QMC methods are often limited by (a) the minus-sign problem, which restricts simulations to high temperatures and/or small systems, (b) the fact that the calculation of dynamical properties, e.g., the one-electron Green function, requires analytic continuation to the real-time axis which is an ill-posed problem (see Sec. 2.1.6), and (c) by strong autocorrelations and large statistical errors.

This section outlines the basic ideas behind MC simulations for quantum-mechanical systems. Specific details concerning the application to the Holstein and Holstein-Hubbard model will be discussed in the corresponding chapters.

### 2.1.1 Basic ideas and importance sampling

The *partition function* of a quantum-mechanical system is defined as

$$\mathcal{Z} = \text{Tr} e^{-\beta H} = \int dX \langle X | e^{-\beta H} | X \rangle \quad (2.1)$$

where  $\beta = (k_B T)^{-1}$  denotes the inverse temperature,  $H$  is the Hamiltonian, and the integral is over all possible configurations (states)  $|X\rangle$ . The expectation value of an operator  $\hat{O}$ , corresponding to a physical observable, can be obtained from<sup>2</sup>

$$\langle O \rangle = \frac{1}{\mathcal{Z}} \text{Tr} (\hat{O} e^{-\beta H}) = \frac{1}{\mathcal{Z}} \int dX \langle X | \hat{O} e^{-\beta H} | X \rangle . \quad (2.2)$$

Upon identifying the inverse temperature  $\beta$  with a so-called imaginary time  $i\tau$ , statistical mechanics can be directly related to Feynman's path-integral formulation of quantum mechanics [50], which is the starting point of many QMC simulations. The expectation value in Eq. (2.2) is then given by

$$\langle O \rangle = \frac{1}{\mathcal{Z}} \int \mathcal{D}X e^{-S(X)} O(X) \quad , \quad \mathcal{Z} = \int \mathcal{D}X e^{-S(X)} . \quad (2.3)$$

<sup>1</sup>That is, exact apart from statistical errors which can, in principle, be made arbitrarily small.

<sup>2</sup>Throughout this work, we will denote an operator associated with an observable, matrix or scalar variable  $O$  by  $\hat{O}$ .

Here  $S$  denotes the action defined in Euclidean (imaginary) time, and the integrals are over all possible configurations  $X$  of the classical “*auxiliary*” fields on which  $\hat{O}$  and  $S$  depend. Using the path-integral approach, any quantum-mechanical problem in  $D$  dimensions can be mapped onto a classical problem in  $D + 1$  dimensions, with the additional dimension being the imaginary time. The difficulty consists in finding an appropriate set of basis states for this mapping, as the choice strongly depends on the problem under consideration.

For many-particle systems, the dimensionality of the integrals in Eq. (2.3) is far beyond anything that can be handled using standard integration techniques, and an illuminating discussion of these difficulties is given by Negele and Orland [51]. The basic idea of (Q)MC is to exploit the fact that from the whole of phase space, usually only a very small number of configurations contributes significantly to the average in Eq. (2.3). Hence, one sets out to sample an ensemble of configurations  $X_i$ , labeled by  $i = 1, 2, \dots, N_{\text{meas}}$ , which are distributed according to

$$\rho(X_i) = \frac{e^{-S(X_i)}}{\sum_i e^{-S(X_i)}}. \quad (2.4)$$

Using this *importance sampling*, the expectation value in Eq. (2.3) becomes

$$\langle O \rangle = \lim_{N_{\text{meas}} \rightarrow \infty} \frac{1}{N_{\text{meas}}} \sum_{i=1}^{N_{\text{meas}}} O(X_i). \quad (2.5)$$

For a finite number  $N_{\text{meas}}$  of samples, an estimate for  $\langle O \rangle$  is given by

$$\bar{O} = \frac{1}{N_{\text{meas}}} \sum_{i=1}^{N_{\text{meas}}} O(X_i). \quad (2.6)$$

Owing to the limited number of measurements, the random variable  $\bar{O}$  will fluctuate around the true expectation value as  $\bar{O} = \langle O \rangle \pm \Delta\bar{O}$ . The statistical error  $\Delta\bar{O}$  depends on the (unknown) intrinsic variance

$$\sigma_O^2 = \langle \bar{O}^2 \rangle - \langle \bar{O} \rangle^2. \quad (2.7)$$

If the  $N_{\text{meas}}$  configurations  $X_i$  are all statistically independent,  $\Delta\bar{O}$  can be obtained from

$$(\Delta\bar{O})^2 = \frac{\bar{\sigma}_O^2}{N_{\text{meas}}}, \quad \bar{\sigma}_O^2 = \frac{1}{N_{\text{meas}}(N_{\text{meas}} - 1)} \sum_{i=1}^{N_{\text{meas}}} [O(X_i) - \bar{O}]^2. \quad (2.8)$$

Equation (2.8) reveals one of the most important features of MC methods. The statistical error decreases with the number of measurements, so that, in principle, one can obtain results of arbitrary accuracy. Moreover, the number of configurations required for a certain accuracy does not explicitly depend on the dimensionality of the problem, in strong contrast to the necessary number of grid points in standard integration methods [51].

### 2.1.2 Markov chains and updating schemes

From the above discussion, it becomes clear that it is not necessary to sample configurations from all regions of phase space. Instead, one can restrict the simulation to those states of the system which have a significantly large probability. Given a physically relevant configuration, we are confronted with the question of how the system should be evolved so that subsequent configurations are also distributed according to  $\rho$  [Eq. (2.4)]. A very common way to sample new configurations is the *Metropolis algorithm* [52]. Starting from the current state of the system, denoted as  $X$ , a new configuration  $X'$  is proposed by making a small change  $\Delta X$ , i.e.,  $X' = X + \Delta X$ , and calculating the ratio

$$P(X \rightarrow X') = \frac{\rho(X')}{\rho(X)}, \quad (2.9)$$

where  $\rho$  is given by Eq. (2.4). We next draw a random number  $r$  from a uniform distribution between 0 and 1, and accept the state  $X'$  if  $r < P$ . Hence, a new configuration is always accepted if it has a larger weight  $\rho$  than the current state ( $P > 1$ ). Otherwise, it is accepted with the probability  $P < 1$ , given by Eq. (2.9). This procedure generates a sequence of states  $X_1, X_2, \dots$  distributed according to Eq. (2.4), which is called a *Markov Chain* if the probability  $P(X_n \rightarrow X_{n+1})$  exclusively depends on the current configuration  $X_n$  but not on the previous states  $X_1, \dots, X_{n-1}$ . The initial configuration is usually chosen at random, and a *warm-up* phase is required to allow the system to reach thermal equilibrium before measurements can be made.

The reason for the restriction to small changes is that, according to Eqs. (2.4) and (2.9), the acceptance is determined by the change of the action  $S$ . Since large changes in the state of the system are usually accompanied by large variations of  $S$ , such moves in phase space are very unlikely to be accepted. On the other hand, depending on the structure of  $\rho$ , it may take a large number of attempts to leave a given region of phase space and traverse to other important states. This gives rise to *autocorrelations* between successive configurations, and to the phenomenon of *critical slowing-down* in the vicinity of phase transitions. The issue of autocorrelations, which are particularly pronounced in the case of electron-phonon systems, will be addressed in Sec. 2.1.5. Here we would like to mention that physically motivated global updates can often be used to increase the efficiency of MC simulations [53].

Finally, there exist two necessary conditions for sampling procedures to produce exact results. First, the algorithm has to be *ergodic*, i.e., all states of phase space must be accessible within a finite time period, and second, the sampling has to fulfill *detailed balance*, i.e.,  $P(X \rightarrow X') \stackrel{!}{=} P(X' \rightarrow X)$ .

### 2.1.3 Sign problem

To move from one state of the system to the next using, e.g., the Metropolis algorithm, we have interpreted  $\rho(X)$  as the probability of the configuration  $X$ . Clearly, this requires  $\rho(X)$  to be nonnegative. Unfortunately, in QMC simulations, this condition is sometimes



violated. In fact, negative values of the weight  $\rho$  often occur in the most interesting parameter regimes, making accurate simulations difficult or even impossible. This is referred to as the *sign problem*. Although the latter can sometimes be overcome by, e.g., appropriate transformations of the Hamiltonian, a general solution has not yet been found. Despite the occurrence of a sign problem, simulations can often be carried out using the modified weights

$$\tilde{\rho}(X) = \frac{|\rho(X)|}{\int \mathcal{D}X |\rho(X)|}. \quad (2.10)$$

Thereby, the sign of  $\rho$  is absorbed in the observables, which are calculated as

$$\langle O \rangle = \frac{\int \mathcal{D}X O_X \text{sign}(\rho_X) \tilde{\rho}_X}{\int \mathcal{D}X \text{sign}(\rho_X) \tilde{\rho}_X} \equiv \frac{\langle O \text{sign} \rangle}{\langle \text{sign} \rangle}, \quad (2.11)$$

with the notation  $O_X \equiv O(X)$ , et cetera. While this approach can be expected to work well as long as  $\langle \text{sign} \rangle \approx 1$ , it will clearly break down if  $\langle \text{sign} \rangle \rightarrow 0$ , due to the large fluctuations caused by the denominator in Eq. (2.11). As illustrated in [10], the number of measurements for a given relative error of an observable increases as  $\langle \text{sign} \rangle^{-2}$ . In practice, simulations can usually be carried out down to  $\langle \text{sign} \rangle \gtrsim 0.1$ .

### 2.1.4 Suzuki-Trotter decomposition

While the weight of a given configuration  $X$  can easily be evaluated for classical systems, such as the Ising model, the calculation of  $\rho(X)$  is much more difficult for quantum-mechanical problems. The reason is that the different parts in the Hamiltonian do not commute, so that the latter can in general not be diagonalized. Let us denote the kinetic and interaction parts as  $K$  and  $V$ , respectively, so that  $H = K + V$ . Clearly, for  $[K, V] \neq 0$  we have

$$e^{-\beta(K+V)} \neq e^{-\beta K} e^{-\beta V}. \quad (2.12)$$

For general operators  $\hat{A}$ ,  $\hat{B}$ , Suzuki and Trotter have proved the following identity [10]

$$e^{\hat{A}+\hat{B}} = \lim_{L \rightarrow \infty} \left[ e^{\frac{1}{L}\hat{A}} e^{\frac{1}{L}\hat{B}} \right]^L, \quad (2.13)$$

where  $L$  is an integer number. For a finite value of  $L$ , one finds

$$e^{\hat{A}+\hat{B}} = \left[ e^{\frac{1}{L}\hat{A}} e^{\frac{1}{L}\hat{B}} \right]^L + \mathcal{O}(L^{-2}). \quad (2.14)$$

Equation (2.14) is often used in the context of QMC simulations to separate the kinetic and interaction terms in  $H$ . To this end, we divide the imaginary time interval  $[0, \beta]$  into  $L$  intervals of size

$$\Delta\tau = \beta/L, \quad (2.15)$$

so that for each interval we obtain

$$e^{-\Delta\tau H} = e^{-\Delta\tau(K+V)} = e^{-\Delta\tau K} e^{-\Delta\tau V} + \mathcal{O}(\Delta\tau^2). \quad (2.16)$$

Since each of the exponentials can be diagonalized separately in an appropriate basis, Eq. (2.16) represents a very useful starting point for the evaluation of the path integral in Eq. (2.3) for quantum-mechanical systems.

The error associated with the approximation in Eq. (2.16) can be systematically reduced by using smaller values of  $\Delta\tau$ . In practice, there are two strategies to handle this so-called *Suzuki-Trotter error*. Owing to the large numerical effort usually required to perform QMC simulations,  $\Delta\tau$  is often chosen such that the systematic error is smaller than the statistical errors for observables. A second, more satisfactory, but also more costly method is to run simulations at different values of  $\Delta\tau$ , and to exploit the  $\Delta\tau^2$  dependence of the results to extrapolate to  $\Delta\tau = 0$ . Finally, in some variants of QMC, the Suzuki-Trotter approximation can be avoided completely by working in continuous imaginary time [53].

## 2.1.5 Autocorrelations and the Jackknife method

### Autocorrelations

We have pointed out above that the use of small changes to move through phase space causes statistical correlations between successive configurations. Since the relation (2.8) is only valid for statistically independent samples  $X_i$ , it is crucial to check any results for autocorrelations. This can be done, for example, by looking at the time-series of measurements obtained in the course of a simulation. Typically, there occur visible periodic transitions between values characteristic of different regions of phase space, and the number of MC steps between two such cross overs gives a measure for the autocorrelation time. To quantify these ideas, we follow [10] and [54] by defining the *autocorrelation function*

$$\Phi_O(k) = \frac{\frac{1}{N_{\text{meas}}-k} \sum_{i=1}^{N_{\text{meas}}-k} O(X_i)O(X_{i+k}) - \left[ \frac{1}{N_{\text{meas}}} \sum_i^{N_{\text{meas}}} O(X_i) \right]^2}{\frac{1}{N_{\text{meas}}} \sum_{i=1}^{N_{\text{meas}}} [O(X_i)]^2 - \left[ \frac{1}{N_{\text{meas}}} \sum_{i=1}^{N_{\text{meas}}} O(X_i) \right]^2}. \quad (2.17)$$

For large time separations  $k$ ,  $\Phi_O(k)$  decays exponentially,

$$\Phi_O(k) \xrightarrow{k \rightarrow \infty} \text{const.} e^{-k/\tau_O^{\text{exp}}}, \quad (2.18)$$

where  $\tau_O^{\text{exp}}$  is the *exponential autocorrelation time* for the observable  $O$ . For practical purposes, one usually defines the *integrated autocorrelation time*

$$\tau_O^{\text{int}} = \frac{1}{2} + \sum_{k=1}^{N_{\text{meas}}} \Phi(k). \quad (2.19)$$

As discussed by Janke [54], one can show that  $\tau_O^{\text{int}} \leq \tau_O^{\text{exp}}$ . The integrated autocorrelation time governs the statistical error of the expectation value  $\bar{O}$  via

$$\Delta\bar{O} = \frac{2\tau_O^{\text{int}}}{N_{\text{meas}}} \bar{\sigma}_O^2 \equiv \frac{\bar{\sigma}_O^2}{N_{\text{eff}}}, \quad (2.20)$$

where the effective number of measurements  $N_{\text{eff}} = N_{\text{meas}}/(2\tau_O^{\text{int}})$ . A comparison with Eq. (2.8) reveals that in the presence of autocorrelations, the statistical error of an observable  $O$  for a given number of measurements  $N_{\text{meas}}$  increases with the integrated autocorrelation time  $\tau_O^{\text{int}}$ . In particular, the neglect of autocorrelations yields too small statistical errors, and therefore incorrect results. Once the longest autocorrelation time has been identified, correct statistical errors can be obtained by skipping a large enough number  $\tilde{N}$  of MC steps between successive measurements so that  $\Phi(\tilde{N}) \lesssim 0.1$  [10]. This way, the computationally expensive calculation of observables in each step can be avoided. Nevertheless, a possibly significantly larger number of steps will be required to obtain a certain accuracy compared to uncorrelated simulations.

### Jackknife

Equations (2.8) and (2.20) for the statistical error only hold for observables which can be measured directly in each MC step and with no autocorrelations. In contrast, the calculation of the error of a nonlinear quantity of the form

$$\langle C \rangle = \frac{\langle A \rangle}{\langle B \rangle} \quad (2.21)$$

can be rather cumbersome. Observables of this structure occur quite frequently, e.g., in simulations with a sign problem [cf. Eq. (2.11)].

A very elegant way to deal with such situations is the *Jackknife method* [55]. For simplicity, we restrict the discussion to the special case of Eq. (2.21). Given a set of  $N_{\text{meas}}$  measurements of  $A$  and  $B$ , we employ Eq. (2.6) to calculate the expectation value  $\bar{C}^{(0)} = \bar{A}/\bar{B}$ , using all available data. We then divide the measured values of  $A$  and  $B$  into  $k$  groups of length  $l = N_{\text{meas}}/k$ , where  $l$  must be large compared to the longest autocorrelation time to ensure correct results. We proceed by evaluating the quantities  $\bar{C}^{(j)}$  for  $j = 1, 2, \dots, k$ , by using all data except those in group  $j$ . The Jackknife estimate for the expectation value of  $\langle C \rangle$  is then given by [53]

$$\bar{C} = \bar{C}^{(0)} - \text{Bias}, \quad (2.22)$$

where

$$\text{Bias} = (k-1)(\bar{C}^{\text{av}} - \bar{C}^{(0)}) \quad , \quad \bar{C}^{\text{av}} = \frac{1}{k} \sum_{i=1}^k \bar{C}^{(i)}. \quad (2.23)$$

Finally, the corresponding statistical error can be calculated via

$$\Delta \bar{C} = \sqrt{k-1} \left[ \frac{1}{k} \sum_{i=1}^k \{(\bar{C}^{(i)}) - (\bar{C}^{\text{av}})\}^2 \right]^{1/2}. \quad (2.24)$$

### 2.1.6 Maximum entropy method

An instructive review of the maximum entropy method has been given by Jarrell [56]. Here we only discuss the most important ideas, as necessary for the applications in this work.

It has been pointed out earlier that an important limitation of many QMC methods is that dynamical quantities such as, e.g., the energy- and momentum-dependent one-electron Green function  $G(\mathbf{k}, \omega)$ , can only be calculated in imaginary time, usually at discrete points  $\tau_l = l\Delta\tau$ ,  $l = 0, \dots, L$ . In order to compare results to experiment, a continuation to real frequencies is required. Here we are mainly interested in the one-electron spectral function, which is related to  $G$  by

$$A(\mathbf{k}, \omega) = -\frac{1}{\pi} \text{Im} G(\mathbf{k}, \omega). \quad (2.25)$$

Conversely, the time-dependent Green function can be obtained from

$$G(\mathbf{k}, \tau) = \int_{-\infty}^{\infty} d\omega A(\mathbf{k}, \omega) K(\tau, \omega), \quad K(\tau, \omega) = \frac{e^{-\tau\omega}}{1 + e^{-\beta\omega}}. \quad (2.26)$$

In principle, if  $G(\mathbf{k}, \tau)$  is known from a QMC simulation, an inversion of Eq. (2.26) yields  $A(\mathbf{k}, \omega)$ . However, difficulties arise owing to the form of the kernel  $K(\tau, \omega)$ , which becomes exponentially small for large  $\omega$ . For a finite number  $M$  of points  $\omega_i$ ,  $i = 1, \dots, M$ , on the energy axis, the integral in Eq. (2.26) can be written as a matrix equation

$$G_t = \sum_w K_{tw} A_w, \quad (2.27)$$

where  $G$ ,  $A$  correspond to vectors of length  $L+1$  and  $M$ , respectively, and  $K$  is a  $(L+1) \times M$  matrix. Clearly, a calculation of  $A(\mathbf{k}, \omega)$  requires a solution which, if inserted in Eqs. (2.26) or (2.27), reproduces the Green function  $G(\mathbf{k}, \tau)$  within the errorbars of the QMC data. The inversion of Eq. (2.27) leads to the system of linear equations

$$K^{-1} \mathbf{G} = \mathbf{A}. \quad (2.28)$$

The matrix  $K^{-1}$  is usually extremely ill-conditioned, i.e., the ratio of the largest to the smallest singular value—referred to as the *condition number*—is very large [57]. Consequently, Eq. (2.28) cannot be solved using standard methods. It can be shown that small changes in  $\mathbf{G}$  (within the statistical errors) are magnified by the condition number, thereby leading to large variations in the solution for  $\mathbf{A}$ .

The maximum entropy method represents a consistent and reliable way of performing the inversion of Eq. (2.26). It is based on the rules of probability theory, and yields the most probable spectral function  $A(\mathbf{k}, \omega)$ , compatible with the measured Green function  $G(\mathbf{k}, \tau)$  and all other available information about  $A(\mathbf{k}, \omega)$ , such as sum rules, nonnegativity, et cetera.

Denoting the QMC result for the time-dependent Green function by  $\overline{G}$ , obtained by averaging over  $N_{\text{meas}}$  measurements for each time slice, *Bayes' Theorem* yields the following

result for the probability of a certain solution  $A$  for the spectral function

$$P(A|\bar{G}) = \frac{P(\bar{G}|A)P(A)}{P(\bar{G})}. \quad (2.29)$$

Here  $P(A|B)$  denotes the conditional probability for a proposition  $A$  provided  $B$  is true. For a given  $\bar{G}$ ,  $P(\bar{G})$  is a constant and may thus be ignored.  $P(\bar{G}|A)$  is referred to as the *likelihood function*, and  $P(A)$  is called the *prior*. Skilling [58] proposed a prior of the form

$$P(A|m, \alpha) \sim e^{\alpha S}, \quad (2.30)$$

where  $S$  is the entropy defined as

$$S = \sum_{i=1}^M A_i - m_i - A_i \log(A_i/m_i) \quad (2.31)$$

with the *default model*  $m_i \equiv m(\omega_i)$ . In the absence of any data for  $G$ , the entropy is maximized by the choice  $A = m$ . In practice, one usually chooses  $m$  to be a small constant, corresponding to no previous knowledge about the structure of the spectrum. Alternatively, it is possible to use, e.g., exact limits of the spectral function as a guiding function [56]. As pointed out by Jarrell [56], the *regularization parameter*  $\alpha$  governs the competition between the entropy and the misfit of the data, and is determined by maximizing the probability  $P(\alpha|\bar{G}, m)$ . The *misfit*  $\chi^2$  enters via the likelihood function

$$P(G_t|A) = \frac{1}{\sqrt{2\pi}\sigma} e^{-\frac{1}{2}\chi_t^2} \quad (2.32)$$

and is defined as [56]

$$\chi_t^2 = \frac{1}{\sigma^2} (\bar{G}_t - G_t)^2, \quad \sigma^2 = \frac{1}{N_{\text{meas}}(N_{\text{meas}} - 1)} \sum_{i=1}^{N_{\text{meas}}} (\bar{G}_t - G_t^i)^2, \quad (2.33)$$

Equation (2.33) only holds for uncorrelated data. For the more general case of nonnegligible autocorrelations, we refer the reader to [56]. We would like to emphasize that a detailed analysis of autocorrelations, both between measurements for the same and different time slices, is crucial to ensure reliable results. Finally, the maximum entropy algorithm used in this work incorporates an improved evidence approximation [59], which generally reduces ringing and yields more stable results with respect to statistical errors.

## 2.2 Cluster perturbation theory

While the first ideas similar to cluster perturbation theory (CPT) in the form used here date back to Gros and Valentí [60], the widespread use of this method was initiated by the work of Sénéchal *et al.* [11, 12]. Since then, it has been applied to a variety of models, including

## 2.2. Cluster perturbation theory

(extended) Hubbard models [11, 12, 61–63] and the  $t$ - $J$  model [64, 65]. The following review is largely based on the article by Sénéchal [66].

The principle idea behind CPT is to divide the infinite crystal lattice into identical clusters of  $N$  sites. While the model Hamiltonian is then solved exactly on one of these clusters, the hopping between different clusters is treated within strong-coupling perturbation theory. As a detailed derivation can be found in [12], we restrict the discussion to the resulting equations.

To settle the notation, we consider a Hamiltonian of the form

$$H = \sum_{ij\sigma} t_{ij} c_{i\sigma}^\dagger c_{j\sigma} + H_1, \quad (2.34)$$

where  $H_1$  denotes a local interaction, e.g., a Hubbard term. We set out to calculate the one-electron Green function

$$G(\mathbf{k}, z) = \underbrace{\langle \Psi_0 | c_{\mathbf{k}} \frac{1}{z - (H - E_0)} c_{\mathbf{k}}^\dagger | \Psi_0 \rangle}_{G_e} + \underbrace{\langle \Psi_0 | c_{\mathbf{k}}^\dagger \frac{1}{z + (H - E_0)} c_{\mathbf{k}} | \Psi_0 \rangle}_{G_h}, \quad (2.35)$$

where  $G_e$  and  $G_h$  represent the photoemission and inverse photoemission part,  $c_{\mathbf{k}}^\dagger$  creates an electron with momentum  $\mathbf{k}$ , and we have omitted spin indices for simplicity.  $E_0$  denotes the energy of the ground state  $|\Psi_0\rangle$ , and  $z = \epsilon + i\eta$ . The most interesting observable which can be calculated within CPT, namely the one-electron spectral function, is related to  $G$  via

$$A(\mathbf{k}, \epsilon) = -\frac{1}{\pi} \lim_{\eta \rightarrow 0^+} \text{Im} G(\mathbf{k}, \epsilon + i\eta), \quad (2.36)$$

the negative-frequency part of which can often be directly measured in ARPES experiments (see Sec.1.2).

Typical cluster sizes in CPT range from  $N = 1$  to  $N \lesssim 16$ , depending on the available computer resources and the model under consideration. Examples for the simplest cluster shapes in one and two dimensions are shown in Fig. 2.1. In more than one dimension, it is often advantageous to choose more complicated tilings (see, e.g., Fig. 1 in [12]), although different tilings may lead to slightly different results. This possibility has been investigated for the Hubbard model, and the effect of the cluster shape on  $A(\mathbf{k}, \epsilon)$  was found to be rather small [12]. The hopping integrals in Hamiltonian (2.34) can be labeled as  $t_{ab}^{mn}$ , where the superscripts correspond to different clusters, and the subscripts denote sites inside a given cluster. For an isolated cluster ( $m = n$ ), the Hamiltonian (2.34) can be solved using, e.g., the Lanczos method (Sec. 2.3). To this end, we have to calculate the *cluster Green function*

$$G_{ab}^c(z) = \underbrace{\langle \Psi_0 | c_a \frac{1}{z - (H - E_0)} c_b^\dagger | \Psi_0 \rangle}_{G_{ab,e}^c} + \underbrace{\langle \Psi_0 | c_b^\dagger \frac{1}{z + (H - E_0)} c_a | \Psi_0 \rangle}_{G_{ab,h}^c} \quad (2.37)$$

for all nonequivalent pairs of cluster sites  $(a, b)$ . While  $G_{ab}^c$  contains all the information of the model defined on a single cluster, the hopping between different clusters is taken into

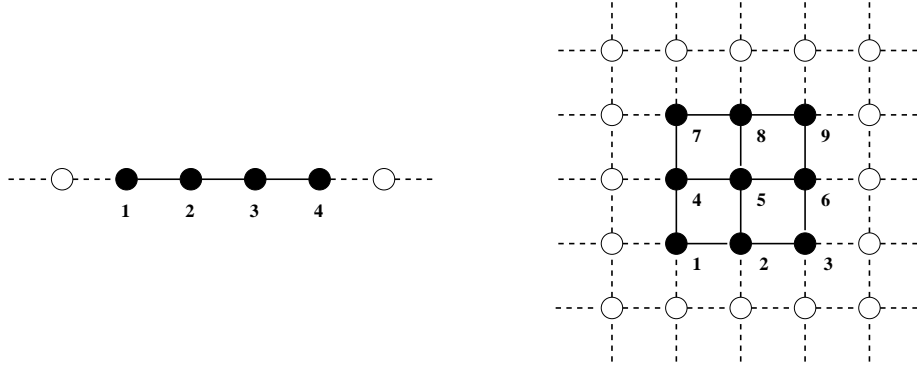


Figure 2.1: Examples of possible cluster tilings in one (left) and two (right) dimensions, with  $N = 4$  and  $N = 9$ , respectively. Filled circles represent lattice sites within the cluster, while empty circles correspond to sites of neighboring clusters. Solid (dashed) lines indicate intracluster (intercluster) hopping processes.

account in an approximate manner. It may be written as

$$t_{ab}^{mn} = t_{ab}^c \delta_{mn} + V_{ab}^{mn} , \quad (2.38)$$

where  $t_{ab}^c$  is the amplitude for hopping within a cluster. CPT treats the remaining intercluster hopping  $V$  using a strong-coupling perturbation expansion in orders of  $|V|/|U|$ , with  $|V|$  and  $|U|$  denoting the strength of the hopping and the local interaction  $H_1$  in Eq. (2.34), respectively. To obtain a tractable algorithm, only the lowest order terms are kept. In matrix notation, this can be expressed as

$$G^{-1} = [G^c]^{-1} - V . \quad (2.39)$$

As discussed by Sénéchal [66], this may also be interpreted as approximating the self-energy of the full problem by that of a finite cluster, i.e.,

$$G^{-1} = G_0^{-1} - \Sigma^c . \quad (2.40)$$

Here,  $G_0$  corresponds to the Green function of the noninteracting system, and  $\Sigma^c$  is the self-energy for a single, isolated cluster.

The Lanczos procedure to obtain the cluster Green function (2.37) will be described in Sec. 2.3. Once  $G_{ab}^c$  is known, we can proceed to calculate the CPT approximation to the full Green function  $G$ . Owing to the different treatment of inter- and intracluster hopping, translational symmetry is broken and has to be restored in some way. We begin by Fourier-transforming the intercluster hopping matrix  $V$ , which can be reduced to a  $N \times N$  matrix  $V_{ab}(\mathbf{K})$ , where  $\mathbf{K}$  is a wavevector of the Brillouin zone of the superlattice of clusters. The result reads [66]

$$V_{ab}(\mathbf{K}) = \sum_n t_{ab}^{0n} e^{i\mathbf{K} \cdot \mathbf{r}_n} . \quad (2.41)$$

## 2.2. Cluster perturbation theory

---

Here  $\mathbf{r}_n$  is the position of the  $n$ th cluster relative to the *base* cluster having  $n = 0$ . Using the above expression, Eq. (2.39) becomes

$$G^{-1}(\mathbf{K}, z) = [G^c(z)]^{-1} - V(\mathbf{K}), \quad (2.42)$$

which is equivalent to

$$G_{ab}(\mathbf{K}, z) = \left( \frac{G^c(z)}{1 - V(\mathbf{K})G^c(z)} \right)_{ab}. \quad (2.43)$$

The Green function  $G$  in Eqs. (2.42) and (2.43) is in a mixed representation—real space within a cluster and reciprocal space between clusters. To obtain the energy- and momentum dependent Green function defined in Eq. (2.35), and to restore translational symmetry, the following procedure has been proposed [11, 12]

$$G(\mathbf{k}, z) = \frac{1}{N} \sum_{a,b=1}^N G_{ab}(\mathbf{k}, z) e^{-i\mathbf{k} \cdot (\mathbf{r}_a - \mathbf{r}_b)}. \quad (2.44)$$

In practice, the method proceeds as follows.

1. calculate the poles and corresponding weights of the cluster Green function  $G_{ab}^c$  [Eq. (2.37)] using the Lanczos method,
2. insert the Lehmann representation of  $G_{ab}^c$  with a smearing parameter  $\eta$  in Eq. (2.43) to obtain  $G_{ab}$ ,<sup>3</sup>
3. carry out the Fourier transformation (2.44).

Since CPT is based on a perturbation expansion in the intercluster hopping, the method can be expected to work especially well in the strong-coupling regime, i.e., if  $H_1$  dominates [see Eq. (2.34)]. This is also illustrated by the fact that it becomes exact in the atomic limit  $t_{ij} = 0$ . On the other hand, for weak or intermediate coupling, the electronic kinetic energy is not small compared to the local interactions. Consequently, the size of the cluster has to be large enough in order to obtain accurate results. In fact, from previous applications of CPT, e.g., to the one- and two-dimensional Hubbard model [11, 12, 61], the cluster size  $N$  emerged as the main control parameter of the method. For the one-dimensional Hubbard model, for example,  $N = 1$  is identical to the Hubbard I approximation [67], while  $N = 2$  already gives a spectral function that contains most of the relevant features such as short-range antiferromagnetic ordering [12]. With increasing  $N$ , the CPT Green function approaches systematically the exact result for the infinite system. Finally, CPT also becomes exact for  $H_1 = 0$  since in this case  $\Sigma^c = 0$  so that Eq. (2.40) yields the correct Green function.

For identical clusters, the CPT spectrum contains many more poles with significant residues than the corresponding results of ED. This is a consequence of the Dyson-like

---

<sup>3</sup>A nonzero smearing parameter is necessary in order to render the matrix inversion in Eq. (2.43) numerically stable.



equation (2.43), which corresponds to a summation of all diagrams consisting of one-particle Green functions to infinite order. We shall see in Sec. 2.3 that one drawback of using Lanczos to calculate spectra is the relatively small number of poles compared to more advanced methods such as, e.g., Chebyshev recursion techniques (Sec. 2.4). However, in combination with CPT, this disadvantage is largely compensated since the real-space Green function obtained with Lanczos only serves as an input to Eq. (2.43). An additional advantage of CPT is the possibility to evaluate  $G(\mathbf{k}, \epsilon)$  at continuous wavevectors  $\mathbf{k}$ , in contrast to ED which restricts  $\mathbf{k}$  to the  $N$  vectors of the first Brillouin zone of the cluster, of which only  $N/2 + 1$  are physically distinct. While other methods such as DMFT also yield results for any  $\mathbf{k}$ , CPT does not rely on the approximation of a local self-energy, which only becomes exact in the limit of infinite dimensions. Finally, finite temperature Lanczos methods may also be combined with CPT to calculate thermodynamic properties [68].

We want to point out that CPT does not, in principle, rely on the Lanczos method. The cluster Green function may be calculated using any suitable technique [12]. Indeed, we will see in Sec. 5.2 that it is possible to combine the exact analytic solution for the atomic-limit Green function with CPT to obtain results which agree surprisingly well with the many-body coherent potential approximation [45] for the spinless Holstein model.

A drawback of CPT when used in combination with ED is the fact that the diagonalization has to be performed using open boundary conditions. It is therefore not possible to exploit translational invariance to save computer memory (Sec. 2.3). Attempts have been made to use periodic BC's and subtract the corresponding terms afterward in the perturbative treatment of the intercluster hopping, but it has been found that the accuracy of the results is much better for the case of open BC's [66]. Other symmetries, such as the inversion group, can be incorporated in principle, but are usually not as effective at reducing the dimension of the Hilbert space. At this point we would like to mention that most of the CPU time for applications of CPT in combination with Lanczos goes into the calculation of the cluster Green function. For example, the number of Lanczos runs required to determine  $G_{ab}^c$  increases proportional to  $N^2$ . In contrast, the effort for the subsequent evaluation of the Green function according to Eqs. (2.43) and (2.44) for the infinite system is negligible, with typical run times of less than 100 seconds.

In addition to the spectral function considered here, other physical properties of the system can also be calculated with CPT. This includes, e.g., the ground-state energy of the infinite system, the electronic kinetic energy, or the Fermi surface [12]. However, the strength of CPT lies in the calculation of the one-particle Green function and related quantities such as the density of states.

Concerning the shortcomings of CPT, we would like to mention that, within the current formulation, two-particle Green functions cannot be calculated. Consequently, it is not possible to compute, for example, optical conductivities. On top of that, the method is in principle restricted to models with local interactions, although it has been applied with some success to the  $t$ - $J$  model [64, 65]. Moreover, an extension of CPT to Hubbard models with nearest-neighbor interaction has recently been proposed by Aichhorn *et al.* [63].

Finally, CPT may also be compared to other cluster methods, such as the cluster DMFT

(CDMFT) or the dynamical cluster approximation (DCA). The main difference to CPT is that, in the latter, the surroundings of the cluster are not treated self-consistently, as is the case, e.g., for the *bath* in DMFT. Attempts to include self-consistency in the CPT lead to the same results as for periodic boundary conditions [66], which are further away from the exact solution than the approach presented here. An important advantage of CPT over CDMFT and DCA is that it can use larger clusters, since no bath sites are required. For a detailed discussion of the relation between these different approaches, we refer the reader to [48, 69].

## 2.3 Lanczos method

The Hilbert space of typical cluster problems which can be treated numerically has dimension  $10^5 - 10^{10}$ . As a result, it is not possible to calculate all eigenvalues and eigenstates of the corresponding Hamiltonian matrix. The Lanczos method represents one of the most popular algorithms for the diagonalization of very large sparse matrices. In this work, it is used, e.g., to calculate the real-space cluster Green function required for CPT. Moreover, the method by itself allows one to calculate static and dynamic properties of strongly correlated systems. This section gives an overview of the most important ideas, while a general discussion can be found in [70].

### 2.3.1 Basis states and Hilbert space truncation

#### Basis states

For electron-phonon models of the Holstein type considered here, the Hilbert space is spanned by the set of basis states [71]

$$\{|\Phi_{uv}\rangle = |u\rangle_{\text{el}} \otimes |v\rangle_{\text{ph}}\} \quad (2.45)$$

with

$$\begin{aligned} |u\rangle_{\text{el}} &= \prod_{i=1}^N \prod_{\sigma} (c_{i\sigma}^{\dagger})^{n_{i\sigma,u}} |0\rangle_{\text{el}}, \quad n_{i\sigma,u} \in \{0, 1\}, \\ |v\rangle_{\text{ph}} &= \prod_{i=1}^N \frac{1}{\sqrt{\nu_{i,v}!}} (b_i^{\dagger})^{\nu_{i,v}} |0\rangle_{\text{ph}}, \quad \nu_{i,v} \in \{0, 1, \dots, \infty\}. \end{aligned} \quad (2.46)$$

Here  $u = 1, \dots, D_{\text{el}}$  and  $v = 1, \dots, D_{\text{ph}}$  are labels for the basis states of the electronic and phononic subspaces with dimensions  $D_{\text{el}} = \binom{N}{N_{\sigma}} \binom{N-N_{\sigma}}{N_-}_{\sigma}$  and  $D_{\text{ph}} = \infty$ , respectively.<sup>4</sup>

The total number of electrons  $N_e = \sum_{\sigma} N_{\sigma}$  and the  $z$  component of the total spin  $S^z$  are conserved quantum numbers. The basis states can therefore be restricted to given values of  $N_e$  and  $S^z$ , which reduces the dimension of the Hilbert space. Furthermore, one

---

<sup>4</sup> $N_{\sigma}$  denotes the number of electrons with spin  $\sigma$ .

can exploit the point group symmetries of the cluster, or translational symmetry—given periodic boundary conditions. As pointed out above, the latter possibility does not exist in the context of CPT due to the need for open boundary conditions in the calculation of the cluster Green function (2.37). Finally, we would like to emphasize that the symmetrized basis states, which can be obtained by applying suitable projection operators [71], may still be written as a tensor product of electronic and phononic states.

### Hilbert space truncation

In principle, an infinite number of phonons can be excited at each lattice site, as expressed by Eq. (2.46). Since a diagonalization can only be carried out for finite dimensions, a truncation of the phonon subspace is required. Following previous work [72], we use the the basis states

$$\{|v\rangle_{\text{ph}}; \quad \nu_v = \sum_{i=1}^N \nu_{i,v} \leq N_{\text{ph}}\}, \quad (2.47)$$

leading to  $D_{\text{ph}}^{N_{\text{ph}}} = (N_{\text{ph}} + N)! / (N_{\text{ph}}! N!)$  allowed phonon configurations [73]. This scheme takes into account all possible dynamical phonon modes, i.e., we do not make any assumptions about the distribution of the  $N_{\text{ph}}$  phonons either in real or momentum space. This ensures a correct description of both local polaron effects and long-range order.

The convergence of the results with  $N_{\text{ph}}$  can be monitored using the ground-state energy  $E_0$ . To this end, we define the relative error

$$\Delta(N_{\text{ph}}) = \frac{|E_0(N_{\text{ph}} + 1) - E_0(N_{\text{ph}})|}{|E_0(N_{\text{ph}})|}. \quad (2.48)$$

Typical values for the results of this work are  $\Delta \approx 10^{-4} - 10^{-7}$ .

For the ED calculations in Chap. 5, an additional condition has been used to ensure convergence. It is based on the phonon distribution function

$$|c^{(\nu)}|(N_{\text{ph}}) = \sum_{u=1}^{D_{\text{el}}} \sum_{\substack{v=1 \\ \{\nu_v=\nu\}}}^{D_{\text{ph}}^{N_{\text{ph}}}} |c_{uv}|^2 \quad (2.49)$$

for which we require that it becomes independent of  $N_{\text{ph}}$  and  $|c^{(N_{\text{ph}})}| \leq 10^{-6}$ . Here the  $c_{uv}$  denote the coefficients of the ground state in the basis  $\{|\Phi_{uv}\rangle\}$  with maximally  $N_{\text{ph}}$  phonons.<sup>5</sup> Equation (2.49) corresponds to the weight of the state with  $\nu$  phonons in the ground state.

---

<sup>5</sup>In Eq. (2.49) we have not taken into account a possible reduction of the electronic Hilbert space  $D_{\text{el}} \rightarrow \tilde{D}_{\text{el}} < D_{\text{el}}$  due to symmetry operations.

### 2.3.2 Ground state and static properties

In a first Lanczos iteration, the Hamiltonian matrix is transformed into a tridiagonal representation, while a second Lanczos run yields the actual ground state. In the  $(n+1)$ th iteration step, one calculates the vector

$$|\phi_{n+1}\rangle = H|\phi_n\rangle - a_n|\phi_n\rangle - b_n^2|\phi_{n-1}\rangle, \quad (2.50)$$

with the coefficients

$$a_n = \frac{\langle\phi_n|H|\phi_n\rangle}{\langle\phi_n|\phi_n\rangle}, \quad b_n^2 = \frac{\langle\phi_n|\phi_n\rangle}{\langle\phi_{n-1}|\phi_{n-1}\rangle}, \quad (2.51)$$

and the initial conditions  $b_0 = 0$ ,  $|\phi_{-1}\rangle = 0$ . The initial state  $|\phi_0\rangle$  can be chosen as a random vector having finite overlap with the true ground state. In every step, it is sufficient to keep only three vectors in memory. After  $L$  steps, the Hamiltonian, represented in the basis consisting of the states  $|n\rangle = |\phi_n\rangle / \sqrt{\langle\phi_n|\phi_n\rangle}$ , becomes

$$H = \begin{pmatrix} a_0 & b_1 & 0 & 0 & \cdots & 0 \\ b_1 & a_2 & b_2 & 0 & \cdots & 0 \\ 0 & b_2 & a_3 & b_3 & \cdots & 0 \\ \vdots & \vdots & \vdots & \vdots & \ddots & \vdots \\ 0 & 0 & 0 & 0 & \cdots & a_N \end{pmatrix}. \quad (2.52)$$

There exist three different criteria to stop the Lanczos iteration:

1. convergence has been achieved for the lowest eigenvalue of  $H$ ,
2. the latest off-diagonal element  $b_n^2$  in Eq. (2.50) is identical to zero within the finite accuracy available on a computer,
3. the number of iterations has reached an upper limit (typically 50–500).

The ground state  $|\Psi_0^L\rangle$  corresponds to the eigenvector belonging to the lowest eigenvalue  $E_0^L$ . At the end of the first Lanczos iteration,  $|\Psi_0^L\rangle$  is known in the basis  $|\phi_n\rangle$ ,  $n = 1, \dots, L$ . However, since the vectors have not been stored in the course of the iteration process, a second run is required to obtain the desired representation of the ground state in the original basis (2.45), using the known coefficients  $\langle\Psi_0^L|\phi_n\rangle$  in each step. Once  $|\Psi_0^L\rangle$  has been calculated in the basis (2.45), the ground-state expectation value of any static observable  $\hat{O}$  may be obtained from

$$\langle O \rangle = \langle\Psi_0^L|\hat{O}|\Psi_0^L\rangle \quad (2.53)$$

using the matrix representation of the operator  $\hat{O}$ .

### 2.3.3 Dynamic properties

The Lanczos method also permits the calculation of dynamical correlation functions. Let us consider a general Green function of the form

$$G^O(z) = \underbrace{\langle \Psi_0 | \hat{O} \frac{1}{z - (H - E_0)} \hat{O}^\dagger | \Psi_0 \rangle}_{G_e^O} + \underbrace{\langle \Psi_0 | \hat{O}^\dagger \frac{1}{z + (H - E_0)} \hat{O} | \Psi_0 \rangle}_{G_h^O}, \quad (2.54)$$

where  $z = \epsilon + i\eta$  as before and  $\hat{O}$  is a fermionic operator. In the sequel, we restrict the discussion to  $G_e^O$ . Inserting a complete set of eigenstates  $\{|\psi_\nu\rangle\}$  of  $H$ , it may be written as

$$G_e^O = \sum_\nu \frac{|\langle \psi_\nu | \hat{O}^\dagger | \Psi_0 \rangle|^2}{z - (E_\nu - E_0)}. \quad (2.55)$$

The eigenstates  $\{|\psi_\nu\rangle\}$  can be expressed in the Lanczos basis  $\{|\phi_i\rangle\}$  obtained from a further Lanczos run with the start vector

$$|\phi_0\rangle = \frac{\hat{O}^\dagger |\Psi_0^L\rangle}{\sqrt{\langle \Psi_0^L | \hat{O} \hat{O}^\dagger | \Psi_0^L \rangle}} \quad (2.56)$$

yielding [71]

$$G_e^O = \langle \Psi_0^L | \hat{O} \hat{O}^\dagger | \Psi_0^L \rangle \sum_{\nu=0}^{L-1} \frac{|c_{\nu,0}^L|^2}{z - (E_\nu^L - E_0^L)}, \quad (2.57)$$

where  $c_{\nu,0}^L = \langle \phi_\nu | \Psi_0^L \rangle$ . A similar expression can be derived for  $G_h^O$  in Eq. (2.54).

While this so-called *spectral decoding method* works well for Green functions of the form (2.54), it cannot directly be used to calculate the real-space cluster Green function (2.37) since the latter generally involves two different operators  $c_a^\dagger \neq [c_b]^\dagger$  for  $a \neq b$ . Consider the first term  $G_{ab,e}$  in Eq. (2.37). In order to proceed in this case, we construct the states  $|\phi\rangle = c_b^\dagger |\Psi_0^L\rangle$  and  $|\phi'\rangle = c_a |\Psi_0^L\rangle$ . After normalization,  $|\phi\rangle$  serves as the initial state for a Lanczos run which gives an approximate eigenbasis  $\{|\psi_\nu^L\rangle\}$  of  $H$ . The latter can be inserted in Eq. (2.37) in the form of an approximate unity operator so that we obtain

$$G_{ab,e}(z) = \sum_{\nu=0}^{L-1} \langle \phi' | \psi_\nu^L \rangle \langle \psi_\nu^L | \phi \rangle \frac{1}{z - (E_\nu^L - E_0^L)}. \quad (2.58)$$

The scalar products in Eq. (2.58) are best calculated by expanding the eigenstates in the basis of Lanczos vectors.

From what has been said so far it is evident that the Lanczos Green function contains  $L$  poles, while the true Green function consists of  $D \equiv D_{\text{el}} D_{\text{ph}}^{N_{\text{ph}}}$  delta peaks. The positions and weights of the peaks in the Lanczos spectrum converge to the true values as  $L \rightarrow \infty$ . Problems associated with the Lanczos method are (a) the nonuniform convergence of

eigenvalues and eigenvectors over the whole energy range, (b) the occurrence of so-called ghost states which appear and disappear in the course of the Lanczos run, and (c) the need for time-consuming reorthogonalization of the Lanczos vectors for large values of  $L$ .

We conclude with a discussion of the numerical effort of the Lanczos method. The main limitation is the available computer memory, since three Lanczos vectors have to be stored for the calculation. As the dimension of the Hilbert space depends exponentially on the number of lattice sites, even shared-memory systems only allow one to include a few additional sites compared to standard personal computers. Moreover, the computer time also increases significantly with the size of the vectors as  $D \ln D$ .

## 2.4 Kernel polynomial method

The shortcomings of the Lanczos method pointed out in the preceding section have led to the development of improved algorithms to calculate dynamical properties of strongly correlated systems. One of these approaches, belonging to the general class of Chebyshev recursion techniques, is the so-called kernel polynomial method (KPM) used here. Following [71], this section reviews the basics of KPM, while a much broader discussion can be found in [74, 75].

We define the spectral function associated with an operator  $\hat{O}$  as

$$\begin{aligned} A^O(\epsilon) &= -\frac{1}{\pi} \lim_{\eta \rightarrow 0^+} \text{Im} \left[ \langle \Psi_0 | \hat{O} \frac{1}{z - (H - E_0)} \hat{O}^\dagger | \Psi_0 \rangle \right] \\ &= \sum_{\nu=0}^{D-1} |\langle \psi_\nu | \hat{O}^\dagger | \Psi_0 \rangle|^2 \delta[\epsilon - (E_\nu - E_0)]. \end{aligned} \quad (2.59)$$

The general idea of Chebyshev recursion techniques is to expand the  $\delta$  functions in Eq. (2.59) in a series of Chebyshev polynomials  $T_m(x)$ ,

$$A^O = \frac{1}{\pi \sqrt{1-x^2}} \left( \mu_0^O + 2 \sum_{m=1}^{\infty} \mu_m^O T_m(x) \right), \quad (2.60)$$

with the coefficients or *moments*

$$\mu_m^O = \int_{-1}^1 dx T_m(x) A^O(x) = \langle \hat{O}^\dagger \Psi_0 | T_m(\hat{X}) | \hat{O}^\dagger \Psi_0 \rangle \quad (2.61)$$

and

$$x = \frac{(\epsilon - b)}{a}, \quad a = \frac{(E_{\max} - E_{\min})}{2(1 - \tilde{\eta})}, \quad b = \frac{(E_{\max} + E_{\min})}{2}. \quad (2.62)$$

Since the  $T_m(x)$  are defined on the interval  $[-1, 1]$ , the Hamiltonian  $H$  has to be replaced by the rescaled operator  $\hat{X} = (H - b)/a$  with eigenvalues  $x_n \in [-(1 - \tilde{\eta}), 1 - \tilde{\eta}]$ . The small constant  $\tilde{\eta}$  has been introduced to circumvent convergence problems near the endpoints of

the interval. For typical values of  $\tilde{\eta} \sim 0.01$  the impact on the energy resolution is merely 1% [75].

The infinite series in Eq. (2.60) is truncated at  $\mu_{\tilde{L}-1}^O$ . From the resulting  $\tilde{L}$  moments, the spectrum can be reconstructed in different ways. Within the KPM, which represents a linear approximation of the spectrum, we set  $A^O \approx A_{\tilde{L}}^O$ , where  $A_{\tilde{L}}^O$  is given by Eq. (2.60) with  $\infty$  replaced by  $\tilde{L} - 1$ . The cutoff of the series gives rise to Gibbs oscillations, which can be minimized using properly chosen damping factors [76].

The actual procedure of the KPM is as follows:

1. use the Lanczos method to calculate the smallest and largest eigenvalues  $E_{\min}$ ,  $E_{\max}$  as well as the ground-state vector  $|\Psi_0\rangle$ ,
2. determine the initial conditions

$$\begin{aligned} |\Phi_0\rangle &= \hat{O}^\dagger |\Psi_0\rangle, & |\Phi_1\rangle &= \hat{X} |\Phi_0\rangle, \\ \mu_0^O &= \langle \Phi_0 | \Phi_0 \rangle, & \mu_1^O &= \langle \Phi_0 | \Phi_1 \rangle, \end{aligned} \quad (2.63)$$

3. exploit the recurrence relations for Chebyshev polynomials to calculate the  $\tilde{L}$  moments via

$$\begin{aligned} |\Phi_m\rangle &= 2\hat{X} |\Phi_{m-1}\rangle - |\Phi_{m-2}\rangle, \\ \mu_{2m}^O &= 2\langle \Phi_m | \Phi_m \rangle - \mu_0^O, \\ \mu_{2m-1}^O &= 2\langle \Phi_m | \Phi_{m-1} \rangle - \mu_1^O. \end{aligned} \quad (2.64)$$

The algorithm only requires the simultaneous storage of two (large) vectors, and  $\tilde{L}/2 + 1$  matrix-vector multiplications yield  $\tilde{L}$  moments for the spectral function. The KPM is numerically very stable, allowing calculations of thousands of moments with good accuracy [71].

To further enhance the energy resolution, we make use of the maximum entropy method to calculate from the  $\tilde{L}$  moments obtained with the KPM a representation of the reconstructed spectral function  $A^O(\phi) = A^O(x) \sin \phi$  with  $x = \cos \phi$  [75]. The resulting spectral function corresponds to a Chebyshev series with  $\tilde{L}_{\text{eff}} = F\tilde{L}$  moments, where typical values of  $F$  range from 4,  $\dots$ , 32. Within the maximum entropy method, the  $\tilde{L}_{\text{eff}}$  moments

$$\mu_m^O = \int_0^\pi d\phi \cos(m\phi) A^O(\phi) \quad (2.65)$$

are determined by maximizing the entropy [cf. Eq. 2.31]

$$S = \int_0^\pi d\phi \left[ A^O(\phi) - A_0^O(\phi) - A^O(\phi) \ln \left( \frac{A^O(\phi)}{A_0^O(\phi)} \right) \right]. \quad (2.66)$$

The constraints or boundary conditions are that the first  $\tilde{L}$  moments have to be identical to the  $\tilde{L}$  moments of the default model  $A_0^O$ , which in our case is the spectral function from the KPM.

## 2.4. Kernel polynomial method

---

Similar to the continuation of QMC dynamical correlation functions from imaginary time to real frequencies (Sec. 2.1.6), the computationally expensive part here is the KPM, as it involves matrix-vector multiplications with very large arrays. Finally, for a comparison of spectra obtained with the KPM, Lanczos and the maximum entropy method we refer the interested reader to [71, 75].



## 3 Holstein polaron

The *Holstein polaron problem*—corresponding to the Holstein model with a single electron—is one of the most studied problems in condensed matter theory, and dates back to the original work of Holstein [46] in the 1950’s. Despite the restriction to a single fermion, one is still confronted with a complex many-body problem, due to the coupling to the phonon degrees of freedom. The term *polaron*, first coined by Landau [77], describes an electron dressed by a phonon cloud or, equivalently, a distortion of the surrounding lattice.

Obviously, in connection with materials such as the cuprates or manganites, we are ultimately interested in studying the many-electron system. However, the one-electron case represents an important first step towards an understanding of more general situations. Moreover, this chapter introduces several important new ideas which will be used for the QMC methods in later chapters.

In this chapter, we use three different approaches. After a review of existing work on the Holstein polaron in Sec. 3.1, we apply CPT to calculate the one-particle spectral function of the Holstein polaron (Sec. 3.2). Section 3.3 describes canonical transformations of the Holstein Hamiltonian, which will be the starting point of both the variational polaron approach (Sec. 3.4) and the QMC method presented in Sec. 3.5. While both the CPT and VPA are restricted to ground-state properties, the QMC approach permits calculations at finite temperature.

### 3.1 Holstein polaron

The Holstein model has been defined in Eqs. (1.13) and (1.17), and can be described using the dimensionless parameters  $\lambda$  [Eq. (1.18)] and  $\bar{\omega}$  [Eq. (1.19)]. Moreover, we express all energies in units of the hopping  $t$ .

The polaron problem has been investigated intensively in the past, using a great variety of methods. Here we focus the discussion on recent progress in the field, and on numerical methods. A comprehensive overview of earlier work can be found, e.g., in the books of Alexandrov and Mott [78] and Mahan [9].

Weak-coupling perturbation theory has been found to be accurate only for very small coupling strengths  $\lambda$  when the phonon frequency is low [79]. In the strong-coupling regime, an adiabatic small-polaron approximation [46, 80] works very well for small values of  $\bar{\omega}$  [81], while a perturbation theory based on the Lang-Firsov transformation [47] gives accurate results for  $\bar{\omega} \gg 1$  [79, 81]. More recently, the Holstein polaron has been investigated us-

ing weak- and strong-coupling perturbation theory (SCPT) [82, 83]. Discrepancies remain, however, in the regime of intermediate coupling and phonon frequency [9]. To bridge this gap, a lot of numerical work has been done using ED, DMRG, QMC and variational methods. ED is limited in the accessible parameter range, since it requires a truncation of the Hilbert space associated with the phonon degrees of freedom (Sec. 2.3). With increasing electron-phonon coupling strength, for example, an increasing number of phonon states have to be included to obtain converged results [72, 79, 81, 84–89], which makes it difficult to study clusters of reasonable size in the strong or even intermediate coupling regime, especially for small phonon frequencies. The same is true for finite-cluster SCPT [90] and CPT (Sec. 2.2), which exactly diagonalize small clusters—for which enough phonon states can be included in the calculation—and extrapolate the results to the thermodynamic limit by treating the rest of the system as a perturbation. The application of CPT to the Holstein polaron will be discussed in Sec. 3.2. DMRG, in particular when implemented on shared-memory systems [91], allows to study large systems by using an optimized phonon basis to reduce the size of the Hilbert space [92–95]. Moreover, several variational methods have been developed which yield very accurate results over a wide range of parameters [96–105]. Nevertheless, it is important to keep in mind that such approaches often rely on assumptions about the ground-state wavefunction, and are therefore not as reliable as exact numerical techniques. Various QMC methods have been developed for the Holstein model, as discussed in Sec. 3.5. The polaron problem considered here has been investigated by Hirsch *et al.* [106, 107], de Raedt and Legendijk [108–110], Kornilovitch [111–113], Kornilovitch and Pike [114], and Mishchenko *et al.* [115]. Finally, the Holstein polaron has also been studied in the infinite-dimensional limit using DMFT [7, 8, 89, 116, 117], which allows an exact analytical solution.

From all this work, many properties of the Holstein polaron are well understood. A cross over occurs from a quasiparticle (QP) with slightly increased effective mass to a heavy small polaron as the electron-phonon coupling strength increases. The two conditions for the existence of a small polaron<sup>1</sup> are  $\lambda > 1$  and  $\sqrt{E_P/\omega} > 1$ , expressing the fact that a “localized” state<sup>2</sup> is formed if (a) the gain in potential energy of the electron exceeds its loss in kinetic energy, and (b) a large enough lattice distortion exists so as to trap the carrier [88]. We will first discuss the weak-coupling state. Concerning its nature in higher dimensions, there exist two different views. From calculations based on the adiabatic approximation, i.e., taking the limit  $\bar{\omega} \rightarrow 0$ , one expects a qualitatively different behavior in one dimension compared to  $D > 1$ , also for  $\bar{\omega} > 0$ . Wellein *et al.* [85] distinguish between the adiabatic ( $\bar{\omega} < 1$ ) and the nonadiabatic ( $\bar{\omega} > 1$ ) regime. In the adiabatic case, and for  $D > 1$ , the electron is expected to remain quasifree with an almost unchanged effective mass and kinetic energy for  $\lambda < 1$ , corresponding to a QP with infinite radius. This contrasts strongly with one dimension, where the electron is always self-trapped by

---

<sup>1</sup>A small polaron corresponds to an electron surrounded by a lattice distortion which only extends over a single site.

<sup>2</sup>In this work, we mean by a localized state a polaron (or bipolaron) wavefunction with small spatial extent. Such a state is still Bloch-like, i.e., the quasiparticle moves in a coherent band, in contrast to localized carriers which are pinned, e.g., by impurities.

the surrounding lattice distortion and forms a polaron with finite radius for any  $\lambda > 0$ . On the other hand, in the nonadiabatic regime  $\bar{\omega} > 1$ , the behavior is very similar in all dimensions, and a very gradual decrease of the kinetic energy (or increase in effective mass) is observed as the coupling strength increases. Due to the large energy of the phonon excitations, only the zero-phonon state contributes significantly. Moreover, the phonons are fast and react almost instantly to the motion of the electron. Consequently, a lattice distortion only persists in the immediate vicinity of the electron, and this rather small QP is sometimes called a *nonadiabatic Lang-Firsov polaron* [85]. Romero *et al.* [83] take on a slightly different viewpoint. Based on results from their variational Global-Local method, they argue that the large polaron state is essentially the same in any dimension, and that the only effect of increasing the dimension of the system is the observed sharpening of the cross over. For  $\lambda > \lambda_c$ , the critical coupling being determined by the aforementioned conditions  $\lambda > 1$  and  $\sqrt{E_P/\omega} > 1$ , both views agree on the existence of a small-sized so-called *Holstein polaron* [85]. The latter is a heavy QP with a strongly reduced mobility. The cross over at  $\lambda_c$  is very sharp, especially for  $\bar{\omega} \ll 1$ , but it does not represent a real phase transition [118], as expected for a translational invariant system. Even though the electron is trapped in the potential well originating from the response of the lattice to its motion, the ground state is still Bloch-like.

## 3.2 One-particle spectral function

### 3.2.1 Introduction

Spectral properties, such as the one-electron spectral function, provide valuable insight into the complex physics of strongly correlated systems. However, reliable results for such quantities are generally difficult to obtain. Analytical methods are often restricted to very simple limiting cases, and results usually cannot be extended to more general situations. Two remarkable exceptions are the Holstein model with a linear electron dispersion [5, 6] and the Hubbard model [119], both in one dimension (1D), which have been solved exactly. Additionally, an exact solution of the polaron problem can be obtained in infinite dimensions [7, 8, 89, 116, 117]. Numerical methods such as ED and QMC have received much attention over the last decades, since they can be used to study more general models. ED methods allow very accurate calculations of ground-state as well as finite-temperature spectral properties, but are restricted to rather small clusters due to the large dimension of the corresponding Hilbert space. QMC can be used to obtain results on large clusters even in higher dimensions, but here the sign-problem and the ill-posed analytic continuation required to obtain dynamic correlation functions for real frequencies (Sec. 2.1.6) are detrimental for many interesting applications. The recently developed CPT [11, 12], which has been reviewed in Sec. 2.2, marks an important improvement of the situation.

For coupled electron-phonon systems, such as the Holstein model and its extensions—e.g., the Holstein-Hubbard or the Holstein-DE model (Sec. 1.3)—the application of ED methods is hampered by the infinite number of possible phonon configurations, which gives

rise to a rapidly growing requirement of computer memory and/or CPU time as the number of lattice sites or phonon states increases. Improved methods such as DMRG, or the use of variational phonon bases allow one to extend the accessible parameter range. Nevertheless, as electron-phonon interaction has been identified as an important ingredient in, e.g., high-temperature superconductors [2] and manganites [3] (Sec. 1.3.1), further progress along these lines is highly desirable.

In this section, we show that CPT can be successfully applied to electron-phonon models with a (local) coupling of the Holstein type [46]. The results for the one-electron spectral function of the Holstein polaron in one and two dimensions reveal that the use of CPT strongly reduces finite-size effects, as compared to ED.

#### 3.2.2 Application of cluster perturbation theory

Following other authors [72, 81, 84, 87, 120, 121], we calculate the Green function

$$G(\mathbf{k}, \epsilon) = \langle 0 | c_{\mathbf{k}} \frac{1}{\epsilon - H} c_{\mathbf{k}}^{\dagger} | 0 \rangle, \quad (3.1)$$

where  $|0\rangle$  represents the ground state of the phonons and the vacuum state for the electrons. Spin indices can be suppressed owing to the symmetry of the problem. The corresponding one-electron spectral function is given by Eq. (2.36).

To obtain the cluster Green function (2.37), we apply the Lanczos recursion method as described in Sec. 2.3. As discussed in Sec. 2.3, the Hilbert space of the electron-phonon problem has to be truncated to permit a numerical diagonalization. Here, the convergence with the maximal number of phonon states  $N_{\text{ph}}$  is monitored according to Eq. (2.48) using the ground-state energy  $E_0^{\uparrow}$  of the the cluster with open boundary conditions and one electron.<sup>3</sup> For the results presented in this chapter,  $N_{\text{ph}}$  was chosen such that  $\Delta(N_{\text{ph}}) < 10^{-5}$ . We find that convergence of  $E_0^{\uparrow}$  also ensures a well-converged spectral function. Moreover, the influence of the number of phonons kept in the calculation is much larger for the incoherent part of the spectrum than for the coherent, low-energy QP peak which determines  $E_0^{\uparrow}$  (Sec. 3.2.3).

Before we come to a discussion of the results obtained with CPT, we want to comment on some of the existing work on spectral properties of the Holstein polaron. As indicated before, the most reliable method to calculate dynamic quantities, such as  $A(\mathbf{k}, \epsilon)$ , is ED which has been used extensively in the past [72, 81, 84–87, 101, 120, 121]. Most of this work has focused on the polaron band structure, denoted here as  $E^{\uparrow}(\mathbf{k})$ , instead of the spectral function, since it is often easier to interpret, especially in the strong-coupling regime where the structure of  $A(\mathbf{k}, \epsilon)$  is rather complicated. However, as pointed out by Wellein *et al.* [85], the two quantities are closely related. In fact the position of the lowest-energy peak in  $A(\mathbf{k}, \epsilon)$ , obtained from the Green function (3.1), follows exactly the polaron band structure for different  $\mathbf{k}$ . Moreover, the integral over this first peak is equivalent to the

---

<sup>3</sup>The convenience of this notation will emerge in Chap. 4. Owing to the spin symmetry of the one-electron case, here we have  $E_0^{\uparrow} = E_0^{\downarrow}$ .

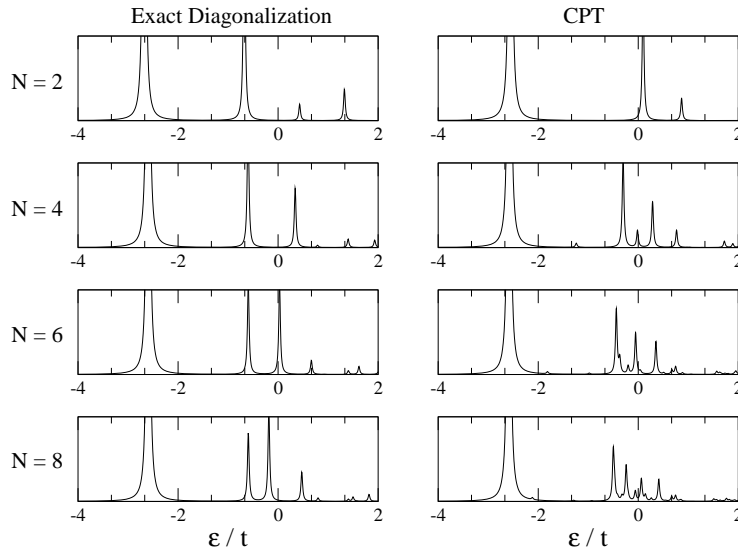


Figure 3.1: Comparison of the one-particle spectral function  $A(0, \epsilon)$  of the one-dimensional Holstein polaron obtained with ED (left column) and CPT (right column) for various numbers of lattice sites  $N$  in the cluster. The plot is for  $\bar{\omega} = 2.0$ ,  $\lambda = 0.5$ , and  $N_{\text{ph}} = 6$ . An artificial smearing parameter  $\eta = 0.02t$  has been used.

QP weight  $z(\mathbf{k}) = |\langle \psi_{0,\mathbf{k}}^{(1)} | c_{\mathbf{k}}^\dagger | 0 \rangle|^2$ , where  $\psi_{0,\mathbf{k}}^{(1)}$  denotes the lowest-energy single-polaron state in the sector with total momentum  $\mathbf{k}$  [86]. Other numerical methods which have been used to calculate spectral properties include DMRG (in one dimension) [92, 94], finite-cluster strong coupling perturbation theory (1D, 2D) [90], QMC (1D–3D) [112, 113], and variational methods (1D–4D) [96–98].

### 3.2.3 Comparison with exact diagonalization

As noted in Sec. 2.2, the critical parameter of CPT is the number of sites in the cluster. To demonstrate the advantage of CPT over the Lanczos method we present in Fig. 3.1 the spectral function  $A(0, \epsilon)$  in one dimension for different cluster sizes  $N$ . We chose  $\bar{\omega} = 2$  and  $\lambda = 0.5$ , which is the regime where an extended polaron exists (Sec. 3.5.3). Consequently, significant finite-size effects can be expected for small clusters, which is exactly what we see in the ED results for periodic boundary conditions. Figure 3.1 clearly shows that the shape of the large QP peak at  $\epsilon \approx -2.4$  changes very little with increasing  $N$  for both ED and CPT, but a noticeable shift can be observed in the ED spectra as we go from  $N = 2$  to  $N = 4$ . The influence of  $N$  is much larger for the incoherent part of the spectrum, which lies about a distance  $\omega$  above the QP peak. The ED spectra display sharp, well-separated peaks, whereas the corresponding CPT data—containing many more poles—resemble much closer the expected results for an infinite system. The latter has been investigated by Marsiglio [72] using Migdal-Eliashberg theory. For the same parameters, he found that the

### 3.2. One-particle spectral function

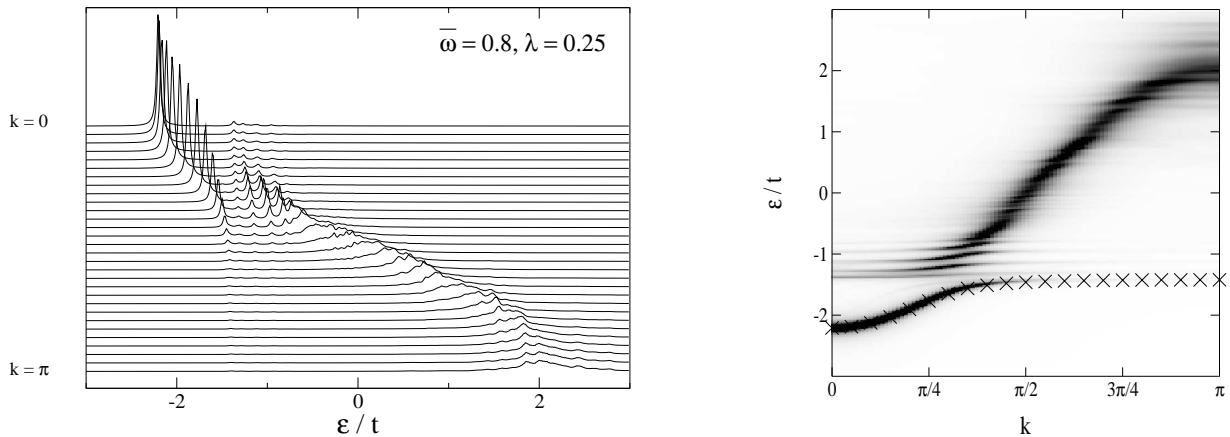


Figure 3.2: Left: One-particle spectral function  $A(k, \epsilon)$  of the one-dimensional Holstein polaron calculated with CPT for  $N = 14$ ,  $N_{\text{ph}} = 6$ , and  $\eta = 0.02t$ . Right: Density plot of the same data for 100 points in  $k$  space. Symbols represent results of Bonča *et al.* [96].

QP peak remains almost unchanged as  $N \rightarrow \infty$ , while the incoherent part evolves into a continuous band that fits well to the CPT results even for rather small clusters  $N \gtrsim 6$ . We have also compared  $A(k, \epsilon)$  for  $k \neq 0$ , and the observed finite-size effects agree perfectly with previous work [86]: As  $k$  increases from  $k = 0$  to  $k = \pi$ , the size of the polaron increases, and the deviations of the ED data from the CPT results become larger. In the strong-coupling or small-polaron regime, not shown here, finite-size effects are known to be small. Consequently, even for very small clusters, ED and CPT both give well-converged results for the QP peak which determines, e.g., the ground-state energy. However, in the case of ED, the incoherent part of the spectrum for wavevector  $k$ , corresponding to excitations of an electron with momentum  $q$  and a phonon with momentum  $k - q$ , still exhibits the typical multipeak structure of a finite system, whereas the CPT results again reproduce much better the incoherent band found in the thermodynamic limit. Moreover, as mentioned in Sec. 2.2, CPT allows us to calculate  $A(k, \epsilon)$  for continuous  $k$ , while ED on a  $N$ -site cluster is restricted to  $N/2 + 1$  physically nonequivalent wavevectors.

A closer look at the CPT results in Fig. 3.1 reveals small additional peaks—not present in the ED spectra—which move from the incoherent part of  $A(k, \epsilon)$  towards the QP peak with increasing  $N$ . Calculations for larger clusters have shown that these peaks vanish systematically with increasing  $N$ , so that the CPT spectrum approaches the exact result in the thermodynamic limit  $N = \infty$ , as expected. Consequently, these peaks are not a defect of CPT, but represent finite-size effects which arise from the approximate treatment of intercluster hopping. The latter, in combination with the open boundary conditions used to calculate the cluster Green function, leads to a system which does not have perfect translational symmetry. The situation is equivalent to ED with open boundary conditions: For  $N \rightarrow \infty$  the spectrum approaches that of an infinite cluster. However, in contrast to CPT, the effects for finite  $N$  are much more significant. Moreover, these finite-size

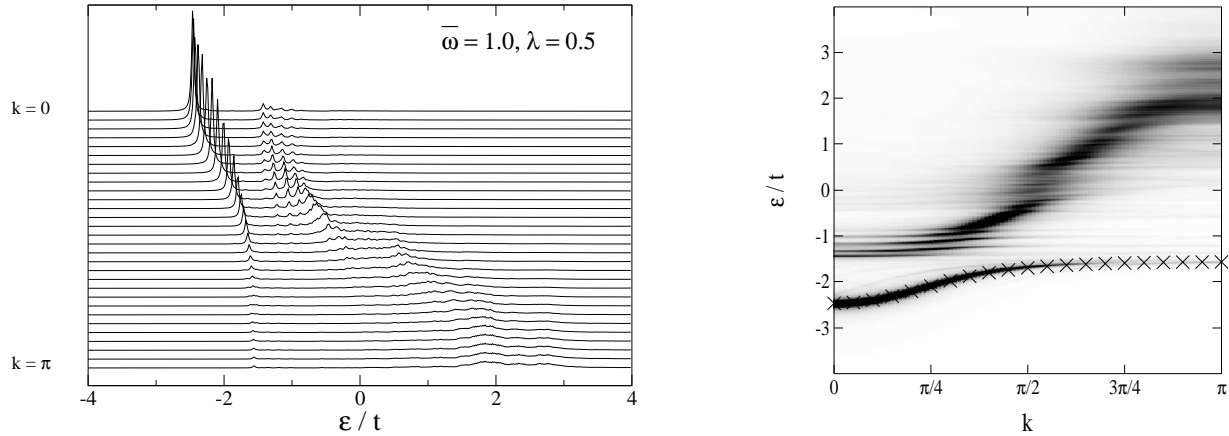


Figure 3.3: Left: One-particle spectral function  $A(k, \epsilon)$  of the one-dimensional Holstein polaron calculated with CPT for  $N = 12$ ,  $N_{\text{ph}} = 6$ , and  $\eta = 0.02t$ . Right: Density plot of the same data for 100 points in  $k$  space. Symbols represent results of Bonča *et al.* [96].

effects manifest themselves in a slightly different way than in the case of periodic boundary conditions, where no additional peaks—showing the aforementioned behavior—are found. In CPT, already for the small cluster sizes shown in Fig. 3.1, the spectral weight of these peaks is extremely small compared to the rest of the spectrum. For other values of  $\bar{\omega}$  and  $\lambda$ , a similar behavior has been found. Although not discussed by the authors, similar effects can also be expected for the Hubbard model [11, 12, 61], although they may be larger for the Holstein polaron due to the higher sensitivity of phonon excitations to the boundary conditions.

### 3.2.4 Results in one dimension

The physics of the one-dimensional Holstein polaron—as it emerges from existing work—has been discussed in Sec. 3.1. In Fig. 3.2 we present results for  $A(k, \epsilon)$  for  $\bar{\omega} = 0.8$ ,  $\lambda = 0.25$  and  $N = 14$  as well as a density plot of the same data. As mentioned before, the spectrum consists of a low-lying QP peak and an incoherent part at higher energies. The physics behind the observed behavior of  $A(k, \epsilon)$  has been discussed, e.g., by Stephan [90], and is typical for electronic systems weakly interacting with dispersionless optical phonons. For small  $k$ , most of the spectral weight resides in the QP peak which corresponds to a weakly dressed electron. For the case considered here, in which the phonon energy lies inside the bare electron band, electron and phonon hybridize and repel each other near the point where they would be degenerate, i.e. for  $|E^\dagger(k) - E^\dagger(0)| \sim \bar{\omega}$ . This coincides with the region where the flattening of the polaron band occurs and, in fact, for larger  $k$  the phonon becomes the lowest-energy excitation. However, most of the spectral weight is contained in the broad, incoherent band which follows the free-electron band dispersion. The density plot in Fig. 3.2 also contains data for the polaron band structure  $E^\dagger(k)$  which

### 3.2. One-particle spectral function

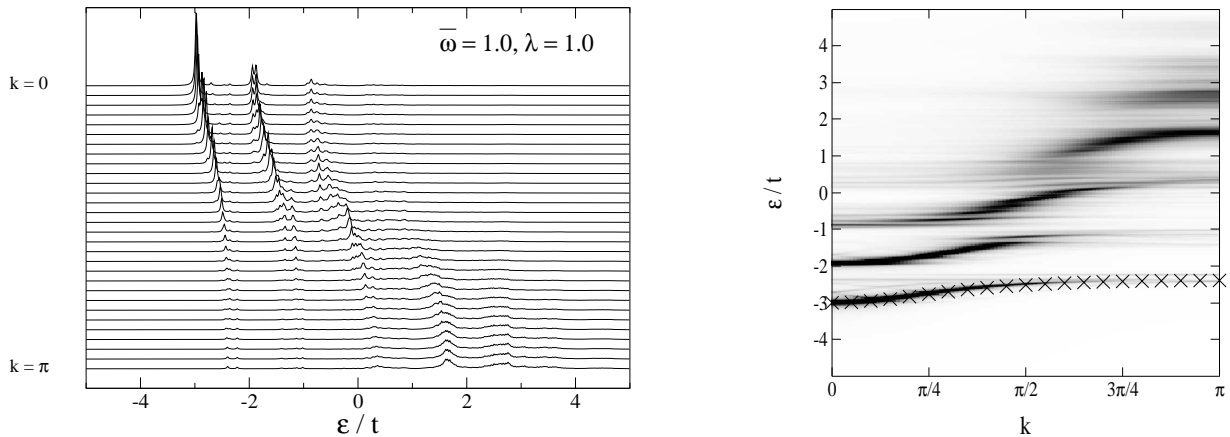


Figure 3.4: Left: One-particle spectral function  $A(k, \epsilon)$  of the one-dimensional Holstein polaron calculated with CPT for  $N = 8$ ,  $N_{\text{ph}} = 9$ , and  $\eta = 0.02t$ . Right: Density plot of the same data for 100 points in  $k$  space. Symbols represent results of Bonča [122].

have been obtained by Bonča *et al.* [96] using their variational diagonalization method. The latter has been shown to give very accurate results for the infinite system, although it becomes somewhat less accurate in the strong coupling regime and for large values of  $k$  [96]. As mentioned before,  $E^\dagger(k)$  corresponds to the lowest-energy band in  $A(k, \epsilon)$  and we find a very good agreement with our data throughout the Brillouin zone.

Figure 3.3 shows results for a similar phonon frequency  $\bar{\omega} = 1.0$  but for stronger electron-phonon coupling  $\lambda = 0.5$  and  $N = 12$ . Compared to the weak-coupling case discussed above, the polaron band is separated more clearly from the incoherent part of the spectrum and, as expected, the bandwidth is further reduced. Additionally, even more spectral weight has been transferred to the high-energy, incoherent band. On top of that, a gap shows up in the upper band at about  $k = \pi/2$ . Again the polaron band fits very well the results for  $E^\dagger(k)$  [96].

We next consider intermediate coupling  $\lambda = 1.0$ , with  $\bar{\omega} = 1$  and  $N = 8$  (Fig. 3.4). For these parameters, an extended polaron exists which still has a relatively large bandwidth, compared to the small-polaron case discussed below. Moreover, the incoherent part of the spectrum has split up into several subbands separated in energy by  $\omega$ , which correspond to excitations of an electron and one or more phonons. As before, we find a very good agreement between the low-energy band in  $A(k, \epsilon)$  and the polaron band dispersion  $E^\dagger(k)$  [122].

Finally, in Fig. 3.5, we report the spectral function for  $\bar{\omega} = 1$  and  $\lambda = 2.0$ . The results have been obtained using only a four-site cluster, which is sufficient to get a very good agreement with Bonča's data for  $E^\dagger(k)$ , with only minor deviations at large values of  $k$  where finite-size effects are most pronounced. This is a consequence of the predominantly local effects in the strong-coupling regime, which also manifest themselves in terms of a very narrow polaron band.



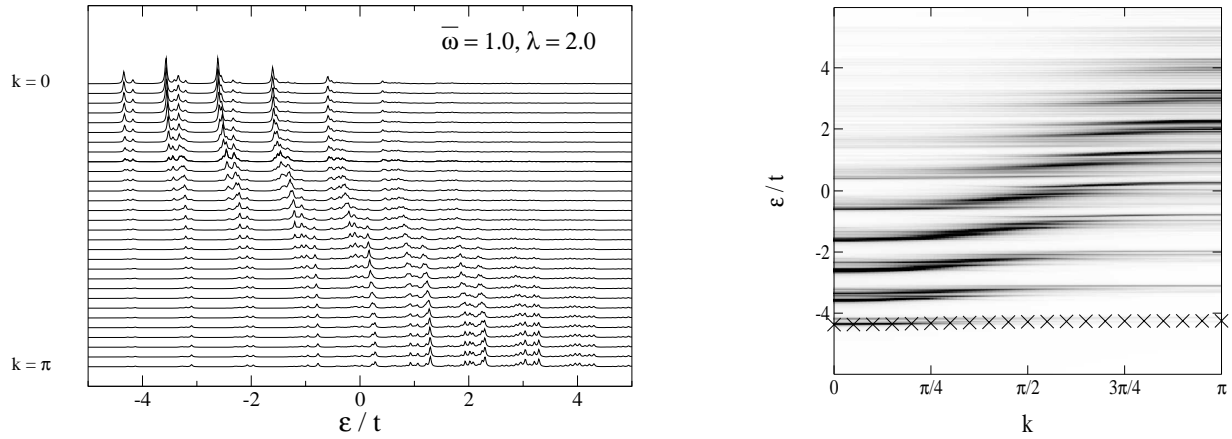


Figure 3.5: Left: One-particle spectral function  $A(k, \epsilon)$  of the one-dimensional Holstein polaron calculated with CPT for  $N = 4$ ,  $N_{\text{ph}} = 25$ , and  $\eta = 0.02t$ . Right: Density plot of the same data for 100 points in  $k$  space. Symbols represent results of Bonča [122].

### 3.2.5 Results in two dimensions

To illustrate the applicability of CPT, we also calculated the spectral function of the Holstein polaron on a two-dimensional cluster of size  $\sqrt{8} \times \sqrt{8}$ , i.e., with eight sites, which has the shape of a tilted square. The influence of the cluster geometry has been discussed in Sec. 2.2. For the Holstein polaron, where the physics is dominated by local correlations, it is expected to be very small.

The two-dimensional Holstein polaron has been reviewed in Sec. 3.1. Here we simply aim to demonstrate the possibility of calculating the 2D spectral function with CPT. Therefore, we restrict ourselves to one set of parameters, namely  $\bar{\omega} = 2.0$  and  $\lambda = 0.945$ , which has also been treated using *finite-cluster* SCPT [90]. In contrast to standard SCPT based on the Lang-Firsov transformation, the latter has been shown to give reliable results also for intermediate  $\lambda$  and  $\bar{\omega}$ , which is a consequence of the inclusion of longer-ranged effects [86, 90]. While in the one-dimensional case the density plot of  $A(\mathbf{k}, \epsilon)$  contains all 100 values of  $k$  used in CPT, in two dimensions we have used 400 points in  $\mathbf{k}$  space. However only 60, lying along  $\Gamma\text{MX}\Gamma$ , are shown in Fig. 3.6.

From the above discussion, and for the parameters considered here, we expect a rather wide polaron band. This is clearly confirmed by the spectral function shown in Fig. 3.6, and the lowest-energy band in our data resembles closely to the findings of Stephan (Fig. 2 of [90]). In particular, as in the one-dimensional case considered in Sec. 3.2.4, a flattening of the polaron band near  $(\pi/2, \pi)$  is found which has also been noted by Wellein *et al.* [85]. Above the polaron band, also similar to 1D, there lie several other incoherent bands which correspond to multiphonon excitations.

In summary, the results of this section clearly demonstrate that CPT is applicable not only in the strong-coupling regime, but also for weak and intermediate electron-phonon interaction. The quality of the resulting spectra is superior to ED data for the same

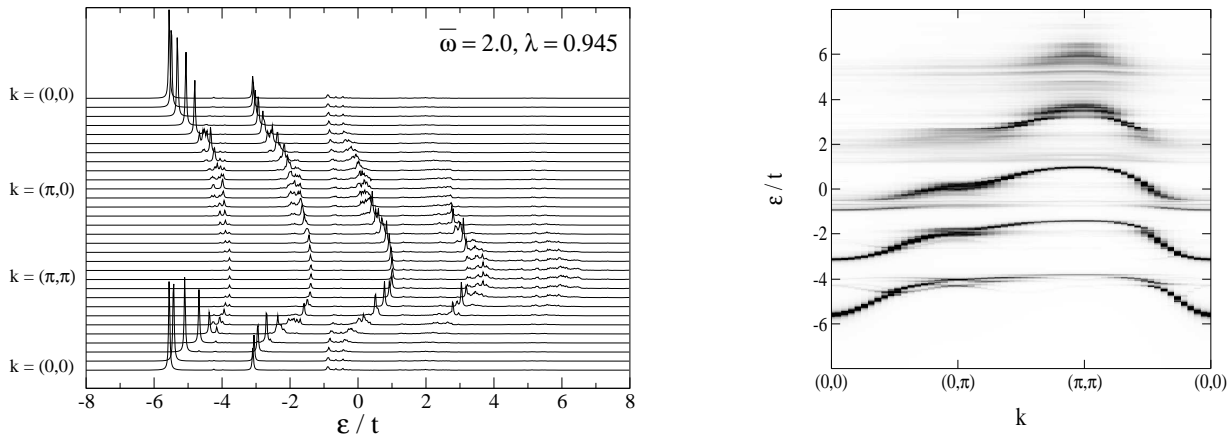


Figure 3.6: Left: One-particle spectral function  $A(\mathbf{k}, \epsilon)$  of the two-dimensional Holstein polaron calculated with CPT for  $N = \sqrt{8}$  (see text),  $N_{\text{ph}} = 9$ , and  $\eta = 0.02t$ . Right: Density plot of the same data (see text).

cluster size, and a very good agreement has been found with the variational method of Bonča *et al.* [96] in one dimension. Moreover, we have shown that CPT also permits accurate calculations in two dimensions.

### 3.3 Transformed Hamiltonians

In this section, we present the canonical *extended Lang-Firsov transformation* of the Holstein Hamiltonian. The original Lang-Firsov (LF) transformation [47] has been used extensively to study Holstein models of various kinds. A well-known approximation due to Holstein [46] consists of replacing the transformed hopping term by its expectation value with respect to a zero-phonon state, thus neglecting phonon emission and absorption during the hopping process. This approach, which we shall call the Holstein-LF (HLF) approximation, yields reliable results only in the nonadiabatic strong-coupling limit<sup>4</sup> [85, 86, 94], while more refined approaches based on strong-coupling perturbation theory provide an accurate description of the Holstein polaron over a larger range of parameters [79, 81]. In the limit  $\lambda = \infty$ , the hopping term in Hamiltonian (3.2) can be neglected, and the LF transformation permits an exact solution of the resulting single-site problem [9]. The transformation has also been used in combination with numerical methods [87, 101, 121]. While the extended LF transformation will be the starting point for the variational approach of Sec. 3.4, Sec. 3.5 discusses, to the best of our knowledge, the first QMC method based on the LF transformation.

<sup>4</sup>This limit corresponds to  $\omega, g \rightarrow \infty$  with  $g/\omega \rightarrow 0$  and  $g^2/\omega = E_{\text{P}}$  finite [cf. Eq. (1.13)].

The Holstein Hamiltonian (see also Sec. 1.3.2) can be written as

$$H = -t \underbrace{\sum_{\langle ij \rangle \sigma} c_{i\sigma}^\dagger c_{j\sigma}}_K + \frac{\omega}{2} \underbrace{\sum_i (\hat{p}_i^2 + \hat{x}_i^2)}_{P=P_p+P_x} - \alpha \underbrace{\sum_i \hat{n}_i \hat{x}_i}_I, \quad (3.2)$$

with the abbreviations  $K$  for the electron hopping,  $P$  for the kinetic ( $P_p$ ) and elastic ( $P_x$ ) energy of the lattice, and  $I$  for the electron-phonon interaction.

We define the unitary operator

$$\hat{\nu} = e^{i \sum_{ij} \gamma_{ij} \hat{n}_i \hat{p}_j} \equiv e^{\hat{S}}, \quad (3.3)$$

where  $i$  and  $j$  run over all  $N$  lattice sites, and with real parameters  $\gamma_{ij}$ .  $\hat{\nu}$  as defined in Eq. (3.3) has the form of a translation operator, and we have  $\hat{\nu}^\dagger = \hat{\nu}^{-1}$ . Given an electron at lattice site  $i$ ,  $\hat{\nu}$  mediates displacements  $\gamma_{ij}$  of the harmonic oscillators at all sites  $j = 1, \dots, N$ . Hence the transformation describes a nonlocal phonon cloud surrounding an electron, corresponding to an extended (large) polaron

Operators have to be transformed according to  $\tilde{\hat{A}} = \hat{\nu} \hat{A} \hat{\nu}^\dagger$ . Introducing the function  $f(\eta) = e^{\eta \hat{S}} \hat{A} e^{-\eta \hat{S}}$  we obtain

$$f'(\eta) = e^{\eta \hat{S}} [\hat{S}, \hat{A}] e^{-\eta \hat{S}}, \quad (3.4)$$

where  $f' \equiv \partial f / \partial \eta$ . A straight-forward calculation leads to

$$[\hat{S}, c_{i\sigma}] = -i \sum_l \gamma_{il} \hat{p}_l c_{i\sigma} \quad , \quad [\hat{S}, c_{i\sigma}^\dagger] = i \sum_l \gamma_{il} \hat{p}_l c_{i\sigma}^\dagger. \quad (3.5)$$

Inserting these results in Eq. (3.4), integrating with respect to  $\eta$  and setting  $\eta = 1$  gives

$$\tilde{c}_{i\sigma}^\dagger = c_{i\sigma}^\dagger e^{i \sum_j \gamma_{ij} \hat{p}_j}, \quad \tilde{c}_{i\sigma} = c_{i\sigma} e^{-i \sum_j \gamma_{ij} \hat{p}_j}. \quad (3.6)$$

For the bosonic operators, the relation

$$\tilde{\hat{A}} = e^{\hat{S}} \hat{A} e^{-\hat{S}} = \hat{A} + [\hat{S}, \hat{A}] + \frac{1}{2!} [\hat{S}, [\hat{S}, \hat{A}]] + \dots, \quad (3.7)$$

yields

$$\tilde{\hat{x}}_i = \hat{x}_i + \sum_j \gamma_{ij} \hat{n}_j, \quad \tilde{\hat{p}}_i = \hat{p}_i. \quad (3.8)$$

With these results, the transformed Hamiltonian becomes

$$\begin{aligned} \tilde{H} = & \underbrace{-t \sum_{\langle ij \rangle \sigma} c_{i\sigma}^\dagger c_{j\sigma} e^{i \sum_l (\gamma_{li} - \gamma_{lj}) \hat{p}_l}}_{\tilde{K}} + P \\ & + \underbrace{\sum_{ij} \hat{n}_j \hat{x}_i (\omega \gamma_{ij} - \alpha \delta_{ij})}_{\tilde{I}_{ep}} + \underbrace{\sum_{ij} \hat{n}_i \hat{n}_j \left( \frac{\omega}{2} \sum_l \gamma_{lj} \gamma_{li} - \alpha \gamma_{ij} \right)}_{\tilde{I}_{ee}}. \end{aligned} \quad (3.9)$$

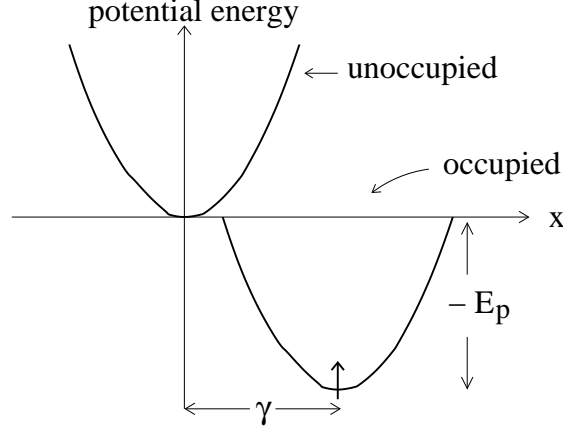


Figure 3.7: Illustration of the energy shift  $E_P$  and lattice displacement  $\gamma$  described by the LF transformation (3.11).

Here the term  $\tilde{I}_{ep}$  describes the coupling between electrons and phonons, while  $\tilde{I}_{ee}$  represents an effective electron-electron interaction. Hamiltonian (3.9) will be the starting point for the variational polaron approach presented in the following section.

For QMC simulations, however, it is more suitable to require that the electron-phonon terms cancel. This can be achieved by setting  $\gamma_{ij} = \gamma\delta_{ij}$  with

$$\gamma = \sqrt{\frac{\lambda W}{\omega}}, \quad (3.10)$$

with the bare bandwidth  $W$  given by Eq. (1.8). Using the definition (3.10), we obtain the standard LF transformation with the transformation operator

$$\hat{\nu}_0 = e^{i\gamma \sum_i \hat{n}_i \hat{p}_i}. \quad (3.11)$$

Following the same steps as above, we find for the transformed operators

$$\tilde{c}_{i\sigma}^\dagger = c_{i\sigma}^\dagger e^{i\gamma \hat{p}_i}, \quad \tilde{c}_{i\sigma} = c_{i\sigma} e^{-i\gamma \hat{p}_i} \quad (3.12)$$

and

$$\tilde{\hat{x}}_i = \hat{x}_i + \gamma \hat{n}_i, \quad \tilde{\hat{p}}_i = \hat{p}_i. \quad (3.13)$$

In contrast to the nonlocal transformation defined by Eq. (3.3), now only the oscillator at the site of the electron is affected, as illustrated in Fig. 3.7. The transformed Hamiltonian reads

$$\tilde{H}_0 = \underbrace{-t \sum_{\langle ij \rangle \sigma} c_{i\sigma}^\dagger c_{j\sigma} e^{i\gamma(\hat{p}_i - \hat{p}_j)}}_{\tilde{K}_0} + \underbrace{P - \frac{1}{2}\gamma^2 \omega \sum_i \hat{n}_i^2}_{\tilde{I}}. \quad (3.14)$$

In the HLF or small-polaron approximation, the ground state of the transformed Hamiltonian is approximated by assuming that no phonons are excited. It has been shown [94] that

the small-polaron wavefunction becomes exact in the strong-coupling, nonadiabatic limit, and agrees qualitatively with the exact results also in the intermediate coupling regime. As discussed by Zhang *et al.* [94], the HLF approximation gives an overestimated shift  $\gamma$  of the equilibrium position of the oscillator in the presence of an electron, and does not reproduce the retardation effects when an electron hops onto a previously unoccupied site. Nevertheless, the local lattice distortion at the site of the electron contains the crucial impact of the electron on the lattice. Consequently, the transformed Hamiltonian (3.14) should be a good starting point to perform QMC simulations, which merely need to account for the rather small fluctuations around the new equilibrium positions. In principle, it would also be possible to develop a QMC algorithm starting with Hamiltonian (3.9), with the parameters  $\gamma_{ij}$  being determined by the variational method discussed in the following section. However, we will see that the simple (local) LF transformation is already sufficient to obtain a very efficient QMC method.

From Eq. (3.14) it is obvious that the LF transformation (3.11) on the one hand removes the electron-phonon coupling term, but on the other hand introduces complex-valued hopping integrals which depend on the phonon momenta at the lattice sites involved in the hopping process. Moreover, as we shall see in Chap. 4, for more than one electron in the system the last term  $\tilde{I}$  introduces a Hubbard-like attractive interaction. In the case of the extended transformation, the electron-phonon interaction term cannot be eliminated entirely, the hopping term involves all phonon momenta  $\hat{p}_i$  as well as the parameters  $\gamma_{ij}$ , and the electron-electron interaction becomes long ranged [Eq. (3.9)]. For these reasons it is expedient to base the QMC simulation on the Hamiltonian (3.14).

For a single electron considered here, we have  $\hat{n}_i\hat{n}_j = \hat{n}_i\delta_{ij}$ , so that the electron-electron interaction term in Hamiltonian (3.9) becomes

$$\tilde{I}_{ee} = \sum_i \hat{n}_i \left( \frac{\omega}{2} \sum_l \gamma_{li}^2 - \alpha\gamma_{ii} \right), \quad (3.15)$$

while the corresponding term in Hamiltonian (3.14) reduces to

$$\tilde{I} = -E_P. \quad (3.16)$$

Equations (3.15) and (3.16) both describe a shift in energy resulting from the original electron-phonon interaction. The polaron binding energy  $E_P$  [Eq. (1.20)] corresponds to the energy shift of the oscillator potential in the presence of an electron (see Fig. 3.7). For two electrons occupying the same site, corresponding to a small bipolaron (Chap. 4), we have  $n_i = 2$  and Eq. (3.14) yields an energy shift of  $4E_P$ .

## 3.4 Variational polaron approach

Here we present a simple variational method which is based on the extended transformation (3.3). Similar work along these lines using different transformations of the Hamiltonian as well as physically motivated wavefunctions can be found, for example, in [102–105]. As

### 3.4. Variational polaron approach

noted above, the zero-phonon ansatz of the simple HLF approximation gives reliable results only in the limit of large  $\bar{\omega}$  and  $\lambda$ . Whereas in HLF the parameter  $\gamma$  of the LF transformation is chosen such that the electron-phonon coupling term  $\tilde{I}_{\text{ep}}$  vanishes, in the variational polaron approach (VPA), we treat the  $\gamma_{ij}$  as variational parameters which are determined by minimizing the ground-state energy in a zero-phonon basis. Like the HLF approximation, the VPA becomes exact in the noninteracting limit ( $\lambda = 0$ ) and in the nonadiabatic strong-coupling limit. We will see in Sec. 3.4.1 that the VPA also gives very accurate results for  $\bar{\omega} \gg 1$  and finite  $\lambda$ . This can easily be understood keeping in mind the discussion of the validity of the HLF approximation given in the preceding section. While the HLF ansatz overestimates the displacement of the local oscillator in the presence of an electron, the VPA determines this shift variationally. Moreover, the missing retardation effects in the response of the oscillators to the motion of the electron become negligible as  $\omega \rightarrow \infty$ . Therefore, in addition to the cases stated above, the VPA also becomes exact in the nonadiabatic limit  $\omega \rightarrow \infty$ . Furthermore, it yields the exact solution for classical phonons ( $\bar{\omega} = 0$ ). Although the limitations of the VPA in or near the adiabatic regime  $\bar{\omega} \lesssim 1$  will clearly emerge when we discuss results in Sec. 3.4.1, it works surprisingly well if we keep in mind the simplicity of the method. Moreover, the reasons for the failure of the VPA in certain parameter regimes are physically clear and can easily be interpreted. Although it is straight forward to extend the VPA to infinite systems, here we restrict ourselves to finite clusters with periodic boundary conditions.

For translational invariant systems the *displacement fields* satisfy the condition  $\gamma_{ij} = \gamma_{|i-j|}$ . Inserting this relation into Eq. (3.15), the expression inside the brackets becomes independent of the index  $i$ . For the single-electron case with  $\sum_i \hat{n}_i = 1$  we have

$$\tilde{I}_{\text{ee}} = \frac{\omega}{2} \sum_l \gamma_l^2 - \alpha \gamma_0. \quad (3.17)$$

We solve the eigenvalue problem of the transformed Hamiltonian (3.9) in a zero-phonon basis for which we make the ansatz

$$\{|l\rangle = c_{l\sigma}^\dagger |0\rangle \otimes \prod_{\nu=1}^N |\phi_0^{(\nu)}\rangle, \quad l = 1, \dots, N\}, \quad (3.18)$$

where  $|\phi_0^{(\nu)}\rangle$  denotes the ground state of the harmonic oscillator at site  $\nu$ . For simplicity, we restrict ourselves to one dimension. The matrix elements of the transformed hopping term in this basis are

$$\begin{aligned} \langle l | \tilde{K} | l' \rangle &= -t_{ll'} \prod_{\nu} \langle \phi_0^{(\nu)} | e^{i(\gamma_{l\nu} - \gamma_{l'\nu}) \hat{p}_{\nu}} | \phi_0^{(\nu)} \rangle \\ &= -t_{ll'} \prod_{\nu} \int dx \phi(x + \gamma_{l\nu}) \phi(x + \gamma_{l'\nu}) \\ &= -t_{ll'} e^{-\frac{1}{4} \sum_{\nu} (\gamma_{l\nu} - \gamma_{l'\nu})^2}, \end{aligned} \quad (3.19)$$

where  $t_{ll'} = t\delta_{ll'}$  is nonzero for nearest-neighbor hopping pairs  $l' = l \pm 1$  and  $\phi(x)$  is the harmonic oscillator ground-state wavefunction in coordinate space. The matrix elements of the other terms of Hamiltonian (3.9) are easily evaluated as

$$\begin{aligned}\langle l|P|l'\rangle &= \delta_{ll'}\frac{\omega}{2}, \\ \langle l|\tilde{I}_{\text{ep}}|l'\rangle &= 0, \\ \langle l|\tilde{I}_{\text{ee}}|l'\rangle &= \delta_{ll'}\left(\frac{\omega}{2}\sum_l\gamma_l^2 - \alpha\gamma_0\right).\end{aligned}\quad (3.20)$$

The eigenstates of the transformed Hamiltonian (3.9) in the zero-phonon subspace, spanned by the basis states defined in Eq. (3.18), are

$$|\psi_k\rangle = c_{k\sigma}^\dagger|0\rangle \otimes \prod_\nu|\phi_0^{(\nu)}\rangle \quad (3.21)$$

with energy

$$\begin{aligned}E(k) &= E_k + \frac{\omega}{2}N + \frac{\omega}{2}\sum_l\gamma_l^2 - \alpha\gamma_0, \\ E_k &= -t\sum_{\delta=\pm 1}e^{ik\delta}e^{-\frac{1}{4}\sum_\nu(\gamma_\nu - \gamma_{\nu+\delta})^2},\end{aligned}\quad (3.22)$$

$E_k$  denoting the kinetic energy of the electron. Defining the Fourier-transformed parameters  $\tilde{\gamma}_q$  as

$$\tilde{\gamma}_q = \frac{1}{\sqrt{N}}\sum_l e^{iq l}\gamma_l \quad (3.23)$$

and using ( $\gamma_l \in \mathbb{R}$ )

$$\sum_\nu\gamma_\nu\gamma_{\nu+\delta} = \sum_q\tilde{\gamma}_q\tilde{\gamma}_{-q}e^{iq\delta} = \sum_q\tilde{\gamma}_q^2\cos q\delta, \quad (3.24)$$

it can be written as

$$\begin{aligned}E_k &= -t\sum_\delta e^{ik\delta}e^{-\frac{1}{2}\sum_q(1-\cos q\delta)\tilde{\gamma}_q^2} \\ &= \tilde{\varepsilon}_0(k)e^{-\frac{1}{2}\sum_q(1-\cos q)\tilde{\gamma}_q^2} \\ &= \tilde{\varepsilon}_{\text{eff}}(k),\end{aligned}\quad (3.25)$$

where  $\tilde{\varepsilon}_0(k) = -2t\cos k$  is the tight-binding band dispersion in one dimension. Using these results the ground-state energy finally becomes

$$E(k) = \tilde{\varepsilon}_{\text{eff}}(k) + \frac{N\omega}{2} + \frac{\omega}{2}\sum_q\tilde{\gamma}_q^2 - \frac{\alpha}{\sqrt{N}}\sum_q\tilde{\gamma}_q. \quad (3.26)$$

The variational parameters  $\tilde{\gamma}_p$  are determined by the condition

$$\frac{\partial E}{\partial \tilde{\gamma}_p} = -\tilde{\gamma}_p \tilde{\varepsilon}_{\text{eff}}(p)(1 - \cos p) + \omega \tilde{\gamma}_p - \frac{\alpha}{\sqrt{N}} \stackrel{!}{=} 0. \quad (3.27)$$

The values for  $\tilde{\gamma}_p$  which minimize  $E$  can then be obtained from

$$\tilde{\gamma}_p = \frac{\alpha}{\sqrt{N}} \frac{1}{\omega + \tilde{\varepsilon}_{\text{eff}}(p)(1 - \cos p)}. \quad (3.28)$$

As  $\tilde{\varepsilon}_{\text{eff}}$  depends on the set of parameters  $\tilde{\gamma}_p$ , this equation has to be solved self-consistently. Equation (3.28) has a typical random-phase approximation form, which is reasonable since a variational ansatz for the ground state of the untransformed Hamiltonian can be written as

$$\hat{\nu}^\dagger |\psi_k\rangle = \frac{1}{\sqrt{N}} \sum_j e^{ikj} c_{j\sigma}^\dagger e^{-i \sum_l \gamma_{jl} \hat{p}_l} |0\rangle \otimes \prod_\nu |\phi_0^{(\nu)}\rangle, \quad (3.29)$$

with  $\hat{\nu}$  as defined in Eq. (3.3).

In addition to the total energy given by Eq. (3.26), we are also interested in the QP weight for momentum  $k = 0$ , defined as

$$\sqrt{z_0} = \langle 0 | \tilde{c}_{k=0,\sigma} | \psi_0 \rangle. \quad (3.30)$$

Here  $|\psi_0\rangle$  denotes the ground state with one electron of momentum  $p = 0$  and the oscillators in the ground state  $|\phi_0\rangle$ . Fourier transformation leads to

$$\begin{aligned} \sqrt{z_0} &= \frac{1}{N} \sum_{ij} \langle \phi_0 | \langle 0 | \tilde{c}_{i\sigma} c_{j\sigma}^\dagger | 0 \rangle | \phi_0 \rangle \\ &= \frac{1}{N} \sum_i \langle \phi_0 | e^{-i \sum_k \gamma_{ik} \hat{p}_k} | \phi_0 \rangle \\ &= e^{-\frac{1}{4} \sum_q \tilde{\gamma}_q^2}, \end{aligned} \quad (3.31)$$

where we have used the same steps as in Eq. (3.19).

#### 3.4.1 Results

In order to test the validity of the VPA we have calculated the total energy [Eq. (3.26)] and the QP weight [Eq. (3.31)] on a cluster of four sites for various phonon frequencies  $\omega$ . A comparison with results from Lanczos diagonalization [123] is depicted in Fig. 3.8. The values of  $\bar{\omega}$  have been chosen to lie in the nonadiabatic regime  $\bar{\omega} \geq 1$  where the zero-phonon approximation of the VPA is sensible. The overall agreement is strikingly good. Minor deviations from the exact results increase with decreasing  $\bar{\omega}$ . For the smallest frequency shown,  $\bar{\omega} = 1.0$ , the curve for the HLF approximation is also shown. It reveals that the VPA represents a significant improvement over the HLF approximation, underlining the importance of the extended polaron cloud.



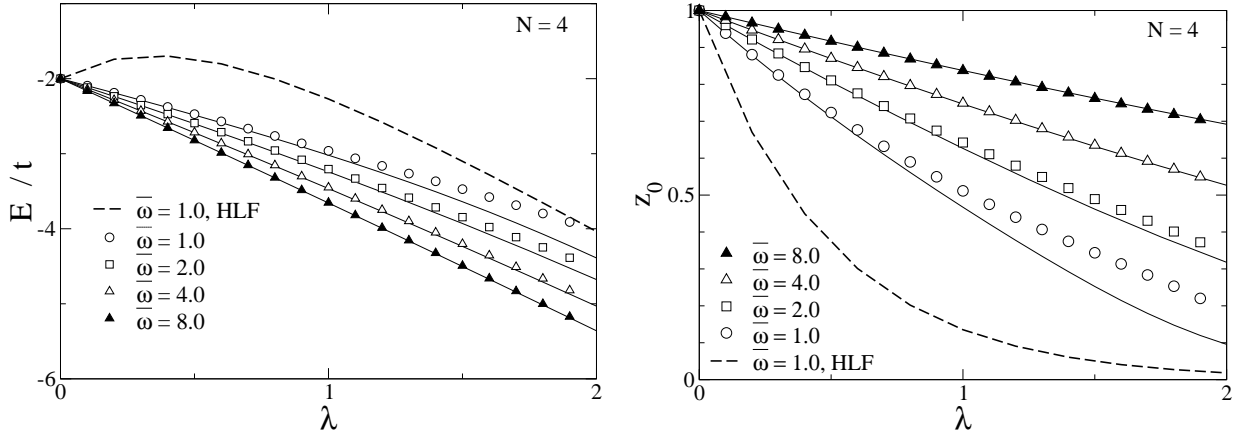


Figure 3.8: Total energy  $E$  (left) and QP weight  $z_0$  (right) as functions of the electron-phonon coupling  $\lambda$  for different values of the adiabatic ratio  $\bar{\omega}$ . Symbols correspond to VPA results, while full lines represent exact  $T = 0$  data obtained with the Lanczos method [123]. Dashed lines are results of the HLF approximation.

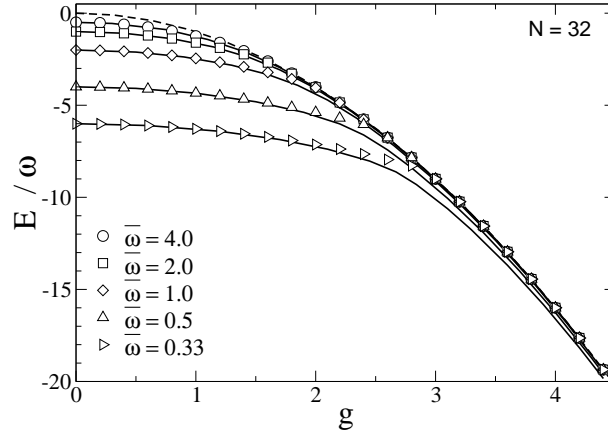


Figure 3.9: Total energy  $E$  as a function of the electron-phonon coupling  $g$  (see text) for different values of the adiabatic ratio  $\bar{\omega}$ . Symbols correspond to VPA results, while full lines represent data obtained with the Global-Local method [99]. The dashed line represents the result for  $\omega = \infty$ .

The comparison with exact results obtained with Lanczos was restricted to small clusters with  $N = 4$  in order to achieve convergence with respect to the number of phonon states included in the calculation. To further scrutinize the accuracy of the VPA we also compare the results of the latter for the total energy with the variational Global-Local method, which has been shown to give accurate results over a large range of parameters [99]. We chose  $N = 32$  for which finite-size effects are already very small (Sec. 3.5.3). Moreover, following Romero *et al.* [99], in Fig. 3.9 we plot  $E/\omega$  over  $g$  with  $g = \sqrt{\lambda W/(2\omega)}$ . Similar to the case  $N = 4$  shown in Fig. 3.8 we find a very good agreement for large values

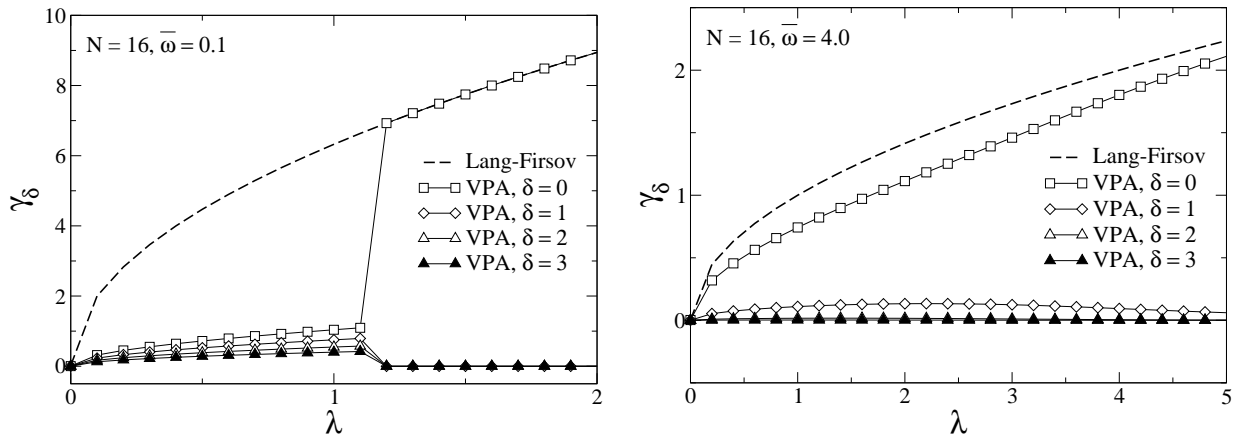


Figure 3.10: Polaron-size parameter  $\gamma_\delta$  as a function of the electron-phonon coupling  $\lambda$  for various distances  $\delta$ . Also shown is the parameter  $\gamma$  [Eq. (3.10)] of the standard LF transformation.

of  $\bar{\omega}$  over the whole range of electron-phonon coupling, whereas for smaller  $\bar{\omega}$  the VPA results begin to bend away from the correct curve and collapse to the nonadiabatic strong-coupling result for large  $g$ . We would like to point out that the maximum electron-phonon coupling strength in Fig. 3.9 corresponds to  $\lambda \approx 40$  (for  $\bar{\omega} = 4.0$ ), in contrast to Fig. 3.8 where  $\lambda \leq 2$ . Figures 3.8 and 3.9 reveal that for  $\bar{\omega} \gg 1$  the VPA yields a very good agreement with the exact data and the Global-Local method even in the intermediate-coupling regime. This behavior can easily be understood considering the assumptions of the VPA. The zero-phonon approximation becomes exact in the nonadiabatic limit  $\omega \rightarrow \infty$ , where the energies of phonon excitations are too high to have an effect on the ground state. Finally, we would like to mention the possibility of comparing the VPA with the QMC results presented in the following section. This has been done for a variety of parameters, but we have found that it is difficult to distinguish between deviations due to the shortcomings of the VPA and due to temperature effects in the QMC results. Consequently, we have decided to confront the VPA with another ground-state method, namely, the Global-Local method, which gives a much clearer picture.

In Fig. 3.10 we present results for the variational displacement fields  $\gamma_\delta$ , which give us a measure for the size of the polaron. For  $\bar{\omega} = 0.1$  we see an abrupt cross over from a large to a small polaron at  $\lambda \approx 1.2$ . For smaller values of the coupling, the electron induces lattice distortions at neighboring sites even at a distance of more than three lattice constants. Above  $\lambda \approx 1.2$  we have a mobile small polaron extending over a single site only. In contrast, for a larger value of the adiabatic ratio  $\bar{\omega} = 4.0$ , there is no obvious cross over and we have a somewhat extended (large) polaron even for large values of  $\lambda$ . The same behavior has been found by Marsiglio [79] who determined the correlation function  $\langle \hat{n}_i \hat{x}_{i+\delta} \rangle$  by Lanczos diagonalization for a restricted phonon basis. Within the VPA we have the relation  $\langle \hat{n}_i \hat{x}_{i+\delta} \rangle = \gamma_\delta$ . The main difference is that in Marsiglio's results, the cross over to a small polaron for  $\bar{\omega} = 0.1$  occurs at a smaller value of the coupling  $\lambda \approx 1$ .

Nevertheless, the simple VPA reproduces the main characteristics of the cross over of the Holstein polaron as the coupling strength  $\lambda$  is increased. Finally Fig. 3.10 also shows the result for the parameter  $\gamma$  of the standard LF transformation (Sec. 3.3). For  $\bar{\omega} = 0.1$ , the curves for  $\gamma$  and  $\gamma_{\delta=0}$  are identical above the critical value  $\lambda \approx 1.2$ . This is not surprising since, in this regime, we have a small polaron extending over a single site only, which is well described by the local LF transformation defined in Eq. (3.11). However, the HLF approximation predicts a spurious exponential decrease of  $\langle \hat{n}_i \hat{x}_i \rangle$  also below the cross over. The same incorrect behavior is also found for the kinetic energy (not shown), corresponding to the well-known overestimation of the polaron band narrowing [3]. For larger values of the phonon frequency,  $\gamma$  and  $\gamma_0$  do not coincide above a critical value of the coupling, but the difference vanishes as  $\lambda \rightarrow \infty$  (see Fig. 3.10). In contrast to the adiabatic regime, the polaron remains an extended object up to very strong coupling, so that the local ansatz of the LF transformation is insufficient for finite values of  $\lambda$  (see also [105]).

## 3.5 Quantum Monte Carlo approach

### 3.5.1 Introduction

A very general QMC method for coupled fermion-boson models, based on an analytic integration over the fermion degrees of freedom, was developed by Blankenbecler *et al.* [124] and Scalapino and Sugar [125]. The simulation is performed using the grand-canonical ensemble with a computation time proportional to the cube of the system size. While the simulations of [124] and [125] were restricted to one dimension, Levine and Su [126, 127] and, using a stabilized version of the same algorithm applicable at low temperatures, Niyaz *et al.* [128] studied charge-density-wave formation and superconductivity in the two-dimensional Holstein model. We shall see in Chap. 5 that the method presented here can be generalized to a grand-canonical algorithm which is very similar to the approach of Blankenbecler *et al.* [124]. A numerically faster method is the world-line algorithm developed by Hirsch *et al.* [106, 107] based on a special breakup of the Hamiltonian and a fixed number of fermions. This results in configuration weights which are simple to evaluate allowing much larger system sizes. In the course of the simulation, both fermions and bosons are sampled simultaneously. The latter method has been successfully applied to the Holstein polaron problem and to the half-filled SSH and Holstein models [106, 107, 129–131]. However, it is restricted to models in one spatial dimension [10]. Scalettar *et al.* [132] applied a rather complicated so-called hybrid molecular dynamics algorithm to the two-dimensional Holstein model near half filling. This work was extended to the low-temperature regime by Noack *et al.* [133]. Finally, Marsiglio [134] developed a low-temperature QMC method to study the same model, also at half filling.

De Raedt and Legendijk [108–110] and Kornilovitch [111] used an alternative approach based on Feynman's path-integral method [135], in which the boson degrees of freedom are integrated out analytically and the resulting fermionic model is treated by MC. Although the method is limited to one electron or two electrons of opposite spin [136] by the sign

problem, it allows efficient simulations in one, two, and three dimensions even for small phonon frequencies near the adiabatic limit, and has been used to investigate a model with dispersive phonons [110]. Also using Feynman's path integral, Kornilovitch and Pike [114] developed a QMC method which exploits the conservation of the total quasimomentum of the system and allows the calculation of dynamical properties such as, e.g., the polaron band structure. Although the method is not restricted to a certain model or dimensionality of the system, it suffers from large statistical errors. Moreover, it is limited to a single fermion at very low temperature, and exhibits a sign problem for nonzero total quasimomentum even in one dimension. Prokof'ev and Svistunov [137] and Mischenko *et al.* [115] used QMC to directly sample the zero-temperature one-electron Green function of the Fröhlich polaron in imaginary time. The method allows calculations for an infinite system in three dimensions, but requires a convergent series for the electron propagator. While all but the last method mentioned so far make use of the Trotter-Suzuki approximation (Sec. 2.1.4), Kornilovitch [112, 113] derived a continuous-time algorithm that works in any dimension and permits simulations on infinite systems. It yields directly dynamical quantities such as the polaron spectrum and effective mass with very high accuracy. Similar to previous work [114], it is restricted to one electron at very low temperatures. Moreover, calculations for small phonon frequencies and/or weak electron-phonon coupling are difficult and a sign problem appears for nonzero total quasimomentum. The projector QMC method [10] in combination with a local updating of the phonon degrees of freedom has been used by Berger *et al.* [138] to investigate the Holstein-Hubbard model at various band fillings, and Green function QMC simulations for the half-filled Holstein model of spinless fermions have been performed by McKenzie *et al.* [139]. Finally, the stochastic series expansion MC technique has been applied recently to an extended, one-dimensional Hubbard model with an electron-phonon interaction of the SSH type [140]. In contrast to other work, the phonons are treated in second quantization. Although the method allows simulations on large lattices in one dimension, it relies on an upper limit for the number of phonons at each site which makes it difficult to study the regime of small phonon frequencies and intermediate or strong coupling.

As the above discussion reveals, the QMC methods of [108–113] are very well suited to study the one-electron problem. Moreover, de Raedt and Legendijk also extended their approach to the bipolaron problem of two electrons with opposite spins [136] (see also Chap. 4). However, as pointed out by Kornilovitch [111], these are all world-line methods. Consequently, despite the possibility of integrating out the phonon degrees of freedom even in the many-electron case, they face a serious sign problem in more than one dimension, for two or more fermions of the same spin, and can therefore not be used to study many-particle systems. On top of that, the advantage gained by the integration over the phonons diminishes quickly with increasing electron density. In the context of superconductivity, the Holstein and the Holstein-Hubbard model with many electrons have been investigated [124–128] using the method of Blankenbecler *et al.* [124]. Due to strong autocorrelations, these simulations were restricted to rather large phonon frequencies  $\bar{\omega} \geq 1$ , while typical materials fall into the adiabatic regime  $\bar{\omega} \ll 1$ . If the phonon degrees of freedom are not integrated out analytically, these correlations predominantly come from

the free harmonic-oscillator dynamics, especially for small phonon frequencies. This often leads to an enormous computational effort even for rather small systems and intermediate temperatures, and is exactly the point where our new approach enters. We shall see below that it completely avoids the problem of autocorrelations. This even remains true for the spinless Holstein model at finite electron density considered in Chap. 5.

This section is organized as follows. In Sec. 3.5.2, we derive the QMC method for the transformed Holstein model, discussing in detail the new concepts used, in particular the reweighting method and the principal component representation, which will also be used in later chapters. We also illustrate the reasons behind the problems encountered with existing methods. The canonical transformation of the Hamiltonian gives rise to a moderate sign problem. The dependence of the latter, and possible explanations of its origin are investigated in Sec. 3.5.3, together with the results obtained with the new method. We conclude with a discussion of the computational effort as compared to other approaches in Sec. 3.5.4.

### 3.5.2 Monte Carlo for the transformed model

In contrast to the approximate variational approach presented in the preceding section, the QMC method discussed here is based on the LF transformation (3.11), which does not contain any free parameters. Therefore, it is exact apart from statistical errors and errors due to the Trotter discretization, which can be systematically reduced.

Due to the fact that the LF transformation contains the crucial electronic influences on the phonons, the MC simulation for the phonon degrees of freedom can be based only on the purely phononic part of the transformed Hamiltonian. The electronic contributions can then be allowed for by reweighting of the probability distribution, corresponding to an exact treatment of the fermion degrees of freedom. This enables us to completely ignore the electronic weights in the updating process, and thereby dramatically reduce the computational effort. Finally, we introduce a principal component representation of the phonon coordinates, which allows exact sampling of the phonons and avoids all autocorrelations.

#### Partition function

Following the general discussion in Sec. 2.1, we begin with the evaluation of the partition function  $\mathcal{Z} = \text{Tr} e^{-\beta H} = \text{Tr} e^{-\beta \tilde{H}_0}$ , with  $\tilde{H}_0$  given by Eq. (3.14). As indicated in the preceding section, for a single electron, the last term in Hamiltonian (3.14) merely represents a constant energy shift. Moreover, we can drop spin indices and are left with the Hamiltonian

$$\tilde{H}_0 = \tilde{K}_0 + P - E_P. \quad (3.32)$$

The polaron binding energy given by Eq. (1.20) can be neglected during the QMC simulation, and needs only to be considered in calculating the total energy. If not indicated otherwise, we assume periodic boundary conditions in real space. Using the Suzuki-Trotter decomposition (Sec. 2.1.4), we obtain

$$e^{-\beta \tilde{H}_0} \approx (e^{-\Delta\tau \tilde{K}_0} e^{-\Delta\tau P} e^{-\Delta\tau P_x})^L \equiv \mathcal{U}^L, \quad (3.33)$$

### 3.5. Quantum Monte Carlo approach

---

where  $\Delta\tau$  has been defined in Eq. (2.15). Splitting up the trace into a bosonic and a fermionic part and inserting  $L$  complete sets of momentum eigenstates we derive the approximation for the partition function

$$\mathcal{Z}_L = \text{Tr}_f \int dp_1 dp_2 \cdots dp_L \langle p_1 | \mathcal{U} | p_2 \rangle \cdots \langle p_L | \mathcal{U} | p_1 \rangle, \quad (3.34)$$

where  $dp_\tau \equiv \prod_i dp_{i,\tau}$ . Each matrix element can be evaluated by inserting a complete set of phonon coordinate eigenstates  $\int dx_\tau |x_\tau\rangle \langle x_\tau|$ . All  $x_\tau$  integrals are of Gaussian form and can easily be carried out. The result is

$$\langle p_\tau | e^{-\Delta\tau P_x} | p_{\tau+1} \rangle = C^N e^{-\frac{1}{2\omega\Delta\tau} \sum_i (p_{i,\tau} - p_{i,\tau+1})^2}, \quad C = \sqrt{\frac{2\pi}{\omega\Delta\tau}}. \quad (3.35)$$

The normalization factor in front of the exponential has to be taken into account in the calculation of the total energy, but cancels when we measure other observables. With the abbreviation  $\mathcal{D}p = dp_1 dp_2 \cdots dp_L$  the partition function finally becomes

$$\mathcal{Z}_L = C^{NL} \int \mathcal{D}p w_b w_f \quad (3.36)$$

with the abbreviations

$$w_b = e^{-\Delta\tau S_b}, \quad w_f = \text{Tr}_f \Omega, \quad \Omega = \prod_{\tau=1}^L e^{-\Delta\tau \tilde{K}_{0,\tau}}. \quad (3.37)$$

Here  $\tilde{K}_{0,\tau}$  is  $\tilde{K}_0$  with the phonon operators  $\hat{p}_i, \hat{p}_j$  in Eq. (3.14) replaced by the momenta  $p_{i,\tau}, p_{j,\tau}$  on the  $\tau$ th Trotter slice. The exponential of the hopping term may be written as

$$e^{-\Delta\tau \tilde{K}_{0,\tau}} = D_\tau \kappa D_\tau^\dagger, \quad \kappa_{jj'} = \left( e^{\Delta\tau t h^{\text{tb}}} \right)_{jj'}, \quad (D_\tau)_{jj'} = \delta_{jj'} e^{i\gamma p_{j,\tau}}, \quad (3.38)$$

where  $h^{\text{tb}}$  is the  $N^D \times N^D$  tight-binding hopping matrix for the  $D$ -dimensional lattice under consideration. Thus we have the same matrix  $\kappa$  for every time slice, which is transformed by the diagonal unitary matrices  $D_\tau$ . The matrix  $\Omega$  can be calculated in an efficient way by noting that the transformation matrices  $D_\tau^\dagger$  and  $D_{\tau+1}$  at time slice  $\tau$  may be combined to a diagonal matrix

$$(\tilde{D}_{\tau,\tau+1})_{ij} = \delta_{ij} e^{i\gamma(p_{i,\tau+1} - p_{i,\tau})}. \quad (3.39)$$

Due to the cyclic invariance of the fermionic trace,  $D_1$  can be shifted to the end of the product, where it combines with  $D_L^\dagger$  to  $\tilde{D}_{L,1}$ . Hence we can write

$$\Omega = \prod_{\tau=1}^L \kappa \tilde{D}_{\tau,\tau+1}, \quad (3.40)$$

with periodic boundary conditions in imaginary time. In the one-electron case, the fermionic weight  $w_f = \sum_n \langle n | \Omega | n \rangle$  is given by the sum over the diagonal elements of the matrix representation of  $\Omega$  in the basis of one-electron states

$$|n\rangle = c_n^\dagger |0\rangle. \quad (3.41)$$

The bosonic action in Eq. (3.37) contains only classical variables and takes the form

$$S_b = \frac{\omega}{2} \sum_{i,\tau} p_{i,\tau}^2 + \frac{1}{2\omega\Delta\tau^2} \sum_{i,\tau} (p_{i,\tau} - p_{i,\tau+1})^2, \quad (3.42)$$

where the indices  $i = 1, \dots, N$  and  $\tau = 1, \dots, L$  run over all lattice sites and Trotter times, respectively, with the periodic boundary conditions  $p_{i,L+1} = p_{i,1}$ . It may also be written as<sup>5</sup>

$$S_b = \sum_i \mathbf{p}_i^T A \mathbf{p}_i \quad (3.43)$$

with  $\mathbf{p}_i = (p_{i,1}, \dots, p_{i,L})$  and a *periodic* tridiagonal  $L \times L$  matrix  $A$  with nonzero elements

$$A_{i,i} = \frac{\omega}{2} + \frac{1}{\omega\Delta\tau^2}, \quad A_{i,i\pm 1} = -\frac{1}{2\omega\Delta\tau^2}. \quad (3.44)$$

Since  $\mathcal{Z}_L$  is a trace, it follows that  $A_{1,L} = A_{L,1} = -1/(2\omega\Delta\tau^2)$ .

At this stage, with the above result for the partition function, a QMC simulation of the transformed Holstein model would proceed as follows. In each MC step, a pair of indices  $(i_0, \tau_0)$  on the  $N \times L$  lattice of phonon momenta  $p_{i,\tau}$  is chosen at random. At this site, a change  $p_{i_0,\tau_0} \mapsto p_{i_0,\tau_0} + \Delta p$  of the phonon configuration is proposed. To decide upon the acceptance of the new configuration using the Metropolis algorithm (Sec. 2.1.2), the corresponding weights  $w_b w_f$  and  $w'_b w'_f$  have to be calculated. Due to the local updating process, the change of the bosonic weight  $\Delta w_b = w'_b/w_b$  can easily be obtained. In contrast, the fermionic weight requires the evaluation of the  $L$ -fold matrix product appearing in the definition of  $\Omega$  in Eq. (3.37). The numerical effort for the calculation of  $w_f$  may be reduced by varying  $\tau_0$  sequentially from 1 to  $L$  instead of picking random values. In this case the calculation of the new fermionic weight, after the change of a single phonon momentum, can be reduced to only two matrix multiplications. We would like to mention that, in contrast to some determinant QMC methods [10], here the matrix product involved in the calculation of the matrix  $\Omega$  is well conditioned also for large systems at low temperatures, so that a time-consuming numerical stabilization is not necessary. Similar to other MC methods, a warm-up phase at the beginning of the simulation would be required for each set of parameters. An additional difficulty arises from the fact that, for the transformed model, the fermionic weight  $w_f$  is no longer strictly positive, even for a single electron in one dimension. This is a consequence of the complex-valued hopping integrals, in contrast

<sup>5</sup>From this point, we shall denote the set of all momenta  $p_{i,\tau}$  ( $i = 1, \dots, N$ ,  $\tau = 1, \dots, L$ ) by  $\mathbf{p}$ , while  $\mathbf{p}_i$  corresponds to the vector  $(p_{i,1}, \dots, p_{i,L})$ , as stated in the text. The same notational convention is used for  $\xi$  and  $x$ .

to simulations of, e.g., the Hubbard model, where a minus-sign problem occurs as a consequence of the Fermi statistics of the electrons [10]. The sign problem encountered here will be discussed in detail below.

A related QMC approach to the original Holstein Hamiltonian (3.2) involves a very similar derivation [124, 125] to obtain the partition function, also in the one-electron limit. In fact the bosonic action  $S_b$  takes exactly the same form, with  $p$  replaced by  $x$ . The main difference is the fermionic part of the partition function, contained in the matrix  $\Omega$ . While the LF transformation leads to a complicated hopping term, the standard approach for the untransformed model only includes the bare hopping operator of Eq. (3.2). However, an interaction term  $I$  [cf. Eq. (3.2)] appears, which contains the phonon coordinates  $\hat{x}_i$ . Hence the matrix  $\Omega$  is replaced by

$$\Omega' = \prod_{\tau=1}^L \kappa V_{\tau}, \quad (V_{\tau})_{jj'} = \delta_{jj'} e^{\Delta\tau\alpha x_{j,\tau}} \quad (3.45)$$

and the path integral in the partition function [Eq. (3.36)] is over all coordinates  $\mathbf{x}$  instead of the momenta  $\mathbf{p}$ . Apart from the fact that the coordinates  $x$  are sampled instead of the phonon momenta, the QMC procedure for the untransformed model is identical to the simulation described above. We shall refer to this less sophisticated QMC method for the original Holstein Hamiltonian as the *standard approach*. For  $\lambda = \alpha = 0$ , i.e., no electron-phonon coupling, we have a set of  $N$  independent harmonic oscillators, and both approaches are alike.

#### Problems with the standard approach

Let us briefly consider the noninteracting limit, in which the partition function can be written as  $Z_L \sim \int \mathcal{D}p e^{-\Delta\tau S_b}$ . As discussed by Batrouni and Scalettar [141], the difficulties encountered in QMC simulations, even for the simple case of a single ( $N = 1$ ) harmonic oscillator, arise from the large condition number, i.e., the ratio of largest to smallest eigenvalue, of the matrix  $A$  in the bosonic action  $S_b$  [see Eqs. (3.43) and (3.44)]. For small values of  $\Delta\tau$  this ratio is proportional to  $(\omega\Delta\tau)^{-2}$  [141], leading to autocorrelation times which grow quadratically with decreasing phonon frequency and the number of Trotter slices  $L$ . The physical reason for these correlations becomes obvious if we look at the bosonic action [Eq. (3.42)]. The latter can be thought of as being proportional to the energy of a given phonon configuration,  $E = \Delta\tau S_b$ . While the first term corresponds to the kinetic energy of the oscillators, the second term describes a coupling in imaginary time, i.e., a pure quantum effect. As pointed out in [141], large changes of a single phonon degree of freedom,  $p_{i,\tau}$  say, are very unlikely to be accepted due to the energy change proportional to  $(\omega\Delta\tau)^{-1}$ , which arises from the coupling to  $p_{i,\tau\pm 1}$ . However, a QMC simulation with only small local changes is extremely ineffective in sampling the relevant regions of phase space. Therefore, successive phonon configurations will be highly correlated. A possible solution might be the use of global updating schemes. Alternatively, the situation could be improved by transforming to the normal modes of the phonons, so that different step sizes



can be used in updating each mode. We will see below that such a principal component representation can indeed be used to completely eliminate these difficulties.

In addition to the abovementioned autocorrelations, which are in fact independent of any electronic influences, standard simulations of the Holstein model become very difficult in the regime where polaron effects are important. This occurs at low temperatures, small phonon frequencies  $\bar{\omega} < 1$ , and for intermediate or strong electron-phonon coupling  $\lambda \gtrsim 1$ . Unfortunately, these are exactly the parameters of interest for simulations of real substances such as, e.g., the manganites [3]. To illustrate the physical origin of these problems let us consider the case of a single electron in the Holstein model. In the polaronic regime, the electron drags with it a cloud of phonons which corresponds to a more or less localized lattice distortion. When the electron hops from site A (with a displaced oscillator corresponding to a small polaron), say, to a neighboring, previously unoccupied site B (with the oscillator in its undisplaced ground state) during a QMC simulation, the current phonon configuration is no longer energetically favorable. Clearly, the oscillator at site A has to return to its undisplaced ground state, while a corresponding phonon cloud has to be built up at site B. Such distortions of the lattice in the presence of an electron are large compared to the zero-point motion of the oscillators. On the other hand, only small changes of the current configuration will be accepted in the simulation. Consequently, it takes an enormous number of single updates to obtain the new configuration in which the polaron has completely moved to site B. Obviously these polaron effects also give rise to strongly autocorrelated configurations, thereby dramatically increasing the numerical effort. The problems due to polaron formation can be overcome by using the LF transformed model, because it separates the large displacements of the local oscillators—due to polaron effects—from the free-oscillator dynamics which correspond to vibrations around the shifted equilibrium positions. The quantities to be sampled, namely the phonon momenta  $p$ , only show a weak dependence on the electron-phonon coupling strength  $\lambda$ , in stark contrast to the coordinates  $x$  in the original, untransformed model, whose expectation values grow linearly with  $\lambda$  in the strong-coupling regime. In fact, the QMC results obtained for the transformed model show that the statistical errors increase in the intermediate coupling regime  $\lambda \approx 1$ , but decrease again as we approach the strong-coupling limit. This is in perfect agreement with the fact that the LF transformation diagonalizes the Hamiltonian (3.2) in the strong-coupling or atomic limit  $\lambda \rightarrow \infty$  (Sec. 3.3), so that the QMC method based on the transformed model becomes very efficient.

## Observables

Thermodynamic expectation values

$$\langle O \rangle = \mathcal{Z}^{-1} \text{Tr} \hat{O} e^{-\beta H} = \mathcal{Z}^{-1} \text{Tr} \hat{\tilde{O}} e^{-\beta \tilde{H}_0} \quad (3.46)$$

of observables  $O$  are computed in the LF transformed representation via

$$\langle O \rangle = \mathcal{Z}^{-1} \text{Tr}_f \int dp \langle p | \hat{\tilde{O}} e^{-\beta \tilde{H}_0} | p \rangle . \quad (3.47)$$

### 3.5. Quantum Monte Carlo approach

---

Here we are interested in the kinetic energy of the electron, the total energy, the mean square of the phonon momenta, and the momentum distribution  $n(k) \equiv \langle \tilde{c}_k^\dagger \tilde{c}_k \rangle$  for various wavevectors  $k$ . We begin with the kinetic energy which is defined as

$$E_k = \langle K \rangle = -t \mathcal{Z}^{-1} \sum_{\langle ij \rangle} \text{Tr} \left( c_i^\dagger c_j e^{i\gamma(\hat{p}_i - \hat{p}_j)} e^{-\beta \tilde{H}_0} \right). \quad (3.48)$$

Using the same steps as in the derivation of the partition function, and noting that the additional phase factors from the operators  $c_i^\dagger$  and  $c_j$  again lead to the same matrix  $\Omega$  as in Eq. (3.40), we find

$$\begin{aligned} E_k &= -t \mathcal{Z}_L^{-1} \sum_{\langle ij \rangle} \int \mathcal{D}p w_b \sum_n \langle n | \Omega c_i^\dagger c_j | n \rangle \\ &= -t \mathcal{Z}_L^{-1} \sum_{\langle ij \rangle} \int \mathcal{D}p w_b \langle j | \Omega | i \rangle \end{aligned} \quad (3.49)$$

with one-electron states  $|n\rangle$  as defined in Eq. (3.41). Using the matrix elements  $\Omega_{ij} = \langle i | \Omega | j \rangle$  and the expectation values

$$\langle O \rangle_b = \frac{\int \mathcal{D}p w_b O(p)}{\int \mathcal{D}p w_b} \quad (3.50)$$

with respect to the purely phononic weights  $w_b$  we obtain

$$E_k = -t \frac{\sum_{\langle ij \rangle} \langle \Omega_{ji} \rangle_b}{\sum_i \langle \Omega_{ii} \rangle_b}. \quad (3.51)$$

Here we have already taken into account the reweighting method which will be discussed in detail below. The total energy can be obtained from the thermodynamic relation  $E = -\partial(\ln \mathcal{Z})/\partial\beta$ , with  $\mathcal{Z}$  given by Eq. (3.36). The result is

$$\begin{aligned} E &= E_k + \frac{\omega}{2} \sum_i \langle p_i^2 \rangle + E'_{\text{ph}} - E_{\text{P}}, \\ E'_{\text{ph}} &= \frac{N}{2\Delta\tau} - \frac{1}{2\omega\Delta\tau^2 L} \sum_{i,\tau} \langle (p_{i,\tau} - p_{i,\tau+1})^2 \rangle, \end{aligned} \quad (3.52)$$

where  $E_{\text{P}}$  is defined in Eq. (3.16) and the expectation values are calculated according to Eq. (3.54) given below. To compare with other work we subtract the ground-state energy of the phonons,  $E_{0,\text{ph}} = N\omega/2$ . Finally,  $n(k)$  can be obtained using Fourier transformation. In one dimension, we find

$$n(k) = \frac{1}{N} \frac{\sum_{ij} \langle \Omega_{ij} \rangle_b e^{ik(i-j)}}{\sum_i \langle \Omega_{ii} \rangle_b} \quad (3.53)$$

with  $k$  from the first Brillouin zone.

Due to the analytic integration over the phonon coordinates  $x$  used here, interesting observables such as the correlation functions  $\langle \hat{n}_i \hat{x}_{i+\delta} \rangle$  are difficult to measure accurately. Other quantities such as the QP weight, and the closely related effective mass [85], can be determined from the one-electron Green function at long imaginary times [142], but results would not be as accurate as in existing work (e.g., [83, 92, 97]). The situation is strikingly different in the more demanding many-electron case, to which our method can be extended (Chap. 5). For the latter, other methods produce far less reliable data than for a single electron and, moreover, other observables, such as the one-electron Green function, are of great physical interest, and can be calculated with our approach.

## Reweighting

In typical QMC simulations a large amount of the total computational effort goes into the calculation of the probability for the acceptance of a proposed change of the configuration. This probability is usually determined by the ratio of the weights of the new and the old configuration, as in the Metropolis algorithm (Sec. 2.1.2). In the notation of Sec. 3.5.2, this involves the calculation of  $w_b$  and  $w_f$  for the two configurations,  $\mathbf{p}$  and  $\mathbf{p}'$  say, in every MC step. While the change in the bosonic weight,  $w_b(\mathbf{p}')/w_b(\mathbf{p})$ , is easily calculated for the case of local updating, the fermionic weight given by Eq. (3.37) involves an  $L$ -fold matrix product of  $N \times N$  matrices for each configuration. Although the numerical effort of the evaluation of such a matrix product can be reduced by scanning sequentially through the time slices, it still requires a lot of total computer time.

This can be avoided by reweighting of the probability distribution to be sampled. Here this corresponds to taking into account only the change  $w_b(\mathbf{p}')/w_b(\mathbf{p})$  in the bosonic weight, and compensating for this by dividing the resulting expectation value of an observable  $O$  by the expectation value of the fermionic weight  $w_f$ , as has been used already in Eq. (3.51). In general, this leads to ratios of the form

$$\langle O \rangle = \frac{\langle O w_f \rangle_b}{\langle w_f \rangle_b}, \quad (3.54)$$

where the subscript “b,” defined in Eq. (3.50), indicates that the average is computed based on  $w_b$  only. Following this procedure, the fermionic weight is treated as part of the observables. The splitting into weight  $w_b$  and observable  $O w_f$  is sensible as long as the variance of  $w_f$  and  $O w_f$  is small, which is the case after the LF transformation. This approach has several additional advantages. With the reweighting method, the updating of the system does no longer require the calculation of  $w_f$  in every step, but only when measurements are performed. Compared to the usual Markov Chain MC procedure (Sec. 2.1.2), this can save an enormous amount of computer time. We will see below that in combination with the principal component representation, the phonon momenta  $\mathbf{p}$  can be sampled exactly without any autocorrelations. This avoids a warm-up phase, and measurements can be made after every MC step. In this final, very efficient procedure, the calculation of  $w_f$  for measurements remains, and is then the most time-consuming part of the simulation. Fi-

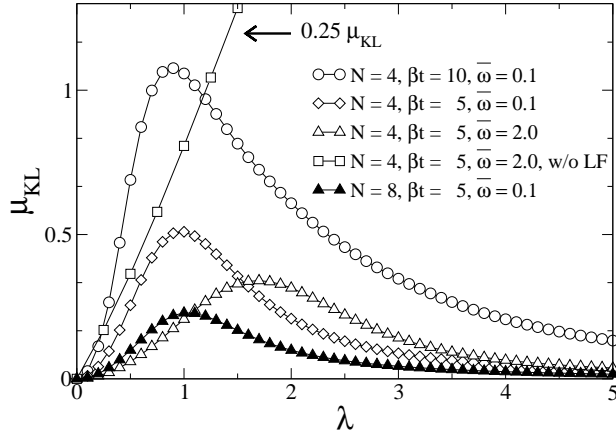


Figure 3.11: Kullback-Leibler number  $\mu_{\text{KL}}$  as a function of electron-phonon coupling  $\lambda$  for various sets of the parameters  $N$  (number of sites),  $\beta$  (inverse temperature) and  $\bar{\omega}$ . As indicated, the results for the untransformed model, denoted in the legend as “w/o LF,” have been scaled by a factor 0.25 (see text). Errorbars are smaller than the symbols shown, and lines are guides to the eye only.

nally, we want to remind the reader once again that here the electronic degrees of freedom are treated exactly, i.e., they are not sampled in the course of the simulation.

Despite the obvious advantages of this approach, it is necessary to scrutinize whether reweighting does not lead to prohibitive statistical noise. If, for example, there was too small an overlap of the actual probability distribution with the one we are sampling with, the method would fail. In fact, our calculations have shown that for the *untransformed* model the reweighting method cannot be applied at low temperatures and for critical values of the parameters  $\bar{\omega}$  and  $\lambda$ .

The distance between two arbitrary probability distributions  $\phi_1(\mathbf{y})$  and  $\phi_2(\mathbf{y})$ , each depending on a set of variables  $\mathbf{y}$ , can be measured by the *Kullback-Leibler number*  $\mu_{\text{KL}}$  defined as [143]

$$\mu_{\text{KL}}(\phi_1, \phi_2) = \int d\mathbf{y} \phi_1(\mathbf{y}) \ln \frac{\phi_1(\mathbf{y})}{\phi_2(\mathbf{y})}. \quad (3.55)$$

For  $\phi_1 \equiv \phi_2$  we have  $\mu_{\text{KL}} = 0$ , while for  $\phi_1 \neq \phi_2$   $\mu_{\text{KL}} > 0$ . The fact that  $\mu_{\text{KL}}$  is a reasonable measure for the distance of two distributions is best illustrated by considering two one-dimensional Gaussian deviates  $\phi_1, \phi_2$  with variance  $\sigma^2$ , centered at  $y_1$  and  $y_2$ , respectively. In this case  $\mu_{\text{KL}} = (y_1 - y_2)^2 / (2\sigma^2)$ . For  $|y_1 - y_2| = \sqrt{2}\sigma$ , where the two peaks begin to be distinguishable, we have  $\mu_{\text{KL}} = 1$ , while a large value of  $\mu_{\text{KL}} \simeq 10$ , for example, corresponds to well-separated Gaussian distributions. Here we use  $\mu_{\text{KL}}$  to investigate the applicability of the reweighting method. As long  $\mu_{\text{KL}} \lesssim 1$ , reweighting works well, while a Kullback-Leibler number strongly exceeding unity indicates severe problems. Two relevant distributions in our case are  $\phi_1(\mathbf{p}) = w_{\text{b}}(\mathbf{p}) / \mathcal{Z}_{\text{b}}$  and  $\phi_2(\mathbf{p}) = w_{\text{b}}(\mathbf{p}) |w_{\text{f}}(\mathbf{p})| / \mathcal{Z}_{\text{bf}}$ , depending on the phonon configuration  $\mathbf{p}$  (or  $\mathbf{x}$  for the untransformed Holstein model).  $\mathcal{Z}_{\text{b}}$  and  $\mathcal{Z}_{\text{bf}}$  are the normalization factors of the probability densities  $\phi_1(\mathbf{p})$  and  $\phi_2(\mathbf{p})$ , and  $w_{\text{f}}$  has been

replaced by its absolute value due to the aforementioned sign problem. Inserting these definitions into Eq. (3.55) we find  $\mu_{\text{KL}} = \ln \langle |w_f| \rangle_{\text{b}} - \langle \ln |w_f| \rangle_{\text{b}}$ . Figure 3.11 shows results for  $\mu_{\text{KL}}$  for different parameters  $\beta$ ,  $\bar{\omega}$ , and  $N$  in one dimension. For  $\lambda = 0$ ,  $w_f$  is independent of the phonon configuration so that  $\mu_{\text{KL}} = 0$ . With increasing electron-phonon coupling, the difference between the two distributions becomes larger. For an intermediate value of the electron-phonon coupling strength,  $\mu_{\text{KT}}$  takes on a maximum and approaches zero again in the strong-coupling limit  $\lambda \rightarrow \infty$ . This is exactly the behavior we would expect for the LF transformed model. For  $\lambda = 0$  the transformation has no effect and  $w_f$  is a constant, just as in the case of the untransformed model. In the intermediate coupling regime, the small-polaron picture mediated by the transformation is not correct as we have an extended (large) polaron in this region. However, as the coupling increases further, the polaron becomes smaller and for  $\lambda = \infty$  it is known that the LF transformation diagonalizes the Holstein Hamiltonian (3.2). The dependence of  $\mu_{\text{KL}}$  on temperature and phonon frequency is also in perfect agreement with the physical picture of the Holstein polaron. As  $\beta t$  increases, polaron effects become more prominent. The same effect occurs if we decrease  $\bar{\omega}$ , and in both cases the maximum of  $\mu_{\text{KL}}$  increases. In Fig. 3.11, the result for a system of eight lattice sites is also shown. The maximum in  $\mu_{\text{KL}}$  is clearly smaller than for the four-site cluster. Calculations for even larger clusters (not shown) reveal that the maximum in  $\mu_{\text{KL}}$  decreases further indicating that the overlap between  $\phi_1$  and  $\phi_2$  increases as  $N \rightarrow \infty$ . This behavior agrees well with the influence of finite-size effects in the cross over region [79]. With increasing system size, the cross over becomes smoother in agreement with the fact that the ground state of the Holstein polaron is an analytic function of the coupling  $\lambda$  [118]. This point will be further illustrated in Sec. 3.5.3. Similar results for  $\mu_{\text{KL}}$  have been found in higher dimensions. To summarize, for all parameters shown in Fig. 3.11,  $\mu_{\text{KL}} \lesssim 1$ , so that we can conclude that the two distributions are indeed very close and the reweighting method can be successfully applied.

We have also calculated the Kullback-Leibler number for the untransformed model, denoted in Fig. 3.11 as “w/o LF,” for which  $|w_f| \equiv w_f$ . The result has been divided by a factor 4 to allow a better representation in Fig. 3.11. The difference between  $\phi_1$  and  $\phi_2$  increases strongly with  $\lambda$  and reaches large values of  $\mu_{\text{KT}} > 10$  already in the intermediate coupling regime  $1 < \lambda < 2$ . Hence, we cannot expect the reweighting method to work in this case. Finally, we want to point out that the distance between  $\phi_1$  and  $\phi_2$  may not affect all observables in the same way. A detailed analysis for each observable  $O$  would be based on the Kullback-Leibler distance of the marginal probability densities

$$\wp_{\alpha}(o) = \int d\mathbf{y} \wp(o|\mathbf{y}) \wp_{\alpha}(\mathbf{y}) = \int d\mathbf{y} \delta[o - O(\mathbf{y})] \wp_{\alpha}(\mathbf{y}), \quad (3.56)$$

where  $O(\mathbf{y})$  is the value of the observable for a given configuration  $\mathbf{y}$  and  $\alpha = 1, 2$  for the two distributions under consideration.

In summary, the reweighting method, together with the LF transformation, allows us to sample a system of independent oscillators, while all the influence of the electrons is transferred to the observable, thereby strongly reducing the numerical effort. In order

to obtain a reliable error analysis for observables calculated according to Eq. (3.54), the Jackknife procedure (Sec. 2.1.5) has been applied.

#### Principal component representation

Although the reweighting method allows us, in principle, to skip enough sweeps between measurements to reduce autocorrelations to a minimum, the computational effort for these MC updates can become the most time-consuming part of the simulation. Even though a single phonon update requires negligible computer time compared to the evaluation of the fermionic weight, in the critical parameter regime, an enormous number of such steps will be necessary between successive measurements. Moreover, reliable results can only be obtained when long enough MC runs have been performed to see even the longest autocorrelation times. In this section, we present a principal component representation for the phonon degrees of freedom, which enables us to create completely uncorrelated samples of phonon configurations.

In order to illustrate the severe problem of autocorrelations with standard updates of the phonons, we have calculated the integrated autocorrelation time  $\tau_p^{\text{int}}$  for the average phonon momentum  $\hat{p}$ . As discussed in Sec. 2.1.5,  $\tau^{\text{int}}$  is a direct measure for the number of MC steps which have to be skipped between measurements in order to obtain uncorrelated data, and is usually given in units of sweeps. We define a sweep as  $N$  times  $L$  proposed local changes of the phonon configuration. For a four-site system, for example, with  $\beta t = 5$ ,  $\lambda = 2$ ,  $\bar{\omega} = 2$ , and  $\Delta\tau = 0.05$  we find  $\tau_p^{\text{int}} \approx 500$ . This corresponds to an autocorrelation time of about  $2 \times 10^5$  single MC steps. For smaller phonon frequencies,  $\tau_{\text{int}}$  increases strongly. For  $\bar{\omega} = 1$  and the same  $\Delta\tau$ , the autocorrelation time is already  $\approx 1700$  sweeps, which agrees quite well with the aforementioned  $(\omega\Delta\tau)^{-2}$  dependence for  $\lambda = 0$ . The dependence of  $\tau_p^{\text{int}}$  on the coupling strength  $\lambda$  is relatively weak, and we have found no systematic behavior of  $\tau_p^{\text{int}}$  as a function of  $\lambda$ . Depending on the other parameters, the autocorrelation times were observed to increase or even decrease slightly as  $\lambda$  is increased. We have also determined the autocorrelation times for observables such as, e.g., the kinetic energy. Although  $\tau_{\text{int}}$  is smaller for electronic observables, the problem still exists, and the determination of the autocorrelation times for various parameter sets is vital to obtain reliable results. This usually requires very long MC runs and a lot of CPU time.

As indicated earlier, the autocorrelations which arise from the structure of the bosonic action  $S_b$  [see Eq. (3.42)] may be overcome by a transformation to the normal modes of the system. Here we represent the bosonic action  $S_b$  in terms of its normal modes along the imaginary time axis, so that we can sample completely uncorrelated phonon configurations. As the fermion degrees of freedom are treated exactly, our QMC method is indeed free of any autocorrelations. This greatly simplifies calculations, since it makes the usual binning analysis (to determine the autocorrelation times) obsolete and, more importantly, leads to significantly shorter simulation times.

All this can be achieved with the simple but effective idea of a transformation to principal components. To this end let us recall the form of the bosonic action given by

Eq. (3.43) which we write as

$$S_b = \sum_i \mathbf{p}_i^T A \mathbf{p}_i = \sum_i \mathbf{p}_i^T A^{1/2} A^{1/2} \mathbf{p}_i \equiv \sum_i \boldsymbol{\xi}_i^T \cdot \boldsymbol{\xi}_i \quad (3.57)$$

with the *principal components*  $\boldsymbol{\xi}_i = A^{1/2} \mathbf{p}_i$ , in terms of which the bosonic weight takes the simple Gaussian form

$$w_b = e^{-\Delta\tau \sum_i \boldsymbol{\xi}_i^T \cdot \boldsymbol{\xi}_i}. \quad (3.58)$$

The QMC can now be performed directly in terms of the new variables  $\boldsymbol{\xi}$ . To calculate observables we have to transform back to the phonon momenta  $\mathbf{p}$  using the matrix  $A^{-1/2}$ . Comparison with Eq. (3.43) shows that instead of the ill-conditioned matrix  $A$  we now have the ideal structure that we can easily generate exact samples of a Gaussian distribution. In terms of the new coordinates  $\boldsymbol{\xi}$ , the probability distribution can be sampled exactly, e.g., by the Box-Müller method [57]. In contrast to a standard Markov chain MC simulation (Sec. 2.1.2), every new configuration is accepted and measurements of observables can be made at each step.

From the definition of the principal components it is obvious that an update of a single variable  $\xi_{i,\tau}$ , say, actually corresponds to a change of all  $p_{i,\tau'}$ ,  $\tau' = 1, \dots, L$ . Thus, in terms of the original phonon momenta  $\mathbf{p}$ , the updating loses its local character. Consequently, a sequential updating of the Trotter time slices can no longer be used to reduce the numerical effort for the evaluation of the fermionic weight. However, in combination with the reweighting method, the latter is only calculated when measurements of observables are made. The enormous advantage of the principal components, leading to completely uncorrelated phonon configurations, clearly outweighs this drawback. Apart from this, the principal component representation can also be applied for more than one electron (see Chaps. 4 and 5), since the bosonic action [Eq. (3.58)], on which the transformation relies, remains unchanged. This even holds for models including, e.g., spin-spin or Hubbard-type interactions (Sec. 1.3), as long as the phonon operators enter in the same form as in the Holstein model.

Another important point is the combination of the principal components with the reweighting method. Using the latter, the changes to the original momenta  $\mathbf{p}$ , which are made in the simulation, do not depend in any way on the electronic degrees of freedom. Thus we are actually sampling a set of  $N$  independent harmonic oscillators, as described by  $S_b$ . The crucial requirement for the success of this method is the use of the LF transformed model, in which the polaron effects are separated from the zero-point motion of the oscillators around their current equilibrium positions. Therefore, the strong dependence of the phonon coordinates on the electron-phonon interaction makes exact sampling impossible for the untransformed model.

### Sign problem

Before we come to a discussion of the sign problem in the approach presented here, we would like to give a quick review of its occurrence in other QMC methods. The situation

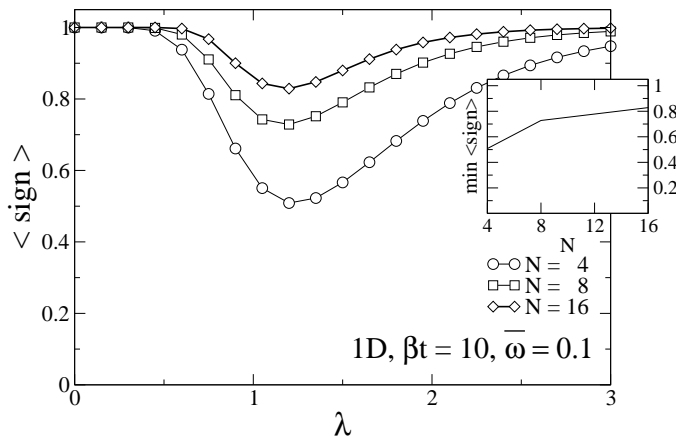


Figure 3.12: Average sign of the fermionic weight  $w_f$  as a function of electron-phonon coupling  $\lambda$  in one dimension for different cluster sizes  $N$ , with parameters as indicated in the figure. Here and in subsequent figures, lines are guides to the eye only, and errorbars are smaller than the symbols shown. The data presented in Figs. 3.12–3.15 are for  $\Delta\tau = 0.05$ . The inset shows the minimum of  $\langle \text{sign} \rangle$  as a function of the system size  $N$  (see text).

is best illustrated for the world-line algorithm (see, e.g., [141]). The use of the latter to simulate systems of interacting fermions is restricted to one dimension by the Fermi statistics of the electrons. This is a consequence of the negative matrix elements  $w$ , which appear when two fermion world lines wind around each other one or more times as they traverse the space-time lattice. Depending on the model parameters, simulations can still be carried out in many situations by using  $|w|$  instead of  $w$ . As discussed in [144], this corresponds to simulating an effective model of hard-core bosons. The average sign in this case may be written as

$$\langle \text{sign} \rangle \equiv \langle \text{sgn}(w) \rangle_{|w|} = e^{-\beta V(f_w - f_{|w|})}, \quad (3.59)$$

where  $f_w$  and  $f_{|w|}$  denote the free energy per site of the fermionic and bosonic model, respectively, and  $V$  is the volume of the system [144]. From Eq. (3.59), it is obvious that  $\langle \text{sign} \rangle$  decreases exponentially with increasing  $\beta$  and  $V$ .

The auxiliary-field method [10] for the Hubbard model faces similar problems. Here the weight of a configuration is given by the product of determinants for  $\uparrow$  and  $\downarrow$  electrons, respectively. The product is strictly positive only for half filling, whereas simulations for other particle densities become very demanding at low temperatures and/or for large systems. Since at large  $U$  the determinant is similar to the weight of world lines of Hubbard-Stratonovitch variables [145], this similarity of the dependence of  $\langle \text{sign} \rangle$  on the parameters of the system is not surprising. Finally, there is no sign problem in determinant grand-canonical simulations of the Holstein model at any filling, since the coupling of electrons and phonons is the same for both spin directions [146].

The sign problem in the current approach clearly has a fundamentally different origin,



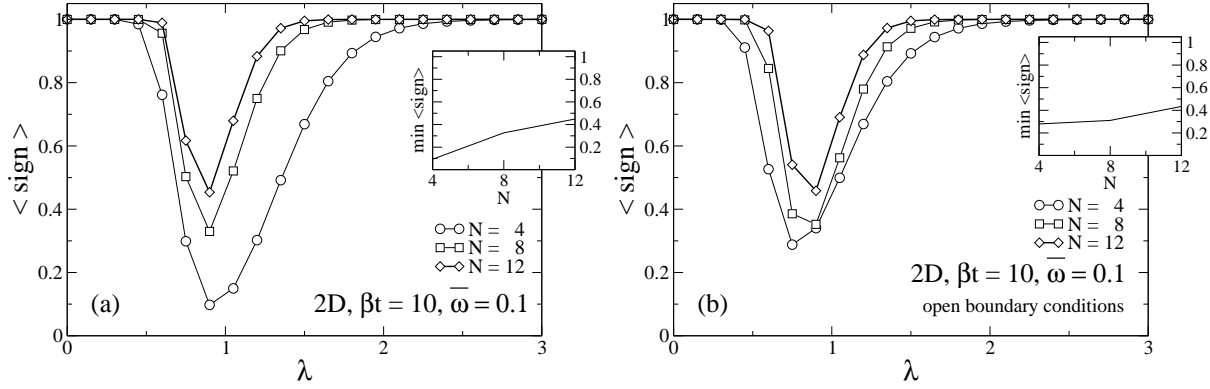


Figure 3.13: As in Fig. 3.12, but for the case of two-dimensional clusters with (a) periodic and (b) open boundary conditions in real space. The insets show the minimum of  $\langle \text{sign} \rangle$  as a function of the linear system size  $N$ .

since there is only a single electron in the system, so that no winding of world lines around each other can take place. To investigate this issue, we calculate the average sign of the fermionic weight  $w_f$

$$\langle \text{sign} \rangle = \frac{\langle w_f \rangle_b}{\langle |w_f| \rangle_b}. \quad (3.60)$$

The expectation value  $\langle \dots \rangle_b$  has been defined in Eq. (3.50). In Fig. 3.12, we show the dependence on electron-phonon coupling and system size. The calculations have been performed for a single, fixed value  $\Delta\tau = 0.05$ , for which the Trotter error is smaller than statistical errors.

From the general discussion above, it is clear that the sign problem encountered in the present approach is of a different nature than in, for example, QMC simulations of the Hubbard model. For the Holstein polaron problem under consideration, it is most pronounced for *small* systems, low temperatures and small phonon frequencies. Therefore, the bulk of results presented below will be for such a set of “worst case” parameters, including  $N = 4$ ,  $\beta t = 10$ , and  $\bar{\omega} = 0.1$ . Figure 3.12 shows that, in one dimension, the average sign of  $w_f$  in the critical region of intermediate electron-phonon coupling increases quickly as the system size increases from  $N = 4$  to  $N = 16$ , which is in strong contrast to Eq. (3.59). This increase of the minimum as a function of  $N$  is also shown in the inset of Fig. 3.12. Since we have only calculated  $\langle \text{sign} \rangle$  for a finite number of  $\lambda$ -values, an approximation for the minimum has been determined using a spline interpolation.

The minimum of  $\langle \text{sign} \rangle$  occurs near  $\lambda = 1$ , where the cross over from a large to a small polaron takes place (see Sec. 3.1). The resulting increase of statistical errors in this regime is similar to the situation encountered in simulations of the untransformed model. However, the use of the transformed model still gives significantly more accurate results for the same number of measurements, in particular for low temperatures and small phonon frequencies. Finally, one may be tempted to explain the unusual system-size dependence of the sign problem by ascribing its origin to the periodic boundary conditions in real space. If

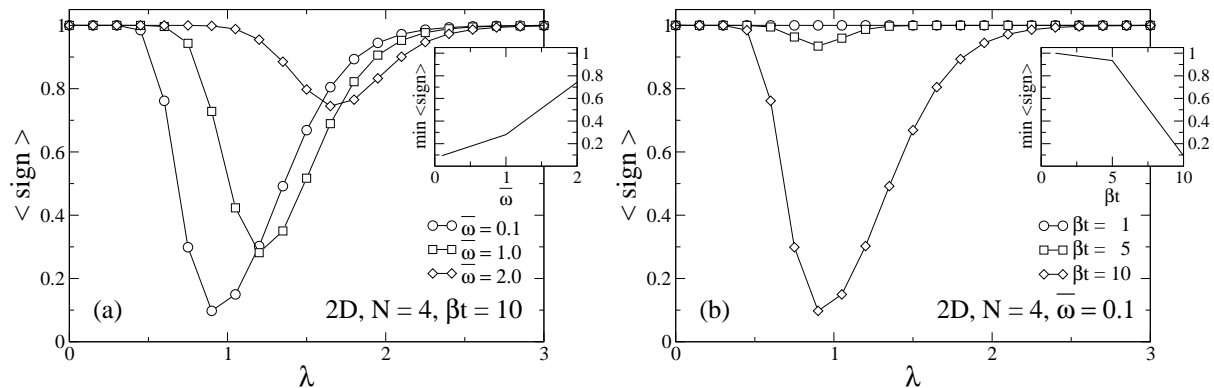


Figure 3.14: Dependence of the average sign on (a) the adiabatic ratio  $\bar{\omega}$  and (b) the inverse temperature  $\beta$  on a  $4 \times 4$  cluster. The insets show the minimum of  $\langle \text{sign} \rangle$  as a function of (a)  $\bar{\omega}$  and (b)  $\beta t$ .

the latter were indeed the source of the sign problem, the boundary effects would decrease with increasing system size, in accordance with the results of Fig. 3.12. This possibility has been investigated, and we shall see below that the sign problem persists also for open boundary conditions.

We now consider the two-dimensional case. In Fig. 3.13(a), we present results for  $\langle \text{sign} \rangle$  for different lattice sizes, again starting with a very small linear dimension  $N$ . All other parameters are the same as before, in particular  $\beta t = 10$  and  $\bar{\omega} = 0.1$ . Obviously, for the smallest cluster size shown, the minimum of the average sign has diminished to a value of approximately 0.1, so that large numbers of measurements will be necessary. Similar to one dimension,  $\langle \text{sign} \rangle$  increases with increasing system size, and for the largest system size shown ( $N = 12$ ), we find a rather uncritical minimum value of about 0.5.

The results for open boundary conditions, shown in Fig. 3.13(b), reveal that for small clusters the average sign is larger than for periodic boundary conditions. However, with increasing system size, it quickly converges to the same values, independent of the boundary conditions. This is just what one would expect, since with increasing  $N$ , the effect of the choice of boundary conditions on the properties of the system diminishes. Moreover, we can conclude that the negative weights do not simply result from hopping processes of the electron across the periodic boundaries, since in that case we would expect  $\langle \text{sign} \rangle \equiv 1$  for open boundary conditions, in contrast to Fig. 3.13(b). The same conclusion can be drawn in one and three dimensions.

The influence of the phonon frequency on the average sign is shown in Fig. 3.14(a). Clearly, the sign problem is most noticeable for small values of  $\bar{\omega}$ , while it diminishes quickly as we increase the adiabatic ratio (see inset). This is very similar to the small-polaron cross over. As discussed in Sec. 3.1, the latter sharpens significantly with decreasing  $\bar{\omega}$ , while a very gradual change with increasing  $\lambda$  takes place in the nonadiabatic regime  $\bar{\omega} > 1$ . Additionally, the position of the minimum of  $\langle \text{sign} \rangle$  is shifted to larger values of  $\lambda$  with increasing  $\bar{\omega}$ .

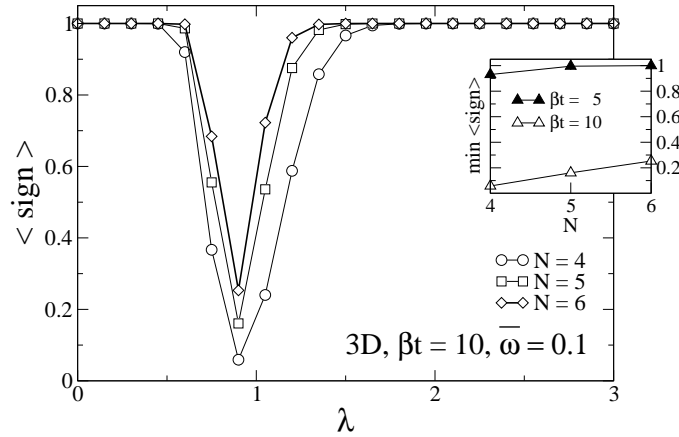


Figure 3.15: Dependence of the average sign on the linear system size  $N$  in three dimensions. The inset shows the minimum of  $\langle \text{sign} \rangle$  as a function of  $N$  for two different temperatures.

In Fig. 3.14(b), we report the average sign as a function of  $\lambda$ , and for different inverse temperatures  $\beta$ . Again we have taken  $N = 4$  and  $\bar{\omega} = 0.1$ , the parameters for which the sign problem is most conceivable. While for  $\beta t = 10$ , the minimum of  $\langle \text{sign} \rangle$  lies below 0.1, the situation is much better already for  $\beta t = 5$ , as shown in the inset. At even higher temperature  $\beta t = 1$ , the fermionic weight is always positive so that we have  $\langle \text{sign} \rangle = 1$  for all  $\lambda$ . The dependence of the sign problem on temperature is therefore similar to other QMC methods [see Eq. (3.59)], although we do not find a simple exponential relation.

Finally, we also present results for  $\langle \text{sign} \rangle$  in three dimensions, for lattices of different linear size  $N$ , and again for the parameters  $\bar{\omega} = 0.1$  and  $\beta t = 10$  as a function of  $\lambda$ . Figure 3.15 reveals that the minimum of  $\langle \text{sign} \rangle$  in 3D has an even more pronounced form than in two dimensions. The sign problem diminishes slightly as we increase the system size from  $N = 4$  to  $N = 6$ . However, accurate simulations in this regime are still quite demanding. For a higher temperature  $\beta t = 5$  and all other parameters unchanged,  $\langle \text{sign} \rangle$  is close to 1 even for  $N = 4$  (see inset in Fig. 3.15), so that accurate results can be obtained even for small phonon frequencies.

In summary, the investigation of the sign problem has shown that our method works well for a large range of values of phonon frequency, electron-phonon coupling and temperature, as long as the system size is large enough. This contrasts, with the world-line algorithm of Kornilovitch [112, 113], which is restricted to intermediate and strong coupling, as well as low temperatures and rather large phonon frequencies, also by a minus-sign problem. Although we have investigated the influence of all important parameters on the sign problem, a physical interpretation of its origin has not emerged. Nevertheless, it is clear that the negative fermionic weights are a result of the phase factors in the LF transformed hopping term in Eq. (3.14). This is similar to the sign problem which occurs, e.g., in simulations of electron-phonon models in an external magnetic field [146], but here the phonon fields  $p_{i,\tau}$  vary with time ( $\tau$ ) and position ( $i$ ), and are coupled in imaginary time by the bosonic

action [see Eqs. (3.43) and (3.44)]. Furthermore, the dependence of the sign problem on  $\bar{\omega}$ ,  $\lambda$ ,  $\beta$  and  $N$  bears a striking resemblance to the influence of these parameters on the properties of the Holstein polaron. In particular, its reduction with increasing system size may be a consequence of the dilution of the system (the particle density  $n \rightarrow 0$  as  $N \rightarrow \infty$  in the one-electron case, see also Sec. 5.3.3). Finally, it is interesting to note that the large statistical fluctuations resulting from the sign problem occur at exactly the same points in parameter space as in the untransformed model. This underlines the correlation between the minimum in  $\langle \text{sign} \rangle$  and the small-polaron cross over, similar to simulations of other models, in which negative weights occur exactly where the most interesting physics is going on, e.g., in the vicinity of phase transitions [10].

#### 3.5.3 Results

We now come to the results obtained with the QMC approach. As a lot of work has already been done on the Holstein polaron problem in the past, we shall exploit the advantages of QMC and study, in particular, finite-size and finite-temperature effects. Furthermore, the comparison with existing results serves as a test of the new ideas presented above. The extension of the current method to the case of more electrons will then allow us to obtain new and interesting results in Chaps. 4 and 5.

Since our approach is based on a discretized imaginary time, it is important to study the convergence of any results with increasing number of time slices  $L$ , which determines the error due to the Suzuki-Trotter approximation of Eq. (3.33). In one dimension,  $L$  was chosen such that systematic errors are smaller than the statistical errors of the results. For all observables considered here we have found the usual  $(\Delta\tau)^2$  dependence of the Suzuki-Trotter error (Sec. 2.1.4). Depending on the adiabatic ratio  $\bar{\omega}$ , values of  $\Delta\tau = 1/30$  (for  $\bar{\omega} \lesssim 1$ ) and  $\Delta\tau = 1/40$  (for  $\bar{\omega} > 1$ ) are sufficient even for the most accurate results. The results in higher dimensions presented below have been obtained by extrapolating results to  $\Delta\tau = 0$  (Sec. 2.1.4). Errorbars for the QMC data presented are always smaller than the symbols used in the figures and are therefore not shown. Finally, lines connecting data points obtained with QMC in Figs. 3.16–3.24 are guides to the eye only.

To test our QMC algorithm we have performed several comparisons with other methods. First, we have checked that the QMC reproduces the exact results obtained with Lanczos on a four-site cluster. Apart from temperature effects, an excellent agreement has been found for several different values of the phonon frequency. Second, as the QMC results are all for finite temperature, we have also compared them with an exact solution for the two-site system valid for arbitrary temperature. We have found a perfect agreement over the whole range of values for  $\beta$ ,  $\bar{\omega}$ , and  $\lambda$ , and can therefore exclude the possibility of any systematic errors.

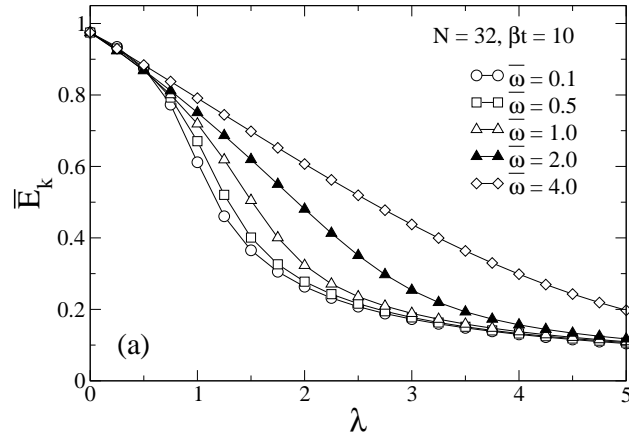


Figure 3.16: Normalized kinetic energy  $\overline{E}_k$  [Eq. (3.61)] as a function of the electron-phonon coupling  $\lambda$  for various values of the adiabatic ratio  $\overline{\omega}$ .

### Holstein polaron in one dimension

**Kinetic energy** The one-electron kinetic energy  $E_k$  is given by Eq. (3.51). In order to compare results for different dimensions later on, we define the normalized quantity

$$\overline{E}_k = E_k / (-2tD) \quad (3.61)$$

with  $\overline{E}_k = 1$  for  $T = 0$  and  $\lambda = 0$ . The kinetic energy of the electron has previously been calculated by several authors [85, 93, 99, 108, 109, 111, 121]. In Fig. 3.16 we show results for  $\overline{E}_k$  on a 32-site cluster, with  $\beta t = 10$  and for several values of the phonon frequency. For large values of  $\lambda$  and  $\overline{\omega} \lesssim 1$  we find  $\overline{E}_k \sim \lambda^{-1}$  as predicted by small-polaron theory [147]. This contrasts strongly with the behavior of the QP weight  $z_0$  [see Fig. 3.8(b)] which decreases much faster and is exponentially suppressed in the small-polaron regime [92]. As pointed out by Fehske *et al.* [101], in the Holstein model, the QP weight is, to a very good approximation, given by the inverse of the ratio  $m_{\text{eff}}/m$  where  $m_{\text{eff}}$  and  $m$  denote the effective and free mass of the electron, respectively. Hence, in the small-polaron regime, the effective mass increases exponentially, while the kinetic energy still has a finite value. We ascribe this behavior to the undirected motion of the electron inside the phonon cloud, which gives rise to a nonzero kinetic energy even for large values of  $\lambda$ , although the polaron is almost localized owing to an exponentially narrowed band. A discussion of the dependence of the cross over on the phonon frequency will be given below for the two-dimensional case.

**Total energy** Next we consider the total energy  $E$ , given by Eq. (3.52). In Fig. 3.17 we present the total energy for various values of the phonon frequency. Finite temperature effects increase as we approach the low-frequency regime, and for  $\overline{\omega} = 0.1$  we clearly see a strong deviation from the ground-state result  $E = -2t$  for  $\lambda = 0$ . The frequency-dependence of the temperature effects can easily be understood if we consider the exact

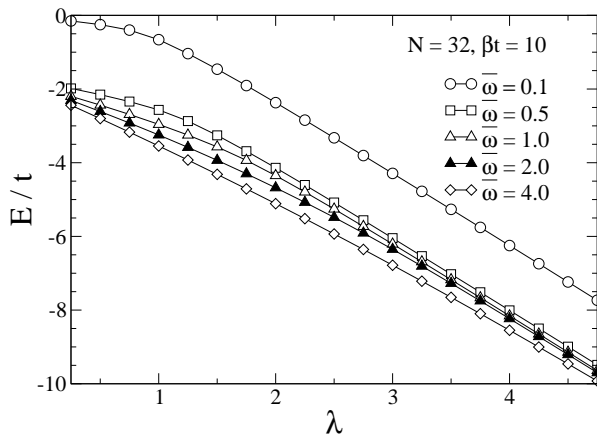


Figure 3.17: QMC results for the total energy  $E$  [Eq. (3.52)] as a function of the electron-phonon coupling  $\lambda$  for various values of the adiabatic ratio  $\bar{\omega}$ .

result for the kinetic energy of  $N$  independent harmonic oscillators

$$E_{\text{k,ph}} = \frac{\omega}{2} \sum_i \langle p_i^2 \rangle = \frac{N\omega}{2} \left( \frac{1}{2} + \frac{1}{e^{\beta\omega} - 1} \right), \quad (3.62)$$

which is identical to the second term in Eq. (3.52). At low temperatures we have  $\langle p^2 \rangle \approx 0.5 + e^{-\beta\omega}$ , with a correction to the ground-state value of 0.5 that increases with decreasing  $\omega$  and is independent of  $\lambda$ . Therefore, the total energy curves are shifted by the same amount for all values of the coupling. As we shall see below, temperature effects are much smaller for other observables, such as the kinetic energy, due to the absence of the strongly temperature-dependent terms  $P_p$  and  $E'_{\text{ph}}$  [see Eqs. (3.2) and (3.52)].

The dependence of  $E$  on  $\bar{\omega}$  in Fig. 3.17 agrees well with existing work [79, 81, 84, 89, 98, 99, 101, 108, 109, 111, 112, 123]. It is interesting to note that in contrast to the kinetic energy  $\bar{E}_k$ , which decreases conceivably near  $\lambda = 1$  in the adiabatic regime (Fig. 3.16), the total energy does not change significantly at the small-polaron cross over since the energy of the system is merely redistributed from kinetic to potential energy [111].

**Momentum distribution and oscillator momenta** Following Zhang *et al.* [94] we have also calculated the momentum distribution  $n(k)$ , given by Eq. (3.53), for different wavevectors  $k$  [Fig. 3.18(a)]. To compare with their DMRG results we chose the same parameters  $N = 6$  and  $\bar{\omega} = 1.0$ . For  $\lambda = 0$  the ground state has momentum  $k = 0$ , so we have  $n(0) = 1$  and  $n(k \neq 0) = 0$ . With increasing coupling  $n(0)$  decreases in a way similar to the kinetic energy (cf. Fig. 3.16), while  $n(k)$  for  $k \neq 0$  increases. In the strong-coupling limit  $\lambda \rightarrow \infty$ ,  $n(k)$  approaches the value  $1/N = 1/6$  for all  $k$ . This is a simple consequence of the localization of the electron for  $\lambda = \infty$ . Although the curve for  $k = 0$  looks very similar to the results of [94] we find a slightly stronger decrease of  $n(0)$  in the intermediate coupling regime. This deviation is no temperature effect of our QMC method but probably

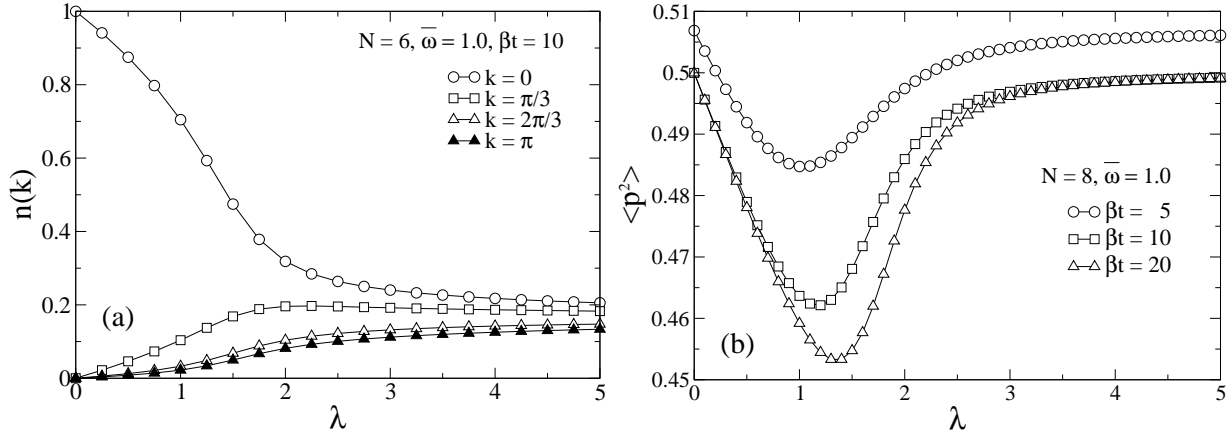


Figure 3.18: (a) Momentum distribution  $n(k)$  [Eq. (3.53)] as a function of electron-phonon coupling  $\lambda$  for various wavevectors  $k$ . (b) Mean square of the phonon momentum  $p$  as a function  $\lambda$ .

originates from the fact that Zhang *et al.* [94] obtained their results for  $n(0)$  by integrating over an approximate spectral function.

In the discussion of the reweighting method, we mentioned that, within the LF approach, the phonon degrees of freedom only show a weak dependence on the electron-phonon coupling, in contrast to the standard approach, where the average oscillator coordinate  $\langle x \rangle$  increases strongly with  $\lambda$  due to the displacement in the presence of an electron. The weak dependence of the vibrational energy of the local oscillator, which is proportional to  $\langle p^2 \rangle$ , on  $\lambda$  is shown in Fig. 3.18(b). For  $\lambda = 0$  we have the result  $\langle p^2 \rangle = 0.5 + [\exp(\beta\omega) - 1]^{-1}$  [see Eq. (3.62)] for a free oscillator. In the intermediate coupling regime,  $\langle p^2 \rangle$  takes on a minimum, corresponding to a reduction of merely 4%, and approaches the value for  $\lambda = 0$  again in the strong-coupling limit. Since the LF transformation does not affect the phonon momenta  $p$  [see Eq. (3.13)], the result for  $\langle p^2 \rangle$  as a function of  $\lambda$  is the same in the untransformed Holstein model. However, the significant advantage of the current method is that the phonon momenta are sampled instead of the coordinates  $x$ . Thus the probability distribution associated with the degrees of freedom to be sampled has only a small variance, which makes simulations much more effective. The dependence of  $\langle p^2 \rangle$  on the coupling strength  $\lambda$  and temperature has first been studied by Ranninger and Thibblin [84] for the two-site model. For such a small system, the minimum of  $\langle p^2 \rangle$  is even more pronounced, while for larger systems the average effect of the electron on a local oscillator is washed out. Ranninger and Thibblin [84] ascribe the deviation of the vibrational energy from the free-oscillator result to anharmonic effects, which are visible only at low enough temperatures. This can clearly be seen in Fig. 3.18(b), where the minimum of  $\langle p^2 \rangle$  becomes less pronounced and is shifted to smaller values of  $\lambda$  as the temperature increases.

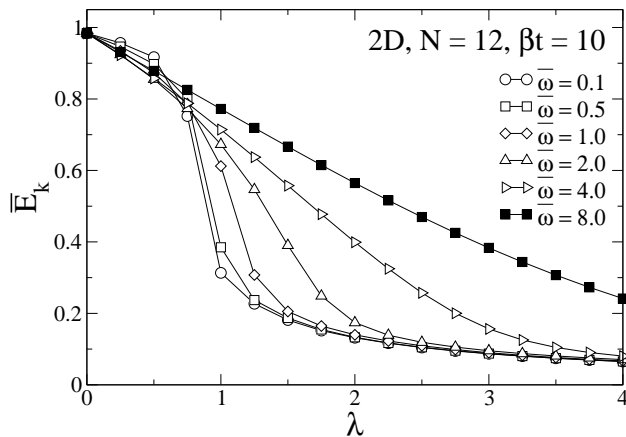


Figure 3.19: Normalized kinetic energy  $\bar{E}_k$  as a function of electron-phonon coupling  $\lambda$  for different values of the adiabatic ratio  $\bar{\omega}$  on a  $12 \times 12$  lattice. The results shown in Figs. 3.19–3.24 have been obtained by extrapolating the QMC data to  $\Delta\tau = 0$  (see text).

### Holstein polaron in two dimensions

While the results in one dimension have been obtained for a single value of  $\Delta\tau$ , here we perform simulations at different values of  $\Delta\tau$ , typically 0.1, 0.075 and 0.05, and exploit the linear dependence of the results on  $(\Delta\tau)^2$  to extrapolate to  $\Delta\tau = 0$ . This is a common procedure in the context of discrete-time QMC methods [10], and allows one to remove the Trotter error if  $\Delta\tau$  is sufficiently small (see also Sec. 2.1.4).

We begin with the dependence of the small-polaron cross over on the phonon frequency. To this end, we present in Fig. 3.19 results for the kinetic energy calculated for  $N = 12$  and  $\beta t = 10$ . The large range of the adiabatic ratio  $0.1 \leq \bar{\omega} \leq 8.0$  demonstrates the ability of our method to give accurate results for almost arbitrary values of the phonon frequency. This contrasts with the method of Kornilovitch [112, 113], which is restricted to  $\bar{\omega} \gtrsim 1$  and  $\lambda \gtrsim 1$  by a minus-sign problem. In our case, the only limitations regarding the accessible values of  $\bar{\omega}$  are the moderate sign problem discussed above, which for small systems and low temperatures gives rise to a noticeable increase of statistical errors as  $\bar{\omega} \rightarrow 0$ , and the increasing Trotter error as  $\omega \rightarrow \infty$ , which requires the use of more and more time slices. Similar to one dimension, the cross over sharpens considerably with decreasing phonon frequency, and the cross over position  $\lambda_c$  increases with  $\bar{\omega}$  in the nonadiabatic regime (see Fig. 3.19).

In the adiabatic regime  $\bar{\omega} \ll 1$ , the cross over is entirely determined by the balance of the electron’s kinetic energy and the polaron binding energy  $E_P$ . As soon as the gain in potential energy outweighs the loss in kinetic energy, the size of the polaron collapses to a single site. The parameter  $\lambda$  is defined as the ratio of these two contributions [Eq. (1.18)] and may be written as  $\lambda = E_P/(W/2)$  ( $-W/2$  is the kinetic energy of a free electron at  $T = 0$ ). Therefore, in the adiabatic regime, the cross over occurs at  $\lambda_c = 1$ . With increasing  $\bar{\omega}$ , the lattice energy becomes important, since more energy is required to excite



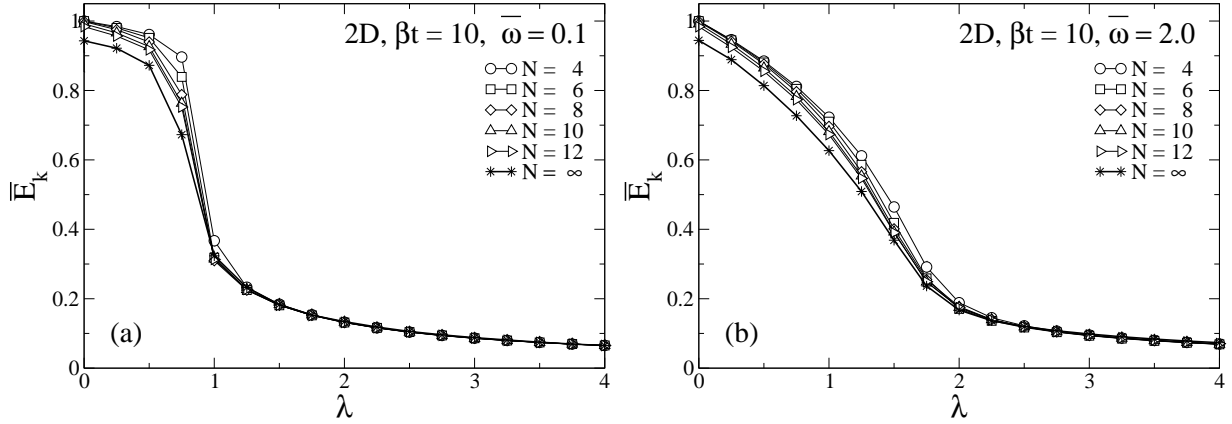


Figure 3.20: Normalized kinetic energy  $\overline{E}_k$  as a function of electron-phonon coupling  $\lambda$  for different linear dimensions  $N$  of the system.

phonons. Consequently, the distortions of the lattice around the position of the electron—giving rise to the large effective mass and low mobility of a small polaron—are much smaller, with the oscillators being predominantly in their ground state. The electron can therefore remain untrapped even for  $\lambda > 1$  if  $\overline{\omega} \gg 1$ . The decrease of  $\overline{E}_k$  with increasing  $\lambda$  is a result of the exponentially decreasing overlap of the ground-state wavefunction of a displaced and an undisplaced harmonic oscillator, which reduces the hopping probability between neighboring lattice sites. In the nonadiabatic regime, a small polaron is formed if  $\sqrt{E_P/\omega} > 1$  (Sec. 3.1). The larger lattice energy in this case also gives rise to the more gradual decrease of  $\overline{E}_k$  for intermediate and large values of  $\overline{\omega}$ . In particular, the kinetic energy is much larger for  $\lambda > 1$  and  $\overline{\omega} > 1$  than for  $\overline{\omega} < 1$ . Finally, for the same  $\overline{\omega}$ , the cross over in two dimensions (Fig. 3.19) is noticeably sharper than in one dimension (Fig. 3.16).

To address the issue of finite-size effects, we have calculated  $\overline{E}_k$  for  $\beta t = 10$ ,  $\overline{\omega} = 0.1$  and different linear lattice sizes  $N = 4-12$  [see Fig. 3.20(a)]. The choice of  $\overline{\omega} = 0.1$  is reasonable since the large polaron, which exists for  $\lambda < \lambda_c$ , is most extended for small phonon frequencies (Sec. 3.1), so that finite-size effects can be expected to be largest. To illustrate this point, we also present results for a larger phonon frequency  $\overline{\omega} = 2.0$  [Fig. 3.20(b)]. For the latter, the local oscillators can respond very quickly to the motion of the electron, and the extension of the phonon cloud or lattice distortion surrounding the electron is much smaller. In contrast, above the critical coupling for the formation of a small polaron, the lattice size is expected to have little influence in both cases. All this is well confirmed by Fig. 3.20, which also reveals that results begin to saturate for  $N \geq 8$ , as pointed out previously by Kornilovitch [111]. Nevertheless, we find a nonnegligible dependence on  $N$  up to the largest system size ( $N = 12$ ). This is better illustrated in Fig. 3.21, in which we show  $\overline{E}_k$  as a function of  $1/N$ , and for several values of  $\lambda$ . To allow a better representation, some curves have been shifted, as indicated in the legend. From Fig. 3.21, we see that  $\overline{E}_k$  changes very little for  $N > 4$  for strong coupling  $\lambda = 2$  and, in fact, remains constant within the errorbars. For smaller values of  $\lambda$ , no such saturation is

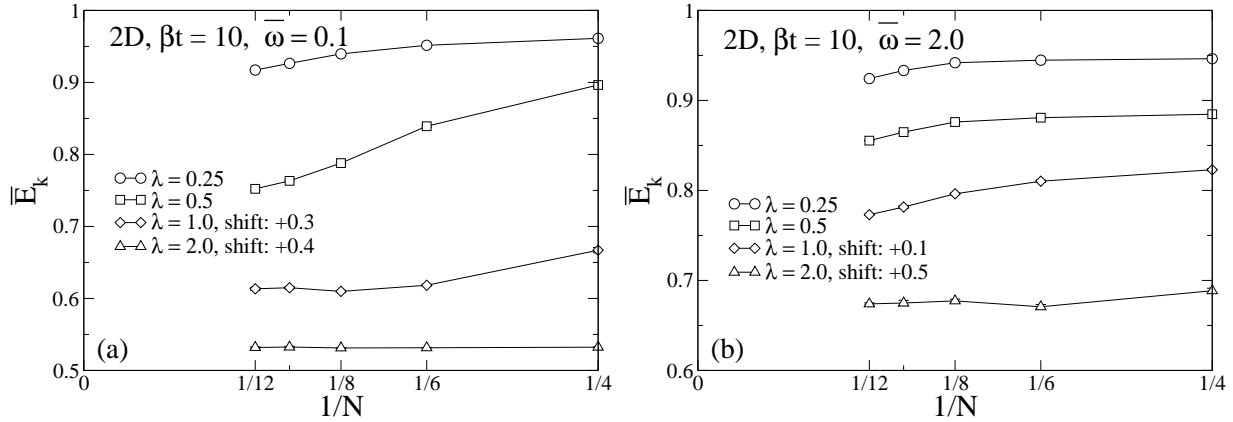


Figure 3.21: Normalized kinetic energy  $\overline{E}_k$  as a function of the inverse of the linear size  $N$  of the system, and for different values of the electron-phonon coupling  $\lambda$ . As indicated in the legend, some curves have been shifted, in order to allow a better representation. All curves are monotonic within statistical errors.

found on the scale of Fig. 3.21, and the behavior of the kinetic energy for large  $N$  is almost linear when plotted as a function of  $1/N$ . We used a linear fit of the data for  $N = 8, 10$ , and  $12$  to obtain an approximation to the thermodynamic limit. The results are presented in Fig. 3.20. Obviously,  $\overline{E}_k$  for  $N = \infty$  has decreased noticeably for small values of  $\lambda$  (including  $\lambda = 0$ ), while it remains almost unchanged in the small polaron regime. The decrease of  $\overline{E}_k$  for  $\lambda < \lambda_c$  can easily be understood if we consider the fact that our method works at a finite temperature  $1/\beta$ . Therefore, for very small  $N$ , the energy gap between the ground state with  $\mathbf{k} = 0$  and the first excited state with  $\mathbf{k} \neq 0$  is larger than the thermal energy  $(\beta t)^{-1}$ . With increasing system size, thermal population of excited states becomes possible. For  $N$  large enough ( $N \approx 20$  for  $\beta t = 10$  and  $\lambda = 0$ ), results converge to those for  $N = \infty$  and, in fact, the extrapolated data for  $\lambda = 0$ , shown in Fig. 3.21, agree well with the results for a free electron on an infinite lattice. We ascribe the smallness of this finite-temperature effect in the strong-coupling regime above  $\lambda_c$  to the narrow polaron band (see Sec. 3.2). Consequently, the low-energy coherent states with different  $\mathbf{k}$  have very similar energies.

We also investigated the effect of temperature, again for  $\overline{\omega} = 0.1$  and  $\overline{\omega} = 2.0$ . The results, presented in Fig. 3.22, indicate that  $\overline{E}_k$  is more affected by the finite temperature of the simulation in the adiabatic case  $\overline{\omega} = 0.1$  [Fig. 3.22(a)]. This is a consequence of the fact that calculations at finite temperatures only give ground-state-like results when  $\beta\omega \gg 1$ . Clearly, this condition is much more difficult to meet for  $\overline{\omega} = 0.1$ , and requires larger values  $\beta t > 10$ .

The changes of  $\overline{E}_k$  with temperature result from an interplay of several effects. For  $\lambda = 0$ , the kinetic energy approaches its full noninteracting value of  $-2tD$  (i.e.,  $\overline{E}_k = 1$ ) as  $T \rightarrow 0$ . At finite  $T$ , however, states with nonzero total quasimomentum  $\mathbf{k}$  will contribute and thereby lead to a decrease of  $\overline{E}_k$ . As discussed above, this effect is expected to decrease

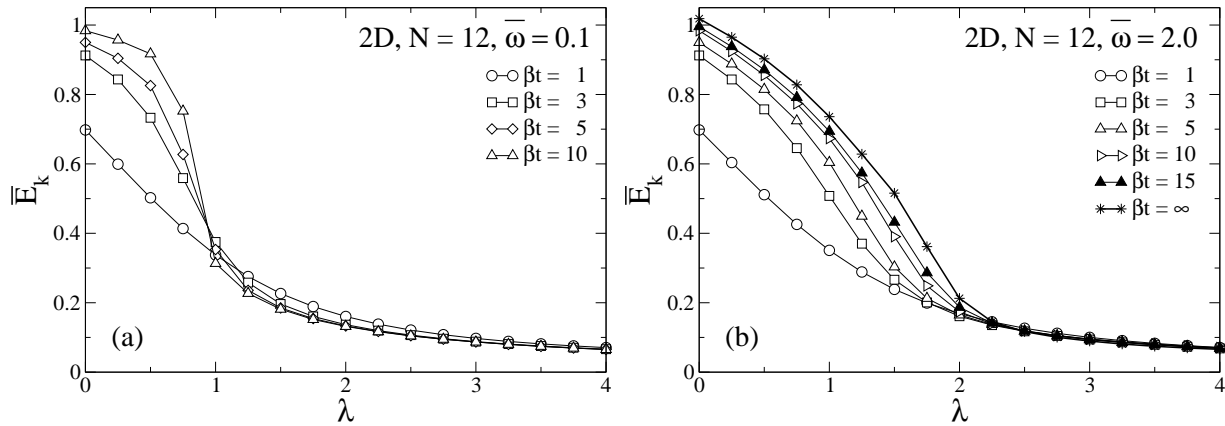


Figure 3.22: Normalized kinetic energy  $\overline{E}_k$  as a function of electron-phonon coupling  $\lambda$  for different inverse temperatures  $\beta$ .

with increasing  $\lambda$ , and to be extremely small in the strong-coupling regime. In the adiabatic case [Fig. 3.22(a)], the cross over at  $\lambda_c = 1$  is smeared out at high temperatures. For both  $\overline{\omega} = 0.1$  and  $\overline{\omega} = 2.0$ , a qualitative change in behavior occurs near  $\lambda_c$ .  $\overline{E}_k$  decreases with increasing temperature for  $\lambda < \lambda_c$ , whereas the opposite is true for  $\lambda > \lambda_c$ . The behavior above  $\lambda_c$  can be understood by considering the electronic hopping amplitude, given by the overlap of the wavefunctions of a displaced and an undisplaced oscillator at neighboring sites. While the latter is exponentially reduced with increasing electron-phonon coupling at  $T = 0$ , it increases with temperature as the oscillators can occupy excited states, corresponding to wavefunctions which are more spread out than the ground state.

Interestingly, the dependence of  $\overline{E}_k$  on temperature is almost linear at low temperatures for  $\overline{\omega} = 2.0$  [see Fig. 3.23(b)]. Similar to the finite-size scaling performed above, we also linearly extrapolated the data for  $\beta t = 10$  and  $15$  to the zero-temperature limit  $\beta t = \infty$ , with the results shown in Fig. 3.22(b). While the general trend agrees well with our expectations based on the finite-temperature data shown, the scaling procedure overestimates the temperature effects in the weak-coupling regime, thereby leading to spurious values  $\overline{E}_k > 1$  at  $\lambda = 0$ . This can easily be understood keeping in mind that results will ultimately saturate at low-enough values of  $\beta t$ , so that the linear extrapolation used here becomes insufficient.

For  $\overline{\omega} = 0.1$ , an inverse temperature  $\beta t = 10$  is not sufficient to obtain well-converged results except for the strong-coupling regime. A linear dependence of  $\overline{E}_k$ , as for  $\overline{\omega} = 2.0$ , may still be found at lower temperatures which have not been investigated here since such calculations, with the accuracy of the results presented here, would be very time-consuming. The situation could be improved by using the checkerboard breakup introduced in Sec. 5.3.

We conclude our discussion of the two-dimensional Holstein polaron by noting that the results of de Raedt and Lagendijk [108–110] were also given for  $\beta t = 5$  (and  $\overline{\omega} = 1$ ), but the small number of Trotter slices ( $L = 32$  in their case) will cause relatively large systematic

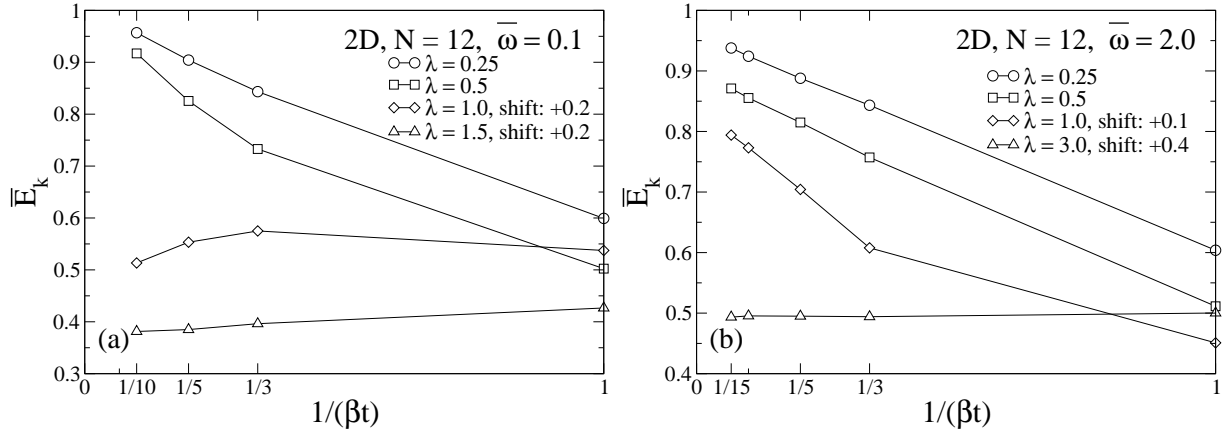


Figure 3.23: Normalized kinetic energy  $\overline{E}_k$  as a function of temperature  $1/(\beta t)$ , and for different values of the electron-phonon coupling  $\lambda$ . As indicated in the legend, some curves have been shifted, in order to allow a better representation.

errors [111]. This is not the case for the results of [111], in which the same extrapolation to  $\Delta\tau = 0$  was employed as here. Finally, the method of Kornilovitch [111, 112] is free of such errors, but only permits one to calculate ground-state properties for restricted values of  $\overline{\omega}$  and  $\lambda$ .

### Holstein polaron in three dimensions

In contrast to the one- and two-dimensional cases discussed above, less work has been done in three dimensions [82, 83, 97, 108–110, 112, 113]. In fact, we are only aware of one calculation of the kinetic energy, which is by de Raedt and Lagendijk (DRL) [109]. To compare with their work, we chose the same parameters  $\overline{\omega} = 1.0$  and  $\beta t = 5$ . The numerical effort for calculations with our method, which is proportional to  $N^{3D}$  for the algorithm in the form used here, restricts us to smaller systems than those considered by DRL [108–110]. For simplicity, we have therefore limited ourselves to a maximum of  $N = 6$ , for which results can easily be obtained within a reasonable amount of computer time, while the data presented in [108–110] is for  $N = 32$ . To be more specific, our calculations for one value of  $\lambda$ , with  $N = 6$  and  $\Delta\tau = 0.05$ , took about 10 h on an Intel Xeon 2600 MHz computer. Due to the relatively small system size in our work, it is important to study to what extent the results are converged with respect to  $N$ . To this end, in Fig. 3.24(a), we present  $\overline{E}_k$  as a function of  $\lambda$  for  $N = 4, 5$ , and 6. Surprisingly, the results are already satisfactorily converged. There is a maximal change of less than 20% in the cross over region at  $\lambda = 1$ , while  $\overline{E}_k$  remains almost constant for small and large  $\lambda$ , as the linear size increases from  $N = 4$  to  $N = 6$ . Thus, increasing  $N$  further will not change the results qualitatively, although the finite temperature of our simulations will manifest itself in a way similar to the two-dimensional case. Our findings agree well with the results of DRL [109]. The main difference is that for weak coupling, our results are closer to the zero-temperature values (e.g.,  $\overline{E}_k = 1$  at  $\lambda = 0$ ). The reason for this discrepancy—despite the fact that we have

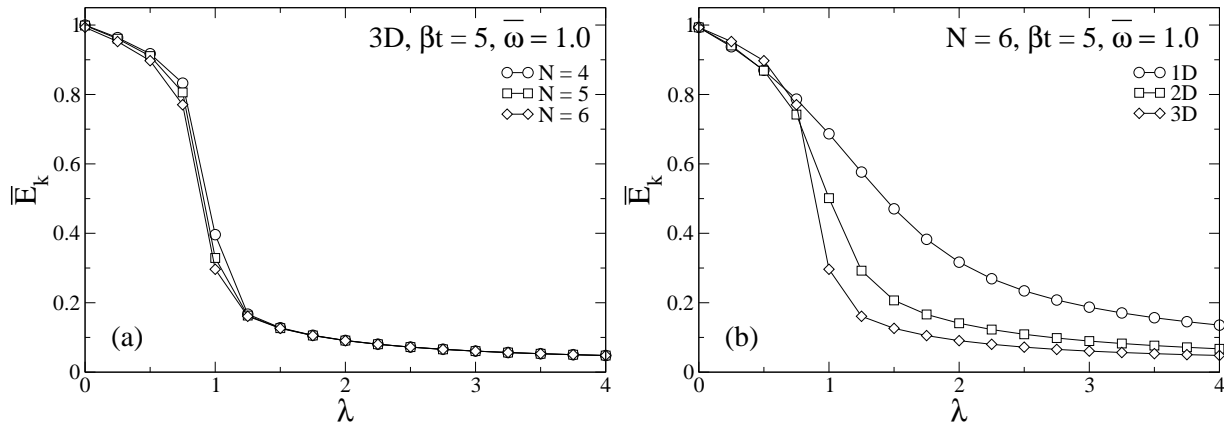


Figure 3.24: Normalized kinetic energy  $\overline{E}_k$  as a function of electron-phonon coupling  $\lambda$  (a) for different linear dimensions  $N$  and (b) for different dimensions  $D$  of the lattice.

used the same temperature—is the smaller lattice size in our calculations. We have not performed a scaling to  $N = \infty$  in 3D, since the clusters under consideration are too small to reveal a systematic power law dependence on  $1/N$ .

Finally, we wish to investigate the effect of dimensionality on the small-polaron cross over. Therefore, we compare  $\overline{E}_k$  in one, two and three dimensions using  $\beta t = 5$ ,  $N = 6$ , and  $\overline{\omega} = 1.0$ . The dependence on  $D$ , which is shown in Fig. 3.24(b), is in perfect agreement with previous work. The cross over from a large polaron to a small polaron sharpens considerably with increasing dimension of the system, and while  $\overline{E}_k$  only displays a gradual decrease in 1D—without any signs of an abrupt change at  $\lambda = 1$ —we find a sharp and well-defined cross over in three dimensions.

To end with, we would like to compare the accuracy of our results to those of DRL [108–111], and Kornilovitch [112, 113]. As discussed in Sec. 3.5.1, the main advantage of their methods is that they allow one to obtain data which are essentially free of finite-size effects, in any dimension  $D = 1–3$ , with modest computational effort. However, we have seen above that even in three dimensions, where the limitation of our algorithm is most noticeable, results are reasonably converged. While the work of [112, 113] is limited to  $T = 0$ , DRL’s method as well as the current approach can, in principle, be used to study any temperature. Apart from the sign problem, the only limitation is that one has to increase the number of Trotter slices as  $\beta \rightarrow \infty$ , so as to keep the Trotter error small. This situation can be greatly improved by extrapolating results to  $\Delta\tau = 0$ . The accuracy of the results presented here depends on  $\overline{\omega}$ ,  $\beta t$ ,  $N$  and  $\lambda$ . Except for the adiabatic regime  $\overline{\omega} \ll 1$  near  $\lambda = 1$ , errorbars are use usually smaller than the linewidth, corresponding to relative errors of less than 0.5%. This is comparable to the accuracy of the results given by Kornilovitch [112] and significantly more accurate than the original results of DRL [108, 109].

### 3.5.4 Performance

The methods of DRL [108–110] and Kornilovitch [111–113] are based on an analytic integration over the phonon degrees of freedom. This separation of electronic and bosonic degrees of freedom greatly reduces the statistical noise due to phonon fluctuations, which increase noticeably with decreasing phonon frequency, decreasing temperature and increasing electron-phonon coupling. Although the LF transformation used here performs a very similar task, namely, to separate polaron effects from the zero-point and thermal fluctuations of the free oscillators, the integral over the bosonic degrees of freedom is calculated with MC, thereby leaving us with a residual influence of the phonons. In fact, the numerical effort for calculations with our approach is proportional to the  $LN^{3D}$ , similar to the grand-canonical determinant method for the Holstein model [124]. This could be improved to a computer time  $\sim LN^{2D}$  by using the checkerboard breakup (Sec. 5.3). The numerical effort for the methods in [108–113] is independent of  $N$ , and depends linearly on  $D$ .

A typical MC run for a 1D cluster with 32 lattice sites,  $\beta t = 5$ ,  $\bar{\omega} = 1.0$ , and  $\lambda \approx 1$  (i.e., near the small-polaron cross over) only takes 5 min of CPU time on a 650 MHz Pentium III personal computer. For such a run relative errors of, for example, the kinetic energy are less than 1.0%. Away from the cross over point, the same accuracy can be obtained within a few seconds. For  $\beta t = 10$ , the temperature used in most of the calculations presented here, a MC run with  $\lambda$  near the cross over value and with similar statistical errors as mentioned above takes about 80 min. The use of the aforementioned checkerboard breakup reduces the CPU times given here by about 65%. For comparison, Kornilovitch [111], using the method of de Raedt and Legendijk [108–110], reports simulation times of several hours on a work station for a  $32 \times 32$  lattice,  $\beta t = 15$  and  $L = 150 - 240$ , and similar CPU times are required for the methods of [112, 113].

## 3.6 Conclusions

We have applied CPT to the Holstein polaron problem in one and two dimensions, and comparison with existing work has revealed a very good agreement. In combination with the Lanczos method to calculate the cluster Green function, reliable results can be obtained for the one-electron spectral function  $A(\mathbf{k}, \epsilon)$ , which become exact in the weak- and strong-coupling limits,  $\lambda = 0$  and  $t = 0$ , respectively. Finite-size effects are significantly reduced compared to standard ED. Our results extend previous applications of CPT to Hubbard and  $t - J$  models, showing that the method is also well suited for electron-phonon models with local interactions. In particular, using CPT, we have been able to calculate the complete spectral function of the Holstein polaron for continuous values of  $\mathbf{k}$ . This is in contrast to ED, which is restricted to rather small numbers of  $\mathbf{k}$  values, and QMC which gives exact results only for the polaron band structure.

Additionally, we have presented a simple variational approach to the Holstein model, which incorporates an extended LF transformation. It can be generalized to infinite systems and represents a marked improvement over the standard small-polaron approximation,

which is only useful in the nonadiabatic, strong-coupling regime.

More importantly, we have introduced an exact QMC method, which is based on the standard LF transformation of the Hamiltonian. The phonon momenta are represented in terms of principal components. This enables us to sample completely uncorrelated configurations, with the electronic degrees of freedom being taken into account by reweighting. The present approach can be applied for a wide range of parameters with relatively small computational effort. In particular, efficient simulations can be performed in the adiabatic regime  $\bar{\omega} < 1$ , which is of special interest in connection with materials such as the manganites. The sign problem resulting from the LF transformation has been found to only weakly affect the statistics, as it diminishes with increasing system size. Comparison with existing work has revealed a very good agreement, although the current QMC approach is not as fast as world-line methods [108–113].

Finally, the method is not restricted to a single electron. Indeed, we shall see in Chap. 4 that it can also be used to investigate the Holstein-Hubbard model with two electrons, and the spinless Holstein model at finite electron density (Chap. 5). The necessary modifications to the algorithm will be discussed in the corresponding chapters.





## 4 Holstein-Hubbard bipolaron

In the previous chapter, we have seen that the coupling of electrons to phonons can lead to the formation of polarons. The next step is to consider the interaction of two such polarons. Depending on the relative strength of the phonon-mediated attractive interaction and the Coulomb repulsion, two electrons may form a bound state which is called a bipolaron. Such QP's have been proposed to play an important role in several classes of materials, including the high-temperature superconductors [13, 14, 148] and the manganites [15]. For the latter, Alexandrov and Bratkovsky [15] derived a theory which assumes the existence of small polarons in the ferromagnetic phase, which bind to bipolarons at the Curie temperature. Although their model can explain some experimental data on the manganites, such as the increase of the resistivity near  $T_C$ , the CMR effect, and the metal-insulator transition, there exist several fundamental problems [3]. Nevertheless, bipolaron formation is still subject of ongoing research work, and much of the recent progress in the field has been achieved using exact numerical methods to perform unbiased studies.

This chapter is concerned with the Holstein-Hubbard model with two electrons, neglecting the interaction between bipolarons which will definitely be present to some degree in real materials. Using CPT, QMC and a variational method, we study in detail the formation of different bipolaron states as a function of the system parameters. While CPT yields accurate results for the one-electron spectral function, QMC and the variational approach can be used to calculate observables such as the kinetic energy of the electrons or electron-electron correlation functions.

The outline of this chapter is as follows. In Sec. 4.1, we review existing work as well as available knowledge about the Holstein-Hubbard bipolaron, while Sec. 4.2 contains the CPT results for the spectral function. Section 4.3 is devoted to canonical transformations of the Holstein-Hubbard Hamiltonian, the results of which are then used for the QMC and variational methods presented in Secs. 4.4 and 4.5. Finally, we conclude in Sec. 4.6.

### 4.1 Holstein-Hubbard bipolaron

The Holstein-Hubbard model has been defined in Eqs. (1.21) and (1.22). While for CPT it is more convenient to use the form (1.22), the starting point of the QMC and variational methods will be Eq. (1.21). For  $U = 0$ , Eqs. (1.21) and (1.22) are identical to the pure Holstein model, while for  $g = 0$  ( $\alpha = 0$ ) we recover the familiar Hubbard model. As in Chap. 3, we use the coupling constant  $\lambda$  [Eq. (1.18)] and the adiabatic ratio  $\overline{\omega}$  [Eq. (1.19)].

Additionally, we define

$$\bar{U} = U/t, \quad (4.1)$$

and express all energies in units of the hopping  $t$ . Consequently, the independent parameters of the model are  $\bar{\omega}$ ,  $\bar{U}$ , and  $\lambda$ .

There exists a considerable amount of work on the Holstein-Hubbard bipolaron, although it is by far not as well understood as the simpler one-electron case. In the sequel, we restrict our discussion to new developments in the field. A very complete review of earlier work has been given by Alexandrov and Mott [78].

While the pairing of electrons in momentum space can be accurately described by Migdal-Eliashberg theory [9] for weak-enough coupling, no reliable theory is available for the formation of bipolarons—corresponding to pairing of electrons in real space—at intermediate to strong electron-phonon interaction. In recent years, progress was made using either variational approaches [149–155] or, more importantly, numerical studies based on ED [79, 84, 85, 121, 156], variational diagonalization [34, 95, 157, 158], DMRG [94], and QMC [136, 159]. The ED and DMRG calculations were restricted to rather small systems consisting of two [84, 121, 156], four [79], six [94], eight [85, 157] or twelve [95] sites, while QMC [136, 159] and the method of [158] are almost free of finite-size effects. The larger number of phonon states required to obtain converged results makes numerical studies with ED methods even more challenging than for a single electron, especially for small phonon frequencies.

Since the Holstein-Hubbard model represents a simplified description of the situation in real materials, it is highly desirable to study more complex models. To this end, it is interesting to note that the QMC methods of de Raedt and Lagendijk [136] and Macridin *et al.* [159] can be generalized to include dispersive phonons. Furthermore, both approaches can be applied to models with long-range Coulomb interaction [136, 159], similar to the work of Bonča and Trugman [160]. Finally, we would like to point out that bipolaron formation in a model with JT modes—as present, e.g., in perovskite manganites—has recently been studied by Shawish *et al.* [34].

To discuss the physics of bipolaron formation in the Holstein-Hubbard model under consideration, we have to distinguish between two cases. The two electrons can either have the same or opposite spin, which leads to a singlet or triplet state, respectively. We consider these possibilities separately.

### Singlet state

For two electrons in a singlet state, the formation of a bound bipolaron state in the absence of Coulomb interaction originates from the fact that the potential well—arising from a displacement of the oscillators—around an occupied lattice site deepens in the presence of a second electron. This may easily be seen in the atomic limit  $t = 0$ , using the LF transformation. As discussed in Sec. 3.3, on different lattice sites, each electron gains an energy  $-E_P$  by distorting the lattice, whereas the energy shift becomes  $-4E_P$  if both particles occupy the same site (*small* or *onsite bipolaron*). For  $t > 0$ , the competition between the kinetic energy of the electrons on the one hand and the displacement or

lattice energy on the other hand determines the cross over from a state with two weakly bound polarons, sometimes also referred to as a *large bipolaron*, for  $\lambda < \lambda_c$  to a small bipolaron for  $\lambda > \lambda_c$ , where  $\lambda_c$  denotes the critical value of the electron-phonon coupling.

In Eq. (1.18),  $\lambda$  has been defined as  $\lambda = 2E_P/W$ , i.e., as the ratio of the energy gain due to polaron formation to the kinetic energy of a free electron. While  $\lambda_c = 1$  in the adiabatic regime for the small-polaron cross over in the model with one electron (Sec. 3.1), here we expect  $\lambda_c = 0.5$  (for  $\bar{\omega} \ll 1$ ) due to the energy gain of  $-2E_P$  per electron compared to  $-E_P$  in the single polaron problem. This is well confirmed by the calculations of Wellein *et al.* [85], who find a strong decrease of the kinetic energy near  $\lambda = 0.5$  for  $\bar{\omega} = 0.4$ .

For  $\bar{\omega} \gg 1$ , the lattice energy becomes important since the trapping of the carriers requires the formation of a sizable lattice distortion. This gives rise to the additional condition  $2\sqrt{E_P/\omega} > 1$  for a small bipolaron [13].<sup>1</sup> Similar to the one-electron problem, the cross over is very gradual in the nonadiabatic regime [85]. The correlation or binding of the two electrons depends crucially on the phonon frequency, since the latter determines the maximum distance across which the two particles feel an attractive interaction due to the phonons. Up to second order in  $g$ , this coupling is given by

$$U_{\text{eff}}(\epsilon) = g^2 \mathcal{D}_{\text{ph}}(\mathbf{q}, \epsilon) = -\frac{2g^2\omega}{\omega^2 - \epsilon^2}, \quad (4.2)$$

where  $\mathcal{D}_{\text{ph}}(\mathbf{q}, \epsilon)$  denotes the phonon propagator. Equation (4.2) reveals that the energy-dependent interaction is attractive for  $\epsilon < \omega$ , and becomes instantaneous in the nonadiabatic limit  $\omega \rightarrow \infty$  where  $U_{\text{eff}} = -2g^2/\omega$ . Hence, the binding always decreases with increasing phonon frequency [79].

For  $U > 0$ , there is a competition between the retarded, attractive interaction mediated by the phonons and the instantaneous, repulsive Hubbard interaction. Consequently, a state with two unbound polarons—stabilized by the onsite repulsion—can exist for sufficiently weak electron-phonon coupling [85]. This is in contrast to the extended Holstein-Hubbard model with long-range interaction, in which a bipolaron state is formed irrespective of the value of  $U$  [161]. The effective electron-electron interaction in the Holstein-Hubbard model which determines the nature of the bipolaron state is

$$U_{\text{eff}} = U - 2E_P. \quad (4.3)$$

From this result, which can be obtained either from the generalization of Eq. (4.2) to  $U \neq 0$  in the limit  $\omega \rightarrow \infty$ , or in the nonadiabatic strong-coupling limit [159], one may be tempted to expect a bipolaron state to exist only for  $U_{\text{eff}} < 0$ , i.e., if there is a net attractive interaction between the particles. While this is true for the effective Hubbard model onto which the Holstein-Hubbard model maps in the nonadiabatic strong-coupling limit, a consideration of virtual hopping processes leads to the less stringent condition  $U < 4E_P$  [158]. The energy gain due to virtual exchange processes of two electrons on neighboring lattice sites—not suppressed by strong electron-phonon coupling—leads to

<sup>1</sup>The corresponding condition for a small polaron is  $\sqrt{E_P/\omega} > 1$  (Sec. 3.1).

the formation of a weakly bound *intersite bipolaron* with the two electrons most likely to reside on neighboring lattice sites [158, 159]. A phase diagram for bipolaron formation as a function of  $\lambda$  and  $\bar{\omega}$  in one dimension has been presented by Weiße *et al.* [95]. Eventually, for sufficiently strong electron-phonon coupling  $2E_P \gtrsim U$ , the effective onsite potential  $U_{\text{eff}}$  becomes attractive, and a small bipolaron is formed.

Starting from a small bipolaron, a cross over to an intersite bipolaron takes place when the Coulomb interaction becomes large enough [158, 159, 161]. The intersite bipolaron has a much smaller effective mass than the small bipolaron and may therefore also exist as a mobile carrier in real materials [158]. In the adiabatic limit  $\bar{\omega} = 0$ , the onsite–intersite bipolaron transition has been shown to be of first order [152, 153], but for finite phonon frequencies it is expected to happen in a more gradual way because of retardation effects, in agreement with recent calculations [158]. Estimates for the region of existence of the intersite bipolaron state for  $\bar{\omega} = 1$  are  $U < 2E_P$  for weak coupling, and  $U < 4E_P$  for strong electron-phonon coupling [158], and phase diagrams in the  $(U, \lambda)$ -plane have been reported in one [158] and two dimensions [159]. While the above conditions are quite accurate in the nonadiabatic regime  $\bar{\omega} \geq 1$ , the case  $\bar{\omega} \ll 1$  remains an open problem.

Finally, the physically most interesting regime, which is unfortunately also the most difficult case to treat theoretically, is defined by  $\bar{\omega} \ll 1$ , and a Coulomb repulsion which is at least as large as the attractive interaction due to the electron-phonon coupling.

### Triplet state

For two electrons of the same spin, the Pauli principle forbids double occupation of a site. Although in principle a bound state may be formed with the two particles being located on different lattice sites, the exchange processes, which stabilize the intersite bipolaron state of two electrons in a spin singlet configuration, are not strong enough to bind two polarons in a triplet state in the strong electron-phonon coupling regime [158]. Since for  $U \rightarrow \infty$  the singlet and triplet state become degenerate, this may also be seen from the strong-coupling condition  $U - 4E_P$ . If  $U = \infty$ , no value  $\lambda > 0$  is sufficient to create a bound state. Furthermore, the ground-state energy of two polarons in a triplet state is always larger than for a singlet state because two particles with parallel spin cannot occupy the same  $\mathbf{k} = 0$  energy level.

## 4.2 One-particle spectral function

### 4.2.1 Method

As in Chap. 3, we use CPT in combination with the Lanczos recursion method (Secs. 2.2 and 2.3). The major difficulty we are facing in the present case is the larger number of phonon states needed to obtain converged results. From a physical point of view, this is not surprising since each of the two electrons will create a lattice distortion or phonon cloud, whereas there is only one dressed particle (polaron) in the one-electron problem (Chap. 3). However, in addition to the simple doubling of the number of particles, it has

been shown by previous authors [79, 85, 94] that multiphonon states play a more important role for the bipolaron, as a result of the phonon-mediated binding. ED (and also CPT) for electron-phonon systems is affected both by finite-size effects and the truncation error due to the restricted number of phonon states kept in calculations. Obviously, if one used very small clusters, good convergence with respect to the phonons could be achieved even for strong electron-phonon coupling. On the other hand, for small numbers of phonon states, rather large clusters can be studied. A common approach is to require the truncation error  $\Delta$  [Eq. (2.48)] to be smaller than a certain limit, and to use the maximal cluster size which can be handled for this number of phonon states.

From the nature of the approximation made (see Sec. 2.2), it is clear that CPT will work particularly well if the local interactions dominate the physics of the system, i.e., for the Holstein-Hubbard model (1.22), if  $g, U \gg t$ . This point will be illustrated in Sec. 4.2.2.

Since here we only consider the one-dimensional case, in the sequel, we shall adopt the notation accordingly. We are interested in the Green function

$$G_\sigma(k, \epsilon) = \langle \downarrow | c_{k\sigma} \frac{1}{\epsilon - H} c_{k\sigma}^\dagger | \downarrow \rangle, \quad (4.4)$$

where  $|\downarrow\rangle$  denotes the ground state with one electron of spin down, and  $\sigma = \uparrow, \downarrow$ . Equation (4.4) only contains the inverse photoemission part of the total one-electron Green function. In the case of  $G_\uparrow$ , the second part—corresponding to photoemission (PE)—vanishes, since there is no  $\uparrow$  electron in the ground state. Moreover, for  $G_\downarrow$ , PE is identical to the spectrum of a single polaron, which has been studied in detail in Sec. 3.2. The situation would be different if we started with a two-electron (singlet or triplet) ground state. Then, the PE part of the one-electron spectral function also contains valuable information. However, due to limited computer memory, such computations involving three-electron states are not possible with the code used here.

In Eq. (4.4), we have omitted the energy  $E_0^\downarrow$  of the ground state  $|\downarrow\rangle$ , which usually enters in the form  $H - E_0^\downarrow$  [Eq. (2.35)], to permit direct comparison with the singlet bipolaron band dispersion  $E^{\uparrow\downarrow}(k)$  in Sec. 4.2.2. We would like to mention that this issue did not arise for the Holstein polaron in Sec. 3.2, since the ground state energy of the state  $|0\rangle$  in Eq. (3.1) is zero. The one-electron spectral function is related to the Green function (4.4) by Eq. (2.36). In the present case, a spin index has to be added, so that we have

$$A_\sigma(k, \epsilon) = -\frac{1}{\pi} \lim_{\eta \rightarrow 0^+} \text{Im} G_\sigma(k, \epsilon + i\eta). \quad (4.5)$$

The phonon Hilbert space is truncated in the same way as in Sec. 3.2 [see Eq. (2.47)], with the number of phonon states used denoted as  $N_{\text{ph}}$ . The latter will be chosen so as to push the truncation error  $\Delta(N_{\text{ph}})$  [Eq. (2.48)] of the energy  $E_0^{\uparrow\downarrow}$  of the two-electron ground state  $|\uparrow\downarrow\rangle$  below  $10^{-4}$ . The use of  $E_0^{\uparrow\downarrow}$  to monitor convergence with respect to  $N_{\text{ph}}$  comes from the observation that—for the same number of phonons—the truncation error of the latter is always smaller than for the triplet state  $|\downarrow\downarrow\rangle$ . This may be ascribed to the fact that for two electrons of the same spin, no bound state exists. In particular, there

will be no large local lattice distortion surrounding an onsite bipolaron, the description of which requires a significant number of phonons. In previous work on the Holstein-Hubbard bipolaron, using ED with periodic boundary conditions [79, 84, 85, 121, 156], the truncation error was usually smaller than  $10^{-6}$ . However, these methods were restricted to only a few  $k$  vectors. Furthermore, our calculations show that even a relative error of  $10^{-4}$  ensures satisfactory convergence of the one-electron spectrum. The smaller number of phonon states enables us to use larger clusters and thereby significantly diminish finite-size effects since, within the CPT, even an increase  $N \rightarrow N + 1$  noticeably improves the results. Once the cluster size has been fixed, we use the maximal possible number of phonons. The accuracy  $\Delta$  varies for the different calculations and will be reported in each figure.

In its present form, our method is restricted to the nonadiabatic regime  $\bar{\omega} \geq 1$ , except for weak electron-phonon coupling. To study smaller phonon frequencies—relevant, e.g., to transition metal oxides—a combination with variational diagonalization techniques, or the use of shared-memory systems would be necessary. As in Chap. 3, we restrict our calculations to the spectral function, which is the most fundamental quantity that can be obtained within CPT [12].

### 4.2.2 Results

The one-electron spectral function of the problem considered here has been calculated before using ED [84, 121, 156] and DMRG [94], both in one dimension. However, results were only given for  $k = 0$ , and for very small systems with  $N = 2$  and  $N = 6$ , respectively. This makes it difficult or even impossible to study the dispersion of QP features. Recently, a parallelized DMRG code has been developed [91], which allows studies of Holstein models on very large one-dimensional clusters even at half filling [162]. However, the calculation of spectral functions within DMRG is very time-consuming, since it has to be done separately for each point on the energy axis. Several authors have also calculated dressed spectral functions [94, 121, 156], with the fermion operators in Eq. (4.4) replaced by their LF transformed (i.e., dressed) counterparts, as well as pair spectral functions [94]. The corresponding spectra show a simplified structure in certain regimes, indicating that polarons and bipolarons are “good” QP’s for these parameters.

De Mello and Ranninger [121] have pointed out that to study the cross over between polarons and bipolarons it is, in general, necessary to investigate both, photoemission and inverse photoemission. This can easily be understood by considering electron emission from the two-electron singlet ground state, i.e., the Green function  $\langle \uparrow\downarrow | c_{k\uparrow}^\dagger (\epsilon - H)^{-1} c_{k\uparrow} | \uparrow\downarrow \rangle$ . Depending on the parameters,  $|\uparrow\downarrow\rangle$  may either consist of two weakly bound polarons or a bipolaron. Consequently, photoemission spectra will only show a single QP band. In contrast, the Green function (4.4) with  $\sigma = \uparrow$  corresponds to adding an  $\uparrow$  electron to the one-electron ground state  $|\downarrow\rangle$ . For example, the additional particle can either go into the ground state to form a bipolaron, or into an excited polaron state. In general, we therefore expect two QP bands in the spectral function, whose weights and energies vary with  $\bar{\omega}$ ,  $\bar{U}$  and  $\lambda$ .

As we will compare our findings with the variational diagonalization method (VDM)

of Bonča *et al.* [34, 158], we would like to comment on the accuracy of the latter. The problem is defined on an infinite system, so that the approach is free of boundary finite-size effects. However, the method involves a variationally determined Hilbert subspace with two variational parameters, namely the maximal allowed distance between electrons and phonons, and between the two electrons, respectively. For the bipolaron problem under consideration, the limiting variational parameter in the regime  $\bar{\omega} \geq 1$  is the maximum distance  $N_h$  between the two electrons. The results presented here have been obtained using  $N_h \leq 18$ . Consequently, while the method gives very accurate results—with errors smaller than the linewidth in the figures—for the case of a small bipolaron ( $U \ll 2E_P$ ), it is less reliable (relative errors  $\lesssim 1\%$ ) for strong onsite repulsion  $U \gg 2E_P$  favoring two weakly bound polarons, similar to ED and CPT. Due to additional towers of phonon excitations that are located in the neighborhood of the electron sites, the method achieves good convergence in the small bipolaron regime even for strong coupling. Nevertheless, the adiabatic regime  $\bar{\omega} \ll 1$  represents a difficult problem, as is the case for other approaches. Finally, as in CPT, results can be obtained at any wavevector.

We shall see below that there is a close correspondence of the QP bands in the spectra to the polaron and bipolaron dispersion relations denoted here as  $E^\uparrow(k)$  and  $E^{\uparrow\downarrow}(k)$ , respectively.<sup>2</sup> Results for  $E^{\uparrow\downarrow}(k)$  have been reported by Wellein *et al.* [85] and Weiße *et al.* [95, 161]. However, in contrast to  $A_\sigma(k, \epsilon)$ ,  $E^\uparrow(k)$  and  $E^{\uparrow\downarrow}(k)$  do not reveal the spectral weight of the corresponding QP's. Nevertheless, the comparison with the spectra will yield valuable insight and serve as a test of the CPT results. Moreover, a direct calculation of energy bands does not suffer from the restricted energy resolution of CPT due to the use of a smearing parameter (Sec. 2.2).

Owing to the limitations regarding the number of phonon states, we shall only show results for  $\bar{\omega} \geq 1$ . To be more specific, we consider two values of the adiabatic ratio, namely  $\bar{\omega} = 4$  and  $\bar{\omega} = 1$ . For  $\bar{\omega} = 4$ , the spectra will turn out to be relatively simple, and we are able to study even strong electron-phonon coupling. Consequently, we start with a discussion of the nonadiabatic regime, and then move on to the more difficult case  $\bar{\omega} = 1$ .

### Nonadiabatic regime

In this section, we restrict the discussion to  $\bar{U} = 0$ , while the influence of Coulomb repulsion will be studied below. Figure 4.1 shows the evolution of the one-particle spectrum with increasing electron-phonon coupling. Here and in subsequent figures, solid lines represent results for  $A_\uparrow$  and dashed lines correspond to  $A_\downarrow$  [see Eq. (4.4)].

For  $\bar{U} = 0$ , two electrons of opposite spin always form a bipolaron state for any  $\lambda > 0$ . At weak coupling  $\lambda = 0.5$  [Fig. 4.1(a)],  $A_\uparrow$  exhibits two well-visible bands, as well as an incoherent part centered at  $\epsilon \approx 0$ . To understand the nature of the coherent excitations, we have also included in Fig. 4.1 the bipolaron band dispersion  $E^{\uparrow\downarrow}(k)$  (solid vertical line), calculated by the VDM [163]. The latter fits well the low-energy band, with the minor deviations at intermediate  $k$ —i.e., the splitting of the low-energy peak into several small

<sup>2</sup>As noted in Chap. 3, the spin is irrelevant for the case of a single electron, i.e., we have  $E^\uparrow(k) = E^\downarrow(k)$ .

## 4.2. One-particle spectral function

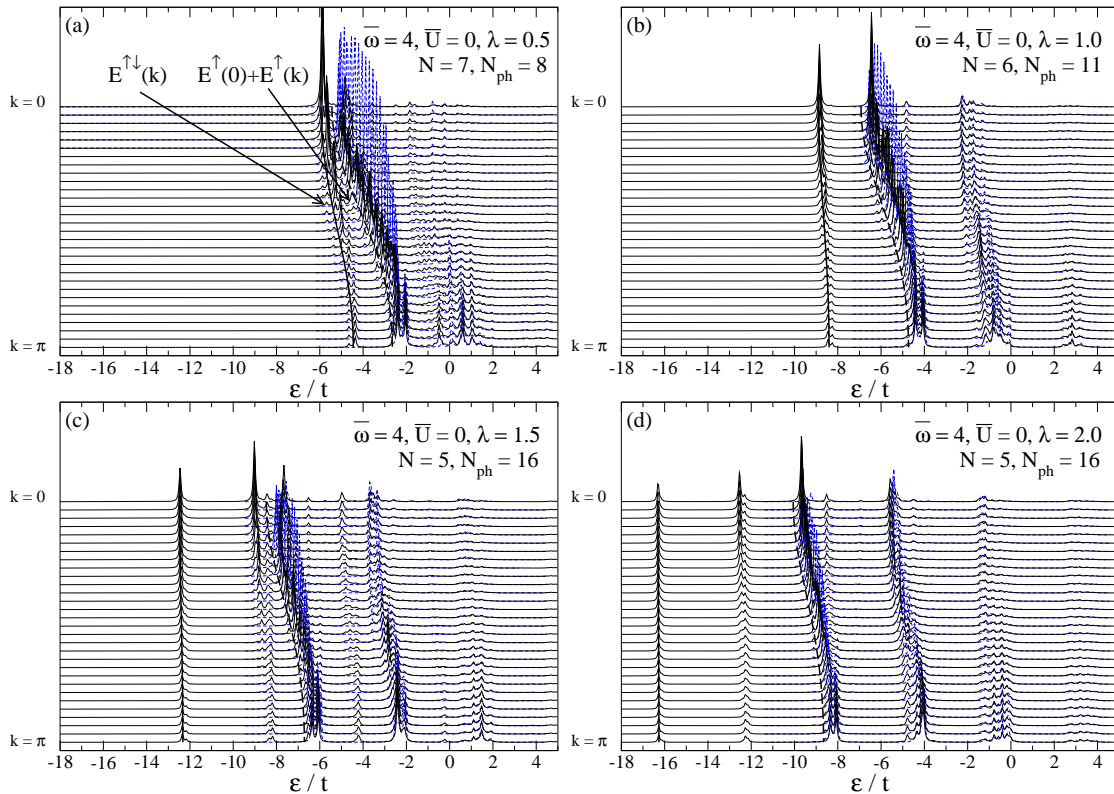


Figure 4.1: One-particle spectral functions  $A_{\uparrow}(k, \epsilon)$  (solid lines) and  $A_{\downarrow}(k, \epsilon)$  (dashed lines) calculated with CPT for different values of the electron-phonon coupling  $\lambda$ , using  $\eta = 0.05t$  [see Eq. (2.36)]. All other parameters as indicated in the figures. The truncation errors are  $\Delta <$  (a)  $5.3 \times 10^{-6}$ , (b)  $1.0 \times 10^{-5}$ , (c)  $2.4 \times 10^{-7}$ , (d)  $6.7 \times 10^{-6}$  (see text). The vertical lines correspond to VDM results for the polaron and bipolaron band dispersions  $E^{\uparrow}(0) + E^{\uparrow}(k)$  (dashed) and  $E^{\uparrow\downarrow}(k)$  (solid), respectively [163].

satellites—being finite-size effects, as has been verified by calculations on smaller and larger clusters for a smaller number of phonon states (not shown). A more detailed discussion of finite-size effects will be given below for  $\bar{\omega} = 1$ . Even at weak coupling  $\lambda = 0.5$ , the bipolaron band already has a relatively small width of  $W'/W \approx 0.37$  compared to the free-electron value  $W$ . Moreover, the spectral weight of the lowest peak, obtained by integration over the CPT spectrum, decreases significantly from about 0.68 at  $k = 0$  to about 0.08 at  $k = \pi$ . At the same time, the weight contained in the incoherent part of the spectrum increases with increasing  $k$ . This behavior is very similar to the single-electron case (Sec. 3.2.4).

We now turn our attention to the second band appearing in Fig. 4.1(a). From the general discussion in Sec. 4.1, we expect that it corresponds to an excited state with two polarons. We therefore compare it to the energy of two independent polarons in an infinite system. Since  $A_{\uparrow}$  [Eq. (4.4)] describes the process of adding an electron with



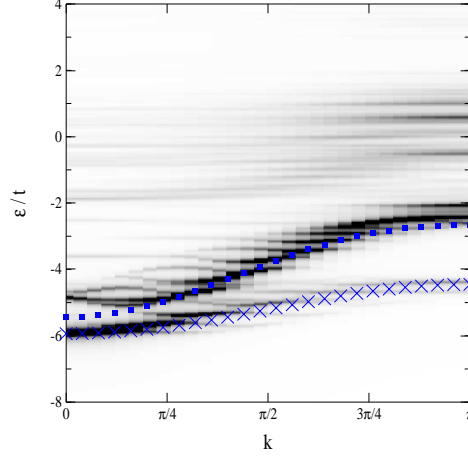


Figure 4.2: Density plot of the one-particle spectral function  $A_{\uparrow}(k, \epsilon)$  for  $\bar{\omega} = 4.0$ ,  $\bar{U} = 0$ , and  $\lambda = 0.5$ , as shown in Fig. 4.1(a). The symbols correspond to VDM results for  $E^{\uparrow}(0) + E^{\uparrow}(k)$  (squares) and  $E^{\uparrow\downarrow}(k)$  (crosses), respectively [163].

momentum  $k$  to the one-polaron ground state with energy  $E^{\uparrow}(0)$ , we show in Fig. 4.1(a) the band dispersion  $E^{\uparrow}(0) + E^{\uparrow}(k)$  (dashed vertical line). The comparison with the spectral function yields a very good agreement at intermediate and large  $k$ , while there are some discrepancies at small momenta. A density plot of  $A_{\uparrow}$  (Fig. 4.2) reveals more clearly that the two coherent bands hybridize and repel each other near the point where they would be degenerate, giving rise to an upper band with inversed dispersion at small  $k$ . The situation is similar to the hybridization of the coherent and incoherent parts in the one-electron case, which occurs for  $|E^{\uparrow}(k) - E^{\uparrow}(0)| \sim \bar{\omega}$  (see Sec. 3.2.4). Of course, such effects are absent in the band dispersion of a system with two independent polarons.

The spectral function  $A_{\downarrow}$ , also shown in Fig. 4.1(a), contains a coherent band at low energies, and an incoherent part which is very similar to that of  $A_{\uparrow}$ . Well away from  $k = 0$ , the band in  $A_{\downarrow}$  follows closely the polaron band in  $A_{\uparrow}$ . Thus the excited two-polaron state of the system with two electrons of opposite spin is very similar to the ground state of the system with two electrons of the same spin. Near  $k = 0$ , the spectral weight of the low-energy peak in  $A_{\downarrow}$  is small ( $\approx 0.08$ ) compared to the polaron peak in  $A_{\uparrow}$  ( $\approx 0.2$ ). This is a result of the abovementioned fact that two polarons with the same spin cannot occupy the same  $k = 0$  state, so that the corresponding excitation in the one-particle spectrum has little weight. The picture changes at larger momenta, where both bands have similar weight, although the sharp peaks in  $A_{\downarrow}$  are higher than the broadened features in  $A_{\uparrow}$ .

With increasing electron-phonon coupling, the low-energy bipolaron band becomes even narrower until it is virtually flat at  $\lambda = 1.5$  [Fig. 4.1(c)]. Here, the two conditions for a small bipolaron (Sec. 4.1) are identical to  $\lambda > 0.5$ . Consequently, finite-size effects are very small in Figs. 4.1(b)–(d), as confirmed by the excellent agreement of the bipolaron band

with the results for  $E^{\uparrow\downarrow}(k)$ . The reduction in bandwidth with increasing  $\lambda$  is accompanied by a loss of spectral weight. For  $k = 0$ , the latter decreases from the value 0.68 at  $\lambda = 0.5$  given above to about 0.10 at  $\lambda = 2.0$ . Both the narrowing and the loss of weight indicate a significant increase of the effective bipolaron mass.

While the polaron band lies relatively close to the bipolaron band at  $\lambda = 0.5$  [Fig. 4.1(a)], the increase of the coupling leads to a clear separation, and to a downward shift proportional to the polaron binding energy  $E_P$ . In the nonadiabatic strong-coupling regime of Fig. 4.1(d), the energy gap between the two bands is well described by atomic-limit value  $2E_P = 8t$ . Similar to  $\lambda = 0.5$ , the two-polaron band dispersion  $E^\uparrow(0) + E^\uparrow(k)$  agrees well with the polaron band in the spectra, with some differences being visible near  $k = 0$ . Interestingly, in Fig. 4.1(c), there is a mixing of the bipolaron state with one phonon excited, which lies an energy  $\omega = 4t$  above the lowest band, and the two-polaron excitation. As expected from the one-electron calculations (Sec. 3.2.4), the polaron band also narrows with increasing electron-phonon coupling. However, the effect is much smaller than for the bipolaron band. Additionally, the spectral weight of the  $k = 0$  polaron peak in  $A_\uparrow$  increases from about 0.20 at  $\lambda = 0.5$  to about 0.32 at  $\lambda = 2.0$ . This may be explained by the fact that for weak coupling [Fig. 4.1(a)], some of the weight of the polaron state is contained in the large low-energy feature. Calculations for a single electron and the same parameters show that the spectral weight of the polaron at  $k = 0$  decreases from about 0.86 ( $\lambda = 0.5$ ) to about 0.52 ( $\lambda = 2.0$ ). Since the spectral weight of the Holstein polaron is, to a very good approximation, equal to the inverse of the ratio  $m_{\text{eff}}/m$  [101], these results indicate that the polaron mass does not increase at the same rate as the bipolaron mass with increasing coupling, as reflected by the corresponding changes in bandwidth in Fig. 4.1. Finally, we also find a comparable reduction of spectral weight for the two-polaron band in  $A_\downarrow$  from about 0.08 to about 0.04 at  $k = 0$ .

To conclude the discussion of the case  $\bar{\omega} = 4$ , we would like to underline the enormous advantage of CPT in the strong-coupling regime. It allows us to perform calculations on a very small cluster ( $N = 4$ )—sufficient to obtain well-converged results—but still yields the spectral function at any desired  $k$ .

### Intermediate phonon frequency

In the preceding section, we have investigated in detail the signatures of polaron and bipolaron states in the one-particle spectrum for  $\bar{\omega} = 4$ . Owing to the large energy of phonon excitations, most of the spectral weight resides in the corresponding bands, allowing a fairly easy identification. We now consider the case  $\bar{\omega} = 1$ , which turns out to be more difficult to study numerically and to interpret. Nevertheless, work in the regime  $\bar{\omega} \leq 1$  is highly desirable to understand many interesting strongly correlated systems such as, e.g., the manganites. Although the latter are usually characterized by  $\omega \ll t$ , quantum effects are already visible for  $\omega = t$ . As a consequence, previous authors [84, 94, 136, 158–160] have often focused on this case, which is numerically much easier to tackle than the region  $\bar{\omega} \ll 1$ . Calculations for  $\bar{\omega} \ll 1$  have been presented, e.g., by Wellein *et al.* [85] and Weiße *et al.* [95, 161]. While the discussion of  $\bar{\omega} = 4$  was restricted to  $\bar{U} = 0$ , here we shall also

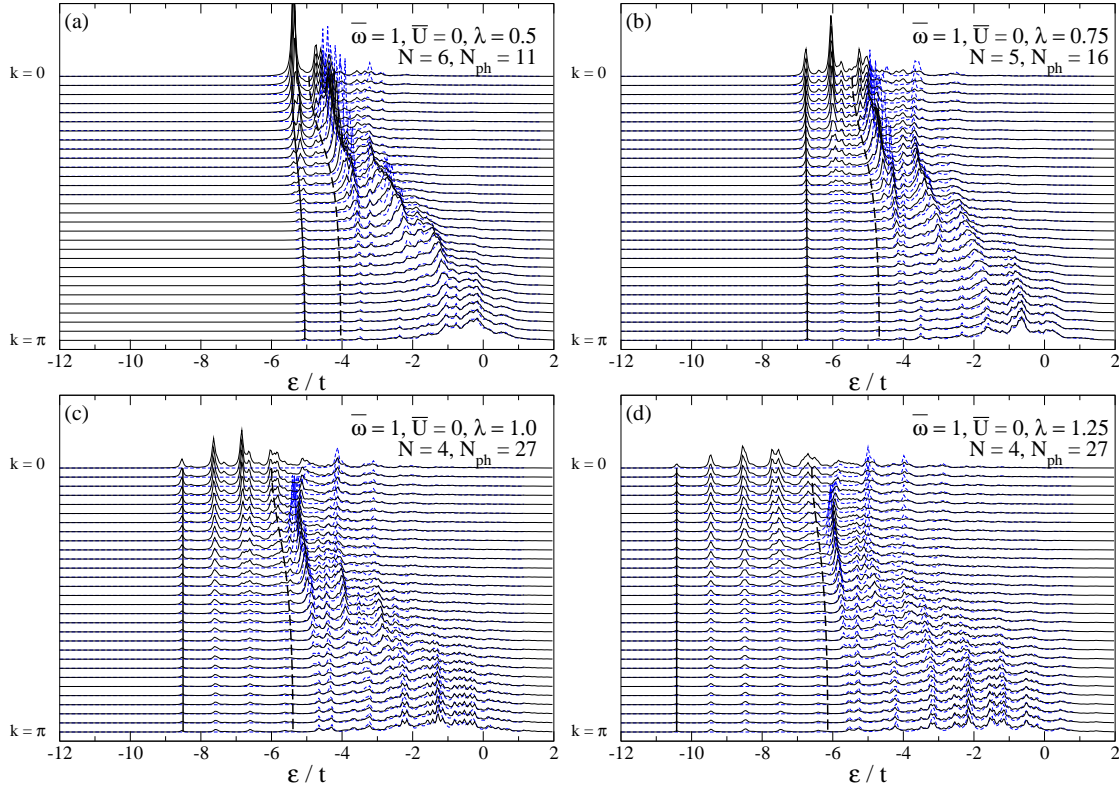


Figure 4.3: One-particle spectral functions  $A_{\uparrow}(k, \epsilon)$  (solid lines) and  $A_{\downarrow}(k, \epsilon)$  (dashed lines) calculated with CPT for different values of the electron-phonon coupling  $\lambda$ , using  $\eta = 0.05t$ . All other parameters as indicated in the figures. The truncation errors are  $\Delta < (a) 9.1 \times 10^{-5}$ , (b)  $9.0 \times 10^{-5}$ , (c)  $1.2 \times 10^{-7}$ , (d)  $2.4 \times 10^{-6}$ . The vertical lines correspond to variational diagonalization results for the polaron and bipolaron band dispersions  $E^{\uparrow}(0) + E^{\uparrow}(k)$  (dashed) and  $E^{\uparrow\downarrow}(k)$  (solid), respectively [163].

take into account a finite Coulomb repulsion.

$\bar{U} = 0$  Since converged results for  $\bar{\omega} = 1$  require more phonon states than for  $\bar{\omega} = 4$ , we have slightly reduced the cluster sizes in our calculations. Consequently, finite-size effects are larger, as discussed below. Moreover, we are not able to reach the strong-coupling regime but instead restrict the range of  $\lambda$  to 0.5–1.25.

Figure 4.3 contains the one-particle spectra for  $\bar{U} = 0$ . In principle, for  $\lambda = 0.5$ , the results look quite similar to Fig. 4.3(a). However, the spectral weight of the two coherent bands is much smaller, as a consequence of the increased importance of incoherent excitations for  $\bar{\omega} = 1$ . In particular, the spectral weight of the latter is strongly enhanced at large  $k$ , so that the bands are no longer easy to identify. Therefore, and because of the strong mixing of the bands with coherent and incoherent excitations, it becomes difficult to accurately determine the spectral weight by integration over the CPT spectra.

Furthermore, we see from Fig. 4.3 that the bipolaron bandwidth is much smaller for  $\bar{\omega} = 1$  ( $W'/W \approx 0.1$ ) than for  $\bar{\omega} = 4$ , despite the fact that the value of  $\lambda$  is the same in both cases. Hence, the effect of electron-phonon interaction on the bipolaron mass is much more pronounced in or near the adiabatic regime due to the larger mass of the oscillators. In principle, the spectrum also contains coherent excited states which are separated from the lowest-energy band by less than the phonon energy  $\omega$ . However, owing to the rather complex structure of the spectrum in the two-electron case, they are difficult to identify. A direct calculation of excited states in the Holstein model with one electron has recently been presented by Barišić [104]. Finally, the relation between  $A_{\downarrow}$  and  $A_{\uparrow}$  is very similar to  $\bar{\omega} = 4$ .

As we increase the electron-phonon coupling, the bipolaron dispersion collapses to an extremely narrow band [Fig. 4.3(b)]. This cross over is again associated with a significant loss of spectral weight. At  $k = 0$ , for example, we find a reduction from about 0.50 at  $\lambda = 0.5$  to about 0.14 at  $\lambda = 0.75$ . Increasing  $\lambda$  further to 1.25, we finally arrive at a bipolaron band with  $W'/W \approx 10^{-4}$  and a spectral weight of less than 0.03 at  $k = 0$ . Similar to Fig. 4.1(d), the spectrum displays several bands equally spaced by  $\omega$  which belong to excited states with one or more phonons. Moreover, the polaron and bipolaron bands are well separated, and the incoherent contributions dominate at large  $k$ .

The agreement between the bipolaron band dispersion and  $E^{\uparrow\downarrow}(k)$  in Fig. 4.3 is again very good. Similar to  $\bar{\omega} = 4$ , the condition for a small bipolaron is given by  $\lambda > 0.5$ , so that CPT yields very accurate results. In contrast, the two-polaron energy  $E^{\uparrow}(0) + E^{\uparrow}(k)$  fits less well to the corresponding bands in the spectral function. We attribute this difference to the nonadiabatic regime [Fig. 4.1] to the stronger retardation effects for  $\bar{\omega} = 1$ . As a consequence, the polaron state is more extended below the small-polaron cross over occurring at  $\lambda = 1$  (Sec. 3.1), leading to a stronger overlap of the two particles. In contrast, for  $\bar{\omega} = 4$ , the lattice distortions around the electrons are very localized, and the two polarons therefore do not experience a significant interaction. Above  $\lambda = 1$ , i.e., in the small-polaron regime, the two-polaron dispersion for  $\bar{\omega} = 1$  again follows closely a two-polaron-like band in the spectrum [Figs. 4.3(c) and (d)].

**$\bar{U} = 4$**  So far, we have only presented results for  $\bar{U} = 0$ , for which a bipolaron state is always favored. However, in materials such as the cuprates or the manganites, strong local correlations hinder the carriers from forming onsite bipolarons even for strong electron-phonon coupling. To model such effects, we therefore consider here a finite value of the electron-electron repulsion  $\bar{U} = 4$ .

In the case of two electrons with opposite spin, the Lanczos results for the cluster Green function converge faster as a function of  $N_{\text{ph}}$  for  $\bar{U} > 0$  compared to  $\bar{U} = 0$  as a result of the reduced effective electron-electron interaction. This is fortunate, since it allows us to use slightly larger clusters, thereby partly compensating for the increased finite-size effects due to the spatially more extended ground-state wavefunction in the weak-coupling regime.

From the general discussion in Sec. 4.1, we expect the ground state to consist of two weakly bound polarons for  $2E_{\text{P}} \ll U$ , and a cross over to a bipolaron state at a critical

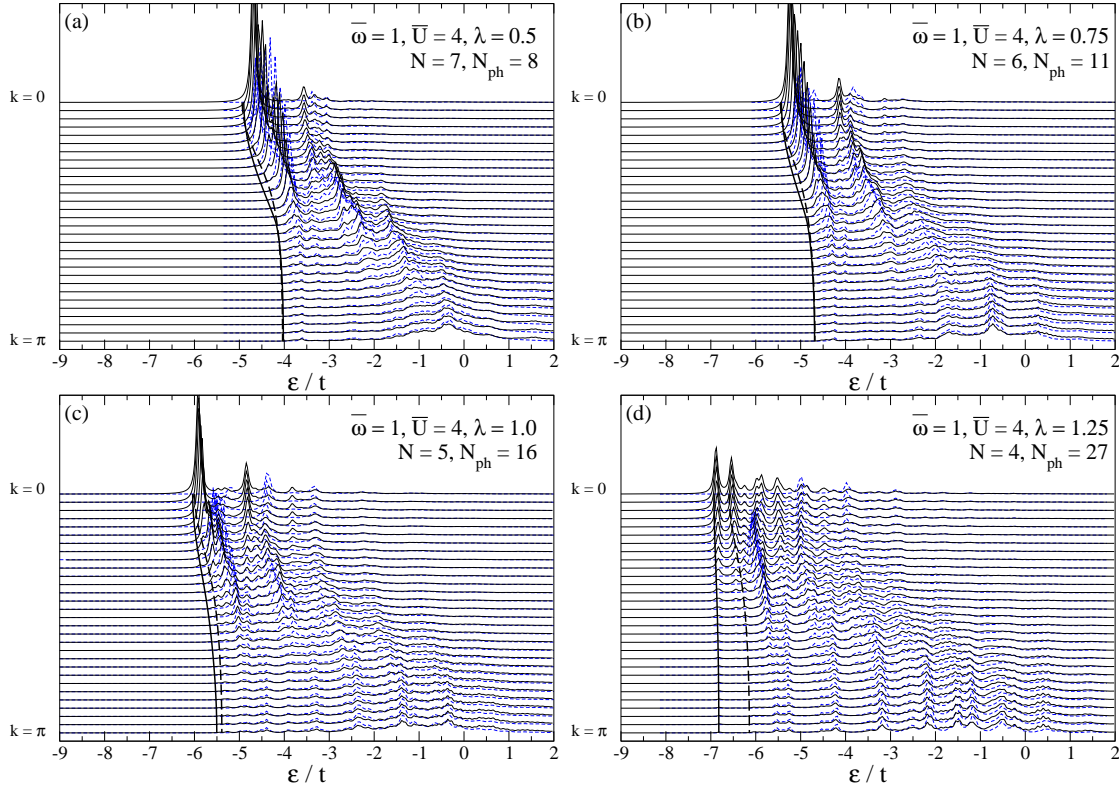


Figure 4.4: One-particle spectral functions  $A_{\uparrow}(k, \epsilon)$  (solid lines) and  $A_{\downarrow}(k, \epsilon)$  (dashed lines) calculated with CPT for different values of the electron-phonon coupling  $\lambda$ , using  $\eta = 0.05t$ . All other parameters as indicated in the figures. The truncation errors are  $\Delta < (a) 3.3 \times 10^{-5}$ , (b)  $2.0 \times 10^{-5}$ , (c)  $9.9 \times 10^{-6}$ , (d)  $6.7 \times 10^{-7}$ . The vertical lines correspond to variational diagonalization results for the polaron and bipolaron band dispersions  $E^{\uparrow}(0) + E^{\uparrow}(k)$  (dashed) and  $E^{\uparrow\downarrow}(k)$  (solid), respectively [163].

value of the electron-phonon interaction  $\lambda$ . In the nonadiabatic limit, the latter is given by  $2E_P = U$  (i.e.,  $\lambda = 1$  for the case considered here) for weak coupling, and by  $4E_P = U$  for strong coupling.

In Fig. 4.4, we present the results for the spectral function, again for  $\lambda = 0.5 - 1.25$ . For weak coupling  $\lambda = 0.5$  [Fig. 4.4(a)], the most striking difference to the  $\bar{U} = 0$  case discussed above is the fact that there is only one band at low energies. Together with the incoherent contributions, and taking into account the doubling of the number of carriers leading to a shift of energies, the spectrum bears a close resemblance to that of a single polaron with the same parameters (Fig. 3.3). This is also underlined by the polaron and bipolaron band dispersions shown in Fig. 4.4(a), which are almost identical throughout the Brillouin zone, and lie just below the corresponding band in the spectral function. In particular, the band displays the typical flattening at large  $k$ , which indicates the phononic character of the low-energy excitation. Furthermore, owing to the finite onsite repulsion, the low-energy band

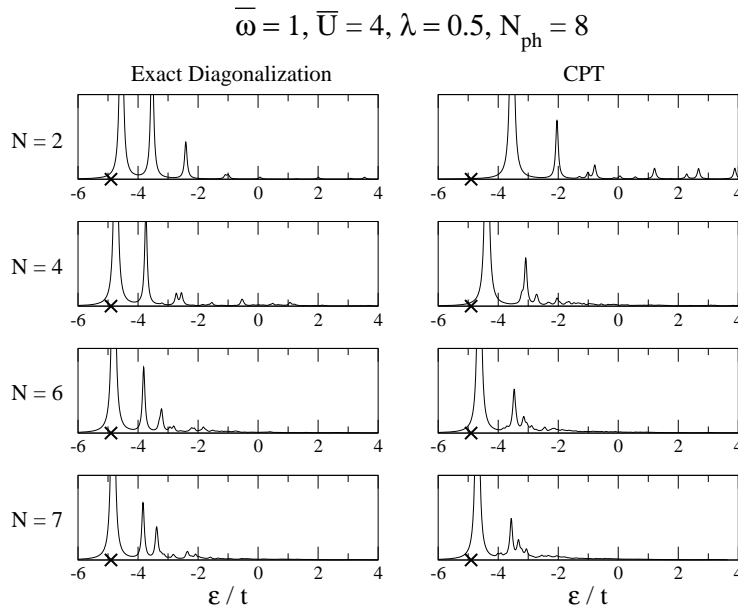


Figure 4.5: Comparison of the one-particle spectral function  $A_{\uparrow}(0, \epsilon)$  calculated with ED and CPT, respectively, for different cluster sizes  $N$ , using  $\eta = 0.05t$ . The crosses correspond to the VDM result for the bipolaron energy  $E^{\uparrow\downarrow}(0)$  [163].

in  $A_{\downarrow}$  is very similar to that in  $A_{\uparrow}$  since, for finite  $\bar{U}$  and weak electron-phonon coupling, the singlet ground state consists of two weakly bound polarons. Consequently, the singlet and triplet state have comparable energies, although the spectral weight in  $A_{\downarrow}$  is again very small near  $k = 0$ .

For  $\lambda = 0.75$  [Fig. 4.4(b)], the ground state of the system is still given by two polarons, and the spectrum is almost indistinguishable from  $\lambda = 0.5$ . In the present case, the condition for the existence of an intersite bipolaron is expected to lie between the weak- and strong coupling results  $U < 2E_P$  and  $U < 4E_P$  [158]. However, owing to the small binding energy, the intersite state is difficult to distinguish from the two-polaron state in the spectral function. At  $\lambda = 1.0$  [Fig. 4.4(c)], the band in the spectral function begins to split. Although the energy difference between the polaron and bipolaron dispersions is still relatively small near  $k = 0$ , an excitation gap clearly emerges at larger  $k$ . Finally, at  $\lambda = 1.25$ , two distinct bands with similar spectral weight have formed which agree very well with  $E^{\uparrow\downarrow}(k)$  and  $E^{\uparrow}(0) + E^{\uparrow}(k)$ , respectively. Interestingly, the band in the triplet spectral function  $A_{\downarrow}$  lies noticeably higher than the polaron band in  $A_{\uparrow}$ . Thus, for the parameters considered here, two polarons of opposite spin can lower their total energy by occupying the same lattice site, which is just the mechanism behind bipolaron formation.

The abovementioned discrepancies between the bipolaron band dispersion  $E^{\uparrow\downarrow}(k)$  obtained by Shawish [163] and the band in  $A_{\uparrow}$  are a result of finite-size effects in the CPT calculations. The latter reduce with increasing coupling  $\lambda$  together with the size of the bipolaron, and for  $\lambda = 1.25$  we find a very good agreement [Fig. 4.4(d)]. To illustrate this point, we compare in Fig. 4.5 the spectral function  $A_{\uparrow}$  at  $k = 0$ ,  $\lambda = 0.5$ , and for different

cluster sizes  $N$ , calculated using ED with periodic boundary conditions (left column) and CPT (right column), respectively. The results reveal that for weak coupling and intermediate  $\bar{U}$ , ED is superior to CPT concerning the convergence of the peak positions with respect to system size. This is not surprising as CPT is based on a strong-coupling expansion in the hopping term (see Sec. 2.2). Here, the electron-electron and electron-phonon interaction are both of about the same magnitude as the hopping, so that the method does not work as well as for  $\bar{U} = 0$ . For  $\bar{U} > 0$ , finite-size effects in both, CPT and ED, are larger due to the extended bipolaron state which exists for weak coupling. Similar to the one-electron case discussed in Chap. 3, deviations from the exact results due to the finite cluster size are usually smallest for  $k = 0$ , while they become larger with increasing  $k$ . Although here the positions of the peaks in the CPT spectral function are less accurate than in the case of ED, the weights of the excited states resemble more closely the results in the thermodynamic limit.

Finally, for  $\bar{U} > 4$ , the cross over to a small bipolaron occurs at even larger values of  $\lambda$ . Apart from the change of the critical coupling, the physics is not altered significantly. Therefore, we have restricted our discussion of the spectral function to  $\bar{U} \leq 4$ , but some results for the bipolaron band dispersion at  $\bar{U} = 8$  will be presented below.

**Bipolaron band dispersion** The bipolaron band dispersion  $E^{\uparrow\downarrow}(k)$  has been calculated before by Wellein *et al.* [85] and Weiße *et al.* [95, 161] for small phonon frequencies  $\bar{\omega} = 0.4$  and  $\bar{\omega} = 0.5$ , respectively. Remarkably, for parameters  $\bar{U} > 0$  and  $\lambda > 0$  such that the effective interaction  $U_{\text{eff}} = U - 2E_{\text{P}} = 0$ , they found a renormalized, free-particle dispersion relation [95, 161]. In this section, we wish to extend these considerations to the case  $\bar{\omega} = 1$ , and to infinite systems. While the narrowing effect due to electron-phonon interaction has been discussed above, here we focus on the form of the band.

Owing to the limited energy resolution and finite-size effects in the CPT results shown above, we use the more accurate data from the VDM. In Fig. 4.6, we show Shawish's [163] results for the bipolaron energy as a function of  $k$ , for different values of  $\bar{U}$  and  $\lambda$ . To permit a direct comparison, we have scaled all curves to the interval  $[-1, 0]$ , with the actual bandwidths given in the legend.

We begin with the regime of a strongly bound small bipolaron. To this end we consider the case  $\bar{U} = 0$  and  $\lambda = 1.25$ . The corresponding band resembles quite closely a cosine dispersion, with some deviations being visible around  $k = \pi/2$ . A different behavior is found for finite  $\bar{U} = 4$ , as well as weak coupling  $\lambda = 0.5$ . For these parameters, which favor a ground state with two polarons [see Fig. 4.4(c)], the form of the band is remarkably different from a simple tight-binding dispersion for nearest-neighbor hopping. This is still true for  $\lambda = 1$ , although a trend towards a cosine dispersion is visible. For even larger  $\bar{U} = 8$ , the noncosine-like form persists even for  $\lambda = 1$ . It is worth mentioning the great similarity of the results for  $\bar{U} = 4$  and  $\bar{U} = 8$  in the weak-coupling regime, which follows from the fact that once the small (onsite) bipolaron state is energetically unfavorable for the two electrons due to the Coulomb repulsion, a further increase of the latter has very little effect.

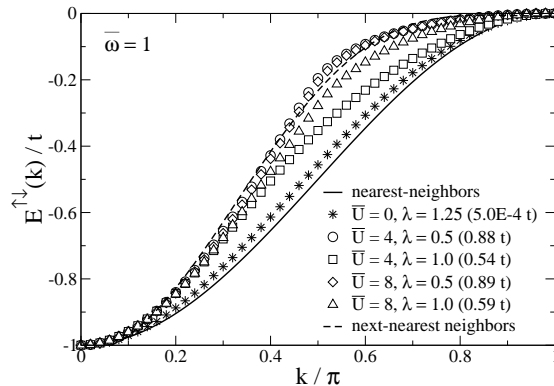


Figure 4.6: Bipolaron band dispersion  $E^{\uparrow\downarrow}(k)$  as a function of the wavevector  $k$  [163]. Also shown is the bare tight-binding dispersion relation for nearest-neighbor hopping, and a fit to the results for  $\bar{U} = 4$ ,  $\lambda = 0.5$  using a dispersion for nearest- and next-nearest neighbor hopping (see text). All curves have been scaled to the interval  $[-1, 0]$ , with the actual bandwidths given in the legend.

To identify the origin of the deviations from a free-electron band, we also included in Fig. 4.6 a fit of a free-electron model with nearest and next-nearest neighbor hopping to the band for  $\bar{U} = 4$  and  $\lambda = 0.5$ , which yields an amplitude  $t' \approx 0.6t$  for two-site hopping processes. As proposed by Wellein *et al.* [85], the importance of long-range hopping for the band dispersion of a single polaron may be due to a residual polaron-phonon interaction, with the phonons and the polaron residing on different sites. Since we find substantial deviations of the bipolaron band from a cosine dispersion only in the regime of two weakly bound polarons, it stands to reason to assume the same underlying mechanism.

Finally, we would like to comment on the fact that despite  $U_{\text{eff}} = 0$  for  $\bar{U} = 4$  and  $\lambda = 1$  in Fig. 4.6, we do not have a simple cosine band, in contrast to the findings of Wellein *et al.* [85] and Weiße *et al.* [161], which have been attributed to the formation of an intersite bipolaron [161]. In contrast, here we observe noncosine-like behavior even in the regime where an intersite state exists. These differences are expected to be a result of the larger value of the phonon frequency (here  $\bar{\omega} = 1$ , while  $\bar{\omega} = 0.4$  and  $0.5$  in [85] and [161], respectively), which leads to a noticeable reduction of retardation effects. Moreover, since the critical coupling  $\lambda_c$  decreases as  $\bar{\omega} \rightarrow 0$ , the bipolaron is more strongly bound in the work of [85, 161], thereby suppressing the abovementioned nonlocal phonon-polaron interaction. Further work along these lines is highly desirable, to investigate the dependence of the bipolaron band dispersion on the phonon frequency in the regime  $\bar{\omega} \leq 1$ .

### 4.3 Transformed Hamiltonians

The basis of both the variational approach and the QMC method presented below is a unitary transformation of the Hamiltonian (1.21). Compared to the one-electron calculations in Chap. 3, the situation is slightly more complicated owing to (a) the presence of two elec-



trons instead of one, and (b) the additional Hubbard term  $I_{ee}$ . After the transformation  $\tilde{H} \equiv \nu H \nu^\dagger$ , with  $\nu$  given by Eq. (3.3), Hamiltonian (1.21) becomes

$$\tilde{H} = \underbrace{-t \sum_{\langle ij \rangle \sigma} c_{i\sigma}^\dagger c_{j\sigma} e^{i \sum_l (\gamma_{li} - \gamma_{lj}) \hat{p}_l}}_{\tilde{K}} + P + \underbrace{\sum_{ij} \hat{n}_j \hat{x}_i (\omega \gamma_{ij} - \alpha \delta_{ij})}_{\tilde{I}_{ep}} + \underbrace{\sum_{ij} v_{ij} \hat{n}_i \hat{n}_j - \frac{U}{2} \sum_i \hat{n}_i}_{\tilde{I}_{ee}}, \quad (4.6)$$

with

$$v_{ij} = \frac{\omega}{2} \sum_l \gamma_{lj} \gamma_{li} - \alpha \gamma_{ij} + \frac{1}{2} \delta_{ij} U \quad (4.7)$$

and  $P$  as defined in Eq. (3.2). The extended transformation  $\nu$  takes into account nonlocal lattice displacements, which are essential for an accurate description in the regime  $\bar{\omega} \lesssim 1$ .

For the QMC method, we resort to the standard LF transformation (3.11), which yields

$$\tilde{H}_0 = \underbrace{-t \sum_{\langle ij \rangle \sigma} c_{i\sigma}^\dagger c_{j\sigma} e^{i \gamma (\hat{p}_i - \hat{p}_j)}}_{\tilde{K}_0} + \underbrace{(U - 2E_P) \sum_i \hat{n}_{i\uparrow} \hat{n}_{i\downarrow}}_{\tilde{I}} - 2E_P. \quad (4.8)$$

Hence, in contrast to the polaron problem [Eq. (3.32)], the electron-electron interaction term, which results from the canonical transformation, does not vanish but instead combines with the Hubbard term.

## 4.4 Quantum Monte Carlo

The derivation of the QMC algorithm for the bipolaron problem is very similar to the one-electron case considered in Chap. 3, and we shall therefore focus on the differences occurring. Moreover, we restrict the discussion to one dimension.

### 4.4.1 Partition function

We set out to calculate the partition function  $\mathcal{Z} = e^{-\beta \tilde{H}_0}$ , with  $\tilde{H}_0$  given by Eq. (4.8). To this end, we first notice that the last term in Hamiltonian (4.8) is a constant and can therefore be neglected during the QMC simulation. Using the standard Suzuki-Trotter decomposition (Sec. 2.1.4) we obtain

$$e^{-\beta \tilde{H}_0} \approx \left( e^{-\Delta\tau \tilde{K}_0} e^{-\Delta\tau P_p} e^{-\Delta\tau P_x} e^{-\Delta\tau \tilde{I}} \right)^L \equiv \mathcal{U}^L, \quad (4.9)$$

with  $\Delta\tau$  given by Eq. (2.15). Following the same steps as in Sec. 3.5.2, we find

$$\mathcal{Z}_L = \text{Tr}_f \int dp_1 dp_2 \cdots dp_L \langle p_1 | \mathcal{U} | p_2 \rangle \cdots \langle p_L | \mathcal{U} | p_1 \rangle, \quad (4.10)$$

with  $dp_\tau \equiv \prod_i dp_{i,\tau}$ , and  $\lim_{L \rightarrow \infty} \mathcal{Z}_L = \mathcal{Z}$  [10]. Since the phonon contribution to  $\mathcal{U}$  is the same as for one electron, we can again integrate out the coordinates  $x$ . Upon defining  $\mathcal{D}p = dp_1 dp_2 \cdots dp_L$  the partition function becomes

$$\mathcal{Z}_L = C \int \mathcal{D}p w_b w_f, \quad (4.11)$$

where  $C = [2\pi/(\omega\Delta\tau)]^{NL}$  and

$$w_b = e^{-\Delta\tau S_b}, \quad w_f = \text{Tr}_f \Omega, \quad \Omega = \prod_{\tau=1}^L e^{-\Delta\tau \tilde{K}_{0,\tau}} e^{-\Delta\tau \tilde{I}}. \quad (4.12)$$

Here the bosonic action  $S_b$  and the hopping operator  $\tilde{K}_0$  are identical to Sec. 3.5.2. To evaluate the fermionic trace we choose the two-electron basis states

$$\left\{ |l\rangle \equiv |i, j\rangle \equiv c_{i\uparrow}^\dagger c_{j\downarrow}^\dagger |0\rangle, \quad i, j = 1, \dots, N \right\}, \quad (4.13)$$

where we have introduced a combined index  $l$  running from 1 to  $N^2$  in one dimension. We begin with the contribution of the kinetic term  $\tilde{K}_0$  [Eq. (4.8)]. It follows that the tight-binding hopping matrix, denoted as  $\kappa$ , has dimension  $N^2 \times N^2$ . The exponential of the transformed hopping term can be written as

$$e^{-\Delta\tau \tilde{K}_{0,\tau}} = D_\tau \kappa D_\tau^\dagger, \quad (4.14)$$

where

$$(D_\tau)_{ll'} = \delta_{ll'} e^{i\gamma(p_{i,\tau} + p_{j,\tau})} \quad (4.15)$$

is diagonal in the basis (4.13).

The second contribution to the matrix  $\Omega$  comes from the effective electron-electron interaction term  $\tilde{I}$  [Eq. (4.8)] in terms of the diagonal matrix

$$(\mathcal{V}_\tau)_{ll'} = \delta_{ll'} e^{\Delta\tau(U-2E_F)\delta_{ij}}. \quad (4.16)$$

The random variables  $\mathbf{p}$  merely enter the diagonal matrix  $D$ , while the  $N^2 \times N^2$  matrices  $\mathcal{V}_\tau$  and  $\kappa$  are fixed throughout the entire MC simulation. Thus, in total, we have

$$\Omega = \prod_{\tau} D_\tau \kappa D_\tau^\dagger \mathcal{V}_\tau, \quad (4.17)$$

and the fermionic trace can be calculated as

$$\text{Tr}_f \Omega = \sum_{ij} \langle i, j | \Omega | i, j \rangle, \quad (4.18)$$

which is identical to the sum over the diagonal elements of the matrix  $\Omega$  in the basis (4.13).

Similar to the one-electron case, we use the principal component representation and the reweighting procedure. A detailed discussion of these ideas and their applicability has been given in Chap. 3.

### 4.4.2 Observables

The first observable of interest is the kinetic energy of the electrons defined as

$$E_k = -t \sum_{\langle ij \rangle \sigma} \langle \tilde{c}_{i\sigma}^\dagger \tilde{c}_{j\sigma} \rangle = -2t \sum_{\langle ij \rangle} \langle c_{i\uparrow}^\dagger c_{j\uparrow} e^{i\gamma(\hat{p}_i - \hat{p}_j)} \rangle, \quad (4.19)$$

where we have exploited spin symmetry. Following the same steps as in the derivation of the partition function we get

$$\langle \tilde{c}_{i\uparrow}^\dagger \tilde{c}_{j\uparrow} \rangle = \mathcal{Z}_L^{-1} \int \mathcal{D}p w_b e^{i\gamma(p_{i,1} - p_{j,1})} \text{Tr}_f(\Omega c_{i\uparrow}^\dagger c_{j\uparrow}). \quad (4.20)$$

Writing out explicitly the fermionic trace we obtain

$$\begin{aligned} \text{Tr}_f(\Omega c_{i\uparrow}^\dagger c_{j\uparrow}) &= \sum_{i'j'} \langle i', j' | \Omega c_{i\uparrow}^\dagger c_{j\uparrow} | i', j' \rangle \\ &= \sum_{j'} \langle j, j' | \Omega | i, j' \rangle, \end{aligned} \quad (4.21)$$

and the kinetic energy finally becomes

$$E_k = -2t \mathcal{Z}_L^{-1} \int \mathcal{D}p w_b \sum_{\langle ij \rangle} \sum_{j'} e^{i\gamma(p_{i,1} - p_{j,1})} \langle j, j' | \Omega | i, j' \rangle. \quad (4.22)$$

In addition to  $E_k$ , we shall also consider the correlation function

$$\rho(\delta) = \sum_i \langle \hat{n}_{i\uparrow} \hat{n}_{i+\delta\downarrow} \rangle, \quad \delta = 0, 1, \dots, N/2 - 1 \quad (4.23)$$

depending on the distance  $\delta$ . A simple calculation leads to

$$\rho(\delta) = \mathcal{Z}_L^{-1} \int \mathcal{D}p w_b \sum_i \langle i, i + \delta | \Omega | i, i + \delta \rangle. \quad (4.24)$$

Finally, we would like to point out that other observables, such as the total energy and the momentum distribution  $\langle c_{k\sigma}^\dagger c_{k\sigma} \rangle$ , may also be measured within the current approach, while correlation functions such as  $\langle \hat{n}_i \hat{x}_j \rangle$  or the quasiparticle weight cannot be determined accurately (Sec. 3.5).

### 4.4.3 Numerical details and performance

The most significant difference between the present calculations and the one-electron case in Chap. 3 is the dimension of the matrices involved. While for one electron all matrices have size  $N \times N$ — $N$  being the extension of the 1D lattice under consideration—here the dimension is  $N^2 \times N^2$ . Clearly, this restricts calculations with respect to the number of

lattice sites, especially in higher dimensions  $D > 1$  where  $N^2 \mapsto N^{2D}$ . The total numerical effort for the current approach is proportional to  $N^{6D}L$ . In contrast, the one-electron algorithm displays the same dependence  $\propto N^{3D}L$  as the determinant QMC method of Blankenbecler *et al.* [124] for the many-electron case, which can be reduced to  $N^{2D}L$  by employing the checkerboard breakup of the hopping matrix (Sec. 5.3). The increase in required computer time for the bipolaron results from the fixed number of electrons. Additionally, in contrast to Chap. 3, we find that numerical stabilization is required in evaluating the  $L$ -fold matrix product in Eq. (4.17). In fact, the necessary singular value decomposition [164] becomes the dominant contribution to computer time for large  $N$  and low temperatures. Despite these shortcomings, we shall see below that the present algorithm allows one to study lattices of reasonable sizes  $N \leq 14$ , for a wide range of the parameters  $\bar{\omega}$ ,  $\lambda$  and  $\bar{U}$ . In particular, we can obtain accurate results in the adiabatic regime  $\bar{\omega} < 1$ .

Let us briefly compare our method to other QMC approaches to the Holstein-Hubbard bipolaron. The method of de Raedt and Lagendijk [136] is based on an analytic integration over the phonon degrees of freedom, leading to a model with retarded electron-electron interaction. Similar to our approach, it employs a Suzuki-Trotter approximation and gives results at finite temperatures. For simplicity, de Raedt and Lagendijk only considered the adiabatic limit  $\bar{\omega} = 0$ , in which there are no retardation effects. The numerical effort grows as  $L^2$ , but is virtually independent of the system size, so that simulations can be carried out even for large clusters in three dimensions. However, it is not clear how a small but finite adiabatic ratio  $\bar{\omega} < 1$  will affect the computer time.

Macridin *et al.* [159] used the diagrammatic QMC method to study two electrons on a  $25 \times 25$  lattice. Although their approach does not rely on the Suzuki-Trotter decomposition (Sec. 2.1.4), it is limited to zero temperature, and statistical errors increase noticeably for  $\bar{\omega} < 1$ . Moreover, the accuracy also decreases for large values of  $\lambda$  and/or  $\bar{U}$ , whereas we shall see in Sec. 4.4.4 that we can easily study the strong electron-phonon coupling regime also for  $\bar{U} > 0$ .

The numerical effort for the present method can be reduced by exploiting the translational invariance of the model. To this end, the basis states (4.13) would have to be replaced by states  $\{|k, \Delta\rangle\}$  with total quasimomentum  $k$ , and with the two electrons separated by a distance  $\Delta$ . A similar idea has been used by Kornilovitch [112, 113] for a single electron. In one dimension, the use of the basis  $\{|k, \Delta\rangle\}$  would reduce the size of the matrices in the algorithm from  $N^2 \times N^2$  to  $N \times N$ . However, in the course of the simulation, we had to evaluate the matrix product over  $\tau$  [Eq. (4.17)] for each allowed value of  $k$ . In total, we could therefore reduce the numerical effort by a factor  $N$ . Additionally, owing to the smaller size of the matrices, numerical stabilization may not be necessary to the same extent as here. The major drawback of using the reduced basis in momentum space is that it significantly complicates the program code. Consequently, in this work, we have restricted ourselves to the straight-forward extension of the one-electron algorithm presented above.

Finally, the minus-sign problem, which has been discussed in detail in Chap. 3, also occurs for the two-electron case considered here. However, as for one electron, it quickly diminishes with increasing system size, and does therefore not conceivably affect simula-

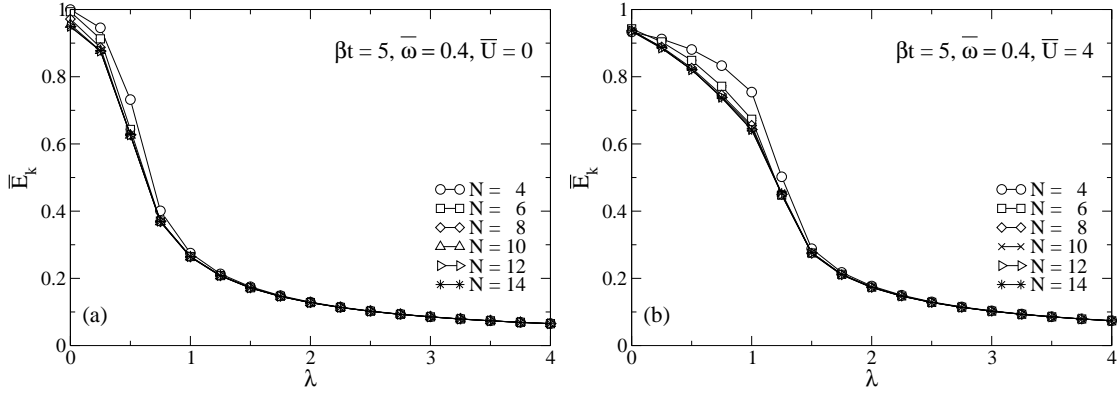


Figure 4.7: Normalized kinetic energy  $\overline{E}_k$  [Eq. (4.25)] from QMC as a function of electron-phonon coupling  $\lambda$  for different cluster sizes  $N$ . Here and in subsequent figures QMC results have been extrapolated to  $\Delta\tau = 0$  (see text), errorbars are smaller than the symbol size, and lines are guides to the eye.

tions.

#### 4.4.4 Results

As in Chap. 3, we extrapolate the QMC results to  $\Delta\tau = 0$ , to remove the error  $\sim (\Delta\tau)^2$  due to the Suzuki-Trotter approximation. In contrast, this error is expected to be relatively large (on the order of a few percent) in the calculations of de Raedt and Lagendijk, due to the use of a rather small number of Trotter slices ( $L = 32$  at  $\beta = 5$ , so that  $\Delta\tau \approx 0.16$  [136]). Here we have performed simulations for three different values of  $\Delta\tau$ , typically 0.1, 0.075 and 0.05. The errorbars in the figures below are usually as small as the linewidth, and will not be shown if smaller than the symbols used.

We define the effective kinetic energy of the two electrons as

$$\overline{E}_k = E_k / (-4t). \quad (4.25)$$

Owing to the increased numerical effort compared to the one-electron case, we will mainly show results for  $N = 12$ . Calculations for  $N = 4-14$ ,  $\overline{\omega} = 0.4$  and  $\beta t = 5$ , presented in Fig. 4.7, show that the kinetic energy is converged within the symbol size, corresponding to changes of less than 0.5%. As expected, finite-size effects are largest near the cross over between a large and a small bipolaron, and very small in the strong-coupling regime. Similar behavior has been found for the correlation function  $\rho(\delta)$ .

In Fig. 4.8 we show  $\overline{E}_k$  as a function of the electron-phonon coupling for different values of  $\overline{\omega}$  and  $\overline{U}$ , at  $\beta t = 5$ . An inverse temperature of  $\beta t = 5$  has been shown [136] to be low enough to study bipolaron formation, in agreement with Fig. 4.9. Although the cross over still becomes more abrupt as we lower the temperature further, it is already well visible at  $\beta t = 5$ .

Figure 4.8 reveals a strong decrease of  $\overline{E}_k$  near  $\lambda = 0.5$  for small phonon frequencies and  $\overline{U} = 0$ . With increasing  $\overline{\omega}$ , the cross over becomes less pronounced, and shifts to

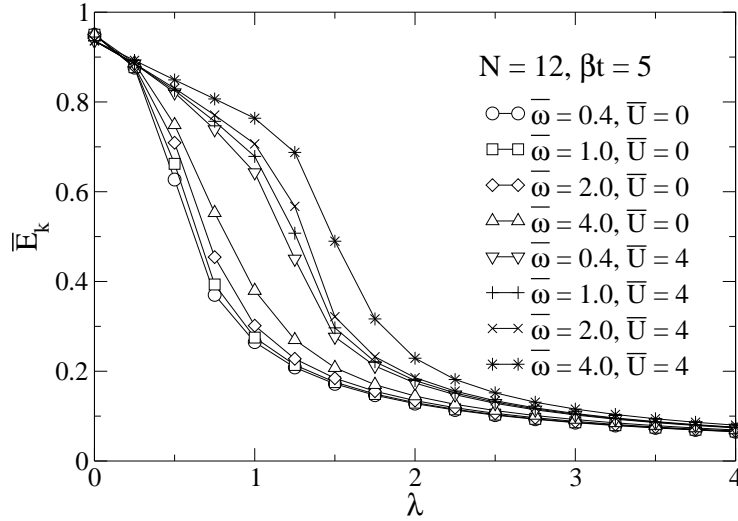


Figure 4.8: Normalized kinetic energy  $\bar{E}_k$  as a function of the electron-phonon coupling  $\lambda$  for different values of the adiabatic ratio  $\bar{\omega}$  and the Hubbard repulsion  $\bar{U}$ .

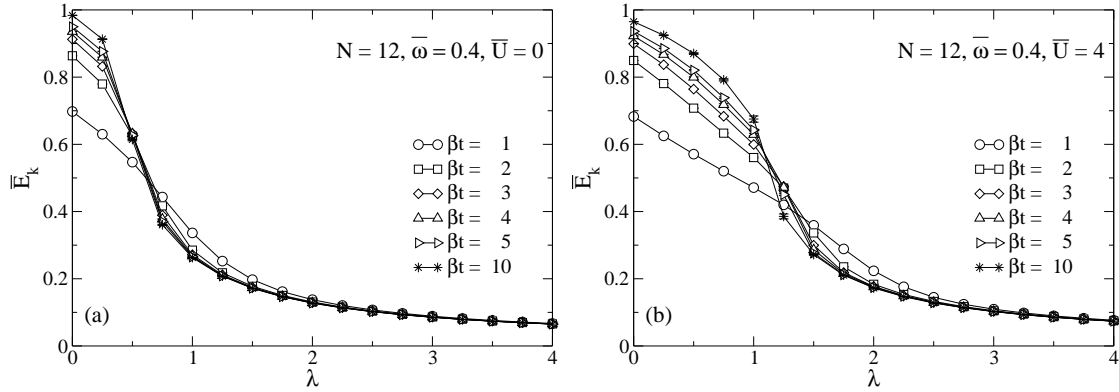


Figure 4.9: Normalized kinetic energy  $\bar{E}_k$  from QMC as a function of electron-phonon coupling  $\lambda$  for different inverse temperatures  $\beta$ .

larger values of  $\lambda$ . A comparison with Fig. 3.16 reveals that for the same value of  $\bar{\omega}$ , the cross over to a small bipolaron is sharper than the small-polaron cross over in the Holstein model with one electron. The small but finite kinetic energy even for strong electron-phonon interaction is a result of undirected, internal motion of the two electrons inside the phonon cloud. For a finite onsite repulsion  $\bar{U} = 4$  between the electrons,  $\bar{E}_k$  remains fairly large up to  $\lambda \approx 1$  (for  $\bar{\omega} \lesssim 2.0$ ), in agreement with the strong-coupling result  $\lambda_c = 1$  for  $U = 4$  (see Sec. 4.1). At even stronger coupling, the Hubbard repulsion is overcome, and a small bipolaron is formed. Again, we see that the critical coupling increases with increasing phonon frequency. We would like to mention that the kinetic energy has also been calculated by ED on clusters of up to twelve sites [85, 95, 157], but results for  $\bar{\omega} > 1$  were restricted in the accessible range of  $\lambda$ . In the regime where ED is applicable, a very

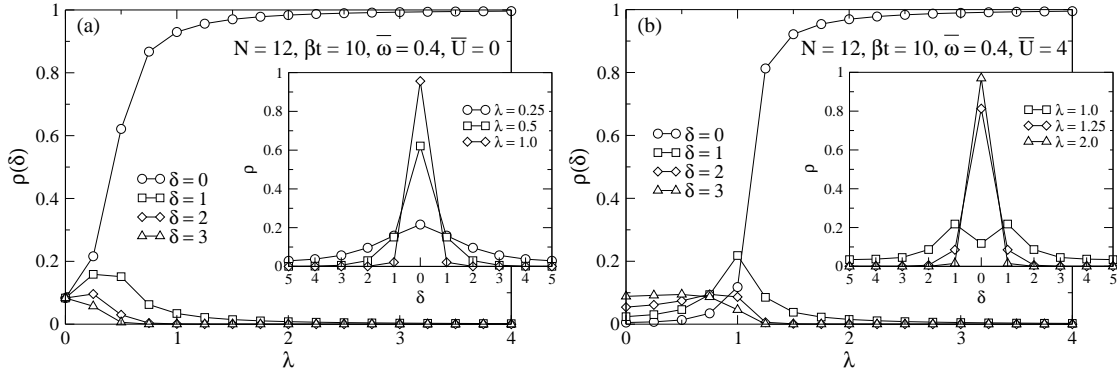


Figure 4.10: Correlation function  $\rho(\delta)$  [Eq. (4.23)] as a function of electron-phonon coupling  $\lambda$  for different values of  $\delta$ . [(a)  $\bar{U} = 0$ , (b)  $\bar{U} = 4$ ]. Inset: Correlation function  $\rho(\delta)$  as a function of the distance  $\delta$  of the electrons for different values of  $\lambda$ .

good agreement has been found with our QMC data.

The nature of the bipolaron state can be revealed by the correlation function  $\rho(\delta)$  defined by Eq. (4.23), which gives the probability for the two electrons to be separated by a distance  $\delta$ , and therefore represents a direct measure for the size of the bipolaron. Clearly, we have the sum rule  $\sum_{\delta} \rho(\delta) = 1$ . As pointed out, e.g., by Marsiglio [79], the phonon frequency determines the degree of retardation of the electron-phonon interaction, and thereby sets the maximal allowed distance between the two electrons compatible with a bound state. In the sequel, we shall focus on the most interesting regime of small phonon frequencies, which has often been avoided in previous work for reasons outlined in Sec. 4.1.

Figure 4.10(a) shows  $\rho(\delta)$  as a function of  $\lambda$  for  $\bar{U} = 0$ . Starting from the noninteracting state ( $\lambda = 0$ ) with  $\rho = 1/N$ , we see a pronounced increase of  $\rho(0)$  near  $\lambda = 0.5$ . For large  $\lambda \gtrsim 2$ , we have  $\rho(0) \approx 1$  and  $\rho(\delta) \approx 0$  for  $\delta > 0$ , which is characteristic for the aforementioned onsite bipolaron. The decrease of the spatial extent of the bipolaron with increasing electron-phonon interaction is better illustrated in the inset of Fig. 4.10(a), where we depict  $\rho$  as a function of  $\delta$ . For finite onsite repulsion  $\bar{U} = 4$ , an extended bipolaron state is stabilized for small  $\lambda$  [Fig. 4.10(b)], while a small bipolaron is found for  $\lambda = 2$ . Additionally, we see that for  $\lambda = 1$ , the electrons are most likely to occupy neighboring lattice sites [intersite bipolaron, see also inset in Fig. 4.10(b)].

As pointed out earlier, a cross over from a small bipolaron to an intersite bipolaron to two weakly bound polarons takes place as a function of the Hubbard interaction. Since the latter competes with the retarded electron-phonon interaction, the phonon frequency is expected to be an important parameter. In Fig. 4.11, we show the kinetic energy and the correlation function  $\rho(\delta)$  as a function of  $\bar{U}$ . We have fixed the electron-phonon coupling to  $\lambda = 1$ . Starting from a small bipolaron for  $\bar{U} = 0$  [see Fig. 4.10(a)], the kinetic energy increases with increasing Hubbard repulsion, which is equivalent to a reduction of the effective mass [34, 158]. Although the cross over is slightly washed out by the finite temperature in our simulations, there is a well-conceivable increase in  $\bar{E}_k$  between  $\bar{U} = 3$

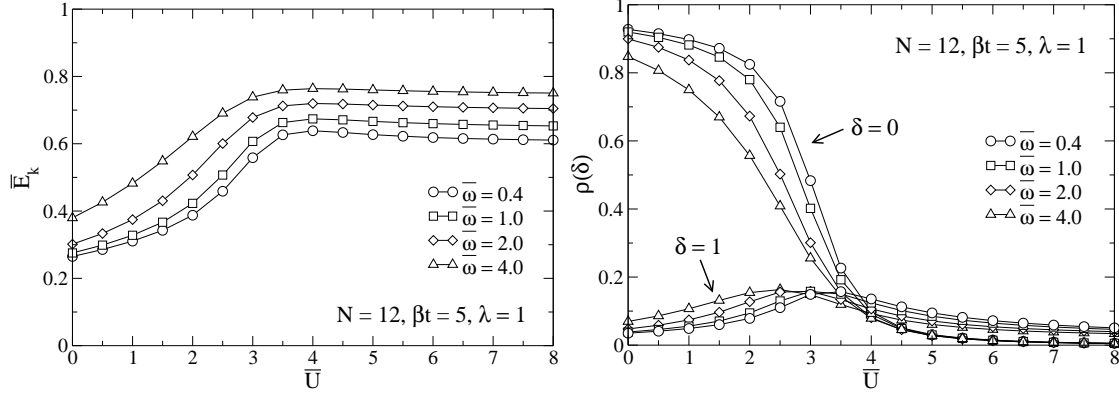


Figure 4.11: (a) Normalized kinetic energy  $\overline{E}_k$  and (b) correlation functions  $\rho(0)$ ,  $\rho(1)$  as a function of the Hubbard repulsion  $\overline{U}$  for different values of the adiabatic ratio  $\overline{\omega}$ .

and  $\overline{U} = 4$ . It originates from the breakup of the small bipolaron, as indicated by the decrease of  $\rho(0)$  in Fig. 4.11(b). Close to  $\overline{U} = 4$ , the curves for  $\rho(0)$  and  $\rho(1)$  cross, and it becomes more favorable for the two electrons to reside on neighboring sites. The intersite bipolaron only exists below a critical Hubbard repulsion  $U_c$ . As discussed in Sec. 4.1, the latter is given by  $U_c = 2E_P$  (i.e., here  $\overline{U}_c = 4$ ) at weak electron-phonon coupling, and by  $U_c = 4E_P$  at strong coupling. For an intermediate value  $\lambda = 1$  as in Fig. 4.11, the cross over from the intersite state to two weakly bound polarons is expected to occur somewhere in between, but is difficult to identify from the QMC results.

Figure 4.11 further illustrates that the cross over becomes steeper with decreasing phonon frequency. In the adiabatic limit  $\overline{\omega} = 0$ , it has been shown to be a first-order phase transition [153], while for  $\overline{\omega} > 0$  retardation effects suppress any nonanalytic behavior. At the same  $\overline{U}$ ,  $\overline{E}_k$  increases with  $\overline{\omega}$  since for a fixed  $\lambda$ , the bipolaron becomes more weakly bound. For the same reason, the cross over to an intersite bipolaron—showing up in Fig. 4.11 as a crossing of  $\rho(0)$  and  $\rho(1)$ —shifts to smaller values of  $\overline{U}$ .

Let us now consider the effect of temperature. While the kinetic energy shows a similar temperature dependence as in the one-electron case—with the cross over being smeared out at high temperatures (see Fig. 4.9)—it is much more interesting to look at  $\rho(\delta)$ . In Figs. 4.12(a)–(c) we plot  $\rho(\delta)$  at different temperatures, for parameters corresponding to the three regimes of a large, intersite and small bipolaron, respectively.

We begin with the large bipolaron in Fig. 4.12(a). For the parameters chosen ( $\overline{U} = 0$ ,  $\lambda = 0.25$ ) the two electrons are most likely to occupy the same site, but the bipolaron extends over a distance of several lattice constants. Clearly, in this regime, the cluster size  $N = 12$  used here is not completely satisfactory, but still provides a fairly accurate description as can be deduced from calculations for  $N = 14$  (not shown). Nevertheless, on such a small cluster, no clear distinction between an extended bipolaron and two weakly bound polarons can be made. As the temperature increases from  $\beta t = 10$  to  $\beta t = 1$ , the probability distribution broadens noticeably, so that it becomes more likely for the two



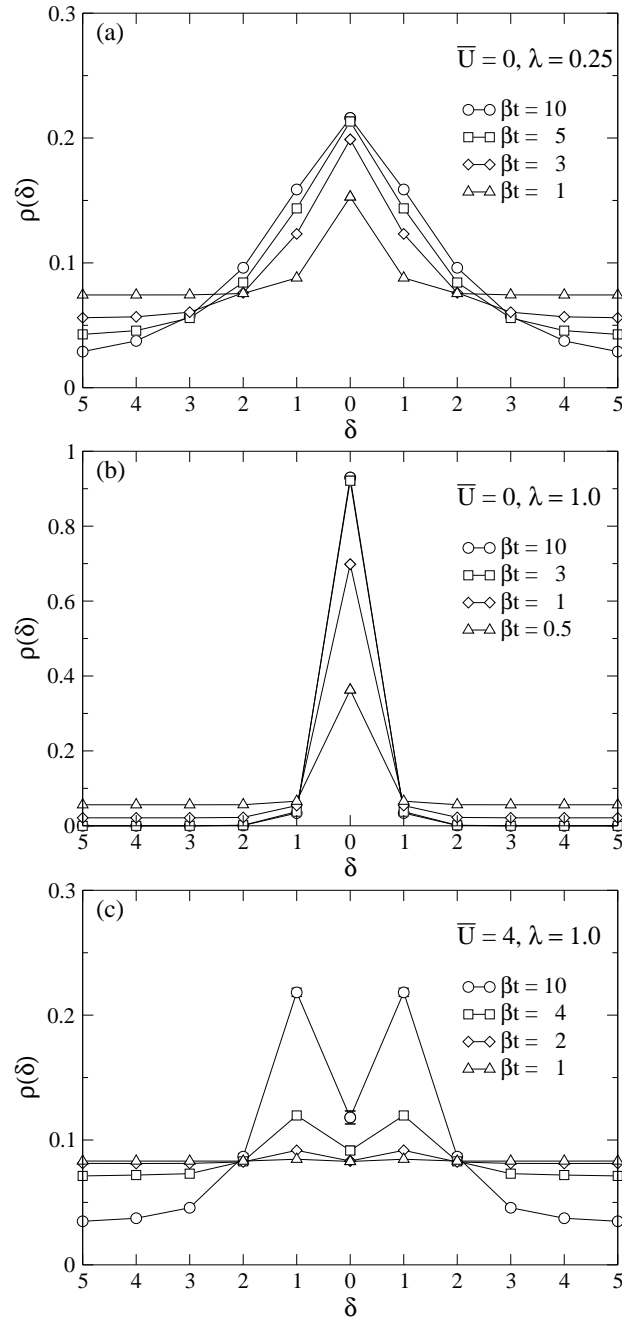


Figure 4.12: Correlation function  $\rho(\delta)$  as a function of  $\delta$  for different inverse temperatures  $\beta$ ,  $N = 12$  and  $\bar{\omega} = 0.4$ .

electrons to be further apart. In particular, for the highest temperature shown,  $\rho(0)$  has reduced by about 30 % compared to  $\beta t = 10$ .

A different behavior is found for the small bipolaron, which exist at stronger electron-phonon coupling  $\lambda = 1.0$ . Figure 4.12(b) reveals that  $\rho(\delta)$  peaks strongly at  $\delta = 0$ , while

it is very small for  $\delta > 0$  at low temperatures. Increasing the temperature, we observe that  $\rho(\delta)$  remains virtually unchanged up to  $\beta t = 3$ . Only at very high temperatures there occurs a noticeable transfer of probability from  $\delta = 0$  to  $\delta > 0$ . At the highest temperature,  $\beta t = 0.5$ , the two electrons have a nonnegligible probability for traveling a finite distance  $\delta > 0$  apart, although most of the probability is still contained in the peak located at  $\delta = 0$ .

Finally, we consider in Fig. 4.12(c) the intersite bipolaron, which has been found above for  $\bar{U} = 4$  and  $\lambda = 1.0$  (Fig. 4.10). At low temperatures,  $\rho(\delta)$  takes on a maximum for  $\delta = 1$ . For smaller values of  $\beta t$ , the latter diminishes, until at  $\beta t = 1$ , the distribution is completely flat, so that all  $\delta$  are equally likely.

The different sensitivity of the bipolaron states to changes in temperature can be explained by their different binding energies. The large and the intersite bipolaron are relatively weakly bound as a result of the rather small effective interaction  $U_{\text{eff}} \approx U - 2E_P$  (see Sec. 4.1). In contrast, the small bipolaron in Fig. 4.12(b) is strongly bound, and therefore only weakly affected by a moderate increase in temperature. It is important to compare the temperatures used here to the physically relevant temperatures, e.g., in the manganites. The Curie temperatures of compounds such as, e.g.,  $\text{La}_{1-x}\text{Sr}_x\text{MnO}_3$  or  $\text{La}_{1-x}\text{Ca}_x\text{MnO}_3$  with  $x \approx 0.3$  take on values of  $T_C \approx 200 - 350$  K depending on sample preparation and dopant ion [3] (see also Fig. 1.3). In order to make a connection between our one-dimensional calculations and the 3D manganites, we use the bandwidth  $W$  as a unit of energy. For the pseudocubic compounds, the latter is about  $W = 2$  eV [19]. Using  $W = 4t$  shows that  $\beta t = 2 - 10$  corresponds to  $T \approx 1 - 10T_C$ . In fact, the thermal dissociation of intersite bipolarons—with two holes residing on neighboring oxygen ions—has been proposed by Alexandrov and Bratkovsky [15] to explain the slowly decreasing resistivity in the paramagnetic state above  $T_C$ .

## 4.5 Variational approach

In this section we extend the variational approach of Sec. 3.4 to the bipolaron problem. Although the method can easily be applied also in higher dimensions, we wish to keep the notation simple and therefore restrict the derivation to  $D = 1$ . The approximation consists of the use of a zero-phonon basis after the extended unitary transformation, which leads to  $\tilde{I}_{\text{ep}} = 0$  [Eq. (4.6)]. Furthermore, neglecting the ground-state energy of the oscillators, we also have  $P = 0$ , so that

$$\tilde{H} = \tilde{K} + \tilde{I}_{ee}, \quad (4.26)$$

with the transformed hopping term

$$\tilde{K} = -t_{\text{eff}} \sum_{\langle ij \rangle \sigma} c_{i\sigma}^\dagger c_{j\sigma} = \sum_{k\sigma} \varepsilon(k) c_{k\sigma}^\dagger c_{k\sigma} \quad (4.27)$$

and  $\varepsilon(k) = -2 t_{\text{eff}} \sum_{\sigma} \cos(k)$ . Here, the effective hopping amplitude is given by (Sec. 3.4)

$$t_{\text{eff}} = \frac{1}{z} \sum_{\delta} e^{-\frac{1}{4} \sum_l (\nu_l - \delta - \nu_l)^2}, \quad (4.28)$$

where  $\delta = \pm 1$  in one dimension,  $z$  is the number of nearest neighbors, and rotational invariance has been exploited. For two electrons of opposite spin, the interaction term  $\tilde{I}_{ee}$  in Eq. (4.6) simplifies to

$$\tilde{I}_{ee} = 2v_0 - U + 2 \sum_{ij} v_{ij} \hat{n}_{i\uparrow} \hat{n}_{j\downarrow} \quad (4.29)$$

if we use  $v_{ij} = v_{|j-i|}$  and  $\hat{n}_{i\sigma} \hat{n}_{j\sigma} = 0$  for  $i \neq j$ . The two-electron eigenstates of the Hamiltonian (4.26) have the form

$$|\psi_k\rangle = \sum_p \tilde{d}_p c_{k-p\downarrow}^\dagger c_{p\uparrow}^\dagger |0\rangle. \quad (4.30)$$

Here we have suppressed the phonon component which is simply given by the ground state of  $N$  free harmonic oscillators. The states (4.30) may be written as

$$|\psi_k\rangle = \frac{1}{\sqrt{N}} \sum_i e^{ikx_i} \sum_l d_l c_{i\downarrow}^\dagger c_{i+l\uparrow}^\dagger |0\rangle, \quad (4.31)$$

where the Fourier transform

$$\mathbf{d} = F \tilde{\mathbf{d}} \quad (4.32)$$

with  $F_{lp} = e^{ix_l p} / \sqrt{N}$  has been employed. The normalization of Eq. (4.30) reads

$$\langle \psi_k | \psi_k \rangle = \sum_p |d_p|^2. \quad (4.33)$$

The expectation value of the transformed hopping term with respect to the states defined by Eq. (4.30) becomes

$$\begin{aligned} \langle \psi_k | \tilde{K} | \psi_k \rangle &= \sum_{pp'} \tilde{d}_p^* \tilde{d}_{p'} \sum_q \varepsilon(q) \\ &\quad \times \left( \underbrace{\langle 0 | c_{p\uparrow} c_{k-p\downarrow} \hat{n}_{q\uparrow} c_{k-p'\downarrow}^\dagger c_{p'\uparrow}^\dagger | 0 \rangle}_{\delta_{p,p'} \delta_{q,p}} + \underbrace{\langle 0 | c_{p\uparrow} c_{k-p\downarrow} \hat{n}_{q\downarrow} c_{k-p'\downarrow}^\dagger c_{p'\uparrow}^\dagger | 0 \rangle}_{\delta_{p,p'} \delta_{q,k-p}} \right) \\ &= \sum_p |\tilde{d}_p|^2 [\varepsilon(p) + \varepsilon(k-p)] \\ &= -4 t_{\text{eff}} \mathbf{d}^\dagger T_k \mathbf{d}. \end{aligned} \quad (4.34)$$

In the last step we introduced vector notation, defined  $T_k = F \text{diag}[\cos(p) + \cos(k-p)] / 2 F^\dagger$  and used Eq. (4.32). The expectation value of the interaction term is best computed in

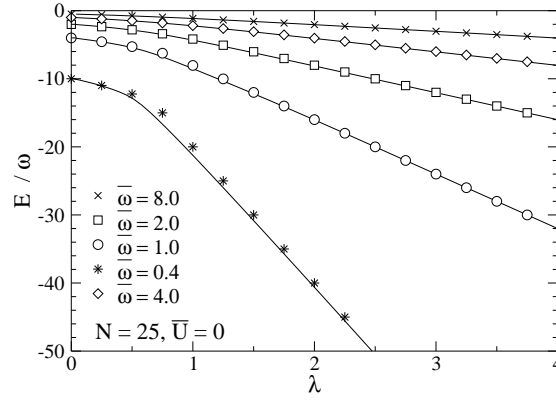


Figure 4.13: The ratio of the ground-state energy  $E$  to the phonon frequency  $\omega$  as a function of electron-phonon coupling  $\lambda$ , for different values of  $\bar{\omega}$ . Symbols corresponds to VPA results, and lines represent data obtained by the VDM [163].

the real-space representation (4.31). We find

$$\begin{aligned}
 \langle \psi_k | \tilde{I}_{ee} | \psi_k \rangle &= (2v_0 - U) \sum_l |d_l|^2 + \frac{2}{N} \sum_{ij} v_{ij} \sum_{j'j''} \sum_{ll'} d_l^* d_{l'} e^{ik(x_l - x_{l'})} \\
 &\quad \times \underbrace{\langle 0 | c_{j'+l\uparrow} c_{j'\downarrow} \hat{n}_{i\uparrow} \hat{n}_{j\downarrow} c_{j''\downarrow}^\dagger c_{j''+l'\uparrow}^\dagger | 0 \rangle}_{\delta_{jj'} \delta_{jj''} \delta_{i,j+l} \delta_{l,l'}} \\
 &= (2v_0 - U) \sum_l |d_l|^2 + \frac{2}{N} \sum_{j,l} v_{j+l,j} |d_l|^2 \\
 &= (2v_0 - U) \mathbf{d}^\dagger \mathbf{d} + 2\mathbf{d}^\dagger V \mathbf{d}, \tag{4.35}
 \end{aligned}$$

where the diagonal matrix  $V_{ij} = \delta_{ij} v_i$  has been introduced. The minimization with respect to  $\mathbf{d}$  yields the eigenvalue problem

$$(-4t_{\text{eff}} T_k + 2V) \mathbf{d} = (E_0 - 2v_0 + U) \mathbf{d}. \tag{4.36}$$

The vector of coefficients  $\mathbf{d}$  and thereby the ground state are determined by minimizing the ground-state energy  $E_0$  through variation of the displacement fields  $\gamma_{ij}$ . In contrast to the local LF transformation, this procedure takes into account displacements of the oscillators not only at the same but also at surrounding sites of the two electrons. This represents a physically much better ansatz to describe the extended bipolaron state which exists for weak electron-phonon coupling and/or strong Coulomb repulsion.

### 4.5.1 Results

While the above QMC approach is limited to finite temperatures and relatively small clusters, the variational method presented here yields ground-state results on much larger

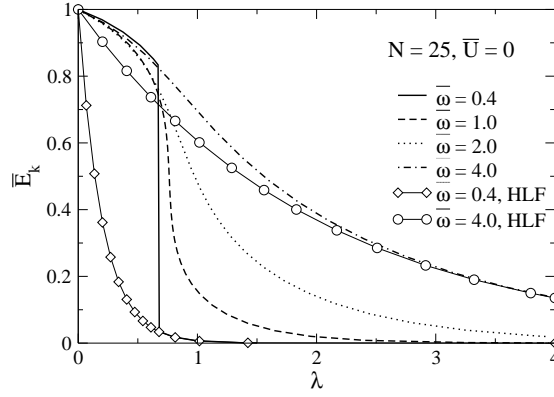


Figure 4.14: Variational results for the normalized kinetic energy  $\overline{E}_k$  as a function of the electron-phonon coupling  $\lambda$ , and for different adiabatic ratios  $\overline{\omega}$ . Also shown are results of the HLF approximation (see text).

systems. It becomes exact in several limits. First, for  $\lambda = 0$  (i.e., no electron-phonon coupling), we obtain the exact solution  $\gamma_{ij} = 0$  for all  $i, j$ . Second, as  $\omega \rightarrow \infty$ , no phonons can be excited so that the use of a zero-phonon basis is justified. Similarly, in the classical limit  $\omega = 0$ , the phonons do not have any dynamics, and the variational determination of the displacement fields allows one to obtain exact results for any  $\lambda$ . In contrast, the HLF approximation<sup>3</sup> generally overestimates the local displacement of the phonons at a given site in the presence of an electron, even for  $\omega = \infty$ . Finally, the variational approach becomes exact in the nonadiabatic strong-coupling limit  $\lambda, \omega \rightarrow \infty$ . Since the two-electron problem is diagonalized exactly without phonons, the above statements hold for any value of the Hubbard repulsion  $U$ .

To scrutinize the quality of the variational approach, we compare in Fig. 4.13 the total energy for  $\overline{U} = 0$ —normalized by the phonon frequency—as a function of electron-phonon coupling for different values of  $\overline{\omega}$ , to the most accurate approach currently available in one dimension, namely the VDM [158]. For  $U \ll 2E_P$ , the latter yields the energy of the infinite system with errors smaller than the linewidth (see also Sec. 4.2.2). We have chosen  $N = 25$  to ensure small finite-size effects. Figure 4.13 reveals a good agreement between our simple variational approach and the data of Shawish [163] over the whole range of  $\lambda$ . Slight deviations are visible for  $\overline{\omega} \leq 1$ , whereas for larger phonon frequencies the variational energies are very accurate.

Despite the good agreement of the total energy with other results, one has to be careful not to overestimate the validity of any variational method. To reveal the shortcomings of the current approach, we show in Fig. 4.14 the normalized kinetic energy [Eq. (4.25)] as a function of electron-phonon coupling, and for different  $\overline{\omega}$ . As before, we have set  $N = 25$  and  $\overline{U} = 0$ . In principle, Fig. 4.14 displays a behavior similar to the QMC data in Fig. 4.8. There is a strong reduction of  $\overline{E}_k$  near  $\lambda \approx 0.7$  for  $\overline{\omega} = 0.4$ , which becomes washed out and

<sup>3</sup>Similar to the one-electron problem, the HLF approximation can be obtained from the VPA by replacing  $\gamma_{ij}$  with  $\gamma\delta_{ij}$ , where  $\gamma$  is given by Eq. (3.10).

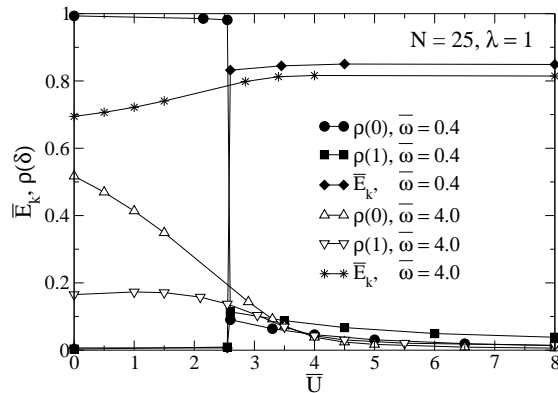


Figure 4.15: Variational results for the normalized kinetic energy  $\overline{E}_k$  and the correlation functions  $\rho(0)$ ,  $\rho(1)$  as a function of the onsite repulsion  $\overline{U}$ .

moves to larger  $\lambda$  with increasing phonon frequency. Compared to the exact QMC results in Fig. 4.8, the cross over to a small bipolaron is much too steep in the adiabatic regime, regardless of the fact that the variational results are for  $T = 0$ . This is a common defect of variational approaches. Moreover, for  $\overline{\omega} = 0.4 - 2.0$ , the variational kinetic energy is too small above the bipolaron cross over compared to the QMC data, while for  $\overline{\omega} = 4$ , the decay of  $\overline{E}_k$  with increasing  $\lambda$  is too slow. The reason for the discrepancies is the absence of retardation effects, which play a dominant role in the formation of bipolaron states. The increased importance of the phonon dynamics—not included in the variational method—for the two-electron problem leads to a less good agreement with exact results than for one electron (Sec. 3.4). In particular, our variational results overestimate the position of the cross over (Fig. 4.14) compared to the value  $\lambda_c = 0.5$  expected in the adiabatic regime. Nevertheless, the method represents a significant improvement over the HLF approximation due to the variational determination of the parameters  $\gamma_{ij}$ . This is illustrated in Fig. 4.14, where we also show the HLF result  $\overline{E}_k = \exp(-E_P/\omega)$  (see, e.g., [159]) for  $\overline{\omega} = 0.4$  and 4.0. In contrast to the variational approach, it yields an exponentially decaying kinetic energy for all values of the phonon frequency. While such a behavior actually occurs in the nonadiabatic limit  $\omega \rightarrow \infty$ , the situation is different for small  $\overline{\omega}$  (see Figs. 4.8 and 4.14). The variational method presented here accounts qualitatively for the dependence on the phonon frequency.

Next, we wish to study the influence of Coulomb repulsion  $\overline{U}$ . Similar to Fig. 4.11, we take  $\lambda = 1$ , so that an onsite bipolaron state is formed at  $\overline{U} = 0$ . For small phonon frequency  $\overline{\omega} = 0.4$ , Fig. 4.15 reveals a sharp cross over near  $\overline{U} = 2.5$ , i.e., at a smaller value of  $\overline{U}$  than in the QMC results of Fig. 4.11, the reason being again the neglect of the retarded nature of the effective electron-electron interaction. As in the QMC results, the Coulomb repulsion breaks up the onsite bipolaron, leading to an increase of the kinetic energy. Moreover, the curve for  $\rho(1)$  peaks at the cross over point, indicating the existence of an intersite bipolaron in this regime. A similar picture is found for larger phonon frequency  $\overline{\omega} = 4$ , also shown in Fig. 4.15, although the changes with increasing  $\overline{U}$  are much

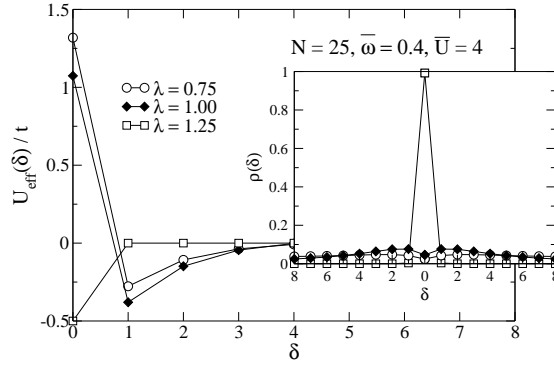


Figure 4.16: Variational results for the effective interaction  $U_{\text{eff}}(\delta)$  (see text) and the correlation function  $\rho(\delta)$  (inset) as a function of the electron-electron distance  $\delta$ .

more gradual than for  $\bar{\omega} = 0.4$ .

Finally, we report in Fig. 4.16 the effective interaction  $U_{\text{eff}}(\delta)$  between the two electrons as a function of their relative distance  $\delta$ , which is given by  $v_\delta$  [Eq. (4.7)]. We have chosen  $\bar{\omega} = 0.4$  and  $\bar{U} = 4$ , the same parameters as in Fig. 4.10(b). For  $\lambda = 0.75$ , the finite Coulomb repulsion stabilizes two weakly bound polarons, as illustrated by the results for  $\rho(\delta)$  shown in the inset of Fig. 4.16. While  $U_{\text{eff}}$  is repulsive (positive) for  $\delta = 0$ , the two electrons can form a bound state by traveling a finite distance  $1 \leq \delta \lesssim 4$  apart. This is still true for  $\lambda = 1$ , for which the atomic limit yields  $U_{\text{eff}}(0) = U - 2E_P = 0$ . Nevertheless, the two electrons experience an attractive interaction and form an intersite bipolaron. Finally, for even stronger coupling  $\lambda = 1.25$ , the phonon-mediated electron-electron interaction has overcome the onsite repulsion, so that  $U_{\text{eff}}(\delta = 0) < 0$ . At the same time, the size of the bipolaron has collapsed to a single site. It is worth mentioning that the values of  $U_{\text{eff}}(0)$  in Fig. 4.16 are larger than the strong-coupling prediction  $U - 2E_P$  for all values of  $\lambda$  considered. This may be attributed to the overestimated bipolaron binding energy in the atomic limit.

As pointed out in several places, the shortcomings of the variational approach presented here are a result of the missing dynamical phonon effects. Significantly more accurate results could be obtained by making an ansatz for the eigenstates of the untransformed Hamiltonian (1.21) of the form

$$|\Psi_k\rangle = \frac{1}{N} \sum_{ij} \sum_p e^{ipx_i + (k-p)x_j} \left( \tilde{d}_p^{(1)} \nu^\dagger \{ \gamma^{(1)} \} + \tilde{d}_p^{(2)} \nu^\dagger \{ \gamma^{(2)} \} \right) |i, j\rangle, \quad (4.37)$$

with  $|i, j\rangle$  defined as in Eq. (4.13), two canonical transformations depending on the displacement fields  $\gamma_{ij}^{(1)}$  and  $\gamma_{ij}^{(2)}$  (see Sec. 4.3), and additional variational parameters  $\tilde{d}_p^{(1)}$ ,  $\tilde{d}_p^{(2)}$ . Thereby, one can take into account lattice distortions not centered at the sites of the electrons, which become important as  $\bar{\omega} \rightarrow 0$ .

## 4.6 Conclusions

In this chapter, we have presented a detailed study of the Holstein-Hubbard model with two electrons of either the same or opposite spin, using CPT, QMC and a variational approach.

The one-electron spectral function obtained with CPT reveals that polaron and bipolaron states manifest themselves as QP bands, whose widths, weights and dispersions change as a function of the electron-phonon and electron-electron interaction strength. Results have been compared to accurate data for the bipolaron energy dispersion. For weak coupling or strong Hubbard repulsion, finite-size effects are visible, but are much smaller than in previous work which was restricted to small clusters. The major advantage of CPT is that the spectrum can be obtained at any point in  $\mathbf{k}$ -space, even when using clusters with only a few lattice sites for which enough phonon states can be kept in the calculation. This has allowed us to investigate, for the first time, the dispersion and the spectral weight of the QP features throughout the Brillouin zone. The results and their dependence on the model parameters have been discussed, and a perfect agreement has been found with the physical picture of the Holstein-Hubbard bipolaron emerging from previous work. A comparison of the bipolaron band dispersion with a simple tight-binding band has revealed an important contribution from next-nearest-neighbor hopping processes in the regime of a weakly bound state. Finally, the adiabatic regime of small phonon frequencies, which is characteristic of many real materials, remains an interesting and demanding open issue for future work.

The QMC method used here represents an extension of the one-electron algorithm developed in Chap. 3. For the present case, it is limited to relatively small clusters in one dimension (up to fourteen sites). However, in contrast to other approaches, it allows one to perform accurate calculations also for small phonon frequencies and finite temperatures. We have studied the dependence of bipolaron formation on the phonon frequency and the Hubbard repulsion. Our results underline the importance of quantum phonon effects, which have often been neglected in previous work. Moreover, we have presented for the first time exact results for the effect of temperature on the bipolaron state in the important adiabatic regime. Thermal dissociation of the large and the intersite bipolaron is observed at high temperatures, as proposed by Alexandrov and Bratkovsky [15] to explain the activated dc conductivity in the paramagnetic state of doped manganites. An interesting open issue remains the effect of dimensionality, which cannot be addressed with the current approach. Instead, one may extend the promising work of de Raedt and Lagendijk [136] to finite phonon frequencies.

Finally, we have proposed a variational approach based on a canonical transformation with variational parameters. The latter represents a significant improvement over the nonadiabatic strong-coupling approximation and reproduces qualitatively many of the physical features of the Holstein-Hubbard bipolaron, especially the dependence on phonon frequency.



Physics is becoming so unbelievably complex that it is taking longer and longer to train a physicist. It is taking so long, in fact, to train a physicist to the place where he understands the nature of physical problems that he is already too old to solve them.

(Eugene Wigner)

## 5 Photoemission spectra of many-polaron systems

Chapters 3 and 4 were devoted to a detailed understanding of the formation of single polarons and bipolarons. In real materials, such as the cuprates or manganites, which are in the focus of current research, strong interactions among these QP's are expected to significantly affect the properties of the system. Unfortunately, the knowledge about many-polaron systems is by far not as complete as that of models with one or two electrons.

In the cuprates, bipolaron formation is strongly suppressed by strong electronic correlations, as described by the Holstein-Hubbard model considered in Chap. 4. Similarly, the large Hund's rule coupling  $J_H$  in the manganites (see Sec. 1.1) imposes a severe energy penalty on configurations with doubly occupied sites, giving rise to a strong tendency of the system to avoid singlet, small bipolarons. Furthermore, the double exchange mechanism tends to align the itinerant spins ferromagnetically below  $T_C$ . Extended bipolarons may still be formed in the paramagnetic state above  $T_C$  [15], but recent experiments as well as theoretical considerations do not quite support such theories [3, 165]. These circumstances motivate studies of many-polaron systems, such as the spinless Holstein model considered here, in which bipolaron formation is suppressed either by the Pauli exclusion principle or by strong Coulomb repulsion among the electrons. For the manganites, the applicability of such models is underlined by recent experimental work [165, 166], which suggests that the charge carriers are polarons rather than bipolarons.

Most previous work on Holstein models with many electrons focused on the Peierls instability and superconductivity, while the polaron physics has received relatively little attention apart from the work for one and two electrons (see Chaps. 3 and 4). Consequently, small-polaron theory [9]—valid for a single electron strongly coupled to the lattice—is frequently used to more or less successfully interpret experimental results for materials with strong electron-phonon interaction and high carrier density.

For the many-electron case, Eliashberg theory [9] works well if the phonon frequency is much smaller than the Fermi energy, i.e.,  $\omega \ll E_F$ . Similarly, perturbative approaches based on the LF transformation (Sec. 3.3) yield reasonable results for strong electron-phonon coupling and intermediate or large phonon frequencies  $\bar{\omega} \gtrsim 1$ . However, neither of these methods can be extended to the most interesting regime of intermediate coupling and small but finite phonon frequency, which is realized, e.g., in the abovementioned classes of materials. The resulting gap in knowledge may be filled by making use of unbiased numerical methods. Although the latter can, in principle, be applied for any values of the model parameters, limitations in computer power and memory have so far imposed severe

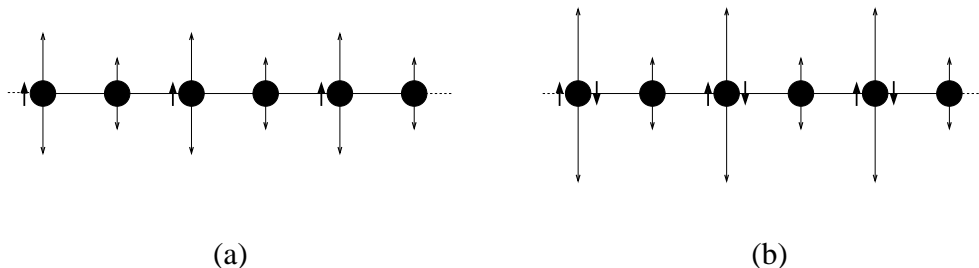


Figure 5.1: Illustration of the charge-ordered Peierls state in the (a) spinless and (b) spinfull Holstein model at half filling. Filled circles correspond to lattice sites, and thick (thin) arrows indicate electrons (lattice distortions).

restrictions on calculations. Here we tackle this challenging theoretical problem by means of a novel QMC algorithm as well as ED performed on parallel supercomputers.

This chapter is organized as follows. We begin with a brief review of the spinless Holstein model in Sec. 5.1. In Sec. 5.2, we use CPT together with an exact solution for the atomic-limit Green function to calculate approximate spectral functions. The extension of the QMC method presented in previous chapters to the many-electron case is discussed in Sec. 5.3. We then use QMC and ED to investigate in detail the spectral properties of many-polaron systems over a wide range of band filling and electron-phonon interaction, both in the adiabatic and nonadiabatic regime (Sec. 5.4). Finally, Sec. 5.5 contains our conclusion.

## 5.1 Spinless Holstein model

The spinless Holstein model can be obtained by dropping spin indices in Eqs. (1.13) and (1.17), respectively. The electron density operator is then given by  $\hat{n}_i \equiv c_i^\dagger c_i$  with eigenvalues 0, 1. As before, we use the dimensionless parameters  $\lambda$  [Eq. (1.18)] and  $\bar{\omega}$  [Eq. (1.19)].

Since we are interested in polaron physics, we restrict the discussion of previous work to the case of quantum phonons. In the latter, the fluctuations of the lattice enable the electrons to hop even in the strong-coupling regime, while in models with classical phonons the carriers become trapped by the lattice distortions and no coherent polaron states exist.

We begin with the half-filled model, which has been studied in one dimension using QMC [129, 131, 167], ED [168], DMRG [169] and variational methods [170–173]. Similar to the spinfull Holstein model at half filling, i.e., with one electron per site, the spinless model with one electron per two lattice sites displays a quantum phase transition from a metallic state to a Peierls insulating state with charge-density-wave (CDW) order. Figure 5.1(a) illustrates that in the spinless model, every other site is occupied by one electron which causes a local lattice distortion. In contrast, in the spinfull case, the ground state consists of singlet bipolarons [Fig. 5.1(b)]. While the insulating CDW state of the spinless model is stable for any  $\lambda > 0$  in the adiabatic limit  $\bar{\omega} = 0$ , it is destroyed by quantum phonon fluc-

tuations for  $\bar{\omega} > 0$ . At zero temperature, and for finite phonon frequencies, the transition to the Peierls state occurs when  $\bar{\omega}$  becomes smaller than a critical value  $\bar{\omega}_c$ , or  $\lambda > \lambda_c$ .

Capone *et al.* [174] used ED to study the cross over from a single polaron to a many-electron system. Although their work is for the Holstein-Hubbard model, the latter behaves very similar to the spinless Holstein model in the limit of large  $U$  considered in [174].

Finally, using DMFT, Capone and Ciuchi [175] found a cross over from a metallic to a polaronic state in infinite dimensions, in which a charge-ordered insulating state is suppressed even at half filling. This is similar to the work of Green [25], who developed a many-body coherent potential approximation for the Holstein and the Holstein-DE model which will be discussed in some detail in Sec. 5.2.1.

## 5.2 Strong-coupling perturbation theory

The CPT calculations in Chaps. 3 and 4 were restricted to one and two electrons, respectively. Although the method has been successfully applied, e.g., to the many-electron Hubbard model [11, 12, 61, 68], the phonon degrees of freedom in the Holstein model severely limit calculations using the Lanczos method. Here we consider a finite electron density  $n = 0.5$  by combining CPT with the exact analytic result for the atomic-limit Green function, which can readily be obtained for many models using the equation-of-motion method [9]. The results for the one-electron spectrum in two dimensions will be compared to the many-body coherent potential approximation [25].

### 5.2.1 Many-body coherent potential approximation

Extending previous work of Edwards *et al.* [176, 177] for the pure DE model (Sec. 1.3.2), Green [25] studied the Holstein-DE model using a many-body coherent potential approximation (CPA) which, owing to the more complicated form of the Holstein-DE Hamiltonian [Eq. (1.10)], constitutes a considerable extension of the Hubbard III approximation [178]. The many-body CPA successfully describes many aspects of the manganites, and we refer the reader to a recent review of this and other work by Edwards [3]. Here we only consider the special case of a completely saturated ferromagnetic state at temperature  $T = 0$ , with all itinerant spins having  $\uparrow$  spin, say. Consequently, the DE term—coupling local and itinerant spins (Sec. 1.3.2)—becomes merely a constant shift in energy, and the Holstein-DE model is equivalent to the pure Holstein model of spinless fermions, i.e., with no doubly-occupied sites (Sec. 1.3.2). An important feature of the many-body CPA is that for hopping  $t = 0$  the one-electron Green function reduces to the exact atomic limit [45]

$$G_{\uparrow}^{\text{AL}}(\epsilon) = e^{-\tilde{\alpha}} \left\{ \frac{1}{\epsilon} + \sum_{r=1}^{\infty} \frac{\tilde{\alpha}^r}{r!} \left( \frac{n}{\epsilon + \omega r} + \frac{1-n}{\epsilon - \omega r} \right) \right\}, \quad (5.1)$$

where  $\tilde{\alpha} = g^2/\omega^2$  and the polaron binding energy  $E_P$  has been absorbed into the chemical potential. The general result for  $G^{\text{AL}}$  of the spinfull Holstein model has been given by

## 5.2. Strong-coupling perturbation theory

---

Green [25], and we drop the spin index in the sequel. As discussed by Edwards [3], for an elliptic density of states, the local Green function  $G(z)$  for complex energy  $z$  satisfies the CPA equation

$$G(z) = G^{\text{AL}}(z - W^2G/16), \quad (5.2)$$

$W$  denoting the bare bandwidth [Eq. (1.8)], and the self-energy can be obtained from [3]

$$\Sigma(z) = z - G^{-1} - W^2G/16. \quad (5.3)$$

Finally, the one-electron spectral function is given by [cf. Eq. (2.36)]

$$A(\mathbf{k}, \epsilon) = -\frac{1}{\pi} \text{Im} \frac{1}{z - \epsilon_{\mathbf{k}} - \Sigma(z)}, \quad (5.4)$$

where

$$\epsilon_{\mathbf{k}} = -2t \sum_{m=1}^{\text{D}} \cos k_m \quad (5.5)$$

is the band energy for wavevector  $\mathbf{k}$  in  $D$  dimensions.

In order to compare with ARPES data on the bilayer manganite  $\text{La}_{1.2}\text{Sr}_{1.8}\text{Mn}_2\text{O}_7$ , nominally with  $n = 0.6$ , Hohenadler and Edwards [45] chose a strong electron-phonon coupling  $g/W = 0.1$  (corresponding to  $\lambda = 0.8$  in two dimensions where  $W = 8t$  [Eq. (1.18)]), as deduced from the low Curie temperature of this material. To simplify calculations, they also used  $n = 0.5$  for which the chemical potential  $\mu = 0$  by symmetry. We want to point out that the many-body CPA assumes a homogeneous system, so that no tendencies toward CDW order occur as  $n$  is varied [25]. As in previous work [25], Hohenadler and Edwards [45] used  $W = 2$  eV and  $\omega/W = 0.025$  ( $\bar{\omega} = 0.2$ ). The results [45] for  $A(\mathbf{k}, \epsilon)$ , shown in Fig. 5.2, support the theory of Alexandrov and Bratkovsky [179] that in these manganites, small polarons exist in the ferromagnetic state. A similar interpretation of the experimental data—based on standard small-polaron theory—had also been given by Dessau *et al.* [180]. Well away from the Fermi surface, a well-defined peak exists which broadens as  $\mathbf{k}$  approaches the Fermi level  $E_{\text{F}}$  at  $y = 0.5$ . If  $y$  is increased further, most of the spectral weight is transferred above  $E_{\text{F}}$ . Moreover, the peaks never approach the Fermi level closely, in agreement with the experimental data. This indicates the existence of a pseudogap in the one-electron density of states. However, in the gap, there exist small polaron subbands (see Fig. 4 of [25]) and one of them, at the Fermi level, presumably gives rise to the low but finite conductivity of the system. As discussed by Edwards [3], the many-body CPA does not give coherent states with infinite lifetime at the Fermi level, even for  $T = 0$ . This is typical for any CPA, and here it leads to an incoherent polaron subband around the Fermi level. Nevertheless, outside the central band around  $E_{\text{F}}$ , the imaginary part of the self-energy displays the correct behavior, i.e., it vanishes in the gap, between the polaron bands.

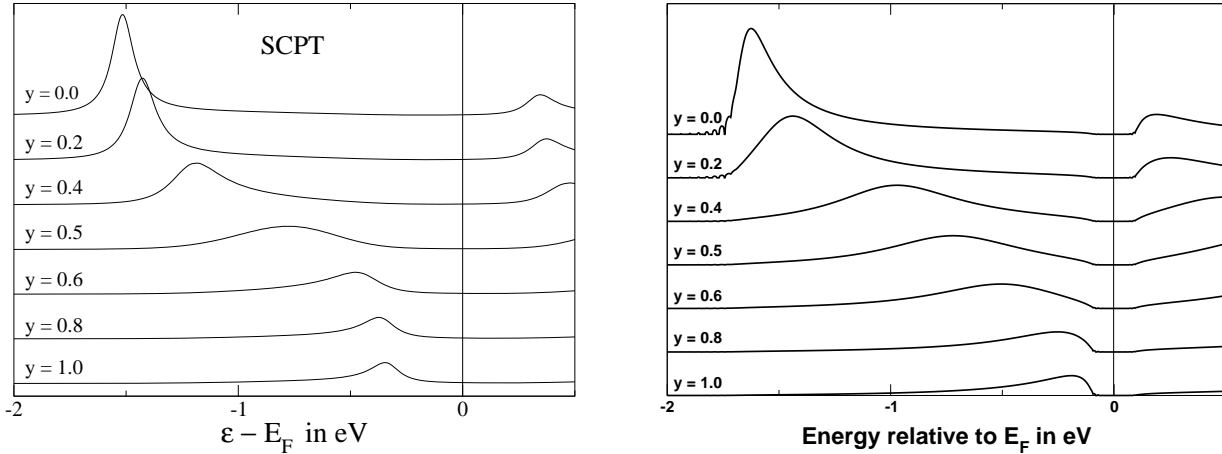


Figure 5.2: Comparison of the one-particle spectral function of the spinless Holstein model at  $T = 0$ , calculated with the SCPT (left) and with the many-body CPA (right, taken from [45]). Here the wavevector  $\mathbf{k}$  is given by  $\mathbf{k} = \pi(1, y)$  with  $y$  as indicated in the figure [45]. The plot is for  $\omega/W = 0.025$  and  $g/W = 0.1$ . The SCPT results have been broadened using a smearing parameter  $\eta/W = 0.025$ .

## 5.2.2 Strong coupling perturbation theory

In this section we use the atomic-limit Green function (5.1), and combine it with CPT to compare the resulting spectrum with the many-body CPA. For this case of a one-site cluster ( $a \equiv b$ ), Eqs. (2.43) and (2.44) reduce to a single equation for the one-electron Green function [12]

$$G(\mathbf{k}, z) = \frac{G^{\text{AL}}(z)}{1 - \varepsilon_{\mathbf{k}} G^{\text{AL}}(z)} = \frac{1}{z - \varepsilon_{\mathbf{k}} - \Sigma^{\text{AL}}(z)} \quad (5.6)$$

with  $\varepsilon_{\mathbf{k}}$  as defined by Eq. (5.5). Hence, CPT for  $N = 1$  is equivalent to the Hubbard I approximation [67], but here with the more complicated atomic-limit Green function of the Holstein model given by Eq. (5.1). In the sequel, we shall refer to this approximation as SCPT. This is justified by the fact that the approach becomes exact for  $t = 0$ . Historically, a similar strong-coupling expansion for the Hubbard model [181, 182]—including higher order corrections—has been the starting point for the development of CPT.

Before we discuss the results, we would like to comment on the quality of the SCPT used here. While the many-body CPA requires a self-consistent, iterative solution of Eq. (5.2), the SCPT Green function is obtained from the Lehmann representation of  $G^{\text{AL}}$ , and the subsequent use of the resulting self-energy  $\Sigma^{\text{AL}}$  in Eq. (5.6). Similar to the original Hubbard I approximation [67], the resulting Green function consists of  $\delta$  peaks corresponding to states with infinite lifetime. However, due to the poles in the self-energy, there are no states at the Fermi level and the system is not a Fermi liquid. As in the many-body CPA,  $G$  depends on  $\mathbf{k}$  only through the band energy  $\varepsilon_{\mathbf{k}}$ , whereas the self-energy is local. This reliance on the atomic limit is reasonable in the strong-coupling regime considered

here, where small polarons move in an extremely narrow band. Consequently, the simple perturbative treatment of the hopping term can be expected to give sensible results. Nevertheless, in the SCPT, we have to use an artificial imaginary part  $\eta$ —which does not depend on energy—to obtain peaks of finite width. Although for large enough  $\eta$  there will be states at the Fermi level, the latter have only finite lifetime even for  $T = 0$ . Hence, both the SCPT and the many-body CPA never give a Fermi liquid, but the self-consistent CPA Green function yields an imaginary part of the self-energy that shows the correct, strong energy dependence except for the region inside the very small, incoherent polaron band around  $E_F$ , as discussed above. Thus, as could be expected from the Hubbard I-like approximation in Eq. (5.6), the many-body CPA is superior to the SCPT, although both approaches become exact in the atomic limit. Exact results for the spectral function in one dimension will be presented in Sec. 5.4.

The one-particle spectral function obtained with the SCPT using Eq. (2.36), also shown in Fig. 5.2, resembles quite closely to the results of [45]. Although there are some differences concerning the width and the position of the peaks, the overall behavior is very similar. In particular, the broadening of the QP peak near the Fermi level at  $y = 0.5$  is well reproduced. Clearly, the success of the SCPT consists of a surprisingly good agreement with the CPA data for all  $\mathbf{k}$ . Despite this agreement, the SCPT fails to reproduce the polaron subbands, and the sharp edge to the pseudogap for large values of  $y$ . Moreover, the gap is larger than in the case of the CPA. These shortcomings are a consequence of the rather crude approximation. Nevertheless, keeping in mind the simplicity of the ansatz, the agreement with the many-body CPA is satisfactory.

We would like to point out that the SCPT presented here can also be generalized to the Holstein-DE model with quantum spins (see Sec. 1.3) and at finite temperature, using the atomic-limit Green function given by Edwards [3]. Finally, the approximation could be systematically improved by increasing the number of sites in the cluster, which is exactly the idea behind CPT (Sec. 2.2). Since for  $N > 1$  the cluster Green function can no longer be calculated analytically, one has to resort to numerical techniques such as the Lanczos method (Sec. 2.3). However, calculations are extremely difficult for two- or three dimensional clusters with, e.g., quarter filling, small phonon frequency and strong electron-phonon coupling.

## 5.3 Quantum Monte Carlo method

In this section, we extend the one-electron QMC algorithm developed in Chap. 3 to the spinless Holstein model with many electrons. We begin by applying the standard LF transformation (Sec. 3.3) to obtain the Hamiltonian (3.14). For spinless fermions, the last term in Eq. (3.14) simplifies to  $-E_P \sum_i \hat{n}_i$ . We define the grand-canonical Hamiltonian

$$\tilde{\mathcal{H}} = \tilde{H}_0 - \mu \hat{N} = -t \underbrace{\sum_{\langle ij \rangle} c_i^\dagger c_j e^{i\gamma(\hat{p}_i - \hat{p}_j)}}_{\tilde{K}_0} + \frac{\omega}{2} \underbrace{\sum_i (\hat{p}_i^2 + \hat{x}_i^2)}_{P \equiv P_p + P_x} - \underbrace{(E_P + \mu) \sum_i \hat{n}_i}_{\tilde{I}}, \quad (5.7)$$

where  $\mu$  denotes the chemical potential,  $E_P$  is the polaron binding energy [Eq. (1.20)], and the parameter  $\gamma$  of the LF transformation is given by Eq. (3.10).

For the case of a half-filled band, i.e.,  $N/2$  electrons on  $N$  sites for the spinless model (5.7), the chemical potential is given by  $\mu = -E_P$ . Away from  $n = 0.5$ ,  $\mu$  has to be adjusted accordingly to yield the right density of electrons  $n$ .

We would like to point out that for the spinfull case, the LF transformation yields an attractive Hubbard term (see Sec. 4.3). For the determinant QMC method to be applicable, the latter has to be decoupled using auxiliary fields [10]. In contrast, for the spinless model considered here, the algorithm is almost identical to the one-electron case. The following derivation assumes a hypercubic lattice in  $D$  dimensions.

### 5.3.1 Partition function

To calculate the partition function we use the Suzuki-Trotter decomposition (Sec. 2.1.4)

$$e^{-\beta\tilde{\mathcal{H}}} \approx \left( e^{-\Delta\tau\tilde{K}_0} e^{-\Delta\tau P_p} e^{-\Delta\tau P_x} e^{-\Delta\tau\tilde{I}} \right)^L, \quad (5.8)$$

where  $\Delta\tau$  is given by Eq. (2.15). The trace appearing in the partition function  $\mathcal{Z} = \text{Tr} e^{-\beta\tilde{\mathcal{H}}}$  can be split up into a bosonic and a fermionic component leading to the approximation

$$\begin{aligned} \mathcal{Z}_L = \text{Tr}_f \int dp_1 dp_2 \cdots dp_L \langle p_1 | e^{-\Delta\tau\tilde{K}_0} e^{-\Delta\tau P_p} e^{-\Delta\tau P_x} e^{-\Delta\tau\tilde{I}} | p_2 \rangle \cdots \\ \times \cdots \langle p_L | e^{-\Delta\tau\tilde{K}_0} e^{-\Delta\tau P_p} e^{-\Delta\tau P_x} e^{-\Delta\tau\tilde{I}} | p_1 \rangle, \end{aligned} \quad (5.9)$$

where  $dp_\tau \equiv \prod_i dp_{i,\tau}$ . The phonon coordinates  $\hat{x}$  in  $\mathcal{Z}_L$  can be integrated out analytically in the same manner as in Chaps. 3 and 4. Moreover, the momenta  $\hat{p}$  can be replaced by their eigenvalues on each time slice, and the partition function can be written as

$$\mathcal{Z}_L = C \int \mathcal{D}p e^{-\Delta\tau S_b} \text{Tr}_f(\hat{B}_1 \hat{B}_2 \cdots \hat{B}_L) \quad (5.10)$$

with  $\mathcal{D}p = \prod_\tau dp_\tau$ ,  $C = [2\pi/(\omega\Delta\tau)]^{NL}$  and

$$\hat{B}_\tau = e^{-\Delta\tau\tilde{K}_{0,\tau}} e^{-\Delta\tau\tilde{I}}, \quad \tilde{K}_{0,\tau} = -t \sum_{\langle ij \rangle} c_i^\dagger c_j e^{i\gamma(p_{i,\tau} - p_{j,\tau})}. \quad (5.11)$$

The bosonic action  $S_b$  is identical to Eq. (3.42) and may again be expressed in terms of principal components (see Sec. 3.5.2). As first shown by Blankenbecler *et al.* [124] (see also [183]), the fermion degrees of freedom can be integrated out exactly leading to

$$\text{Tr}_f(\hat{B}_1 \cdots \hat{B}_L) = \det(1 + B_1 \cdots B_L) \equiv \det(1 + \Omega), \quad (5.12)$$

where the  $N^D \times N^D$  matrix  $B_\tau$  is given by

$$B_\tau = D_\tau \kappa D_\tau^\dagger \mathcal{V} \quad (5.13)$$

with

$$\kappa_{ij} = (e^{\Delta\tau th^{\text{tb}}})_{ij} \quad , \quad (D_\tau)_{ij} = \delta_{ij} e^{i\gamma p_{i,\tau}} \quad , \quad \mathcal{V}_{ij} = \delta_{ij} e^{\Delta\tau(E_F + \mu)} . \quad (5.14)$$

Here  $h^{\text{tb}}$  is the usual tight-binding hopping matrix. The matrix product in Eq. (5.12) can be evaluated using a generalization of Eq. (3.40).<sup>1</sup> To save some computer time, we employ the checkerboard breakup [164]

$$e^{\Delta\tau t \sum_{\langle ij \rangle} c_i^\dagger c_j} \approx \prod_{\langle ij \rangle} e^{\Delta\tau t c_i^\dagger c_j} . \quad (5.15)$$

Using Eq. (5.15), the numerical effort scales as  $N^{2D}$  instead of  $N^{3D}$ , while the error due to this additional approximation is of the same order  $(\Delta\tau)^2$  as the Trotter error in Eq. (5.8).

Defining the bosonic and fermionic weights  $w_b = e^{-\Delta\tau S_b}$  and  $w_f = \det(1 + \Omega)$  respectively, the partition function finally becomes

$$\mathcal{Z}_L = C \int \mathcal{D}p w_b w_f . \quad (5.16)$$

One of the advantages of Blankenbecler *et al.*'s [124] formalism as well as the current approach is the close relation to the one-electron Green function

$$G_{ij} = \underbrace{\langle \tilde{c}_i \tilde{c}_j^\dagger \rangle}_{G_{ij}^a} + \underbrace{\langle \tilde{c}_i^\dagger \tilde{c}_j \rangle}_{G_{ij}^b} . \quad (5.17)$$

Working in real space and imaginary time, we have [124, 183]

$$G_{ij}^a = \langle \tilde{c}_i \tilde{c}_j^\dagger \rangle = (1 + \Omega)_{ij}^{-1} , \quad (5.18)$$

and

$$G_{ij}^b = \delta_{ij} - G_{ij}^a = (\Omega G^a)_{ji} . \quad (5.19)$$

We would like to mention that despite the formal similarity to the method of Blankenbecler *et al.* [124], the numerical realization of the present approach is quite different. While the grand-canonical method of [124] benefits enormously with respect to performance from a local updating scheme for the phonons, here we use a global updating in terms of the principal components together with the reweighting method, as described in Sec. 3.5. Although this requires us to recalculate the full matrix  $\Omega$  in each step, the resulting statistically independent configurations clearly outweigh the loss in performance, especially for small  $\omega$  for which autocorrelation times can exceed  $10^5$  sweeps when using the original grand-canonical QMC method [124]. The approach proposed here allows one to perform uncorrelated measurements after each update. Moreover, our calculations show that numerical stabilization by means of a time-consuming singular value decomposition [146] is not necessary for all parameters considered below. Finally, owing to the phase factors in the transformed hopping term, all the matrices become complex-valued. An important

---

<sup>1</sup>Since the interaction matrix  $\mathcal{V}$  is diagonal, it commutes with  $D_\tau^\dagger$  in Eq. (5.13).



practical test in simulations therefore is the reality of expectation values of observables, i.e., the disappearance of the imaginary part within statistical errors.

Similar to the calculations for one and two electrons, the phase factors in the hopping term [Eq. (5.7)] give rise to a minus-sign problem, i.e.,  $w_f$  can take on negative values. While for a fixed number of electrons the sign problem diminishes with increasing system size (Sec. 3.5.3), the opposite is true at finite electron densities. We find an exponential decrease of the average sign with increasing cluster size, and a strong dependence on the electron density (Sec. 5.3.3).

### 5.3.2 Observables

The calculation of observables within the formalism presented here is similar to the standard determinant QMC method [124, 164, 183]. An important difference is that we have to use the transformed operators, i.e.,

$$\langle O \rangle = \frac{1}{\mathcal{Z}} \text{Tr} (\hat{O} e^{-\beta \tilde{\mathcal{H}}}). \quad (5.20)$$

As mentioned above, the MC sampling is based purely on the bosonic weight  $w_b$ . This corresponds to a reweighting of the probability distribution so that the fermionic weight  $w_f$  is treated as part of the observables (see Sec. 3.5). Hence, we have

$$\langle O \rangle = \frac{\langle O w_f \rangle_b}{\langle w_f \rangle_b} \quad (5.21)$$

where the expectation value  $\langle O \rangle_b$  for an equal-time observable  $\hat{O}$  is defined as

$$\langle O \rangle_b = \frac{\int \mathcal{D}p w_b w_f \text{Tr}_f (\hat{O} \hat{B}_1 \cdots \hat{B}_L)}{\int \mathcal{D}p w_b}. \quad (5.22)$$

#### Static quantities

The calculation of static (equal-time) observables is straight forward. We begin with the particle density

$$n = \frac{1}{N^D} \sum_i \langle \hat{n}_i \rangle. \quad (5.23)$$

The expectation value in Eq. (5.23) can be calculated from the diagonal elements of the Green function  $G^b$  [Eq. (5.18)], i.e.,  $\langle \hat{n}_i \rangle = \langle G_{ii}^b \rangle$ . Similarly, the absolute value of the electronic kinetic energy per site is given by

$$\bar{E}_k = \frac{t}{N^D} \sum_{\langle ij \rangle} \langle G_{ji}^b \rangle. \quad (5.24)$$

The QP weight at the Fermi momentum in one dimension can be obtained from [184]

$$z(k_F) = \lim_{\substack{k_\nu^+ \rightarrow k_F \\ k_\nu^- \rightarrow k_F}} [\langle n(k_\nu^+) \rangle - \langle n(k_\nu^-) \rangle]. \quad (5.25)$$

On a finite cluster, the expression in brackets in Eq. (5.25) yields an upper bound for  $z(k)$ , with  $k_\nu^\pm$  taken to be the wavevectors just above and below  $k_F$ . A finite-size scaling has to be performed to obtain an approximation for the value of  $z(k)$  in the thermodynamic limit. While Eq. (5.25) can produce fairly accurate results within projector QMC approaches for the ground state, it is less reliable in the case of finite-temperature calculations. In addition to the scaling with system size, one has to check for each cluster size that the temperature used is indeed low enough so as to ensure converged results. Due to these difficulties, we shall not present results for the QP weight in the sequel. Finally, an alternative way to calculate  $z(k)$  from the zero-temperature imaginary-time Green function has been suggested by Brunner and Assaad [142].

Equal-time two-particle correlation functions such as

$$\rho(\delta) = \sum_i \langle \hat{n}_i \hat{n}_{i+\delta} \rangle \quad (5.26)$$

may be calculated in the same way as in the standard determinant QMC method [124, 183]. For a given phonon configuration, we can use Wick's Theorem [9] to get

$$\langle \hat{n}_i \hat{n}_j \rangle_p = \langle c_i^\dagger c_i c_j^\dagger c_j \rangle_p = \langle c_i^\dagger c_i \rangle_p \langle c_j^\dagger c_j \rangle_p + \langle c_i^\dagger c_j \rangle_p \langle c_i c_j^\dagger \rangle_p = G_{ii}^b G_{jj}^b + G_{ij}^b G_{ij}^a. \quad (5.27)$$

The expectation value  $\langle \hat{n}_i \hat{n}_j \rangle$  is then determined by averaging over all phonon configurations.

### Dynamic quantities

An observable of great interest is the time-dependent one-particle Green function

$$G^b(\mathbf{k}, \tau) = \langle c_{\mathbf{k}}^\dagger(\tau) c_{\mathbf{k}} \rangle = \langle e^{\tau \mathcal{H}} c_{\mathbf{k}}^\dagger e^{-\tau \mathcal{H}} c_{\mathbf{k}} \rangle \quad (5.28)$$

which is related to the spectral function

$$A(\mathbf{k}, \epsilon - \mu) = -\frac{1}{\pi} \text{Im} G^b(\mathbf{k}, \epsilon - \mu) \quad (5.29)$$

through

$$G^b(\mathbf{k}, \tau) = \int_{-\infty}^{\infty} d\epsilon \frac{e^{-\tau(\epsilon - \mu)} A(\mathbf{k}, \epsilon - \mu)}{1 + e^{-\beta(\epsilon - \mu)}}. \quad (5.30)$$

The inversion of the above relation is ill-conditioned and requires the use of the maximum entropy method (MEM). Fourier transformation leads to

$$G^b(\mathbf{k}, \tau) = \frac{1}{N} \sum_{ij} e^{i\mathbf{k} \cdot (\mathbf{r}_i - \mathbf{r}_j)} G_{ij}^b(\tau). \quad (5.31)$$

The allowed imaginary times are  $\tau_l = l\Delta\tau$ , with nonnegative integers  $0 \leq l \leq L$ . Within the QMC approach, we have [124, 183]

$$G_{ij}^b(\tau_l) = (G^a B_1 \cdots B_l)_{ji}. \quad (5.32)$$

Another interesting quantity is the one-electron density of states

$$N(\epsilon - \mu) = -\frac{1}{\pi} \text{Im} G(\epsilon - \mu), \quad (5.33)$$

where  $G(\epsilon - \mu) = N^{-1} \sum_{\mathbf{k}} G(\mathbf{k}, \epsilon - \mu)$ . It may be obtained numerically via

$$N(\tau) = G_{ii}^b(\tau), \quad (5.34)$$

and subsequent use of the MEM (Sec. 2.1.6).

### 5.3.3 Sign problem

Since the sign problem crucially affects the performance of any QMC method, this section is devoted to a detailed investigation of the dependence of the average sign on the parameters of the simulations.

While Hamiltonian (5.7) is symmetric with respect to a particle-hole transformation for  $\mu = -E_P$  (half filling), this symmetry is broken if we use the checkerboard approximation (5.15), so that  $n \neq 0.5$  for the above choice of the chemical potential. To simplify calculations, the results for the average sign at  $n = 0.5$  presented below have therefore been obtained using the full hopping term. For general band fillings, we find that the checkerboard breakup requires different values of  $\mu$  to perform simulations at the same electron densities, but results are identical within statistical errors if  $\mu$  is adjusted accordingly.

The derivation of the QMC algorithm in Sec. 5.3.1 is independent of the dimension  $D$  of the lattice under consideration. Nevertheless, here we only report results for the sign problem in  $D = 1$ , the case considered in Sec. 5.4, and make some remarks about the influence of the dimensionality at the end.

The average sign of the fermionic weight, denoted as  $\langle \text{sign} \rangle$ , has been defined in Eq. (3.60), with the fermionic weight in the present case given by  $w_f = \det(1 + \Omega)$  [Eq. (5.12)]. We begin with the dependence of  $\langle \text{sign} \rangle$  on the electron-phonon coupling strength. For simplicity, we show results for  $n = 0.5$ , while the effect of band filling will be discussed later. The choice  $n = 0.5$  is convenient since we know the chemical potential, and we shall see below that the sign problem is most pronounced for a half-filled band. Moreover, all existing QMC results for the spinless Holstein model are for half filling, and it is thus interesting to see how the sign problem affects simulations within the current approach.

Figure 5.3(a) reveals a similar dependence of  $\langle \text{sign} \rangle$  on electron-phonon coupling as in the one-electron case (Sec. 3.5.3). It takes on a minimum near  $\lambda = 1$  (in the adiabatic regime considered here) that becomes more pronounced with decreasing temperature. At weak and strong coupling, the average sign is close to 1, so that accurate simulations can be carried out. This feature will be exploited in Sec. 5.4. The dependence on the phonon frequency shown in Fig. 5.3(b) also bears a close resemblance to the polaron problem [cf. Fig. 3.14(b)]. Whereas  $\langle \text{sign} \rangle$  becomes very small for  $\bar{\omega} \ll 1$ , it increases noticeably in the nonadiabatic regime  $\bar{\omega} > 1$ . Owing to the absence of any autocorrelations in our approach,

### 5.3. Quantum Monte Carlo method

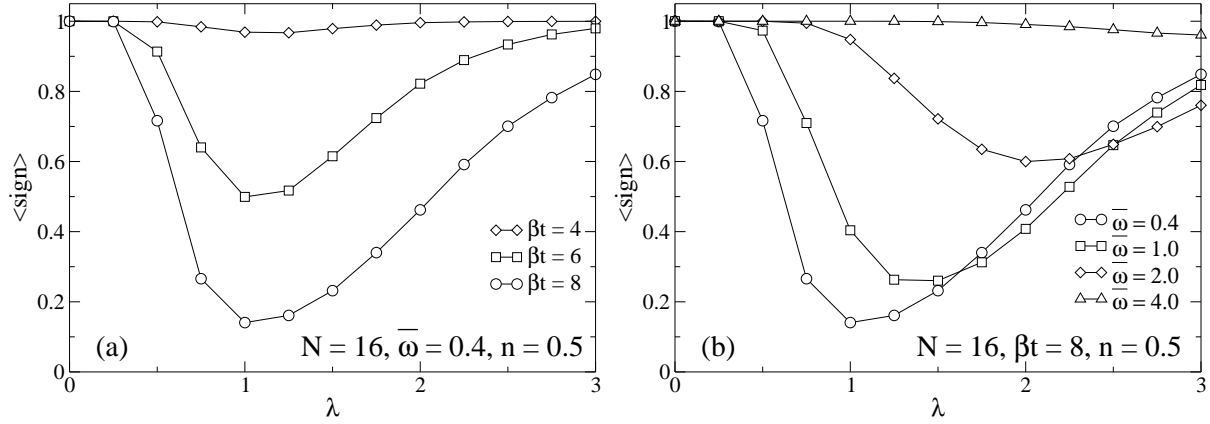


Figure 5.3: Average sign  $\langle \text{sign} \rangle$  [Eq. (3.60)] of the fermionic weight  $w_f$  as a function of electron-phonon coupling  $\lambda$  in one dimension (a) for different inverse temperatures  $\beta$ , and (b) for different values of the adiabatic ratio  $\bar{\omega}$ . Here and in subsequent figures showing QMC results lines are guides to the eye only, and errorbars are suppressed if smaller than the symbols shown. The data presented in Figs. 5.3 and 5.4 are for  $\Delta\tau = 0.05$ .

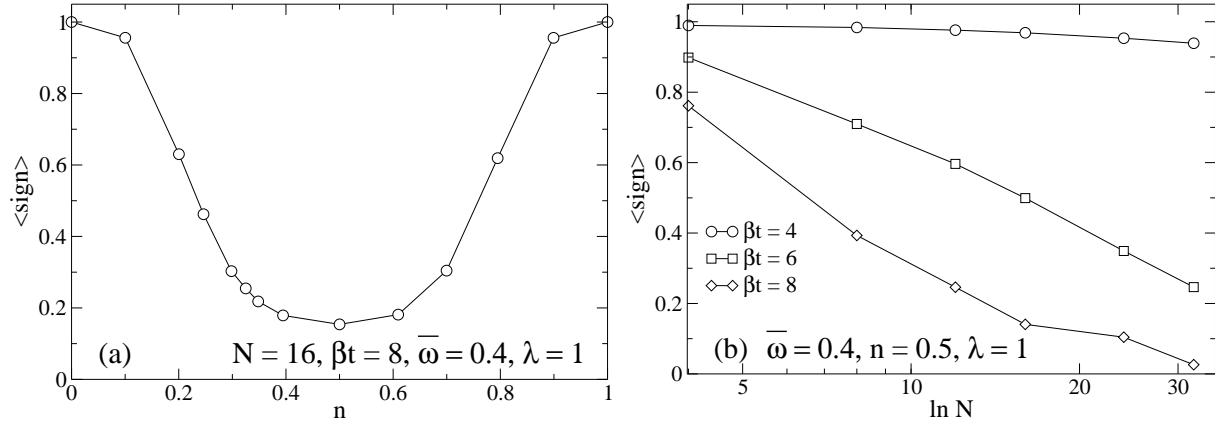


Figure 5.4: Average sign as a function of (a) band filling  $n$ , and (b) system size  $N$ .

the present method therefore represents a significant improvement of existing algorithms, as the latter face severe autocorrelations even for  $\bar{\omega} \gtrsim 1$ , thereby limiting the temperature range and cluster size.

As illustrated in Fig. 5.4(a), the average sign depends strongly on the band filling  $n$ . While it is close to one in the vicinity of  $n = 0$  or  $n = 1$ , a significant reduction is visible near half filling  $n = 0.5$ . The minimum occurs at  $n = 0.5$ , and the results display particle-hole symmetry as expected. Here we have chosen  $\beta t = 8$ ,  $\bar{\omega} = 0.4$  and  $\lambda = 1$ , for which the sign problem is most noticeable according to Fig. 5.3. The statistical error of  $n$  in Fig. 5.4 is smaller than the symbol size.

Finally, in Fig. 5.4(b), we report the average sign as a function of system size, again

for  $n = 0.5$ . The behavior is strikingly different from the one-electron case considered in Chap. 3. While in the latter  $\langle \text{sign} \rangle \rightarrow 1$  as  $N \rightarrow \infty$ , here the average sign decreases nearly exponentially with increasing system size. Obviously, this limits the applicability of our method. However, we shall see below that we can nevertheless obtain accurate results at low temperatures, small phonon frequencies, and over a large range of the electron-phonon interaction. Moreover, we would like to point out that for such parameters, existing methods suffer strongly from autocorrelations, rendering simulations extremely difficult.

The dependence of the sign problem on the dimension of the system is similar to the single-electron case (Sec. 3.5.2). The minimum in  $\langle \text{sign} \rangle$  at intermediate  $\lambda$  becomes more pronounced for the same parameters  $N$ ,  $\bar{\omega}$ ,  $\beta t$  and  $\lambda$  as one increases the dimension of the cluster.

To conclude with, we would like to point out that, in principle, the sign problem can be compensated by performing sufficiently long QMC runs, although we have to keep in mind that the statistical errors increase proportional to  $\langle \text{sign} \rangle^{-2}$  (Sec. 2.1.3). Owing to the purely phononic updates, the algorithm is very fast and we have made up to about  $2.6 \times 10^7$  single measurements to obtain the results presented in Sec. 5.4. Due to the use of the reweighting method, the measured values of observables have to be stored in every MC step, in order to perform the Jackknife analysis at the end of the run (see Sec. 3.5.2). For example, in the case of the Green function (5.28),  $L+1$  complex values for each momentum  $k$  have to be stored in every step. Depending on the observables of interest, this sets a practical limit for the maximal number of measurements due to restrictions in available disk space.

## 5.4 QMC and ED results

We have seen in Chap. 3 that a single electron undergoes a cross over to a small polaron at a critical value of the electron-phonon coupling. The important question to be addressed here is what happens if the density of electrons (or polarons) is increased. We do not expect significant changes in the strong-coupling regime due to the "localized" nature of the small polaron state. On the contrary, for intermediate electron-phonon interaction and  $\bar{\omega} \ll 1$ , each electron is surrounded by a phonon cloud extending over several lattice sites, whose overlap with other dressed electrons may lead to a dissociation of the individual polarons. Such a scenario has recently been observed in the optical properties of Sr and Ca doped manganites [165, 166], in which the charge carriers are considered to be large and small polarons, respectively.

As pointed out in Sec. 3.1, within the Holstein model, an extended polaron state is only stable in one dimension, while in higher dimensions the electrons are either free or form small (onsite) polarons. This is in contrast to the Fröhlich model with long-range interaction, in which large polarons may exist also in  $D > 1$ . In the sequel, we therefore restrict ourselves to the one-dimensional case, assuming periodic boundary conditions in real space. Existing work on the spinless Holstein model with many electrons is mainly concerned with the formation of an insulating charge-ordered state at half filling (see

Sec. 5.1). The effect of an increase of electron density on the polaronic state has not received much attention in the past, apart from the work by Capone *et al.* [174], who applied ED to study the Holstein-Hubbard model in the large  $U$  limit on a very small cluster of five sites.

In this section we use QMC and the KPM to calculate, in particular, one-particle spectra. As pointed out in previous chapters, ED and QMC both yield unbiased results. In principle, the KPM (Sec. 2.4) allows to obtain exact results for spectral functions with very high energy resolution. However, even for relatively small clusters of ten sites—the size used here—this method requires parallel supercomputers to handle the extremely large Hilbert space (matrix dimension  $\approx 10^8 - 10^{10}$ ). In contrast, the QMC simulations can be performed on personal computers, and for larger clusters. The drawback is that (a) the method is limited to finite temperatures, and (b) the calculation of spectral properties requires the MEM (see Sec. 2.1.6) which limits the energy resolution and often introduces uncontrolled errors. For this reason, we lay considerable stress on a critical examination of the MEM results by confronting them with exact KPM data.

Concerning the QMC simulations, we have mainly used a value of  $\beta t = 8$  for the inverse temperature. For the critical parameters studied below, calculations at even lower temperatures are very demanding due to the sign problem (Sec. 5.3.3), although we shall present results for the density of states at  $\beta t = 10$  and half filling in Fig. 5.9. Already for  $\beta t = 8$  we have  $(\beta t)^{-1} = k_B T/t = 0.125 \lesssim \bar{\omega}$  for the values of  $\bar{\omega} \geq 0.4$  used in the sequel, so that direct thermal excitation of phonons can be expected to be rather unimportant.

For the Trotter decomposition, we chose  $\Delta\tau = 0.1$  for dynamical properties—the larger error being negligible compared to the uncertainties introduced by the MEM inversion—and  $\Delta\tau = 0.05$  for static observables. According to the discussion in Sec. 3.5.3, the Trotter error in the Holstein model becomes important mainly for large phonon frequencies and very strong electron-phonon interaction. Since we do not consider this regime here, the abovementioned values of  $\Delta\tau$  yield satisfactorily small systematic errors. An extrapolation of results to  $\Delta\tau = 0$  similar to Chaps. 3 and 4 has not been performed for several reasons. First, the dynamic properties calculated in imaginary time explicitly depend on the number of time slices, making a scaling to  $\Delta\tau = 0$  impossible. Second, for static observables such as the kinetic energy, the value of  $\Delta\tau$  changes the filling  $n$  even if the chemical potential  $\mu$  is kept the same. Consequently, calculations for different  $\Delta\tau$  would have to be done for different values of  $\mu$ . Besides the significant practical effort, the value of  $n$  cannot be fixed to arbitrary accuracy due to statistical errors, thus rendering a  $\Delta\tau$  extrapolation inconsistent.

Away from half filling, the electron density has to be adjusted to the values of interest by varying the chemical potential. Due to the computational effort associated with this trial-and-error procedure, the actual band filling  $n'$ , say, is usually only very close to a desired value, e.g.,  $n = 0.4$ , but not exactly the same. Furthermore, within the QMC simulations, the filling can only be determined up to a statistical error  $\Delta n'$ , similar to other observables. For the results presented here, the relative deviation  $(n - n')/n$  of the actual value in the QMC simulations from the value  $n$  reported is always smaller than  $5 \times 10^{-3}$ . The same is true for the relative statistical error  $\Delta n'/n$ . Finally, all QMC simulations have been run

on personal computers (e.g., Intel XEON 2000), with CPU times varying between several minutes and a couple of days.

While our method is completely free of autocorrelations between subsequent phonon configurations, results for the imaginary-time Green function at different times are usually not statistically independent.[185] However, in the present case, owing to the exact sampling and the large number of measurements, these correlations are very small and have been neglected since they have negligible influence on the results. An additional, stringent test of the QMC results consists of a comparison to ED data which will be presented in Sec. 5.4.2.

The KPM has been employed to compute the spectral functions

$$\begin{aligned} A^+(k, \epsilon) &= \sum_l |\langle \Psi_{l,k}^{(N_e+1)} | c_{k-q}^\dagger | \Psi_{0,q}^{(N_e)} \rangle|^2 \delta[\epsilon - (E_{l,k}^{(N_e+1)} - E_{0,q}^{(N_e)})], \\ A^-(k, \epsilon) &= \sum_l |\langle \Psi_{l,k}^{(N_e-1)} | c_{q-k} | \Psi_{0,q}^{(N_e)} \rangle|^2 \delta[\epsilon + (E_{l,k}^{(N_e-1)} - E_{0,q}^{(N_e)})], \end{aligned} \quad (5.35)$$

where  $|\Psi_{l,k}^{(N_e)}\rangle$  denotes the  $l$ th eigenstate with  $N_e$  electrons, momentum  $k$  and energy  $E_{l,k}^{(N_e)}$  (see also Secs. 2.3 and 2.4). The cluster size has been fixed at  $N = 10$ , with as many as 12 dynamical phonons and resulting truncation errors  $\Delta(N_{\text{ph}}) < 10^{-6}$  [Eq. (2.48)] of the ground-state energy. Additionally, the convergence with the number of phonons has been monitored by means of the phonon distribution function defined in Eq. (2.49). It is important to point out that such a small number of dynamical phonons only yields accurate results for the parameters considered here if the symmetric phonon mode with  $q = 0$  is separated from the Hamiltonian analytically before the diagonalization [87, 186]. In the present case, this phonon mode—corresponding to a homogeneous shift of the oscillator equilibrium positions—together with that for  $q = \pi$  represents the dominant contribution to phonon excitations, so that the separation is very efficient at reducing the computational effort. The parallel code developed by G. Wellein and H. Fehske was run on six compute nodes of the Hitachi SR8000-F1 of the LRZ Munich using up to about 2.4 GB of memory for the largest matrix dimension  $7.5 \times 10^7$ . The energy resolution of the resulting spectral function with 512 moments has been enhanced by a factor of 8 by the MEM described in Sec. 2.4.

Owing to our interest in materials such as the manganites, we shall mainly consider the adiabatic regime, taking  $\bar{\omega} = 0.4$ . To illustrate the important differences between  $\bar{\omega} \ll 1$  and  $\bar{\omega} \gg 1$ , some results for the nonadiabatic value  $\bar{\omega} = 4$  will also be shown.

### 5.4.1 Limiting cases

As we shall see below, the spectra in the intermediate coupling region turn out to have a fairly complex structure. In order to interpret these results, we therefore begin with the limiting cases of weak and strong electron-phonon coupling.

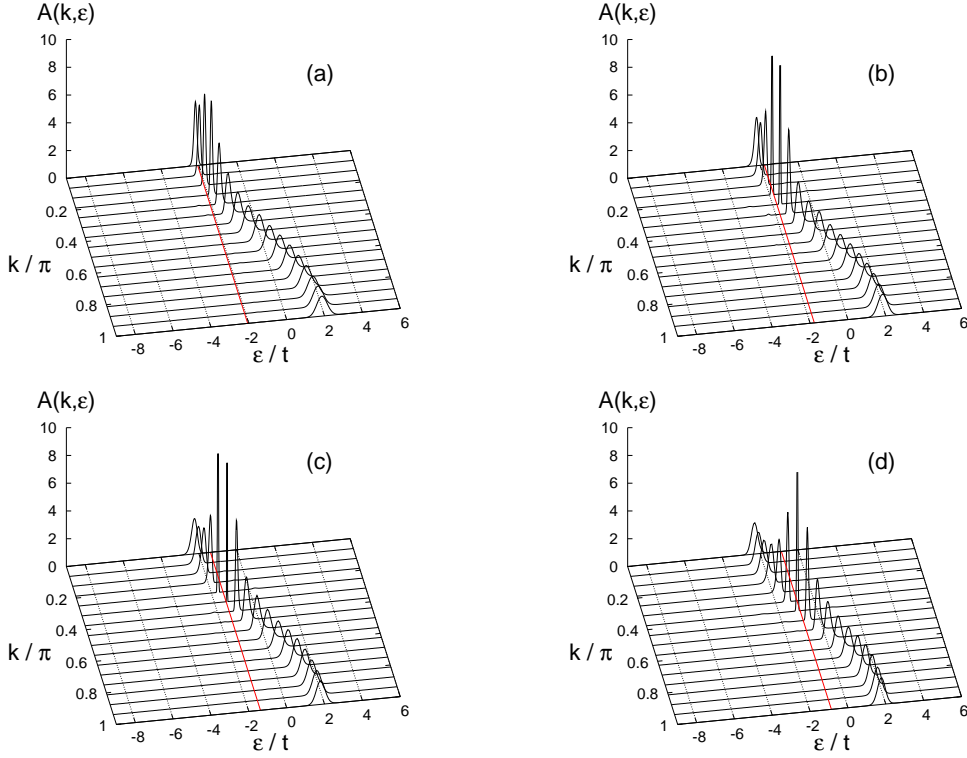


Figure 5.5: One-electron spectral function  $A(k, \epsilon)$  from QMC for weak coupling  $\lambda = 0.1$ ,  $\bar{\omega} = 0.4$ ,  $\beta t = 8$ ,  $N = 32$  and (a)  $n = 0.1$ , (b)  $n = 0.2$ , (c)  $n = 0.3$ , (d)  $n = 0.4$ . Here and in subsequent figures  $\Delta\tau = 0.1$ , and red lines indicate the position of the chemical potential  $\mu$ .

### Weak coupling

For weak coupling  $\lambda = 0.1$ , the sign problem is not severe (Sec. 5.3.3) and the QMC simulations can easily be performed for large lattices with  $N = 32$ , thereby making the dispersion of QP features well visible. As indicated in Eq. (5.30), the MEM inversion yields  $A(\mathbf{k}, \epsilon - \mu)$ . To allow a direct comparison with the ED spectral functions [Eq. (5.35)], the QMC results in Figs. 5.5, 5.7, 5.8 and 5.10 have been shifted by the chemical potential.

Figure 5.5 shows the evolution of the one-electron spectral function  $A(k, \epsilon)$  with increasing electron density  $n$ . At first sight, we see that the spectra bear a close resemblance to the free-electron case, i.e., there is a strongly dispersive band running from  $\epsilon = -2t$  to  $\epsilon = 2t$ . The latter can be attributed to weakly dressed electrons with an effective mass similar to the noninteracting case  $\lambda = 0$ . As expected, the height of the peaks increases significantly in the vicinity of the Fermi momentum  $k_F$ , which is determined by the crossing of the band with the chemical potential (red line).

Since the peaks in Fig. 5.5 are very sharp, it is important to check the results from the inversion with the MEM. To this end, we show in Fig. 5.6 the band dispersion and allowed wavevectors of free electrons for  $N = 32$  and periodic boundary conditions. By computing



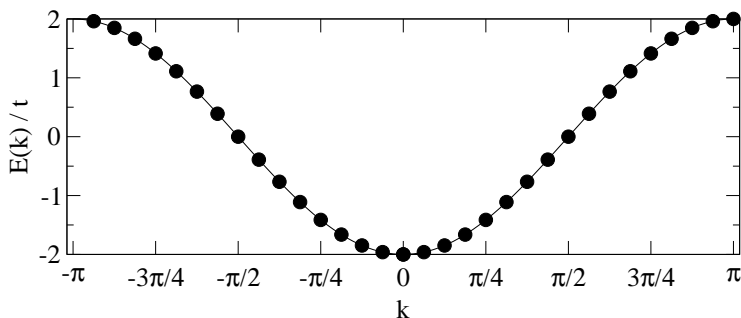


Figure 5.6: Wavevectors (●) and band dispersion of a free-electron system with  $N = 32$ .

the approximate number of electrons corresponding to the fillings of  $n = 0.1 - 0.4$  of the 32-site system, we can roughly determine  $k_F$  from Fig. 5.6. Although the nonzero electron-phonon interaction will affect the band dispersion  $E(k)$ , the weak coupling considered here justifies the use of a rigid band approximation, as reflected by the free-particle character of the spectra in Fig. 5.5.

For  $n = 0.1$ , i.e., about three electrons, the Fermi momentum is expected to lie between  $k = \pi/16$  and  $k = \pi/8$ , which correspond to the second and third curve from the top in Fig. 5.5(a). From Fig. 5.5(a) we see that the largest peaks are those for  $k = \pi/16$  and  $\pi/8$ —having almost the same height. Above and below these momenta, the peaks are noticeably smaller. We ascribe this slight discrepancy to the fact that the MEM becomes less reliable for spectra with extremely sharp peaks. A similar analysis carried out for the other fillings in Figs. 5.5(b)–(d) shows a very good agreement between the location of the highest peaks and the estimated values of  $k_F$ . Finally, we would like to point out that the apparent absence of any phonon signatures in Fig. 5.5 is not a defect of the MEM, but results from the large scale of the  $z$ -axis chosen. As a consequence, the large peaks running close to the bare band dominate the spectra and suppress any small phonon peaks present.

### Strong coupling

We now turn our attention to the opposite limit of the spinless Holstein model, namely the case of strong electron-phonon coupling  $\lambda = 2$ . While many other numerical methods such as, e.g., standard QMC or ED, have difficulties in obtaining accurate results in this regime, the QMC approach used here yields quite accurate results even for large systems. As pointed out in Sec. 3.5.2, this is a consequence of the LF transformation on which the method relies. The latter causes a significant reduction of statistical errors compared to other approaches by separating polaron effects from the free lattice vibrations. The improved statistics in the strong-coupling regime is also reflected in the dependence of the average sign on  $\lambda$  (Fig. 5.3). As before, we study the dependence of the spectral function on the band filling, again for  $N = 32$ . The results are depicted in Fig. 5.7.

In the low-density regime  $n = 0.1$  [Fig. 5.7(a)], the spectrum consists of two separate features located above and below the chemical potential, respectively. Of course there

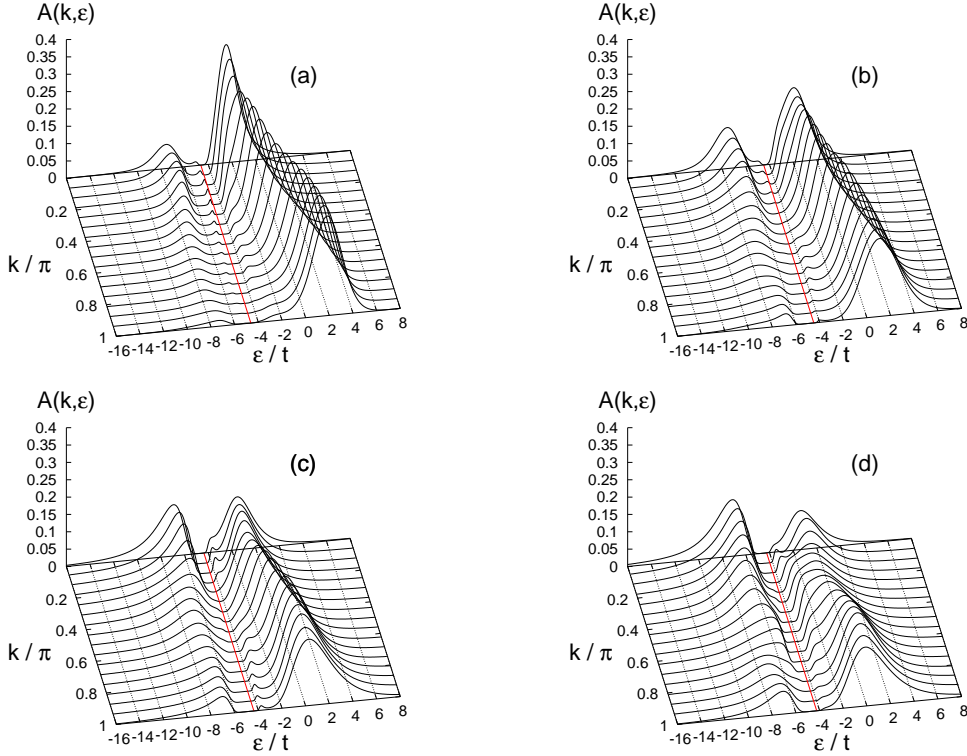


Figure 5.7: One-electron spectral function  $A(k, \epsilon)$  from QMC for strong coupling  $\lambda = 2.0$ ,  $\bar{w} = 0.4$ ,  $\beta t = 8$ ,  $N = 32$  and (a)  $n = 0.1$ , (b)  $n = 0.2$ , (c)  $n = 0.3$ , (d)  $n = 0.4$ .

is a free-electron like incoherent feature with bandwidth  $\approx 4t$ . However, we also find a polaron band at lower energies which is almost flat throughout  $k$  space and has relatively little spectral weight. Moreover, its energy difference relative to  $\mu$  is roughly given by the polaron binding energy ( $E_P = 4t$  for the parameters considered here). Furthermore, we can see that the chemical potential, which roughly lies at the center between the upper and the lower band, shifts downward with increasing coupling, as reflected by the condition  $\mu = -E_P$  for half filling [cf. Eq. (5.7)].

With increasing band filling, the two features mix strongly, and for  $n = 0.4$ , no clear distinction between the coherent and incoherent parts of the spectrum can be made. Finally, the spectrum in Fig. 5.7(d) is almost symmetric with respect to the chemical potential, and already reveals the gapped structure due to CDW-formation at  $n = 0.5$ . The latter point will be discussed in more detail below.

It is interesting to compare the results of this section to those of Sec. 5.2, which are also for strong coupling. Before we comment on the structure of the spectral function, we would like to point out that the coupling constant  $\lambda$  takes on different values in the CPA/SCPT calculations ( $\lambda = 0.8$ ). However, we have to keep in mind that the results of Sec. 5.2 are for two dimensions and  $\bar{w} = 0.2$ . In one dimension, for  $n = 0.5$ ,  $\bar{w} = 0.4$  and  $\lambda = 2$ , the SCPT based on the atomic limit yields a spectrum which bears a close resemblance to

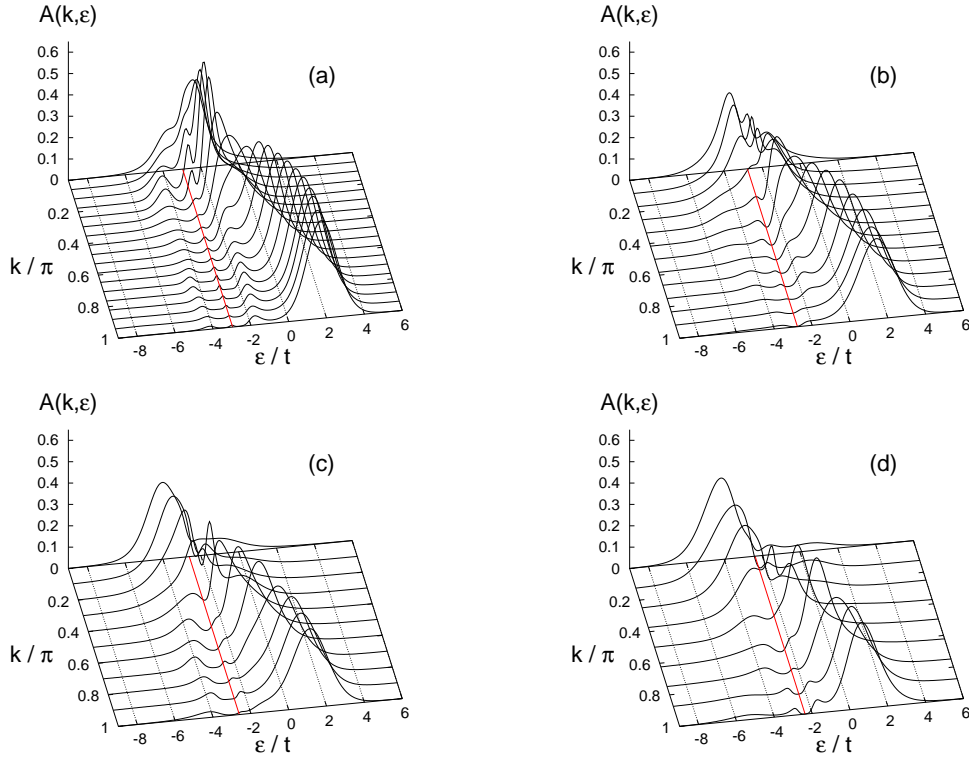


Figure 5.8: One-electron spectral function  $A(k, \epsilon)$  from QMC for intermediate coupling  $\lambda = 1.0$ ,  $\bar{\omega} = 0.4$ ,  $\beta t = 8$ , and (a)  $n = 0.1$ ,  $N = 32$ , (b)  $n = 0.2$ ,  $N = 24$ , (c)  $n = 0.3$ ,  $N = 20$ , (d)  $n = 0.4$ ,  $N = 16$ .

Fig. 5.7(d). In particular, the large low-energy peak never approaches closely the Fermi level, indicating the existence of a pseudogap centered at  $\mu$ . Finally, whereas CDW order becomes important in the QMC results as we approach half filling, the pseudogap in the CPA/SCPT exclusively arises from the polaronic state at strong coupling (Sec. 5.2).

## 5.4.2 Intermediate coupling

As discussed in the introduction, a cross over from a polaronic state to a system with weakly dressed electrons can be expected in the intermediate coupling regime. Here we choose  $\lambda = 1$ , which corresponds to the critical value for the small-polaron cross over in the one-electron problem (Chap. 3).

We first discuss the QMC results. Owing to the sign problem, which is particularly noticeable for  $\lambda = 1$  (Fig. 5.3), we have to decrease the system size as we increase the electron density  $n$ . To scrutinize the accuracy of the MEM inversion, we shall compare the QMC results with ED data. The latter will also yield a more detailed understanding of the spectra.

## QMC

Figure 5.8 shows the spectral function for  $\lambda = 1$  and increasing band filling. We again start with the low-density case  $n = 0.1$  [Fig. 5.8(a)]. Compared to the spectral function for  $\lambda = 2$  [Fig. 5.7(a)], we notice that the low-energy polaron band lies much closer to the incoherent band. Moreover, even for  $n = 0.1$ , there is a mixing of these two parts of the spectrum at small values of  $k$ . As for  $\lambda = 2$ , with increasing density, the polaron band merges with the incoherent peaks at higher energies. This is exactly the density-driven cross over from a polaronic to a metallic state anticipated above. At  $n = 0.4$ , we find a band with large effective width ranging from  $\epsilon \approx -4t$  to  $\epsilon \approx 2t$ .

At this point, we would like to mention the exact relation [187]

$$M_1(k) = \int_{-\infty}^{\infty} d\epsilon \epsilon A(k, \epsilon) = \varepsilon_{\mathbf{k}} - \mu - 2E_{\text{P}}n \quad (5.36)$$

for the first moment of the one-particle spectral function of the spinless Holstein model, with  $\varepsilon_{\mathbf{k}} = -2t \cos k$ .

While the zeroth moment is identical to the normalization of  $A(k, \epsilon)$  for each  $k$ ,  $M_1(k)$  depends in a nontrivial way on the parameters of the system. In principle, Eq. (5.36) may be used as a boundary condition in the MEM.[188] However, in the present case, we have found that while the normalization is virtually exact for all results shown, the first moment deviates from the exact values. Moreover, the use of the exact values for  $M_1$  as a condition in the inversion causes the MEM not to converge for some parameters. Additional calculations on small systems reveal that this disagreement results from the finite Trotter error, despite the relatively small value  $\Delta\tau = 0.1$  used. Away from parameters such that  $M_1 \approx 0$ ,  $M_1$  as determined from the MEM spectra deviates from the exact values by maximally 10–20 percent. Nevertheless, the peak positions and weights in the spectra shown are fairly accurate, as illustrated by the comparison with ED below. Finally, we would like to point out that calculations of  $A(k, \epsilon)$  for  $\Delta\tau < 0.1$  become very time-consuming due to the increasing requirement in disk space and longer simulation times.

Further information about the density-dependence can be obtained from the one-electron density of states (DOS)  $N(\epsilon - \mu)$  given by Eq. (5.33). The latter is presented in Fig. 5.9 for different fillings  $n = 0.1 - 0.5$ . As in Fig. 5.8, the cluster size is reduced with increasing  $n$  in order to cope with the sign problem. To reveal the influence of finite-size effects, Fig. 5.9 also contains results for  $N = 10$ .

At  $n = 0.1$ , the DOS for  $N = 32$  displays a peak at the chemical potential, while such a feature is absent for  $N = 10$ . To understand this behavior, we again resort to the rigid band approximation, although the rather strong coupling in the present case only allows qualitative conclusions. According to Fig. 5.6, for a cluster with  $N = 32$  and filling  $n = 0.1$ , the three lowest-lying energy levels are completely filled, and states with zero energy are still available leading to a large DOS at  $\epsilon = \mu$ . In contrast, for  $N = 10$ , we have a “closed-shell” configuration, i.e., a finite energy is required to add an electron, in agreement with Fig. 5.9. The features above and below  $\mu$  correspond to electronic excitations and become sharper as we increase  $N$  from 10 to 32.

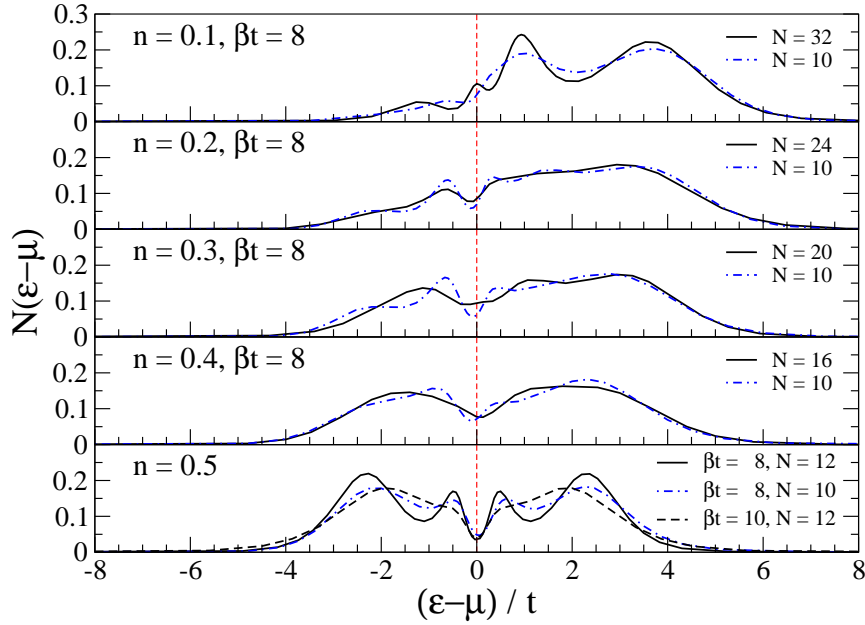


Figure 5.9: One-electron density of states  $N(\epsilon - \mu)$  from QMC for different band fillings  $n$ ,  $\bar{w} = 0.4$  and  $\lambda = 1.0$ .

When the density is increased to  $n = 0.2$ , the DOS at the chemical potential is noticeably reduced, which may again be attributed to an almost full shell for  $N = 24$ . Clearly, such effects are absent in the case of an infinite system, for which the energy levels lie dense in momentum space. The DOS contains two humps situated above and below  $\mu$ . In contrast to  $n = 0.1$ , the smaller structures in the DOS become slightly washed out for  $N = 24$  as compared to  $N = 10$ .

As we increase  $n$  further, a gap begins to form at  $\mu$ , which is a precursor of the CDW gap at half filling. Similar to  $n = 0.2$ , the relatively sharp peaks present for  $N = 10$  evolve into rather broad features for larger system sizes. For  $n = 0.4$ , the spectral weight above and below the chemical potential is already very similar.

Finally, in the case of half filling  $n = 0.5$ , the DOS has become symmetric with respect to  $\mu$ . There are two maxima situated at about  $\pm E_P$  ( $E_P = 2$  for the parameters here). The gap of size  $\sim \lambda$  expected for the insulating charge-ordered state at  $T = 0$  is partially filled in due to the finite temperature considered here. Furthermore, we find additional features separated from  $\mu$  by the bare phonon frequency  $\omega$ , whose height decreases with decreasing temperature, as revealed by the results for  $\beta t = 10$  (Fig. 5.9). These peaks—not present at  $T = 0$  [186]—arise from thermally activated transitions to states with an additional phonon excited.

Despite the wealth of information contained in the QMC results presented so far, it is obvious that an interpretation of the various peaks is far from being easy. In particular, the QMC method does not allow to separately calculate the photoemission and inverse photoemission parts  $A^-$  and  $A^+$  [Eq. (5.35)], respectively. Moreover, the finite temperature

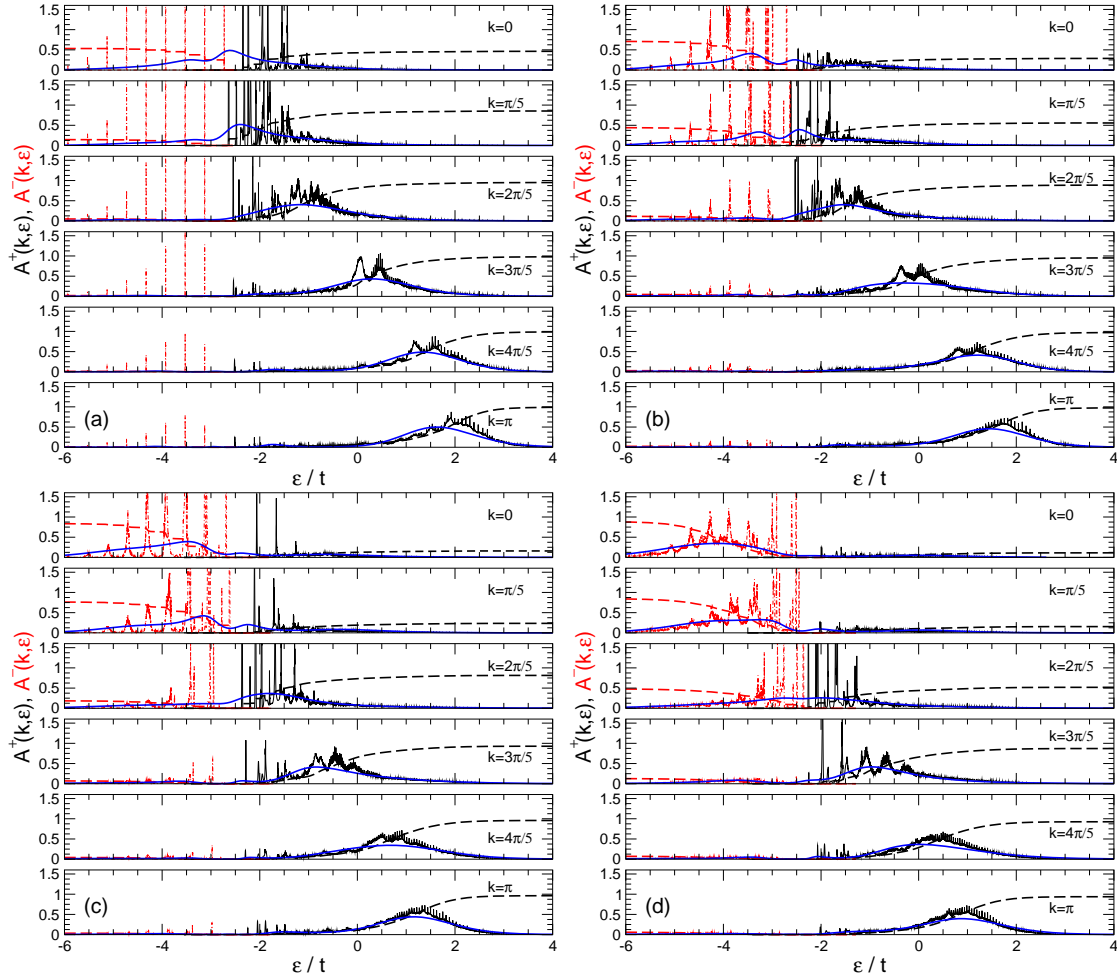


Figure 5.10: One-electron spectral functions  $A^-(k, \epsilon)$  (dot-dashed red lines) and  $A^+(k, \epsilon)$  (solid black lines) from ED for intermediate coupling  $\lambda = 1.0$ ,  $\bar{w} = 0.4$ ,  $N = 10$  and (a)  $n = 0.1$ , (b)  $n = 0.2$ , (c)  $n = 0.3$ , (d)  $n = 0.4$ . Also shown are the integrated spectral weights of  $A^-$  and  $A^+$  (red and black dashed lines), as well as  $A(k, \epsilon)$  from QMC for  $N = 10$  and  $\beta t = 8$  (solid blue lines).

and the use of the MEM limits the energy resolution and introduces uncertainties concerning the positions and weights of structures in the spectra. These circumstances make it difficult, e.g., to distinguish between phononic and electronic contributions, especially if  $\lambda \approx \bar{w}$ . To gain further insight, we therefore supplement the QMC data with ED results.

## ED and QMC

In order to overcome the abovementioned limitations of QMC, here we use the KPM, as described in Sec. 2.4, to calculate the one-particle spectral functions defined by Eq. (5.35). To test the quality of the QMC spectra, we directly compare the two methods, keeping

in mind that the QMC calculations have been performed at a finite temperature  $\beta t = 8$ , whereas ED yields ground-state results.

Figure 5.10 displays the ED results for the same parameters as in Fig. 5.8, i.e.,  $\bar{\omega} = 0.4$ ,  $\lambda = 1$  and  $n = 0.1 - 0.4$ . The red dot-dashed lines correspond to the photoemission part  $A^-$ , while the black solid lines correspond to the inverse photoemission part  $A^+$ . Additionally shown are the integrated spectral weights of  $A^-$  and  $A^+$  (red and black dashed lines). Finally, the solid thick blue lines represent QMC results for the same system size and  $\beta t = 8$ . The values for  $n$  are given in the caption.

We see from Fig. 5.10 that the QMC results are in a very good agreement with the ED data. Due to the finite temperature and the smearing of the MEM, the QMC data represent an envelope of the sharp ED peaks. In addition to the possibility of distinguishing between  $A^+$  and  $A^-$ —crucial for an identification of polaron bands at intermediate coupling—the greater energy resolution of ED also allows to resolve signatures of phonon excitations.

Starting with the case  $n = 0.1$  [Fig. 5.10(a)], we notice that there is a polaron band at the Fermi level, excitations to/from which are given by the highest peak of  $A^-$  and the lowest peak of  $A^+$ , respectively. The photoemission part  $A^-$  reflects the Poisson-like phonon distribution of the one-electron ground state ( $n = 0.1$  and  $N = 10$ ). The integrated spectral weight (dashed lines) gives a measure for the weight of the various poles in the one-electron spectrum. For example, it reveals that the phonon peaks in  $A^-$  have very little weight. In fact, the integrated weight jumps to a finite value at the first peaks near the Fermi level for  $k = 0$  and  $k = \pi/5$ , while it changes very little as one moves further down in energy. For  $k > \pi/5$ , the small spectral weight contained in  $A^-$  is continuously distributed among the phonon peaks.

We also observe the well-known flattening of the polaron band at large values of  $k$ . Similar to the one-electron case discussed in Sec. 3.2, the low-energy states have mostly electronic character at small  $k$ , and become mostly phononic at large values of  $k$ . While this effect is expected to occur in the low-density regime, we find that it persists even for  $n = 0.4$  [Fig. 5.10(d)]. Moreover, Fig. 5.10 reveals that the maximum in the incoherent contribution follows closely the free-electron dispersion for all densities  $n = 0.1 - 0.4$ .

With increasing electron density, the equally spaced peaks in  $A^-$  broaden significantly, until at  $n = 0.4$  they have merged to form a broad band. The polaron band is still visible at  $n = 0.2$  [Fig. 5.10(b)], but becomes indistinguishable from the incoherent excitations at even larger  $n$ . Eventually, at  $n = 0.4$  [Fig. 5.10(d)], we find an almost symmetric behavior of  $A^+$  and  $A^-$  with respect to the Fermi level at  $k = 2\pi/5$ . This indicates the metallic character of the system expected for large polaron densities and intermediate electron-phonon coupling.

### 5.4.3 Nonadiabatic regime

Until here, we have only presented results for the adiabatic case  $\bar{\omega} = 0.4$ . Although the latter is most relevant for strongly correlated materials, it is interesting to compare the above findings to the nonadiabatic strong-coupling regime. To this end, we chose  $\bar{\omega} = 4$  as well as  $\lambda = 2$ . As discussed in Sec. 3.1, the condition for a small polaron in this case

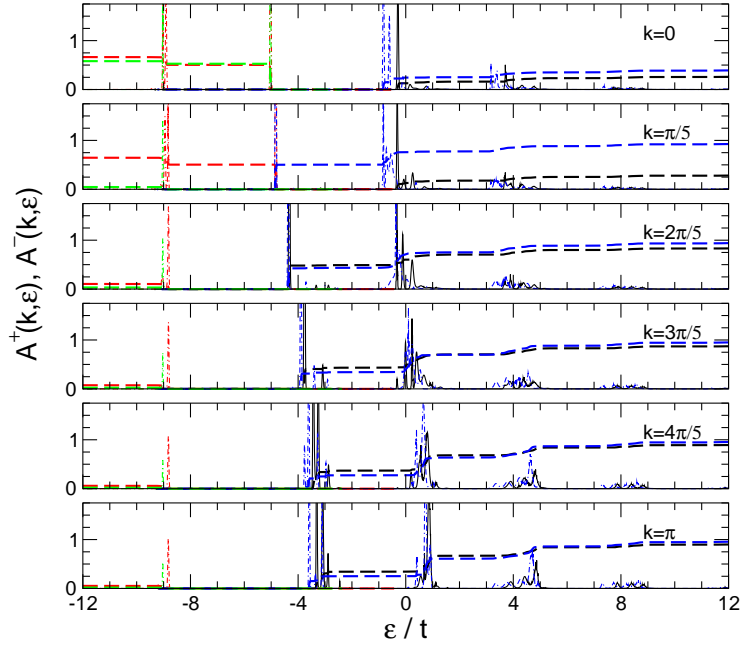


Figure 5.11: One-electron spectral functions  $A^-(k, \epsilon)$  (dot-dashed lines) and  $A^+(k, \epsilon)$  (solid lines) from ED for  $\lambda = 2.0$ ,  $\bar{\omega} = 4.0$ ,  $N = 10$ . Here  $n = 0.1$  (red and black lines) and  $n = 0.3$  (green and blue lines). Dashed lines correspond to the integrated spectral weight of  $A^-(k, \epsilon)$  (red and green lines) and  $A^+(k, \epsilon)$  (black and blue lines).

is  $\sqrt{E_P/\omega} > 1$ , which expresses the fact that a large enough lattice distortion is required to trap an electron. This is in contrast to the criterion  $\lambda > 1$  in the adiabatic regime, which is purely based on the balance of kinetic and potential energy. Since these energies are expected to undergo noticeable changes as the particle density varies, small-polaron formation for  $\bar{\omega} < 1$  should significantly depend on  $n$ , in agreement with the results of Sec. 5.4.2.

The spectral function for  $n = 0.1$  and  $n = 0.3$  is displayed in Fig. 5.11. The most striking difference to the case  $\bar{\omega} = 0.4$  considered above is that the bands in the spectrum are now separated by the phonon energy  $\omega$ , with their width being determined by the electronic excitations. This is the opposite of the adiabatic regime, in which the bands correspond to electronic excitations surrounded by phononic satellites.

A comparison of the spectral functions for  $n = 0.1$  and  $n = 0.3$  in Fig. 5.11 indicates that there is no density-driven cross over of the system as observed in the adiabatic case. Since for the parameters considered here  $E_P/\omega = 1$ , virtually noninteracting small polarons are formed also at finite electron densities, in accordance with the findings of Capone *et al.* [174].



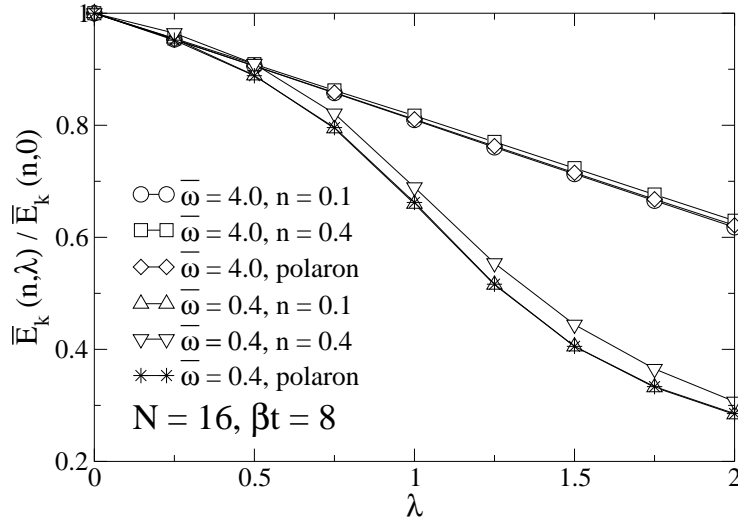


Figure 5.12: Normalized kinetic energy as a function of electron-phonon coupling  $\lambda$  for different band fillings  $n$  and adiabatic ratios  $\bar{\omega}$ . Also shown are the results for a single polaron. Errorbars are smaller than the symbols used and  $\Delta\tau = 0.05$ .

#### 5.4.4 Kinetic energy

The electronic kinetic energy has been studied extensively in the past to identify the polaron and bipolaron cross over discussed in Chaps. 3 and 4, respectively. It is therefore interesting to see if the density-driven changes of the one-particle spectrum also manifest themselves in the kinetic energy defined by Eq. (5.24). In order to be able to compare different band fillings, we consider the normalized quantity  $\bar{E}_k(n, \lambda)/\bar{E}_k(n, 0)$ , which is shown in Fig. 5.12 as a function of electron-phonon coupling for different fillings and phonon frequencies.

We begin with the nonadiabatic regime ( $\bar{\omega} = 4$ ). Obviously, the results for  $n = 0.1$  and  $n = 0.4$  are very similar, with slightly larger values of the kinetic energy for  $n = 0.4$ . In addition to these two fillings, we have also included in Fig. 5.12 the result for a single polaron with the same parameters. Remarkably, the corresponding curve is indistinguishable from the result for  $n = 0.1$ , calculated with the QMC method of Chap. 3. In total, this underlines the conclusion drawn above that in the nonadiabatic regime the band filling does not significantly affect the properties of the system.

A noticeably different behavior is found for  $\bar{\omega} = 0.4$ . Similar to the one-electron problem (Sec. 3.5.3), the decrease of the kinetic energy with increasing electron-phonon coupling is much stronger than for  $\bar{\omega} = 4$ . Nevertheless, translational symmetry is not broken so that the cross over does not represent a phase transition [118]. While the low-density result  $n = 0.1$  is again virtually identical to that of a single polaron, there is a well-conceivable change as we go from  $n = 0.1$  to  $n = 0.4$ . For the same value of  $\lambda$ , the kinetic energy is larger for  $n = 0.4$  than for  $n = 0.1$  as a result of the polaron-polaron interaction which leads to an effective, weaker electron-lattice coupling. Finally, despite the fact that there is a visible change between low and high densities in Fig. 5.12, it is obvious that  $\bar{E}_k$  does

by far not contain as much information as the one-particle spectra considered above. This is not surprising if we recall that the kinetic energy can be obtained by integrating the product of the spectral function and the band energy  $\varepsilon_{\mathbf{k}}$  up to the chemical potential and summing over all  $k$  [9].

## 5.5 Conclusions

Theoretical considerations [3] as well as recent experimental work [165] suggest that the charge carriers in the manganites are large and small polarons, depending on the specific material and temperature. The one-dimensional spinless Holstein model represents a generic model which exhibits a cross over from large to small polarons with increasing electron-phonon coupling. Owing to the complexity of the problem in the adiabatic regime, the many-electron case cannot be accurately described by analytical methods, and also represents a challenge to present-day numerical techniques. In this chapter, this model has been studied using both analytical and numerical methods.

In the strong-coupling regime, CPT together with the exact atomic-limit Green function yields a surprisingly good agreement with the spectrum from the many-body CPA.

To address the regime of small phonon frequencies and intermediate to strong electron-phonon interaction, we have extended the one-electron QMC method of Chap. 3 to the many-electron case. The new approach, which is similar to the determinant method of Blankenbecler *et al.* [124], overcomes the problem of autocorrelations at the expense of a sign problem. Compared to existing algorithms, it enables us to perform significantly more accurate simulations in the most difficult adiabatic regime.

Using the improved QMC method as well as the KPM, we have calculated the one-particle spectral function, the density of states and the kinetic energy at different band fillings. While the KPM is restricted to relatively small clusters, QMC can be used to study larger cluster at finite temperatures but limits the energy resolution of dynamical quantities. The reliability of the results from the maximum entropy inversion is scrutinized by a direct comparison with exact data. In the adiabatic case, we observe a carrier density-driven cross over from a polaronic state to a metallic system at intermediate electron-phonon coupling. In contrast, for large phonon frequencies and strong coupling, the individual polarons remain virtually unaffected upon increasing the electron density. Our results underline the shortcomings of single-polaron theory to describe strongly correlated systems such as the manganites.

## Summary

The challenging problem of strongly correlated electron-phonon models with a coupling term of the Holstein type has been addressed using, in particular, unbiased numerical techniques. While a large part of this work was concerned with the cases of one and two electrons, we also presented results for finite carrier densities characteristic for many interesting materials.

A novel quantum Monte Carlo (QMC) method has been developed which overcomes the problem of strong autocorrelations usually inherent to simulations of electron-phonon models, especially for finite band filling. To separate polaron effects from the zero-point and thermal fluctuations of the lattice, we chose as the starting point the Hamiltonian obtained by the canonical Lang-Firsov transformation. In combination with a reweighting of the probability distribution, the Monte Carlo sampling can be performed exactly in terms of principal components. For the spinless Holstein model with many electrons considered here, the method is quite similar to the standard determinant approach. Phase factors in the electron hopping term arising from the transformation cause a minus-sign problem. For one and two electrons, the latter diminishes with increasing system size, while an exponential reduction of the average sign is found in the grand-canonical version of the algorithm. Nevertheless, accurate calculations have been carried out for the most difficult parameters of small phonon frequencies and intermediate to strong electron-phonon coupling in the low-temperature regime.

Cluster perturbation theory (CPT) in combination with the Lanczos recursion method has been successfully applied for the first time to electron-phonon models. Similar to previous work on the Hubbard and the  $t$ - $J$  model, this method enabled us to compute accurate one-particle spectra at continuous wavevectors and with strongly reduced finite-size effects.

An understanding of polaron formation and its dependence on the phonon frequency can be attained by investigating the Holstein model with one electron. Owing to the absence of any autocorrelations, the QMC method allows to span the whole range of the phonon frequency and the electron-phonon coupling. Furthermore, a simple variational approach, which is based on an extended Lang-Firsov transformation has been shown to represent a significant improvement of the widely used zero-phonon, strong-coupling approximation. Finally, the cross over from a large to a small polaron also manifests itself in the one-particle spectrum, which has been calculated using CPT.

The next rung up the ladder of complexity is the case of two electrons, which may form bound bipolaron states depending on the relative strength of the phonon-mediated, attractive interaction and the Coulomb repulsion. The corresponding Holstein-Hubbard model is by far not as well understood as the one-electron case. Again using QMC, we

---

have presented results in one dimension for the adiabatic regime into which many strongly correlated materials fall. In addition to an investigation of the cross over from an onsite to an intersite bipolaron state with increasing Hubbard repulsion, the intersite bipolaron has been found to dissociate at high temperatures. A similar mechanism has been proposed to explain the thermally activated conductivity of the paramagnetic phase of some manganites. Ground-state results on large clusters have been obtained by a variational method similar to the one-electron problem. Remarkably, the latter approach is able to account qualitatively for retardation effects. The one-particle spectral function of the Holstein-Hubbard bipolaron, calculated for the first time by using CPT, displays bands associated to polaron and bipolaron states, whose form, position and spectral weight change upon variation of the parameters. Due to the large Hilbert space, results could only be obtained in one dimension, and for intermediate to large phonon frequencies. We have also found a pronounced deviation of the bipolaron band dispersion from a simple cosine band for parameters favoring a weakly bound bipolaron state, which can be attributed to next-nearest-neighbor hopping processes.

Although the results for one and two electrons may be related to, e.g., dilute semiconductors or doped insulators, many fascinating materials such as the manganites have high carrier densities. Therefore, we set out to understand the effects of polaron-polaron interaction by considering the spinless Holstein model in one dimension. Employing QMC and exact diagonalization, we have studied the cross over from low to high densities at weak, intermediate and strong electron-phonon coupling by computing the one-electron spectrum. For small phonon frequencies and intermediate coupling, the system exhibits a density-driven change from a polaronic state to a metallic state with increased kinetic energy, caused by the dissociation of individual large polarons due to their mutual interaction. In contrast, such changes are completely absent in the nonadiabatic, strong-coupling regime, where the polarons are small and do not overlap.

To end with, we would like to mention two interesting perspectives opened up by this work. First, the successful application of CPT to electron-phonon problems may be substantially expanded by employing parallelized exact diagonalization methods. Thereby, it will be possible to study the adiabatic regime, higher dimensions and even the many-electron case. Second, the QMC approach also allows to calculate transport properties such as the optical conductivity, for which a wealth of experimental data on the manganites is available. Owing to the lack of unbiased theoretical results for high electron densities, their interpretation is still under debate.

# Bibliography

- [1] J. Mehra, *The beat of a different drum* (Oxford University Press, Oxford, UK, 1994).
- [2] *Lattice Effects in High Temperature Superconductors*, edited by Y. Bar-Yam, J. Mustre de Leon, and A. R. Bishop (World Scientific, Singapore, 1992).
- [3] D. M. Edwards, *Adv. Phys.* **51**, 1259 (2002).
- [4] M. Aichhorn *et al.*, *Phys. Rev. B* **69**, 245108 (2004).
- [5] O. Gunnarsson, V. Meden, and K. Schönhammer, *Phys. Rev. B* **50**, 10 462 (1994).
- [6] V. Meden, K. Schönhammer, and O. Gunnarsson, *Phys. Rev. B* **50**, 11 179 (1994).
- [7] H. Sumi, *J. Phys. Soc. Jpn.* **36**, 770 (1974).
- [8] S. Ciuchi, F. de Pasquale, S. Fratini, and D. Feinberg, *Phys. Rev. B* **56**, 4494 (1997).
- [9] G. D. Mahan, *Many-Particle Physics*, 2nd ed. (Plenum Press, New York, 1990).
- [10] W. von der Linden, *Phys. Rep.* **220**, 53 (1992).
- [11] D. Sénéchal, D. Perez, and M. Pioro-Ladrière, *Phys. Rev. Lett.* **84**, 522 (2000).
- [12] D. Sénéchal, D. Perez, and D. Plouffe, *Phys. Rev. B* **66**, 075129 (2002).
- [13] B. K. Chakraverty, J. Ranninger, and D. Feinberg, *Phys. Rev. Lett.* **81**, 433 (1998).
- [14] B. K. Chakraverty, J. Ranninger, and D. Feinberg, *Phys. Rev. Lett.* **82**, 2621 (1999).
- [15] A. S. Alexandrov and A. M. Bratkovsky, *Phys. Rev. Lett.* **82**, 141 (1999).
- [16] G. H. Jonker and J. H. V. Santen, *Physica* **16**, 337 (1950).
- [17] J. H. Van Santen and G. H. Jonker, *Physica* **16**, 599 (1950).
- [18] J. M. D. Coey, M. Viret, and S. von Molnár, *Adv. Phys.* **48**, 167 (1999).
- [19] S. Satpathy, Z. S. Popović, and F. R. Vukajlović, *Phys. Rev. Lett.* **76**, 960 (1996).
- [20] C. Zener, *Phys. Rev.* **82**, 403 (1951).

- [21] Y. Tomioka *et al.*, Phys. Rev. B **53**, R1689 (1996).
- [22] P. Schiffer, A. P. Ramirez, W. Bao, and S.-W. Cheong, Phys. Rev. Lett. **75**, 3336 (1995).
- [23] A. Urushibara *et al.*, Phys. Rev. B **51**, 14103 (1995).
- [24] D. N. McIlroy *et al.*, Phys. Rev. B **54**, 17438 (1996).
- [25] A. C. M. Green, Phys. Rev. B **63**, 205110 (2001).
- [26] A. P. Ramirez, J. Phys.: Condens. Matter **9**, 8171 (1997).
- [27] R. Joynt, Science **284**, 777 (1999).
- [28] <http://www.physics.bc.edu/arpes/arpes.htm>.
- [29] K. Yodida, *Theory of Magnetism* (Springer-Verlag, Berlin Heidelberg New York, 1998).
- [30] P. B. Allen and V. Perebeinos, Phys. Rev. B **60**, 10 747 (1999).
- [31] H. Fröhlich, H. Pelzer, and S. Zienau, Philos. Mag. **41**, 221 (1950).
- [32] W. P. Su, J. R. Schrieffer, and A. J. Heeger, Phys. Rev. Lett. **42**, 1698 (1979).
- [33] A. Weiße and H. Fehske, Eur. Phys. J. B **30**, 487 (2002).
- [34] S. El Shawish, J. Bonča, L. C. Ku, and S. A. Trugman, Phys. Rev. B **67**, 014301 (2003).
- [35] P. Benedetti and R. Zeyher, Phys. Rev. B **59**, 9923 (1999).
- [36] J. A. Vergés, V. Martín-Mayor, and L. Brey, Phys. Rev. Lett. **88**, 136401 (2002).
- [37] A. J. Millis, R. Mueller, and B. I. Shraiman, Phys. Rev. B **54**, 5405 (1996).
- [38] J. Zang, A. R. Bishop, and H. Röder, Phys. Rev. B **53**, R8840 (1996).
- [39] T. Hotta, A. L. Malvezzi, and E. Dagotto, Phys. Rev. B **62**, 14 (2000).
- [40] H. Röder, J. Zang, and A. R. Bishop, Phys. Rev. Lett. **76**, 1356 (1996).
- [41] K. Held and D. Vollhardt, Phys. Rev. Lett. **84**, 5168 (2000).
- [42] N. W. Ashcroft and N. D. Mermin, *Solid State Physics* (Saunders College Publishing, Orlando, Florida, 1976).
- [43] A. J. Millis, R. Mueller, and B. I. Shraiman, Phys. Rev. B **54**, 5389 (1996).

- 
- [44] A. J. Millis, P. B. Littlewood, and B. I. Shraiman, *Phys. Rev. Lett.* **74**, 5144 (1995).
- [45] M. Hohenadler and D. M. Edwards, *J. Phys.: Condens. Matter* **14**, 2547 (2002).
- [46] T. Holstein, *Ann. Phys. (N.Y.)* **8**, 325; **8**, 343 (1959).
- [47] I. G. Lang and Y. A. Firsov, *Zh. Eksp. Teor. Fiz.* **43**, 1843 (1962), [*Sov. Phys. JETP* **16**, 1301 (1962)].
- [48] T. Maier, M. Jarrell, T. Pruschke, and M. Hettler, cond-mat/0404055 (unpublished).
- [49] D. P. Landau and K. Binder, *Monte Carlo Simulations in Statistical Physics* (Cambridge University Press, Cambridge, UK, 2000).
- [50] R. P. Feynman and A. R. Hibbs, *Quantum Mechanics and Path Integrals* (McGraw-Hill Book Company, New York, 1965).
- [51] J. W. Negele and H. Orland, *Quantum Many-Particle Systems* (Perseus Books, Reading, Massachusetts, 1998).
- [52] N. Metropolis, A. Rosenbluth, A. Teller, and E. Teller, *J. Chem. Phys.* **21**, 1087 (1953).
- [53] H. G. Evertz, *Adv. Phys.* **52**, 1 (2003).
- [54] W. Janke, in *Quantum Simulations of Complex Many-Body Systems: From Theory to Algorithms*, Vol. 10 of *NIC series*, edited by J. Grotendorst, D. Marx, and A. Muramatsu (John von Neumann Institute for Computing, Jülich, 2002), pp. 423–445.
- [55] A. C. Davison and D. V. Hinkley, *Bootstrap Methods and their Application* (Cambridge University Press, Cambridge, UK, 1997).
- [56] M. Jarrell, <http://www.physics.uc.edu/~jarrell> (unpublished).
- [57] W. H. Press, *Numerical Recipes in Fortran 77*, <http://www.numrec.com>.
- [58] J. Skilling, in *Maximum Entropy and Bayesian Methods*, edited by J. Skilling (Kluwer Academic, Dordrecht, 1989), p. 45.
- [59] W. von der Linden, R. Preuss, and V. Dose, in *Maximum Entropy and Bayesian Methods*, edited by W. von der Linden, V. Dose, R. Fischer, and R. Preuss (Kluwer Academic Publishers, Dordrecht, 1999).
- [60] C. Gros and R. Valentí, *Phys. Rev. B* **48**, 418 (1993).
- [61] C. Dahnken, E. Arrigoni, and W. Hanke, *J. Low. Temp. Phys.* **126**, 949 (2002).
- [62] D. Sénéchal and A. Tremblay, *Phys. Rev. Lett.* **92**, 126401 (2004).

- [63] M. Aichhorn, H. G. Evertz, W. von der Linden, and M. Potthoff, cond-mat/0402580 (unpublished).
- [64] M. G. Zacher, R. Eder, E. Arrigoni, and W. Hanke, Phys. Rev. Lett. **85**, 2585 (2000).
- [65] M. G. Zacher, R. Eder, E. Arrigoni, and W. Hanke, Phys. Rev. B **65**, 045109 (2002).
- [66] D. Sénéchal, *A cluster method for spectral properties of correlated electrons*, The 17th Annual International Symposium on High Performance Computing Systems and Applications, 2003.
- [67] J. Hubbard, Proc. R. Soc. London **276**, 238 (1963).
- [68] M. Aichhorn, M. Daghofer, H. G. Evertz, and W. von der Linden, Phys. Rev. B **67**, R161103 (2003).
- [69] M. Potthoff, M. Aichhorn, and C. Dahnken, Phys. Rev. Lett. **91**, 206402 (2003).
- [70] J. K. Cullum and R. A. Willoughby, *Lanczos Algorithms for Large Symmetric Eigenvalue Computations* (Birkhäuser, Boston, 1985), Vol. I & II.
- [71] B. Bäuml, G. Wellein, and H. Fehske, Phys. Rev. B **58**, 3663 (1998).
- [72] F. Marsiglio, Phys. Lett. A **180**, 280 (1993).
- [73] B. W. Gnedenko, *Lehrbuch der Wahrscheinlichkeitstheorie* (Verlag Harri Deutsch, Frankfurt, 1997).
- [74] R. N. Silver and H. Röder, Int. J. Mod. Phys. C **5**, 935 (1994).
- [75] R. N. Silver and H. Röder, Phys. Rev. E **56**, 4822 (1997).
- [76] R. N. Silver, H. Röder, A. F. Voter, and J. D. Kress, Int. J. Mod. Phys. C **124**, 115 (1996).
- [77] L. D. Landau, Phys. Z. Sowjetunion **3**, 644 (1933).
- [78] A. S. Alexandrov and N. Mott, *Polaron & Bipolarons* (World Scientific, Singapore, 1995).
- [79] F. Marsiglio, Physica C **244**, 21 (1995).
- [80] V. V. Kabanov and D. K. Ray, Phys. Lett. A **186**, 438 (1994).
- [81] A. S. Alexandrov, V. V. Kabanov, and D. K. Ray, Phys. Rev. B **49**, 9915 (1994).
- [82] A. H. Romero, D. W. Brown, and K. Lindenberg, Phys. Lett. A **254**, 287 (1999).
- [83] A. H. Romero, D. W. Brown, and K. Lindenberg, Phys. Rev. B **60**, 14080 (1999).



- 
- [84] J. Ranninger and U. Thibblin, Phys. Rev. B **45**, 7730 (1992).
- [85] G. Wellein, H. Röder, and H. Fehske, Phys. Rev. B **53**, 9666 (1996).
- [86] G. Wellein and H. Fehske, Phys. Rev. B **56**, 4513 (1997).
- [87] J. M. Robin, Phys. Rev. B **56**, 13 634 (1997).
- [88] M. Capone, W. Stephan, and M. Grilli, Phys. Rev. B **56**, 4484 (1997).
- [89] M. Capone, S. Ciuchi, and C. Grimaldi, Europhys. Lett. **42**, 523 (1998).
- [90] W. Stephan, Phys. Rev. B **54**, 8981 (1996).
- [91] G. Hager, E. Jeckelmann, H. Fehske, and G. Wellein, J. of Comp. Phys. **194**, 795 (2004).
- [92] E. Jeckelmann and S. R. White, Phys. Rev. B **57**, 6376 (1998).
- [93] E. Jeckelmann, C. Zhang, and S. R. White, Phys. Rev. B **60**, 7950 (1999).
- [94] C. Zhang, E. Jeckelmann, and S. R. White, Phys. Rev. B **60**, 14 092 (1999).
- [95] A. Weiße, H. Fehske, G. Wellein, and A. R. Bishop, Phys. Rev. B **62**, R747 (2000).
- [96] J. Bonča, S. A. Trugman, and I. Batistic, Phys. Rev. B **60**, 1633 (1999).
- [97] L. C. Ku, S. A. Trugman, and J. Bonča, Phys. Rev. B **65**, 174306 (2002).
- [98] A. H. Romero, D. W. Brown, and K. Lindenberg, Phys. Rev. B **59**, 13728 (1999).
- [99] A. H. Romero, D. W. Brown, and K. Lindenberg, Phys. Rev. B **60**, 4618 (1999).
- [100] V. Cataudella, G. De Filippis, and G. Iadonisi, Phys. Rev. B **60**, 15 163 (1999).
- [101] H. Fehske, J. Loos, and G. Wellein, Phys. Rev. B **61**, 8016 (2000).
- [102] V. Cataudella, G. De Filippis, and G. Iadonisi, Phys. Rev. B **63**, 52406 (2001).
- [103] O. S. Barišić, Phys. Rev. B **65**, 144301 (2002).
- [104] O. S. Barišić, Phys. Rev. B **69**, 064302 (2004).
- [105] M. Acquarone, M. Cuoco, C. Noce, and A. Romano, Phys. Rev. B **63**, 035110 (2001).
- [106] J. E. Hirsch, D. J. Scalapino, R. L. Sugar, and R. Blankenbecler, Phys. Rev. Lett. **47**, 1628 (1981).
- [107] J. E. Hirsch, R. L. Sugar, D. J. Scalapino, and R. Blankenbecler, Phys. Rev. B **26**, 5033 (1982).

- [108] H. De Raedt and A. Lagendijk, Phys. Rev. Lett. **49**, 1522 (1982).
- [109] H. De Raedt and A. Lagendijk, Phys. Rev. B **27**, 6097 (1983).
- [110] H. De Raedt and A. Lagendijk, Phys. Rev. B **30**, 1671 (1984).
- [111] P. E. Kornilovitch, J. Phys.: Condens. Matter **9**, 10675 (1997).
- [112] P. E. Kornilovitch, Phys. Rev. Lett. **81**, 5382 (1998).
- [113] P. E. Kornilovitch, Phys. Rev. B **60**, 3237 (1999).
- [114] P. E. Kornilovitch and E. R. Pike, Phys. Rev. B **55**, R8634 (1997).
- [115] A. S. Mishchenko, N. V. Prokof'ev, A. Sakamoto, and B. V. Svistunov, Phys. Rev. B **62**, 6317 (2000).
- [116] S. Fratini, F. de Pasquale, and S. Ciuchi, Phys. Rev. B **63**, 153101 (2001).
- [117] S. Fratini and S. Ciuchi, Phys. Rev. Lett. **91**, 256403 (2003).
- [118] H. Lowen, Phys. Rev. B **37**, 8661 (1988).
- [119] E. Lieb and F. Y. Wu, Phys. Rev. Lett. **20**, 1445 (1968).
- [120] H. Fehske, J. Loos, and G. Wellein, Z. Phys. B **104**, 619 (1997).
- [121] E. V. L. de Mello and J. Ranninger, Phys. Rev. B **55**, 14 872 (1997).
- [122] J. Bonča, private communication.
- [123] F. Marsiglio, in *Recent Progress in Many-Body Theories*, edited by E. Schachinger, H. Mitter, and H. Sormann (Plenum Press, New York, 1995), Vol. 4.
- [124] R. Blankenbecler, D. J. Scalapino, and R. L. Sugar, Phys. Rev. D **24**, 2278 (1981).
- [125] D. J. Scalapino and R. L. Sugar, Phys. Rev. B **24**, 4295 (1981).
- [126] G. Levine and W. P. Su, Phys. Rev. B **42**, 4143 (1990).
- [127] G. Levine and W. P. Su, Phys. Rev. B **43**, 10 413 (1991).
- [128] P. Niyaz, J. E. Gubernatis, R. T. Scalettar, and C. Y. Fong, Phys. Rev. B **48**, 16 011 (1993).
- [129] J. E. Hirsch and E. Fradkin, Phys. Rev. Lett. **49**, 402 (1982).
- [130] E. Fradkin and J. E. Hirsch, Phys. Rev. B **27**, 1680 (1983).
- [131] J. E. Hirsch and E. Fradkin, Phys. Rev. B **27**, 4302 (1983).

- 
- [132] R. T. Scalettar, N. E. Bickers, and D. J. Scalapino, Phys. Rev. B **40**, 197 (1989).
- [133] R. M. Noack, D. J. Scalapino, and R. T. Scalettar, Phys. Rev. Lett. **66**, 778 (1991).
- [134] F. Marsiglio, Phys. Rev. B **42**, 2416 (1990).
- [135] R. P. Feynman, Phys. Rev. **97**, 660 (1955).
- [136] H. De Raedt and A. Lagendijk, Z. Phys. B: Condens. Matter **65**, 43 (1986).
- [137] N. V. Prokof'ev and B. V. Svistunov, Phys. Rev. Lett. **81**, 2514 (1998).
- [138] E. Berger, P. Valášek, and W. von der Linden, Phys. Rev. B **52**, 4806 (1995).
- [139] R. H. McKenzie, C. J. Hamer, and D. W. Murray, Phys. Rev. B **53**, 9676 (1996).
- [140] P. Sengupta, A. W. Sandvik, and D. K. Campbell, Phys. Rev. B **67**, 245103 (2003).
- [141] G. G. Batrouni and R. T. Scalettar, in *Quantum Monte Carlo Methods in Physics and Chemistry*, edited by M. P. Nightingale and C. J. Umrigar (Kluwer Academic Publishers, Dordrecht, 1998), p. 65.
- [142] M. Brunner, S. Capponi, F. F. Assaad, and A. Muramatsu, Phys. Rev. B **63**, R180511 (2001).
- [143] J. N. Kapur and H. K. Kesavan, *Entropy Optimization Principles with Applications* (Academic Press, San Diego, 1992).
- [144] S. Chandrasekharan and U. Wiese, Phys. Rev. Lett. **83**, 3116 (1999).
- [145] J. E. Hirsch, Phys. Rev. B **34**, 3216 (1986).
- [146] E. Y. Loh Jr. *et al.*, Phys. Rev. B **41**, 9301 (1990).
- [147] A. S. Alexandrov and N. F. Mott, Rep. Prog. Phys. **57**, 1197 (1994).
- [148] A. S. Alexandrov, V. V. Kabanov, and N. F. Mott, Phys. Rev. Lett. **77**, 4796 (1996).
- [149] M. H. Cohen, E. N. Economou, and C. M. Soukoulis, Phys. Rev. B **29**, 4496 (1984).
- [150] D. Emin, J. Ye, and C. L. Beckel, Phys. Rev. B **46**, 10 710 (1992).
- [151] A. La Magna and R. Pucci, Phys. Rev. B **55**, 14 886 (1997).
- [152] L. Proville and S. Aubry, Physica D **113**, 307 (1998).
- [153] L. Proville and S. Aubry, Eur. Phys. J. B **11**, 41 (1999).
- [154] L. Proville and S. Aubry, Eur. Phys. J. B **15**, 405 (2000).

- [155] G. De Filippis *et al.*, Phys. Rev. B **64**, 155105 (2001).
- [156] E. V. L. de Mello and J. Ranninger, Phys. Rev. B **58**, 9098 (1998).
- [157] H. Fehske, H. Röder, G. Wellein, and A. Mistriotis, Phys. Rev. B **51**, 16 582 (1995).
- [158] J. Bonča, T. Katrašnik, and S. A. Trugman, Phys. Rev. Lett. **84**, 3153 (2000).
- [159] A. Macridin, G. A. Sawatzky, and M. Jarrell, Phys. Rev. B **69**, 245111 (2004).
- [160] J. Bonča and S. A. Trugman, Phys. Rev. B **64**, 094507 (2001).
- [161] A. Weiße, G. Wellein, and H. Fehske, in *High Performance Computing in Science and Engineering '01*, edited by E. Krause and W. Jäger (Springer-Verlag, Heidelberg, 2002), p. 131.
- [162] H. Fehske *et al.*, Phys. Rev. B **69**, 165115 (2004).
- [163] S. El Shawish, private communication (2004).
- [164] E. Y. Loh and J. E. Gubernatis, in *Electronic Phase Transitions*, edited by W. Hanke and Y. V. Kopaev (Elsevier Science Publishers, North-Holland, Amsterdam, 1992), Chap. 4.
- [165] C. Hartinger, F. Mayr, A. Loidl, and T. Kopp, cond-mat/0406123 (unpublished).
- [166] C. Hartinger *et al.*, Phys. Rev. B **69**, R100403 (2004).
- [167] R. H. McKenzie, C. J. Hamer, and D. W. Murray, Phys. Rev. B **53**, 9676 (1996).
- [168] A. Weiße and H. Fehske, Phys. Rev. B **58**, 13 526 (1998).
- [169] R. J. Bursill, R. H. McKenzie, and C. J. Hamer, Phys. Rev. Lett. **80**, 5607 (1998).
- [170] H. Zheng, D. Feinberg, and M. Avignon, Phys. Rev. B **39**, 9405 (1989).
- [171] H. Zheng and M. Avignon, Phys. Rev. B **58**, 3704 (1998).
- [172] Q. Wang, H. Zheng, and M. Avignon, Phys. Rev. B **63**, 014305 (2000).
- [173] C. A. Perroni *et al.*, Phys. Rev. B **67**, 214301 (2003).
- [174] M. Capone, M. Grilli, and W. Stephan, Eur. Phys. J. B **11**, 551 (1999).
- [175] M. Capone and S. Ciuchi, Phys. Rev. Lett. **91**, 186405 (2003).
- [176] D. M. Edwards, A. C. M. Green, and K. Kubo, J. Phys.: Condens. Matter **11**, 2791 (1999).

- [177] A. C. M. Green and D. M. Edwards, *J. Phys.: Condens. Matter* **11**, 10511 (1999), 2000, 12(E), (9107).
- [178] J. Hubbard, *Proc. R. Soc. London* **281**, 401 (1964).
- [179] A. S. Alexandrov and A. M. Bratkovsky, *J. Phys.: Condens. Matter* **11**, L531 (1999).
- [180] D. S. Dessau *et al.*, *Phys. Rev. Lett.* **81**, 192 (1998).
- [181] S. Pairault, D. Sénéchal, and A.-M. S. Tremblay, *Phys. Rev. Lett.* **80**, 5389 (1998).
- [182] S. Pairault, D. Sénéchal, and A.-M. S. Tremblay, *Eur. Phys. J. B* **16**, 85 (2000).
- [183] J. E. Hirsch, *Phys. Rev. B* **31**, 4403 (1985).
- [184] E. K. U. Gross and E. Runge, *Vielteilchentheorie* (B. G. Teubner, Stuttgart, 1986).
- [185] W. von der Linden, R. Preuss, and W. Hanke, *J. Phys.: Condens. Matter* **8**, 3881 (1996).
- [186] S. Sykora *et al.*, cond-mat/0402184 (unpublished).
- [187] P. E. Kornilovitch, *Europhys. Lett.* **59**, 735 (2002).
- [188] S. R. White, *Phys. Rev. B* **44**, 4670 (1991).



# Acknowledgments

In the two and a half years of work on my dissertation, numerous people contributed in fairly different ways, and it stands to reason to begin with an aspect of utmost importance. Two years of my work were financially supported by the Doctoral Scholarship Program of the Austrian Academy of Sciences (DOC). Additionally, a three-month period at the beginning of my PhD time, as well as several stays abroad have been subsidized by the Austrian Science Fund project No. P15834, and the TU Graz, respectively.

Concerning the scientific part, I first would like to thank my supervisor, Prof. Wolfgang von der Linden, who—despite so many other things filling up his time table—always tried to solve open problems and to answer my questions. Second, I am very grateful to Holger Fehske, David Edwards, Hans Gerd Evertz, Samir El Shawish, Eugene Sherman and Gerhard Wellein for helpful discussions and fruitful collaboration. Furthermore, I would like to acknowledge support by Maria Daghofer, Christine Gabriel, Andreas Hirczy, Winfried Koller, Thomas Lang, Danilo Neuber and Christian Pfaffel. In particular, I have enjoyed sharing a room, discussing physical problems and collaborating with Markus Aichhorn. I would also like to thank David Eagles for stimulating the calculations of the spectral function of the Holstein-Hubbard bipolaron. Finally, some very helpful proof-reading has been done by M. Aichhorn, T. Lang, D. Neuber and G. Wellein.

Turning to the equally important moral and personal support, I want to thank my parents Ferdinand and Verena Hohenadler, who gave me the opportunity to experience the joy of higher education. Last but definitely not least, I am deeply indebted to Kathrin Weinhandl, for continuously expressing her love, helping me to get over less successful times in the course of my PhD work, and for enduring all the weekends full of work.





# Curriculum Vitae

## PERSONAL DETAILS

Name: Martin Hohenadler  
Academic Degree: Dipl.-Ing.  
Date of birth: August 2, 1979  
Place of birth: Graz, Austria  
Nationality: Austrian

## EDUCATION

Since 02/2002: PhD at the Institute for Theoretical and Computational  
Physics (TU Graz), supervised by Prof. W. von der Linden  
28.01.2002 Diploma with first-class honors after 9 semesters  
05–12/2001 Diploma thesis:  
“Colossal Magnetoresistance: spectral properties of the Holstein  
double-exchange model and application to manganites”  
Supervisors:  
Prof W. von der Linden (TU Graz),  
Prof D. M. Edwards (Imperial College London)  
10/1997–01/2002 Studies of Technical Physics at the TU Graz

## AWARDS

2002 DOC Scholarship from the Austrian Academy of Sciences  
2002 “Würdigungspreis des Bundesministeriums für Bildung, Wissenschaft  
und Kultur für herausragende Studienleistungen”  
(appreciation of outstanding success in university studies from the  
Federal Ministry for Education, Science and Culture)  
2001 Grant from the State of Styria (Land Steiermark)  
2001 Scholarship from the Industriellenvereinigung Steiermark  
2000 University grant for excellent success from the TU Graz  
 (“Leistungsstipendium”)  
2000, 2003 University grants for research work at Imperial College London  
 (“Förderungsstipendium”)



# Publications

1. M. Hohenadler and D. M. Edwards,  
*Spectral properties of the Holstein double-exchange model  
and application to manganites*,  
J. Phys. Condens. Matter **14**, 2547-2560 (2002)
2. M. Hohenadler, M. Aichhorn, and W. von der Linden,  
*Spectral function of electron-phonon models by cluster perturbation theory*,  
Phys. Rev. B **68**, 184304 (2003)
3. M. Hohenadler, H. G. Evertz, and W. von der Linden,  
*Quantum Monte Carlo and variational approaches to the Holstein model*,  
Phys. Rev. B **69**, 024301 (2004)
4. M. Aichhorn, M. Hohenadler, E. Ya Sherman, J. Spitaler,  
C. Ambrosch-Draxl, and H. G. Evertz,  
*Charge ordering in quarter-filled ladder systems coupled to the lattice*,  
Phys. Rev. B **69**, 245108 (2004)
5. M. Hohenadler, M. Aichhorn, and W. von der Linden,  
*Spectral function of the Holstein-Hubbard bipolaron*,  
cond-mat/0405391



## Legend of important symbols and abbreviations

$t$	Hopping integral
$W$	Bare bandwidth [Eq. (1.8)]
$\lambda$	Electron-phonon coupling constant [Eq. (1.18)]
$\bar{\omega}$	Adiabatic ratio [Eq. (1.19)]
$E_P$	Polaron binding energy [Eq. (1.20)]
$\beta$	Inverse temperature
$\Delta\tau$	Trotter discretization parameter [Eq. (2.15)]
$\gamma$	Parameter of the Lang-Firsov transformation [Eq. (3.10)]
$\bar{U}$	Hubbard repulsion [Eq. (4.1)]
$T_C$	Curie temperature
$\mu$	Chemical potential
$L$	Number of time slices, number of Lanczos iterations
$N$	Linear system size
$\eta$	Artificial smearing parameter
ARPES	Angle-resolved photoemission spectroscopy
CDW	Charge density wave
CMR	Colossal magnetoresistance
CPA	Coherent potential approximation
CPT	Cluster perturbation theory
DE	Double exchange
DMFT	Dynamical mean field theory
DMRG	Density matrix renormalization group
DOS	Density of states
ED	Exact diagonalization
HLF	Holstein Lang-Firsov
JT	Jahn-Teller
KPM	Kernel polynomial method
LF	Lang-Firsov
MC	Monte Carlo
MEM	Maximum entropy method
SCPT	Strong-coupling perturbation theory
QMC	Quantum Monte Carlo
QP	Quasiparticle
VDM	Variational diagonalization method
VPA	Variational polaron approach

